

NASA CR- 159932

41

Nd:YAG LASER DEVELOPMENT FOR SPACEBORNE LASER RANGING SYSTEM

(NASA-CR-159932) Nd:YAG DEVELOPMENT FOR SPACEBORNE LASER RANGING SYSTEM Final Report, Jan. 1976: - Feb. 1979 (International Laser Systems, Inc.) 310 p HC A14/MF A01

N79-24329

Unclas
CSCS 20E G3/36 22953

Lawrence L. Harper
 K. Edward Logan
 Robert H. Williams
 Don A. Stevens
 International Laser Systems, Inc.
 3404 N. Orange Blossom Trail
 Orlando, Florida 32804

FEBRUARY 1979

Final Report for Period January 1976 - February 1979



Sponsor: NASA GODDARD SPACE FLIGHT CENTER, Greenbelt, MD 20771
 Contract Number: NAS5-22916
 Technical Officer: John J. Degnan

BIBLIOGRAPHIC DATA SHEET

1. Report No.	2. Government Accession No.	3. Recipient's Catalog No.	
4. Title and Subtitle ND:YAG LASER DEVELOPMENT FOR SPACEBORNE LASER RANGING SYSTEM		5. Report Date February 1979	6. Performing Organization Code
7. Author(s) Lawrence L. Harper, K. Edward Logan, Robert H. Williams, Don A. Stevens		8. Performing Organization Report No.	
9. Performing Organization Name and Address International Laser Systems, Inc. 3404 North Orange Blossom Trail Orlando, FL 32804		10. Work Unit No.	11. Contract or Grant No. NAS5-22916
12. Sponsoring Agency Name and Address NASA GODDARD SPACE FLIGHT CENTER Electro-Optics Branch Greenbelt, Maryland 20771		13. Type of Report and Period Covered Final Report January 1976 to February 1979	
		14. Sponsoring Agency Code	
15. Supplementary Notes			
16. Abstract. This report summarizes the results of the development of a unique mode-locked laser device to be utilized in future NASA space-based, ultra-precision laser ranging systems. The engineering breadboard constructed proved the feasibility of the pump-pulsed, actively modelocked, PTM Q-switched Nd:YAG laser concept for the generation of subnanosecond pulses suitable for ultra-precision ranging. The laser breadboard also included a double-pass Nd:YAG amplifier and provision for a Type II KD*P frequency doubler. The specific technical accomplishment was the generation of single 150 psec, 20-mJ pulses at 10 gpps at a wavelength of 1.064 micrometers with 25 dB suppression of pre-and post-pulses. The significant hardware implementations within the engineering breadboard were the rugged, crossed TIR prism, integral Invar optical bed subsystem; the pulsed electro-optical KD*P modelocker; and the pre-lase and switching synchronization control electronic circuits. The success of these subsystems establishes the engineering breadboard as the actual foundation for the planned engineering prototype development.			
17. Key Words (Selected by Author(s)) Laser, Nd:YAG, Modelocked, PTM Q-Switched, Ranging, Space-based, Pulsed		18. Distribution Statement	
19. Security Classif. (of this report) Unclassified	20. Security Classif. (of this page)	21. No. of Pages 288	22. Price*

Acknowledgements

The authors thank Thomas Johnson of the NASA Goddard Space Flight Center for providing access to a computer-controlled streak camera utilized for the pulsewidth measurements. Recognition is also extended to Thomas Johnson, Jeffrey Lesner, and Mark Weiner of NASA for assistance with these measurements. Appreciation is extended to the ILS machine and optical shops for the precision fabrication of the opto-mechanical components. Appreciation is also expressed to Robert Anderson and Thomas Penrose of ILS for the mechanical design of the optical bed and to Robert Hinds of ILS for the fabrication of the optical bed.

TABLE OF CONTENTS

<u>Section</u>	<u>Title</u>	<u>Page</u>
I	INTRODUCTION	1-1
	A. Program Objectives	1-1
	B. Hardware Design Overview	1-2
	C. Status Summary	1-7
II	THEORY	2-1
	A. Concept Analysis	2-1
	B. Q-switched Laser Model	2-5
	C. Transient Modelocking	2-16
	D. Prelase Concepts	2-23
	E. Amplifier Model	2-24
III	DESIGN	3-1
	A. System Overview	3-1
	1. Hardware Description	3-1
	2. Mechanical Configuration	3-4
	3. Electronic System Overview	3-5
	4. Optical Concepts	3-9
	B. Optical Design	3-12
	1. Laser Damage Evaluation	3-12
	2. Resonator Design	3-17
	3. Oscillator Optical Design	3-19
	4. Modulator Analysis	3-23
	5. Pump Cavity Design	3-27
	6. Amplifier Optical System	3-29
	C. Electronic Design	3-32
	1. Modelocker Electronics	3-32
	2. Switching and Control Electronics	3-43
	3. Power Supply	3-52
	D. Mechanical Design	3-66
	1. Transmitter Packaging	3-66
	2. Optical Bed	3-73
	3. TIR Prism Mounting	3-75
	4. Q-switch Modulator Mounting	3-76
	5. Modelocker Cell and RF Cavity	3-76
	6. Pump Cavity	3-77
	7. Passive Optical Mounts	3-78

TABLE OF CONTENTS (cont'd)

<u>Section</u>	<u>Title</u>	<u>Page</u>
IV	EXPERIMENTAL RESULTS	4-1
A.	Electronic Subsystem Tests	4-1
	1. RF Burst Envelope	4-3
	2. Frequency Synthesizer Stability Measurement	4-5
	3. Q-switch/Dump Switch Waveform Measurements	4-9
B.	System Optical Alignment	4-19
	1. Alignment Overview	4-19
	2. TIR Prism Alignment	4-22
	3. Rod-Wedge Alignment	4-24
	4. KD*P Cell-Mirror Leg Alignment	4-24
	5. Mirror-Rod Alignment	4-34
	6. Risley Prism-Polarizer Alignment	4-35
	7. Dynamic Laser Alignment	4-35
C.	Laser Performance Evaluation	4-41
	1. Introduction	4-41
	2. Normal Mode Testing	4-41
	3. PTM Q-switch Testing	4-41
	4. Modelocking Tests	4-49
	5. Amplifier Testing	4-56
D.	Radiation Control Evaluation	5-58
V	CONCLUSIONS AND RECOMMENDATIONS	5-1
	REFERENCES	
APPENDIX A	SPACEBORNE ELECTRONIC DESCRIPTIONS	A-1
APPENDIX B	GENERATION BREAKDOWN	B-1
APPENDIX C	OPTICAL BED THERMAL ANALYSIS	C-1
APPENDIX D	ELECTRONIC DESIGN REVISIONS	D-1
APPENDIX E	AMPLIFIER SUBSYSTEM OPTICAL DRAWINGS	E-1

LIST OF ILLUSTRATIONS

<u>Figure</u>	<u>Title</u>	<u>Page</u>
1-1	Optical System Layout	1-5
1-2	Hardware Subassemblies	1-6
2-1	Simplified Oscillator Optical Diagram	2-2
2-2	Spaceborne Laser Event Sequence	2-2
2-3	Theory Synthesis Diagram	2-4
2-4	Energy Levels and Energy Transfer in Nd:YAG Relevant to Q-switching	2-6
2-5	PTM Q-switched Energy Input/Output Curves vs Resonator Losses	2-13
2-6	Envelope Pulsewidth vs Resonator Losses	2-14
2-7	Modelocked Pulse Amplitude vs Time	2-15
2-8	Nd:YAG Gain vs Frequency	2-18
2-9	Pulsewidth vs Prelase Time	2-22
2-10	Amplifier Energy Extraction as Function of Oscillator Energy Density	2-29
3-1	Hardware Subassemblies	3-2
3-2	System Block Diagram	3-3
3-3	Optical Bed Sketch	3-6
3-4	Electronic System Block Diagram	3-8
3-5	Transmitter Electronic System	3-10
3-6	Spaceborne Oscillator Optical Configuration	3-11
3-7	Spaceborne Amplifier Optical Configuration	3-13
3-8	Dependence of Laser Rod Focal Length on Pump Level	3-20
3-9	Spaceborne Resonator Spot Size Characteristics	3-21
3-10	Spaceborne Oscillator Optical Configuration	3-22
3-11	Typical ILS Pump Cavity	3-27
3-12	Spaceborne Amplifier Optical Configuration	3-30
3-13	Spaceborne Laser Command Sequence and Lase Energy Sequence	3-33
3-14	Electronic System Block Diagram	3-34
3-15	Modelocker Electronics	3-35
3-16	RF Amplifier Block Diagram	3-37
3-17	Frequency Synthesizer Diagram	3-38
3-18	Modelocker RF Cavity Construction	3-40
3-19	RF Cavity Circuit	3-41
3-20	Transmitter Electronic System	3-44
3-21	Simplified Q-switch Interface	3-45

LIST OF ILLUSTRATIONS (cont'd)

<u>Figure</u>	<u>Title</u>	<u>Page</u>
3-22	Simplified Pockels Cell Drive Configuration	3-46
3-23	Effective Capacitance Load for Avalanche Driver	3-48
3-24	Q-switch Interface Schematic	3-49
3-25	Electronic System Block Diagram	3-53
3-26	Spaceborne Power Supply	3-55
3-27	Hardware Subassemblies	3-56
3-28	Spaceborne Power Supply	3-59
3-29	Electronic System Block Diagram	3-60
3-30	Laser Rangefinder Mechanical Assembly	3-67
3-31	Laser Rangefinder Mechanical Assembly	3-68
4-1	Modelock Cell Voltage Measurement Setup	4-2
4-2	Modelock Cell Voltage Waveforms	4-4
4-3	Frequency Synthesizer Stability Measurement Setup	4-6
4-4	Simplified Pockels Cell Drive Configuration ..	4-10
4-5	Effective Capacitance Load for Avalanche Driver	4-13
4-6	Q-switch Interface Schematic	4-15
4-7	Q-switch and PTM Dump Switching Voltage Waveforms	4-18
4-8	Oscillator Optical Diagram	4-20
4-9	Optical Bed Sketch	4-21
4-10	TIR Prism #1	4-23
4-11	Oscillator Laser Rod	4-25
4-12	Compensating Wedge	4-26
4-13	Rod-Wedge Leg Alignment	4-27
4-14	KD*P Crystal	4-28
4-15	KD*P Cell Windows	4-29
4-16	Laser Mirror	4-30
4-17	KD*P Cell-Mirror Leg Alignment (Angles Exaggerated for Clarity)	4-31
4-18	KD*P Cell Deviation Measurement	4-33
4-19	Mirror-Rod Alignment Verification	4-36
4-20	Oscillator Polarizer	4-37
4-21	Risley Prism	4-38
4-22	Risley Prism-Polarizer Alignment (TIR Fold shown in orthogonal plane to actual case for clarity)	4-39
4-23	Normal Mode Performance Curve	4-42

LIST OF ILLUSTRATIONS (cont'd)

<u>Figure</u>	<u>Title</u>	<u>Page</u>
4-24	PTM Timing Synchronization	4-44
4-25	PTM Q-switched Performance Curves (Electronic Timing)	4-45
4-26	PTM Q-switched Performance Curve (Pre-lase and Active Timing)	4-46
4-27	Typical PTM Q-switched Pulse	4-47
4-28	TEM ₀₀ Mode Verification	4-48
4-29	Modelocked Normal Mode Pulse	4-50
4-30	Normal Mode Modelocked Pulses	4-50
4-31	Intracavity Radiation for PTM Q-switched, Modelocked Operation	4-51
4-32	Typical Picosecond Pulse (Temporal Resolution - 700 psec)	4-51
4-33	Picosecond Pulse Showing Pre- and Post-Pulse Suppression	4-52
4-34	Picosecond Pulse Showing Pre- and Post-Pulses	4-52
4-35	Typical Pulse Profiles for Optimum Modelocking (Time Base: 200 = 1 nsec)	4-54
4-36	Oscillator/Amplifier Performance	4-57
4-37	Normal Mode Single Pulse Profile	4-59
4-38	Q-switch Interface Schematic	4-61
4-39	Radiation Control Schematic	4-62
4-40	Radiation Control Schematic - Revised	4-64

LIST OF TABLES

<u>Table</u>	<u>Title</u>	<u>Page</u>
1-1	Spaceborne Program Objectives	1-3
1-2	Spaceborne Laser Specifications	1-4
1-3	Spaceborne Breadboard Design Features	1-8
1-4	Oscillator Performance	1-9
2-1	Energy Transfer Times	2-9
3-1	Critical Power of Selected Optical Media	3-15
3-2	TEM ₀₀ Mode Laser Damage Thresholds	3-16
3-3	TEM ₀₀ Mode Laser Damage Threshold of Dielectric Coatings	3-16
3-4	Properties of KD*P	3-23
3-5	PFN Parameters	3-65
4-1	Oscillator Performance	4-55

Section I

INTRODUCTION

GENERAL - In 1975, ILS was funded by the Instrument Electro-Optics Group of NASA Goddard to engage in the development of a state-of-the-art laser transmitter that could serve as one element of a visible, precision optical rangefinder. The scope of the current contract (NAS5-22916) includes a detailed design analysis of the system and development and test of an operational breadboard that would have the potential for spaceborne qualification. NASA's interest in pursuing a development of this nature stems basically from the recognized need to satisfy geophysical measurement requirements generated by the NASA Earth and Ocean Physics Applications Program (EOPAP). One such application centers upon the use of a spaceborne laser terminal which can range to 2-cm accuracy against ground based retroreflectors. The laser system developed to meet these requirements consisted of a Nd:YAG, sub-nanosecond pulse oscillator, a double-pass Nd:YAG amplifier, and a Type II KD*P frequency doubler. As originally conceived, the program called for completion of preliminary system tests of the engineering model in 1978 followed by an initial space flight demonstration aboard Spacelab in the 1980-81 time frame.

This report describes the results of the design and analysis efforts undertaken to develop the Spaceborne transmitter design and includes details of the constructed hardware. Breadboard performance is also reviewed covering evaluation testing that has been performed to date. A brief overview of the program technical objectives highlighting key physical/functional features of the assembled hardware is given below.

A. PROGRAM OBJECTIVES

The contract statement of work and performance specification are summarized in NASA RFP Solicitation 5-28413/227. The principal elements of the program call for the development and test of the laser transmitter in two phases: The Phase I activity centering primarily on the detailed design, analyses and preliminary evaluation of breadboard performance whereas the Phase II activity (as originally scoped) related to an advanced development leading to the delivery of an engineering prototype suitable for integration into NASA's precision rangefinder engineering model. For background,

it is work noting that early in the program the decision was made to modify the program objectives to reflect construction of the optical bed engineering prototype as part of the Phase I effort. The unanticipated complexity of this optical bed resulted in schedule delays and cost increases in completing the originally forecasted Phase I milestones. However, it is felt the decision to go directly to an optical bed prototype design in the initial program phase could result in savings both with regard to total program cost and hardware delivery schedule. The optical bed design is definitely suited for implementation in Phase II. Table 1-1 summarizes details of the program objectives as they are presently defined.

B. HARDWARE DESIGN OVERVIEW

Based upon rationale to be presented in subsequent sections of this report, a flashlamp-pumped, Q-switched, actively modelocked, and cavity-dumped laser oscillator optical configuration is found to have the highest potential for achieving the level of performance specified for the Spaceborne laser transmitter subsystem. These performance specifications are outlined in Table 1-2. The requirement to generate very narrow optical pulses at reasonably high output pulse energies at a wavelength of 532 nm necessitates implementing an oscillator-amplifier optical configuration with the oscillator operating in what is commonly referred to as pulse transmission mode (PTM) operation. A view of the overall optical system layout is depicted in Figure 1-1. The layout basically reflects implementation of an oscillator-amplifier configuration with provisions incorporated for output frequency doubling. In the oscillator section, two Pockels cells are used to accommodate both modelocking and simultaneous Q-switching operation with single-pulse selection. The oscillator derived output is amplified and frequency doubled to produce the desired pulse output. The optical system is part of the transmitter assembly; remaining portions of the system include:

- A power supply (specially designed for operation from 28 V-dc prime power);
- A liquid-to-air, closed-loop cooling system; and
- An ultrastable RF signal generator module used to actively modelock the system.

A view of the assembled hardware subassemblies is shown in Figure 1-2.

Table 1-1. Spaceborne Program Objectives

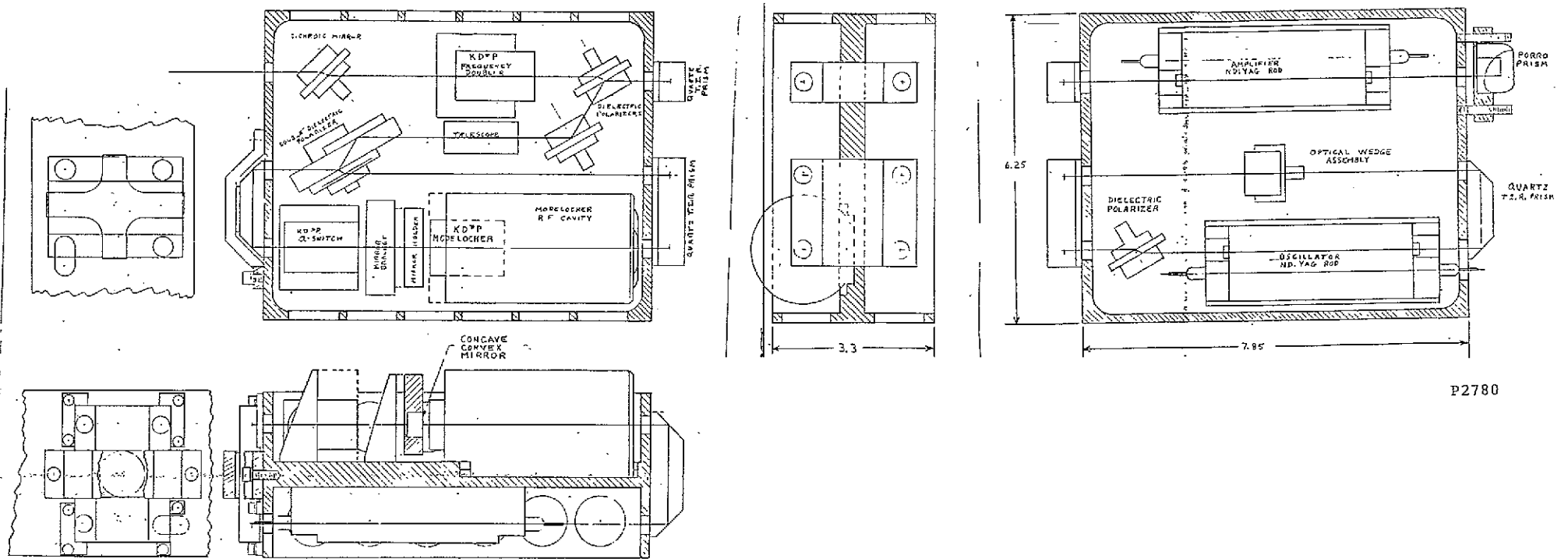
Phase	Objectives
I	<ol style="list-style-type: none"> 1. Analyze laser subsystem and system concepts. 2. Design and fabricate experimental breadboard incorporating PTM Q-switching and active modelocking. 3. Characterize system performance with principal emphasis on oscillator evaluation.
II	<ol style="list-style-type: none"> 1. Generate detailed technical/program plan. 2. Complete experimental breadboard evaluation including SHG testing. 3. Redesign breadboard to reconfigure for deliverable hardware. 4. Test and qualify deliverable prototype.

Table 1-2. Spaceborne Laser Specifications

Characteristic	Specification
Output Energy	0.025 J/pulse
Pulse Rate	10 pps
Pulsewidth (10% PTS)	200 psec
Wavelength	532 nm
Beam Divergence	$\leq 2X$ diffraction limit
Transverse Mode	TEM ₀₀
Polarization	Linear
Pulse Amplitude Stability	$\pm 5\%$ short-term (min) $\pm 15\%$ long-term (days)
Prime Power	50 to 75 W
Lifetime (50% OUTPUT)	10^8 pulses
Volume	1.5 ft ³ (0.023 m ³)
Weight	35 lb (15.9 kg)
System Thermal Sink	20°C

FOLDOUT FRAME

EOLDOUT FRAME 2



P2780

Figure 1-1. Optical System Layout

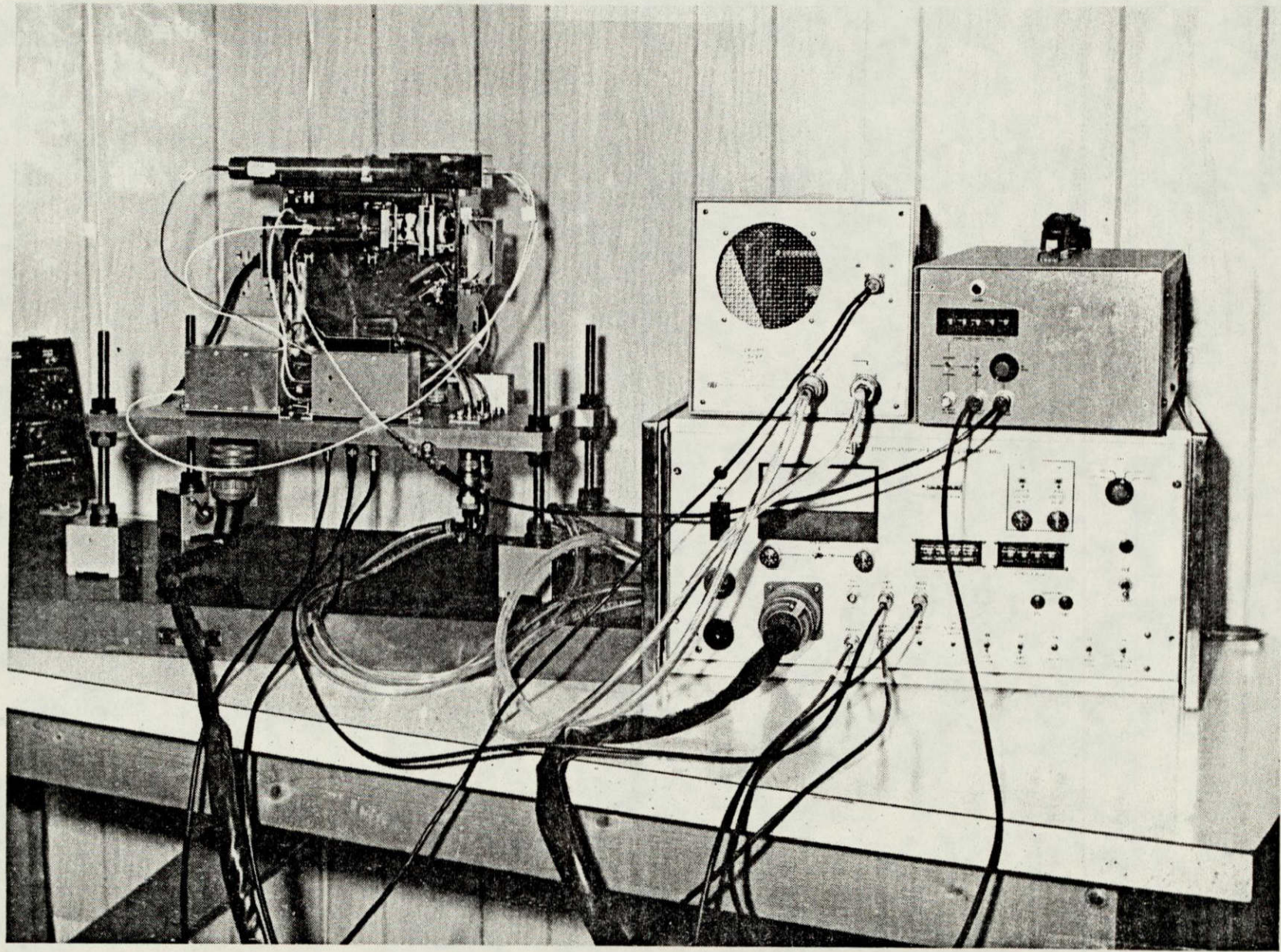


Figure 1-2. Hardware Subassemblies

The Spaceborne laser system developed on the program represents an advancement in the state-of-the-art of neodymium-doped, yttrium-aluminum-garnet (Nd:YAG) laser devices. Several of the fundamental design concepts implemented in this system previously have been experimentally confirmed. However, to the knowledge of ILS they have not been synthesized in one laser device prior to this program. Additionally, the Spaceborne laser implements this synthesis of concepts in a hardware design that ILS believes to be space-qualifiable. The system incorporates many unique design and operational control features which are summarized in Table 1-3. As configured, the system requires a maximum prime power input on the order of 300 W and weighs approximately 150 lb.

C. STATUS SUMMARY

As of the submittal of this report, essentially all Phase I task objectives have been met with the singular exception of experimentally demonstrating frequency-doubled operation. The performance achieved for the modelocked oscillator for optimum operation is summarized in Table 1-4. The 1.0 mJ/pulse energy is a limit for reliable operation imposed by laser damage constraints. The maximum picosecond pulse energy generated by the oscillator was 3.0 mJ. The maximum pulse energy generated by the oscillator and double-pass amplifier when modelocking was 28 mJ with an approximate pulsewidth of 300 psec with operation at 10 pps. The pre- and post-pulse suppression following the amplifier was 25 db.

Table 1-3. Spaceborne Breadboard Design Features

Component	Feature
<u>Transmitter</u>	
Optical Construction	Crossed TIR prism, common-mirror resonator.
	Double-pass amplifier utilizing phase retarder/mirror Porro prism.
	Dual Pockels cells for PTM Q-switching and modelocking.
Electronic Control	PTM synchronization circuit.
	Prelase radiation control loop.
Mechanical Design	Integral Invar optical bed.
<u>Power Supply</u>	Flyback design.
	Flashlamp simmer mode.
<u>Cooling Supply</u>	Closed-loop liquid cooling.

Table 1-4. Oscillator Performance

Parameter	Value
Pulse Energy	1.0 mJ
Efficiency	0.05%
Pulsewidth	150 psec (FWHM)
Beam Divergence	0.98 mrad
Mode Diameter (3ω)	1.92 mm
Pulse Rate	10 pps
Pre- and Post-Pulse Suppression	30 dB
Pulse Amplitude Stability	$\pm 10\%$

Section II

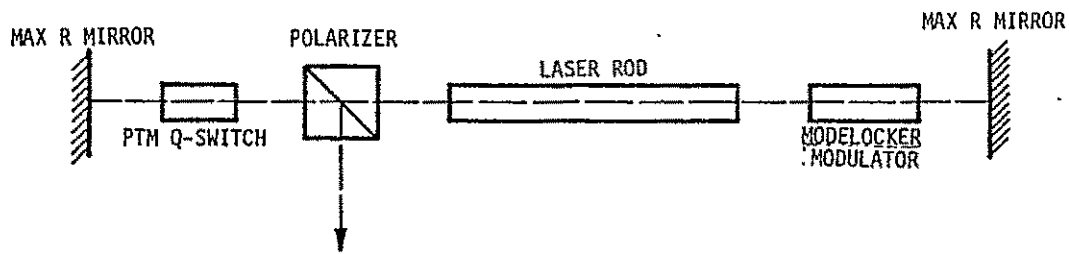
THEORY

A. CONCEPT ANALYSIS

The system concept implemented in the Spaceborne Laser is a flashlamp-pumped, actively modelocked, PTM Q-switched Nd:YAG laser oscillator utilizing prelude and a double-pass Nd:YAG laser amplifier. The laser oscillator concept will be explained in detail in the following paragraphs. Following this explanation will be an overview of the synthesis of theories which provides a mathematical description of the Spaceborne Laser System.

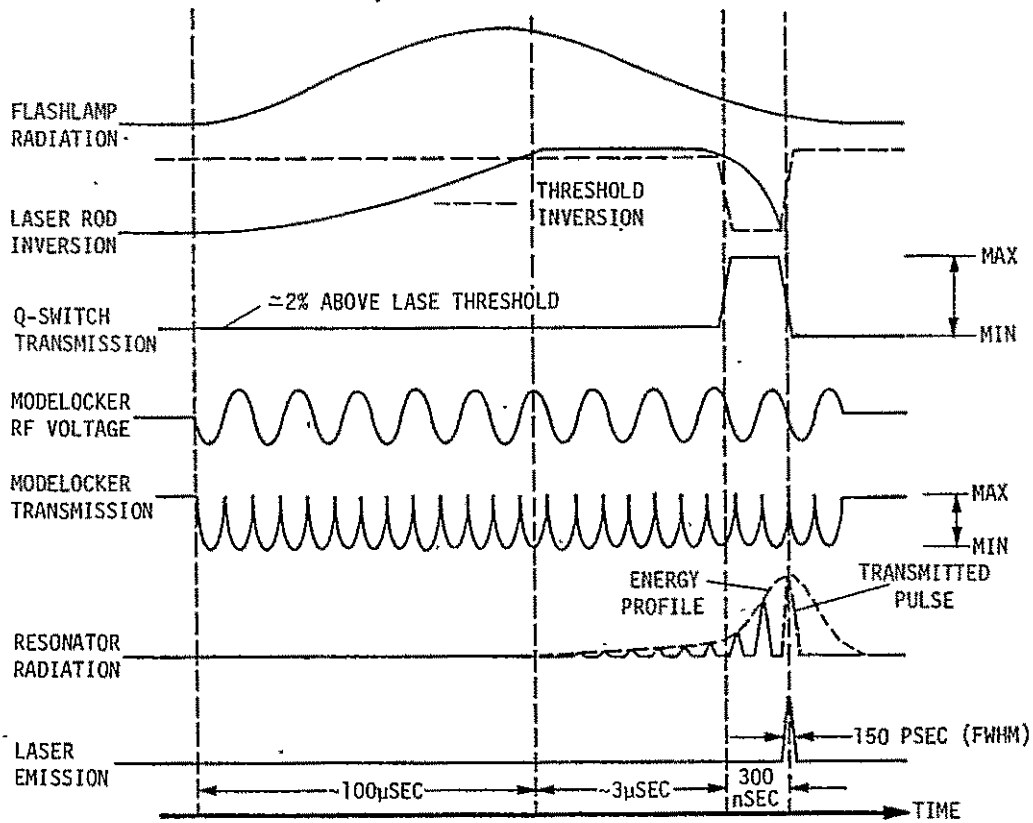
An optical diagram indicating the essential elements necessary to implement the Spaceborne Laser oscillator is given in Figure 2-1. The diagram shows maximum reflectance mirrors terminating the oscillator, a Nd:YAG laser rod, a kickout polarizer, a modelocking modulator, and a Q-switch modulator. Figure 2-2 is a diagram illustrating the operational event sequence for the flashlamp-pumped, actively modelocked, PTM Q-switched laser oscillator. (The time scale for each event is compressed or expanded to simplify illustration of the actual event sequence.) The dynamics of the Spaceborne Laser can be divided naturally into three temporal intervals as indicated in Figure 2-2. Flashlamp and modelocking modulator turn-on simultaneously initiate interval I. This interval is terminated when prelude radiation begins near the time at which the energy stored in the laser rod is maximum.

The dynamics of interval II involve the most fundamental idea of the Spaceborne Laser concept. During this interval prelude radiation is compressed to a subnanosecond pulse via repeated passes through a modulator whose frequency is synchronized to the photon round-trip frequency of the laser resonator. Given fixed laser and modelocking modulator parameters, the pulsewidth at the end of the prelude interval depends on the number of round-trip passes through the modelocking modulator, i.e., the length of the prelude interval.



P1289

Figure 2-1. Simplified Oscillator Optical Diagram



P4733

Figure 2-2. Spaceborne Laser Event Sequence

The buildup time ($\sim 3\mu\text{sec}$) of the first normal mode pulse emitted by the laser is the prelude interval for the present laser device. Radiation feedback control of the Q-switch transmission was initially attempted to extend and stabilize the prelude radiation duration. This approach was unsuccessful as implemented by two different experimental circuit designs. The details of these designs and the results achieved are given in a later section of this report.

Interval III of the Spaceborne Laser event sequence is initiated by Q-switching — that is, the Pockels cell transmission is maximized. The subnanosecond pulse is thus trapped between two maximum reflectance mirrors and is regeneratively amplified by the oscillator laser rod. During this amplification period, the pulsewidth of the seed pulse does not change significantly as will be shown in a following section. When the subnanosecond pulse has achieved maximum amplitude, the Q-switch is closed and the pulse is dumped from the resonator. Synchronization of the dump switching time with the propagation of the subnanosecond pulse is achieved electronically by monitoring the pulse amplitude and the modelocking modulator drive signal. The output of the actively modelocked, PTM, Q-switched, Nd:YAG laser is thus a single subnanosecond pulse.

The overall objective of the theory development on this program is to develop a mathematical description of the Spaceborne Laser System concept which provides information on energy output, pulsewidth, energy output stability, and pulsewidth stability as a function of energy input to the oscillator and amplifier rods, modelocker modulation depth and frequency, resonator and amplifier losses, and prelude temporal interval. The desired mathematical description of the system concept can be synthesized from laser Q-switching, active modelocking, and amplifier theory plus the use of empirically determined relationships between the gains of the oscillator and amplifier and their respective input energies. The details of the above theories together with a discussion of the prelude radiation concept are the topics of the remainder of the theory sections of this report. The following paragraphs discuss the synthesis of these theories.

Figure 2-3 is a block diagram illustrating the inputs required and the outputs obtainable from each of the three theories and how these input/output parameters interrelate. This diagram is essentially self-explanatory with regard to these interrelationships. However, the diagram also illustrates that calcu-

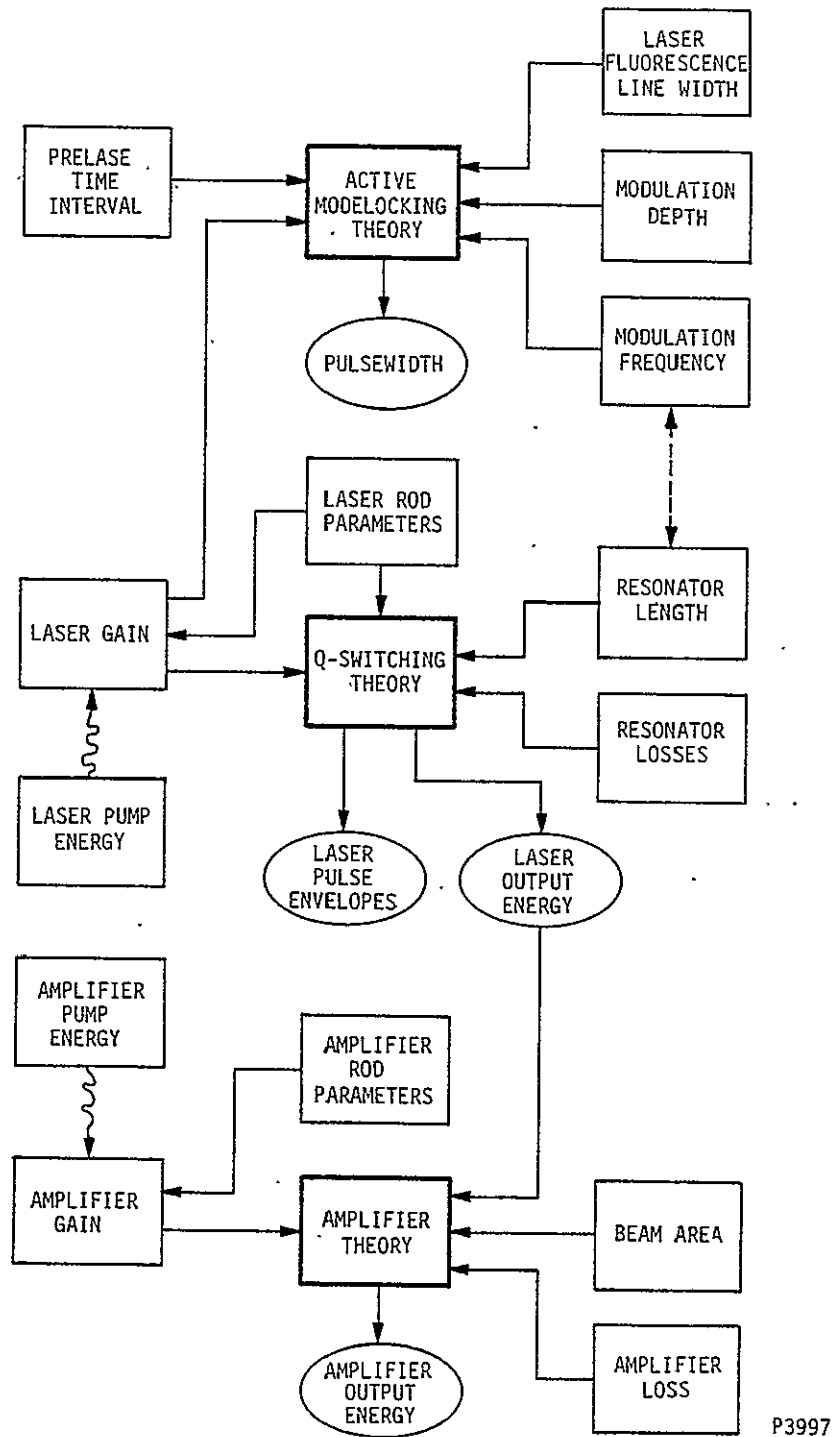


Figure 2-3. Theory Synthesis Diagram

lations using this synthesis of models can proceed in several ways. The constraint on laser output energy imposed by laser material damage limitations indicates the calculational path chosen for use on this program.

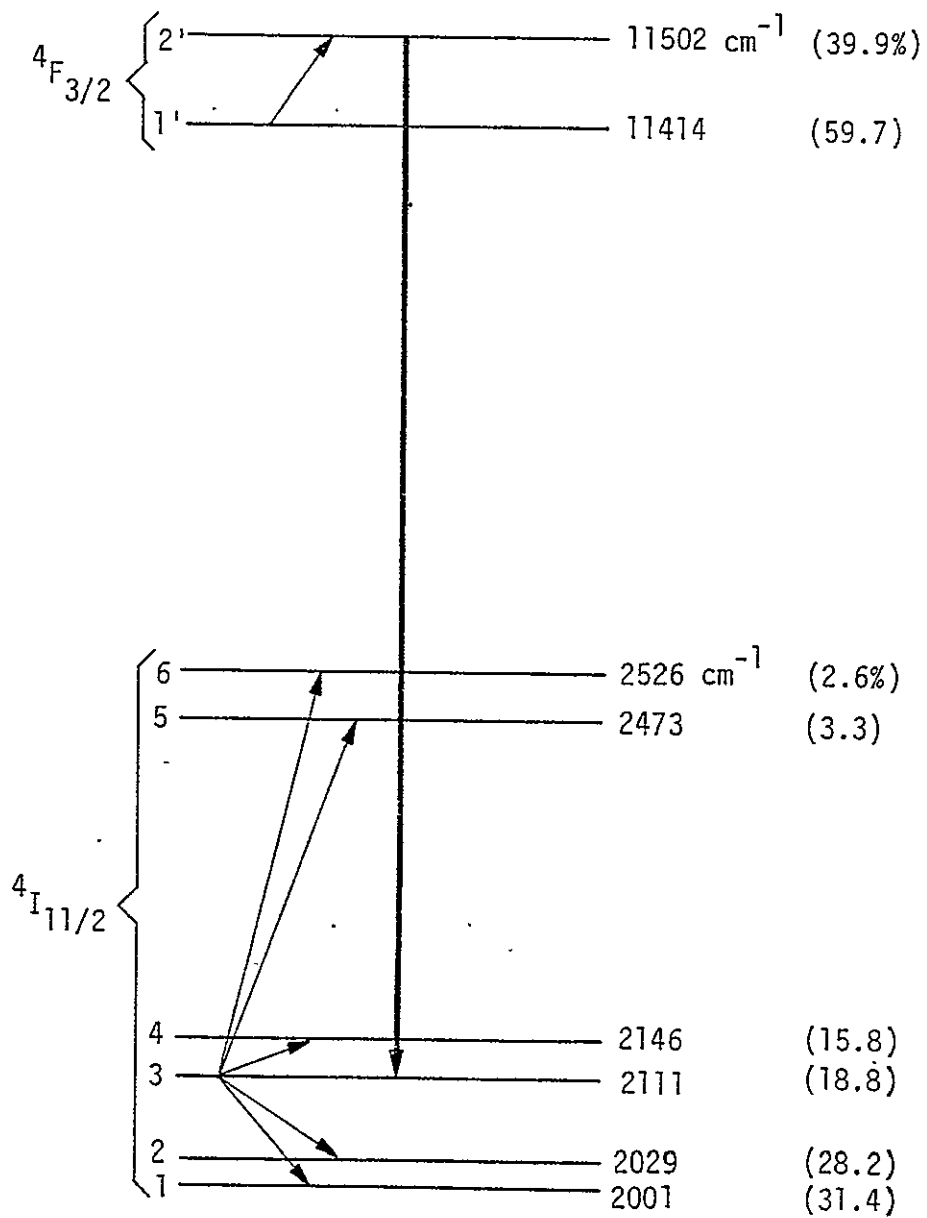
Laser damage constraints on the Spaceborne Laser performance are evaluated in a design section of this report. An important conclusion of this evaluation is that the laser oscillator output energy is limited to low levels. Laser amplifiers, of course, perform most efficiently when the input energy is high level. Thus system efficiency will be maximized for the Spaceborne Laser by operating the oscillator at its highest energy output level within the optical damage constraints. Defining this maximum energy output level is the primary input to calculations using the laser system model.

Most of the input parameters to the Spaceborne Laser System model can be and have been selected via design studies presented in this report. The experimental relationships between the gains and pump energies of the oscillator and amplifier can be determined. Also, the oscillator and amplifier losses can be determined experimentally. Finally, the one remaining parameter, the pre-pulse interval, can be known experimentally. Thus all the information necessary to use the system model is accessible. Parametric calculations using the system model are presented in the theory sections of this report. These calculations indicate the range of overall system performance that can reasonably be expected. The sensitive parameters for energy output and pulse-width stability are also determined.

B. Q-SWITCHED LASER MODEL

The laser model selected to describe the PTM Q-switched Nd:YAG laser is the rate equation model ¹. The Nd:YAG energy levels and energy transfer dynamics are first presented to determine the particular formulation of the rate equations for the Q-switched Nd:YAG laser. Solutions of these equations are then presented which are employed to give characteristic performance of the PTM Q-switched Nd:YAG laser. Finally, energy output and pulse envelope stability are investigated analytically via the laser model.

The energy level structure of Nd:YAG and the energy transfer processes relevant to Q-switching are shown in Figure 2-4.



P2770

Figure 2-4. Energy Levels and Energy Transfers in Nd:YAG Relevant to Q-switching²

The laser transition from the upper sublevel of the ${}^4F_{3/2}$ level to the third sublevel of the ${}^4I_{11/2}$ energy level is indicated in this figure via the thick arrow. The remainder of the arrows indicate energy transfers between the sublevels of the ${}^4F_{3/2}$ and ${}^4I_{11/2}$ energy levels, respectively. These energy transfers between sublevels occur as a result of the neodymium-ion and YAG crystal interactions (phonon-ion interactions). The numbers in parentheses to the right of the energy sublevels of Figure 2-4 are the percentages of the total energy in each energy level that is stored in a particular energy sublevel. These percentages were calculated by assuming a Boltzman ion population distribution within each energy level. This assumption is valid if the energy transfers between sublevels of each energy level are much faster than any other energy transfer processes involving the ${}^4F_{3/2}$ and ${}^4I_{11/2}$ energy levels. This hypothesis will be shown to be true for all processes except stimulated emission in the following paragraph. It will also be shown that energy transfer processes other than the phonon-ion interactions and stimulated emission are much slower than the Q-switching process.

A phenomenological theory of the phonon-ion interaction yields the following equation ³ for the rates of these processes:

$$W_N(T) = B \exp(A\Delta E) [1 - \exp(-h\nu/kT)]^{-N} \quad (2-1)$$

where T = temperature in Kelvin degrees,
 $h\nu$ = phonon energy,
 N = number of phonons in interaction,
 ΔE = energy gap of transition,

and B and A are phenomenological parameters unique to the particular ion host crystal. Although the above equation is for multi-phonon interactions, its extrapolation to the single phonon energy transfer processes between the sublevels of the upper and lower Nd:YAG laser level is assumed to be valid. It is to be noted that phonons of the proper energy to bridge the gap between the sublevels do exist in YAG⁴. The calculations of the sublevel energy transfer times are admittedly an estimate since the extrapolation discussed above may lack accuracy. However, an estimate of the sublevel energy transfer times is necessary since - to the knowledge of ILS - these parameters have not been determined experimentally.

For YAG, $B = 2.24 \times 10^8 \text{ sec}^{-1}$ and $A = 3.5 \times 10^{-3} \text{ cm}^3$. Table 2-1 presents the energy transfer times calculated via the above equation for interactions within the sublevels of the ${}^4F_{3/2}$ and ${}^4I_{11/2}$ energy levels. The time constant calculated for interaction between the ${}^4I_{11/2}$ and ${}^4I_{9/2}$ ground level is 600 nsec. The fluorescence lifetime of the ${}^4F_{3/2}$ energy level is 240 μsec and optical pumping of this level typically extends over 100-200 μsec . Clearly, all three of the latter energy transfer processes are slow compared to the typical time interval of the Q-switching process of 100-200 nsec. Thus, only the stimulated emission and the crystal-ion interactions need to be taken into account in the formulation of the rate equations for the Q-switching of the Nd:YAG laser. It is also obvious that the phonon-ion interactions between sublevels are much faster than any energy transfer processes other than stimulated emission. Thus, the energy distribution among the energy sublevels of the ${}^4F_{3/2}$ and ${}^4I_{11/2}$ levels are as shown in Figure 2-4 prior to laser emission.

From the above discussion, a proper formulation of the rate equation for Q-switching of the Nd:YAG laser is indicated which involves equations describing the ion population dynamics of each of the sublevels of the ${}^4F_{3/2}$ and ${}^4I_{11/2}$ energy levels plus an equation describing the photon density dynamics. These equations could not be soluble analytically. Thus, an approximate formulation of these equations utilizing an empirical parameter is made. This empirical parameter is the time-averaged decrease in population inversion between the upper and lower laser levels per photon emission from the upper level. This parameter, denoted as α , can be estimated from the calculated time constants of the interactions between energy sublevels or can be determined empirically. (Note that $\alpha = 1$ for an ideal four-level laser and $\alpha = 2$ for an ideal three-level laser.) A comparison of the results of the rate equation theory to be presented and a numerical iterative approach developed at ILS indicates that α is between 0.7 and 0.8.

An estimate of α , the decrease in population inversion per photon emitted, is made by time-averaging the laser dynamics over a single round-trip through the laser resonator. From Table 2-1, the time constant for repopulation of the upper laser sublevel of the ${}^4F_{3/2}$ energy level by the lower sublevel is 6 nsec. The time constant for decay of the lower laser sublevel of the ${}^4I_{11/2}$ energy level to the remaining ${}^4I_{11/2}$ sublevels is 1.6 nsec. The round-trip time of a photon within the Spaceborne resonator is 9.48 nsec. When a single photon is emitted by a neodymium ion, the actual population of the upper laser sublevel

Table 2-1. Energy Transfer Times

Transition	Transfer Time (Nanoseconds)
${}^4F_{3/2}$ 1' → 2'	6
${}^4I_{11/2}$ 3 → 1	18
3 → 2	15
3 → 4	5
3 → 5	6
3 → 6	6.5
3 → Σ	1.6

decreases by ~ 0.4 units and the population of the lower laser sublevel increases by 0.2 units if given time to equilibrate after emission of a single photon. The net population inversion decrease is thus 0.6 units per photon emission if equilibration is allowed time to occur. The 9.48 nsec round-trip time of the laser resonator does not permit this to occur. A calculation of the equilibration of the ${}^4F_{3/2}$ and ${}^4I_{11/2}$ levels over the resonator round-trip time after emission of a photon yields a decrease in net population inversion of ~ 0.8 units (exponential equilibration processes are assumed). This value of 0.8 for α will be used in the rate equation model.

The rate equations ¹ for Q-switching of the Nd:YAG laser which takes into account, in an approximate manner, the sublevel dynamics of the ${}^4F_{3/2}$ and ${}^4I_{11/2}$ energy levels are:

$$\frac{d\phi}{dt} = \left(\frac{\sigma N \ell}{T_r} \right) \phi - \left(\frac{\gamma}{T_r} \right) \phi$$

$$\frac{dN}{dt} = - \alpha \left(\frac{\sigma N \ell}{T_r} \right) \phi$$

where

- σ = Stimulated emission cross section,
- ϕ = Photons/unit volume (referenced to rod volume)
- N = $N_2 - N_1$ = active ion inversion/unit volume,
- ℓ = Laser rod length,
- γ = $-\frac{1}{2} \ln(R T_\ell^2)$ = total losses per single pass in resonator,
- T_r = L/c = single-pass resonator transit time,
- L = Resonator length,
- c = Velocity of light,
- R = Reflectivity of output mirror,
- T_ℓ = Single pass transmission of resonator,
- α = Decrease in inversion per photon emission.

The term $(\sigma N \ell / T) \phi$ in the first equation is the increase in the number of photons per unit volume on a single pass through the resonator due to stimulated emission. By the definition of the parameter, α , the term in the second equation is clearly the decrease in the net population inversion during a single resonator transit. The term $-(\gamma/T) \phi$ in the first equation is the decrease in the number of photons on a single resonator transit due to losses and output coupling.

The above rate equations are analytically soluble and explicit equations are obtained for the energy output for the case of PTM Q-switching. A fast Q-switch is assumed as is the case for the Spaceborne Laser. An analytical expression for the Q-switched pulsewidth is not obtainable from the above equations. This must be obtained numerically. However, an approximate analytical treatment of the pulse dynamics yields an explicit equation for the pulsewidth which is accurate within a few percent. The equation for the energy output¹ and the pulsewidth⁵ of the internal radiation intensity of a PTM Q-switched Nd:YAG laser are:

$$E_{\text{out}} = \left(\frac{h\nu}{\sigma} \right) \frac{A g}{\alpha} \left\{ 1 - \frac{1}{\beta} + \frac{1}{\beta} \ln \frac{1}{\beta} \right\}, \quad (2-4)$$

$$E_{\text{out}} = \frac{E_{\text{stored}}}{\alpha} \left\{ 1 - \frac{1}{\beta} + \frac{1}{\beta} \ln \frac{1}{\beta} \right\}, \quad (2-5)$$

$$\tau(\text{FWHM}) = \frac{2.4929 T}{\sqrt{\frac{\beta}{\alpha} \left(1 - \frac{1}{\beta} + \frac{1}{\beta} \ln \frac{1}{\beta} \right)}}, \text{ and} \quad (2-6)$$

where

$$\tau(\text{FWHM}) = \frac{2.4929 T}{\sqrt{\beta (E_{\text{out}}/E_{\text{stored}})}}$$

A = Laser rod cross-section area,

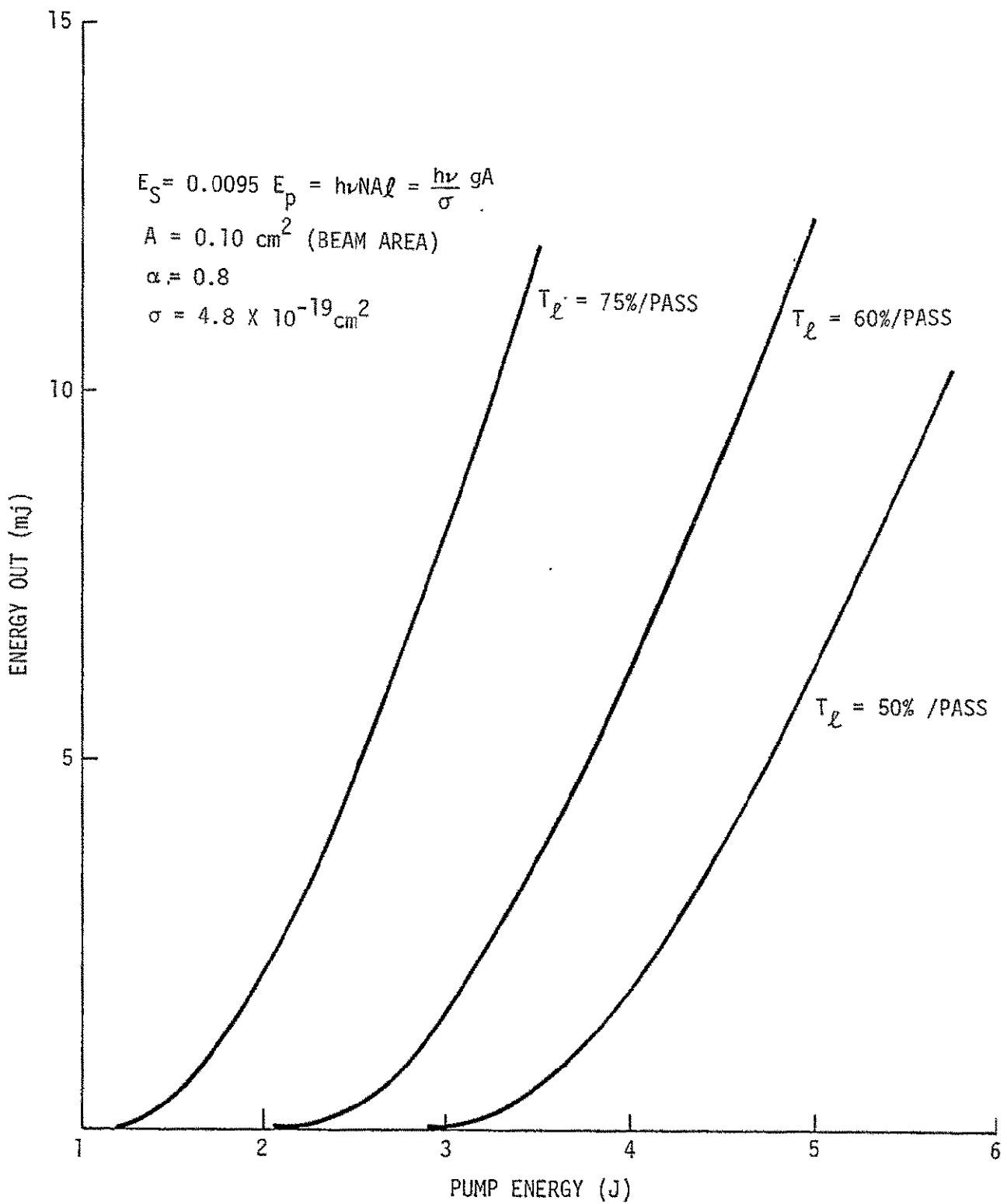
g = $\sigma N \ell$ = Single pass gain coefficient,

$\beta = \frac{g}{\gamma}$ = (pump energy)/(threshold energy),

T = $(2L/c) / \ln(1/RT_{\ell}^2) = L/c\gamma$.

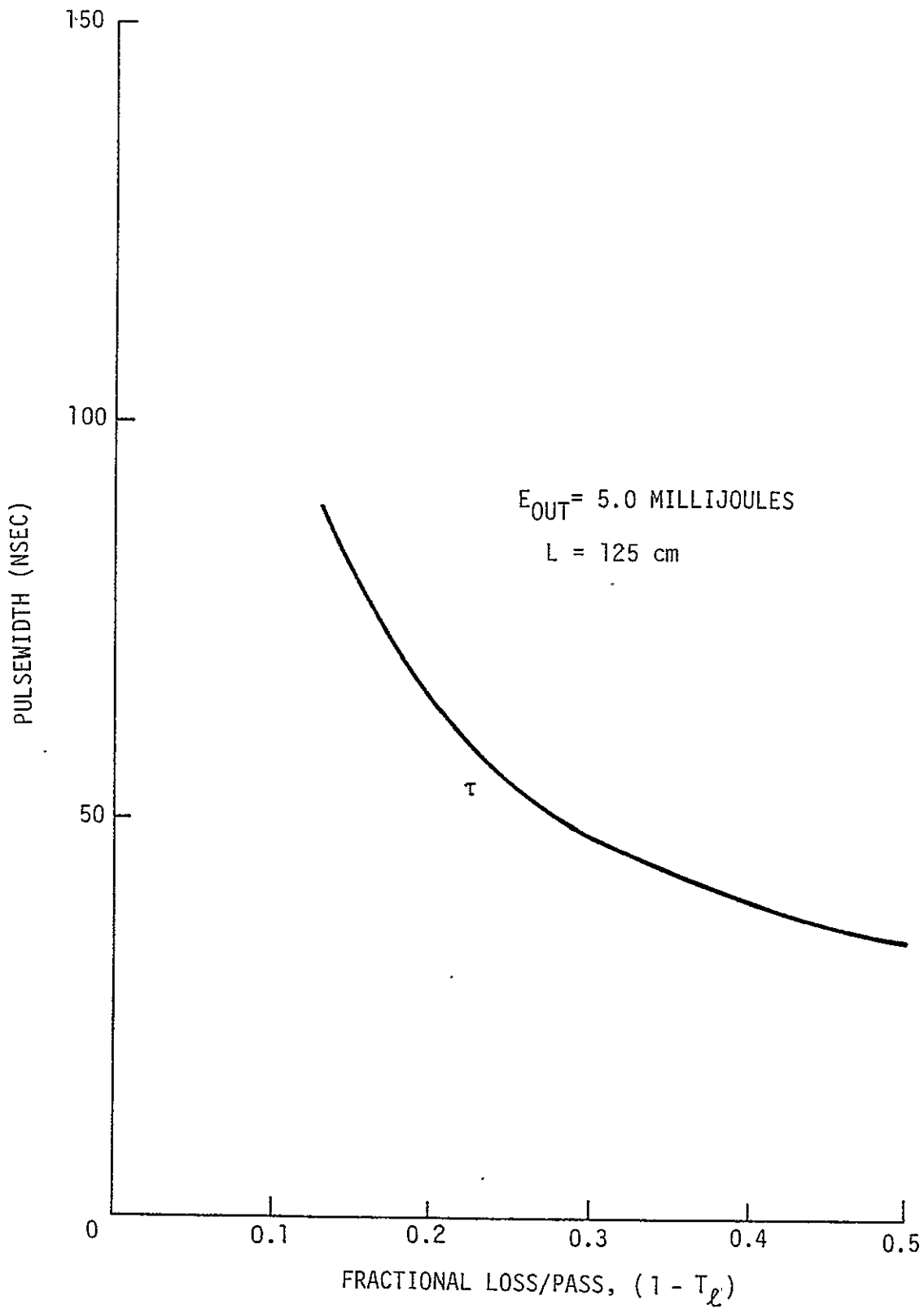
The above equations are utilized to generate characteristic performance curves for the Spaceborne Laser. Figure 2-5 is a graph depicting energy input/output curves versus resonator loss. An empirical relationship between pump energy and energy stored in the laser rod is utilized. Figure 2-6 is a graph showing the pulsewidth of the internal radiation intensity of the PTM Q-switched laser as a function of resonator loss for a fixed output energy of 5.0 mJ/pulse. Figure 2-7 is a graph of the internal radiation intensity envelope as it would appear if the dump switching did not occur in the PTM Q-switching operation. The envelope curve was obtained numerically. Superimposed on this envelope are the modelocked pulses with a pulse centered at the peak of the envelope. The purpose of this graph is to indicate that energy output variation will occur due to jitter between the radiation intensity envelope and modelocked pulse temporal position. This jitter is probably unavoidable and the graph in Figure 2-7 predicts approximately a 5% amplitude jitter in energy output due to this phenomena alone for the case of a 25% resonator loss/pass. From Figure 2-6, it is clear that higher resonator losses result in shorter pulse envelopes. Thus, the energy instability due to the modelocked pulse and envelope positions will increase with increased resonator loss.

This phenomena described above is clearly dominant in importance over other sources of energy output instability such as gain or loss variation from shot-to-shot. The latter parameters can be controlled more carefully, but the envelope-pulse position jitter is apparently unavoidable. Clearly, a low resonator loss to stretch the pulse envelope is the desirable solution to this problem. However, if this is not feasible in practice, operation of the oscillator at lower output energy levels in order to stretch the pulse envelope may resolve the problem.



P2785

Figure 2-5. PTM Q-switched Energy Input/Output Curves vs Resonator Losses



P2786B

Figure 2-6. Envelope Pulsewidth vs Resonator Losses

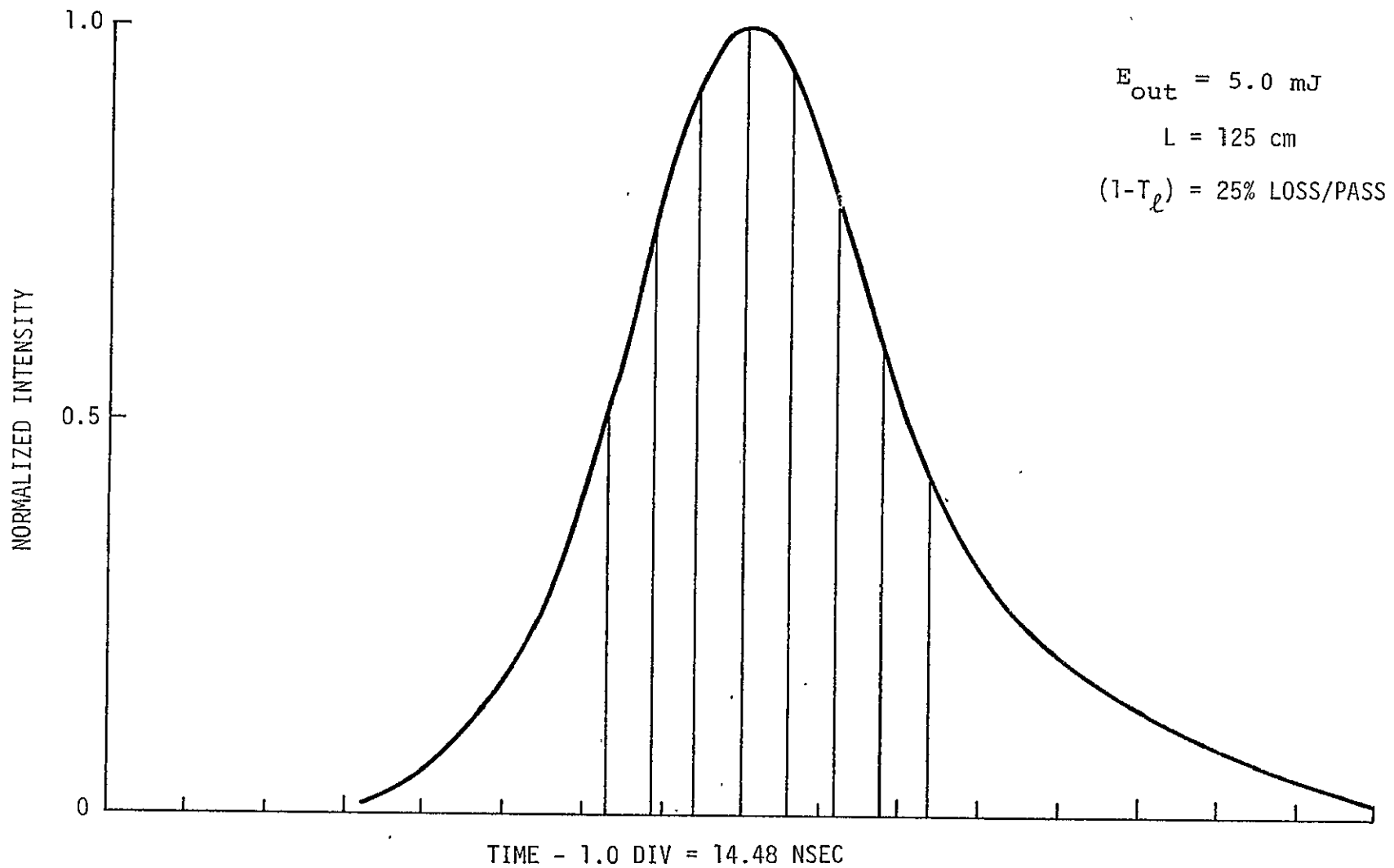


Figure 2-7. Modelocked Pulse Amplitude vs Time

P2787

C. TRANSIENT MODELOCKING

The mathematical treatment of transient and steady-state active modelocking by Kuizenga and Siegman^{6,7} has been proven experimentally to be a viable description of the active modelocking process in Nd:YAG. The basic approach of their treatment is to approximate the laser material gain function, the modulator temporal function, and the initial pulse shape of the intracavity radiation as gaussian curves. Via this approach, the initially gaussian pulse remains gaussian after transmission through the laser material and modulator.

In the steady-state analysis, the changes in the gaussian parameter of the intracavity radiation pulse caused by the modulator and the laser material on one round-trip through the laser interferometer are equated. From this equation, the steady-state value for the gaussian parameter and thus the pulsewidth of the modelocked pulse are determined as a function of the laser material and modulator parameters.

The analysis of active modelocking in the transient regime is initiated by setting up a differential equation in time for the gaussian parameter of the intracavity radiation pulse. The changes in the latter parameter caused by the modulator and the laser material on each round trip through the laser interferometer divided by the round trip transit time are the rate terms in the above mentioned differential equation. This equation is easily solved to yield the modelocked pulsewidth in the transient modelocking temporal regime.

The modulator gaussian parameter derived via the gaussian approximation to the modulator transmission function depends solely on the temporal duration of the modulator gate. Similarly, the laser gain bandwidth determines the gaussian parameter derived from a gaussian fit to the gain curve. The curvature of the gain function at its peak dictates the effective bandwidth of the laser material for the modelocking process since only axial modes near the peak participate in laser action.

The effects of the modulator and the laser rod on the temporal and spectral character of the laser output are competing ones. The gain function of the laser rods acts to decrease the spectral content of the laser radiation and consequently also acts to increase the temporal duration of this radiation. The modulator acts to decrease the temporal duration of the laser

radiation and thus acts to increase the spectral content via the generation of frequency sidebands of the initially oscillating axial modes.

At least two distinct stages of transient modelocking can be identified prior to the achievement of steady-state modelocking on the basis of the relative magnitude of the effects of the modulator and laser rod. For moderate duration modulator time gates, the increase in the spectral width resulting from the application of this gate to the intracavity laser radiation is at first, negligible compared to the frequency bandwidth of the laser material gain. Thus, in the first stage of transient modelocking the modulator essentially governs the temporal and spectral characteristics of the laser radiation. As an example, consider the case where the duration (FWHM) of the time gate is ≈ 3.5 nsec. This corresponds to a sinusoidal modulation at 75 MHz with a modulation depth of 1.0 from the equation for the modulation function $M(t) = \cos[\theta \sin(\omega_m t)]$. This temporal width corresponds to a spectral width of 140^m MHz or $\approx 0.005 \text{ cm}^{-1}$ according to the Fourier relationship between time and frequency. Figure 2-8 clearly shows that this spectral width is negligibly small compared to the Nd:YAG gain curve shown as a function of frequency.

Thus, in the initial stage of transient modelocking the modulator characteristics determine the pulse duration of the modelocked pulse. Kuizenga and Siegman derived the following equation for the modelocked pulsewidth for the first stage of transient modelocking,

$$\tau_p = \sqrt{\frac{\ln 2}{2}} \frac{1}{\pi \theta_m f_m \sqrt{M}} \quad (2-7)$$

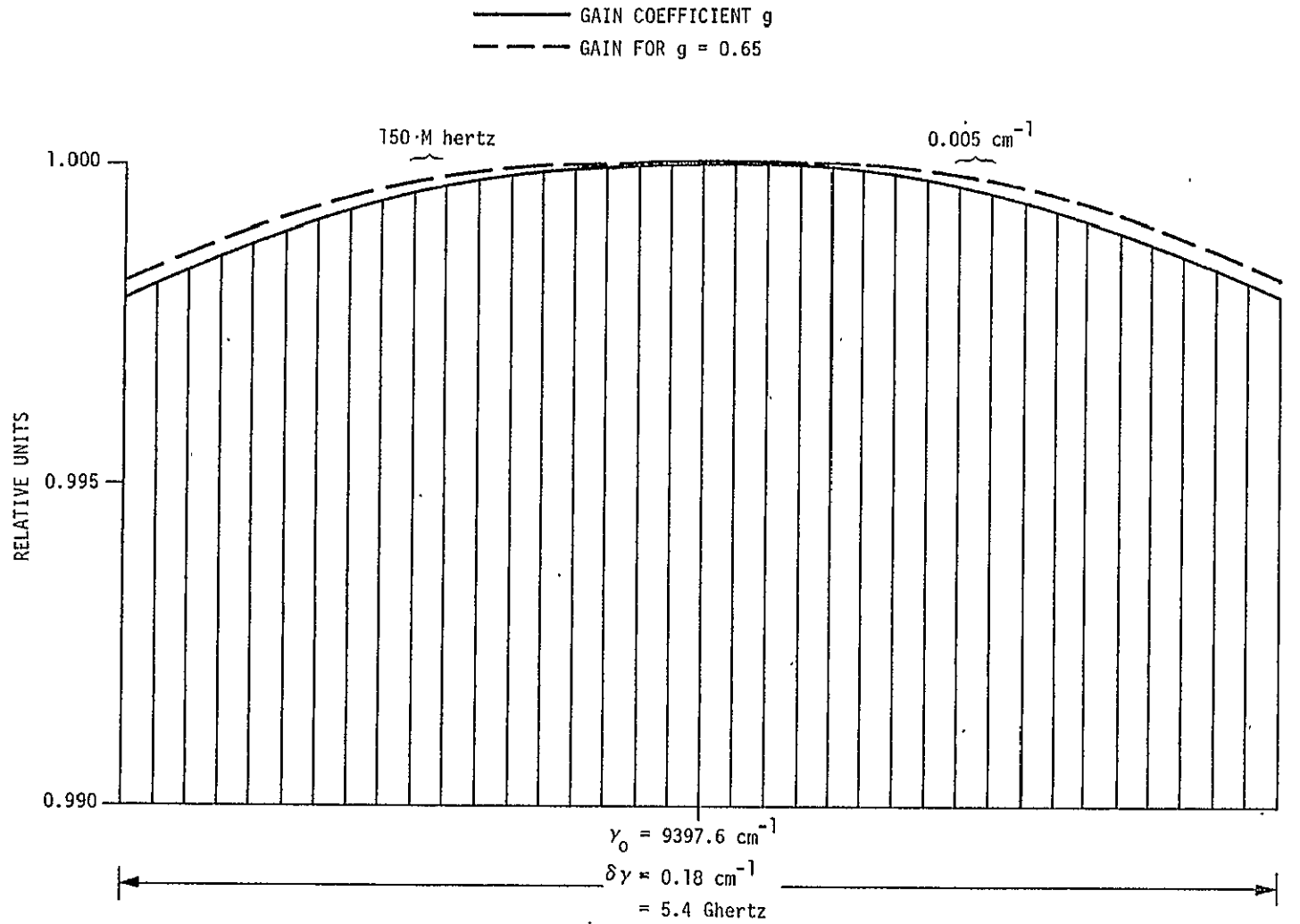
where

θ_m = modulation depth,

f_m = modulation frequency,

M = number of passes through modulator.

To quote Reference 7, "From a physical viewpoint, equation (2-7)



P1779

Figure 2-8. Nd:YAG Gain vs Frequency

remains valid so long as the pulses' spectral width is narrow enough so that it is not affected by the atomic linewidth".

Stage 2 of the transient approach to steady-state modelocking begins when equation (1) ceases to be valid. In this stage the pulsewidth of the modelocked pulse begins to be comparable to the steady-state pulsewidth. Equivalently, in this stage the spectral width of the laser radiation has been increased by the action of the modulator to the point where the frequency dependence of the gain function becomes significant (see Figure 2-8). In this temporal regime of the active modelocking process, the laser rod reduces the effectiveness of the modulator to decrease the pulsewidth via gain discrimination. Kuizenga's and Siegman's derivation ⁷ for the modelocked pulsewidth in stage 2 of the transient approach to steady-state modelocking yielded:

$$\tau_p = \frac{\tau_o}{\sqrt{\tanh (M/M_o)}} \quad (2-8)$$

where

τ_o = steady-state modelocked pulsewidth,

M = number of passes through modulator,

$$M_o = \frac{1}{4\theta_m \sqrt{g_m}} \cdot \frac{\Delta f}{f_m}$$

Δf = laser line bandwidth,

g_o = unsaturated laser gain.

The steady state pulsewidth is given by

$$\tau_o = \frac{\sqrt{2 \ln 2}}{\pi} \left(\frac{\sqrt{g_m}}{\theta_m f_m \Delta f} \right)^{\frac{1}{2}} \quad (2-9)$$

A basic assumption made in all analyses presented previously is the following. It is assumed that the modelocked pulse formed during the prelude or Q-switch buildup time is essentially unchanged during the period of high intracavity radiation intensity just prior to ejection of the pulse from the resonator. The analysis below shows that this assumption is valid.

The change in the temporal gaussian pulse parameter caused by passage through the rod and modulator are given by Reference 6 to be:

$$\Delta\xi_{\text{rod}} = - \frac{4g\xi^2}{\pi^2(\Delta f)^2} \quad (2-10)$$

and

$$\Delta\xi_{\text{modulator}} = 4\pi^2\theta_m^2 f_m^2 \quad (2-11)$$

where g = the saturated gain,

Δf = fluorescence bandwidth of laser line,

θ_m = modulation depth,

f_m = modulation frequency,

and ξ = gaussian pulse parameter of modelocked pulse just prior to entering high intracavity radiation regime.

(ξ is defined by $f(t) = e^{-\xi t^2}$.)

The number of round trip passes made by the pulse in the high intracavity radiation regime prior to extraction of the pulse from the resonator was shown by previous ILS analysis to be ≈ 10 for intracavity losses of 36% per round-trip. The net change in the gaussian pulse parameter is calculated for 10 passes to be

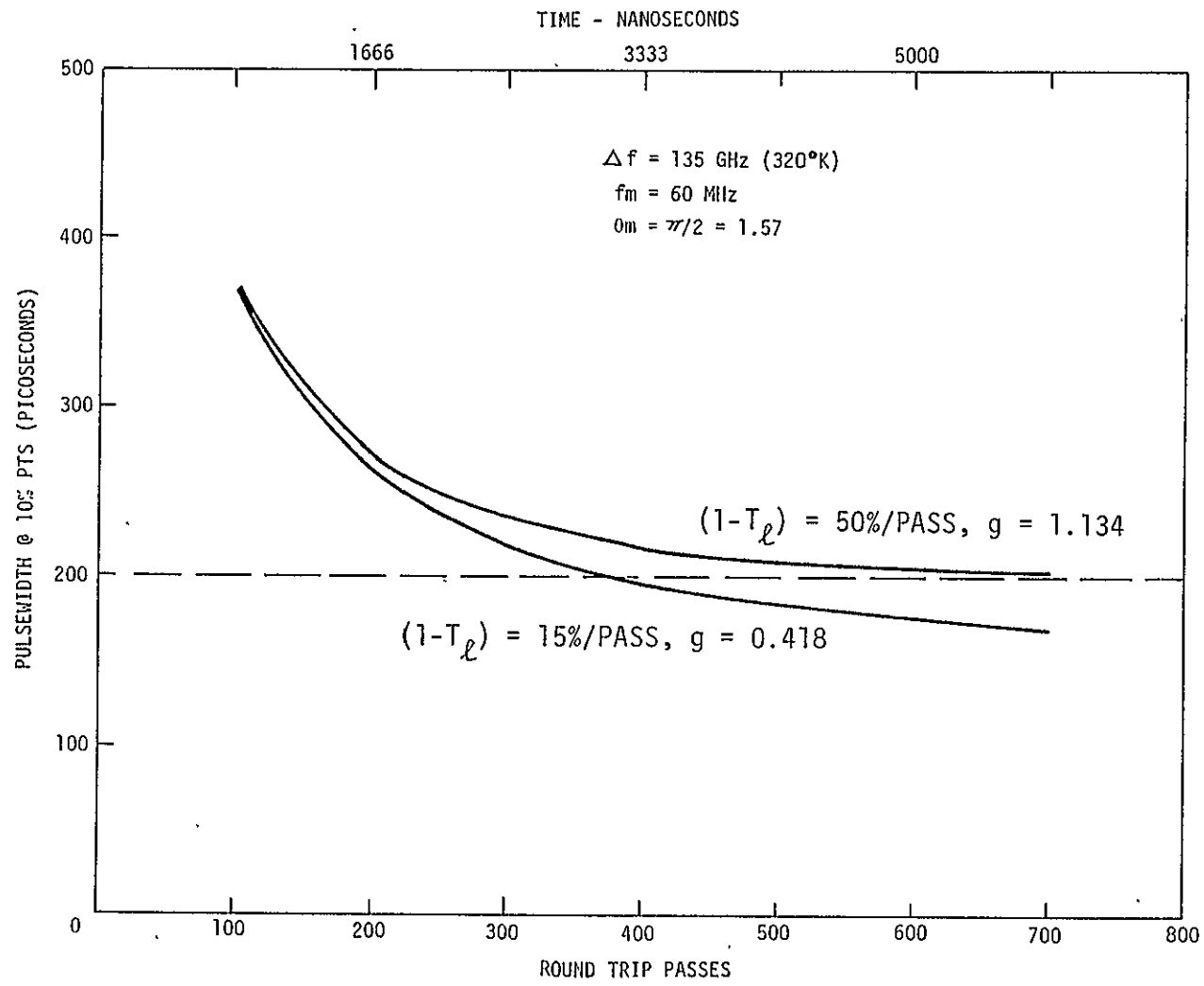
$$\Delta\xi_{\text{net}} = 10 (\Delta\xi_{\text{rod}} + \Delta\xi_{\text{modulator}}) = +15 \times 10^{18} \quad (2-12)$$

where $\theta_m = 1.5$; $f_m = 75$ MHz; $g = 0.96g_0 = 0.624$; and $\Delta f = 160$ GHz. The gaussian pulse parameter corresponding to an initial 200 psec (10% pts) pulsewidth is 2.3×10^{20} . The gaussian pulse parameter following the 10 passes through the interferometer prior to pulse extraction is $\xi + \Delta\xi = 2.45 \times 10^{20}$. This value of the gaussian pulse parameter corresponds to a pulse duration of 194 psec (10% pts). Thus it is seen that the change in pulse duration during the period in which significant energy

is extracted from the rod is negligible and in fact a desirable shortening of the pulse. This could have been predicted from Equations (2-10) and (2-11) which show that the only changes in these equations from the low intensity case is the replacement of g_0 (the unsaturated gain) with g (the saturated gain). Since g is less than g_0 , the laser rod contributes to pulse lengthening less in the high radiation intensity temporal regime than in the low intensity regime (the pre-lase period).

Figure 2-9 presents the pulsewidth versus pre-lase time for two resonator loss parameters and a gain value which in each case yields a 5.0 mJ/pulse output energy.

2-22



P2788

Figure 2-9. Pulsewidth vs Prelase Time

D. PRELASE CONCEPTS

The calculations presented in the previous section show that the desired pulsewidth (200 psec @ 10% points) for the Spaceborne laser can only be obtained by several hundred resonator round-trip transistions. This corresponds to several μ sec, a time much longer than typical Q-switch buildup times ($\sim 100 - 200$ nsec). The generation of low level radiation (prelase radiation) for the necessary temporal duration permits the attainment of the desired laser pulsewidth.

The duration of prelase radiation should be precisely controlled in order to obtain shot-to-shot pulsewidth stability. Also, the level of the prelase radiation should be precisely controlled in order to prevent depletion of the energy stored in the laser rod. In this manner, laser efficiency can be maintained at the level obtained in the absence of prelase radiation. One manner in which precise control of both the duration and level of the prelase radiation can be obtained in a pulsed laser is via an active radiation feedback control loop.

A feedback control loop was implemented in the Spaceborne laser by detection of the leakage radiation from the resonator and control of the Q-switch loss via an applied variable voltage. The detector is the input to an electronic circuit which increases or decreases the differential voltage across the Q-switch cell when radiation within the resonator increases or decreases respectively. Thus, the loss of the cell increases/decreases when the prelase radiation increases/decreases. The two experimental circuits designed to perform the feedback control on prelase radiation were unsuccessful as described elsewhere in this report. The problems encountered were difficult and the prelase approach described in the following paragraph was employed.

Prelase radiation is generated in the present laser device by setting the Q-switch bias voltage slightly below the lase hold-off voltage. In this manner, a low energy normal mode pulse is generated when the maximum gain of the laser rod occurs. The build-up time for this normal mode pulse of ~ 3.0 μ sec is the prelase duration. Q-switching is dynamically synchronized to occur near the peak of the normal mode pulse. The synchronization is accomplished by direct lase detection via a circuit which initiates Q-switching when prelase radiation exceeds a preset level. The preset threshold level can be varied experimentally to adjust prelase radiation

intensity. The disadvantage of the above-described prelude technique is that the prelude interval fluctuates from pulse to pulse. This occurs because of normal mode pulse amplitude fluctuations induced by small net laser gain fluctuations which in turn result from flashlamp-rod coupling variations from pulse to pulse.

Experimentation is planned with the pulsed, quasi-CW flashlamp pumping mode used in the Lawrence Livermore SHIVA modelocked oscillator. This pumping mode with the Q-switch bias voltage set to allow low level lasing results in quasi-CW operation prior to Q-switching. The duration of this lase period is set by the CW pumping duration to allow damping of normal mode spiking prior to Q-switching. The above prelude technique will provide prelude durations of ~ 150 μsec and thus ensure the generation of steady-state modelocked pulses with insignificant variations in pulse profile or pulsewidth from pulse to pulse. The disadvantage of this prelude technique relative to the one presently used is an increase in oscillator flashlamp power from 25 to 75 Watts.

E. AMPLIFIER MODEL

The theoretical model which describes the characteristics of amplifier action for modelocked pulses is developed with consideration given to equilibration times of the energy transfer processes. For subnanosecond pulses with double pass transit times of less than 2 nsec through the amplifying medium, one may assume that equilibration effects between levels are negligible. With reference to the description of energy transfer processes as developed in the section on Q-switching dynamics, the value of α , the time-averaged decrease in population inversion, may then be established. By neglecting equilibration times, the decrease in the upper laser level population per photon emitted is just equal to the increase in the population of the lower laser level. Thus, $\alpha=2$ represents the change in the population inversion per photon emitted for amplification of modelocked pulses using Nd:YAG.

The rate equations ⁸ which describe the amplifier dynamics with consideration given to the sublevel dynamics of the laser medium are:

$$\frac{\partial \phi(X,t)}{\partial t} + c \frac{\partial \phi(X,t)}{\partial t} = \sigma c n(X,t) \phi(X,t) \quad (2-13)$$

$$\frac{\partial n(X,t)}{\partial t} = - \alpha \sigma c n(X,t) \phi(X,t) \quad (2-14)$$

where

$\phi(X,t)$ = Photon/Unit Volume,

$n(X,t)$ = Inversion/Unit Volume,

σ = Simulated emission cross section,

c = Velocity of light,

α = Decrease in inversion per photon emitted.

The rate of change of the photon density is proportional to the product of the functions of the photon density and inversion density with the stimulated emission cross section for the particular laser level under consideration. The rate of change of the inversion density is just the negative of the rate of the photon density multiplied by the factor α . These equations may be solved analytically to yield:

$$\phi(X,t) = \frac{\phi_i(t-X/c)}{1 - \left(1 - e^{-\sigma n_0 X}\right) \exp \left\{ -\alpha \sigma c \int_0^T \phi_i(\tau) d\tau \right\}} \quad (2-15)$$

Where

n_0 = Uniform inversion/unit volume,

ϕ_i = Input photon density.

Application of a square pulse input given by:

$$\phi_i(t) = \phi_0 \quad 0 \leq t \leq T, \text{ and} \\ 0 \text{ otherwise;}$$

yield an accurate approximation to the solution of the energy gain equation. The energy gain equation⁸ for the square input pulse is:

$$G_E = \frac{1}{\alpha \sigma \phi} \ln \left\{ 1 + e^{\sigma n_0 \ell} \left(e^{\alpha \sigma \phi} - 1 \right) \right\}$$

Where

ϕ = Input photons/unit area,

α = Decrease in inversion per photon emitted,

σ = Stimulated emission cross section,

ℓ = Laser rod length,

n_0 = Initial uniform inversion/unit volume.

The energy gain equation expressed in terms of the energy stored in the upper laser level and the amplifier input energy is:

$$G_E = \frac{h\nu/\sigma\alpha}{E_{IN}/A} \ln \left\{ 1 + \exp \left(\frac{E_{\text{stored}}/A}{h\nu/\sigma} \right) \left[\exp \left(\frac{E_{IN}/A}{h\nu/\sigma\alpha} \right) - 1 \right] \right\} \quad (2-17)$$

E_{IN} = Amplifier input energy,

E_{stored} = Energy stored in upper laser level

A = Amplifier rod area,

$\frac{h\nu}{\sigma}$ = Saturation energy ($0.39\text{J}/\text{cm}^2$ for Nd:YAG).

Employing this expression for the energy gain equation one may determine the output energy for a given set of input and energy storage conditions. Given initially an energy storage of 179 mJ (corresponding empirically with a 9.0 Joule pump energy) with a .2827 cm area exposed to an input energy of 5 mJ/pulse one may calculate the expected output energy for a double-pass amplifier system. On the first pass:

$$G_E = \frac{.200}{.0177} \ln \left\{ 1 + e^{(.619/.4)} \left[e^{(.0177/.2)} - 1 \right] \right\} \quad (2-18)$$

$$= 4.08$$

which multiplied by the input energy yields an output energy of 20.4 mJ/pulse. The beam is then folded back on itself with an assumed loss of 5% which makes the input energy on the second pass equal to 19.0 mJ/pulse.

The energy storage in the rod has dropped to 149 mJ/pulse as a result of the energy extracted on the first pass. For the second pass

$$G_E = 2.88,$$

)
)

which yields a final output energy of 54.6 mJ/pulse for the double pass amplifier.

Using the equation for the energy gain with $\alpha = 0.8$, values were computed for the relative extracted energy per unit amplifier cross sectional area as a function of oscillator input energy. This value of α corresponds to ~20 nsec input pulses. These results are shown in Figure 2-10 with experimental data also presented. A close correspondence can be seen between the theoretical curve and the experimental data. Thus a theoretical model is available which accurately predicts amplifier performance characteristics.

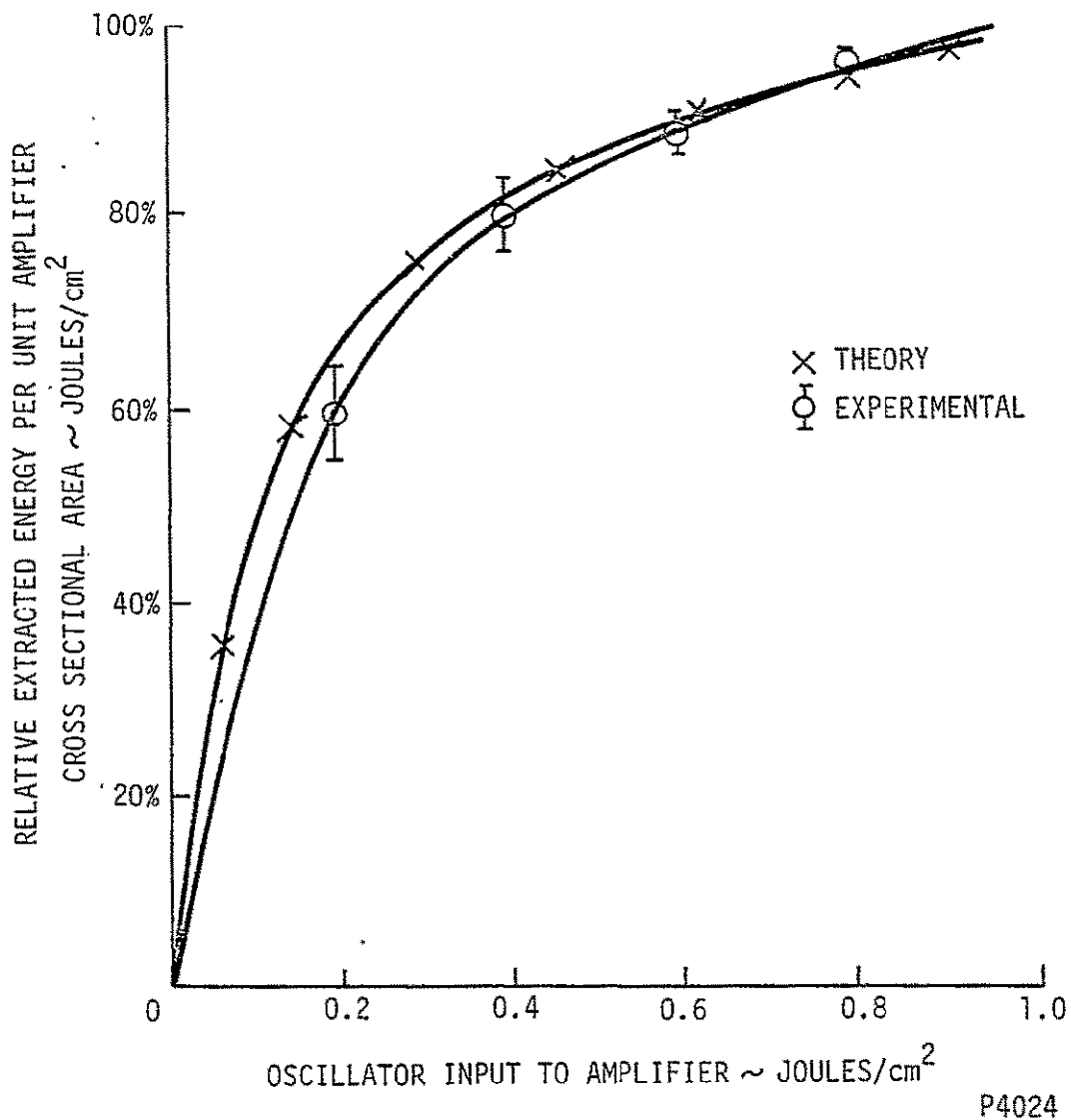


Figure 2-10. Amplifier Energy Extraction as Function of Oscillator Energy Density

Section III

DESIGN

A. SYSTEM OVERVIEW

1. Hardware Description

The Spaceborne Laser System consists of four units: the laser transmitter, power supply, cooling system and modelocker driver. Figure 3-1 is a photograph of these units and Figure 3-2 is a system block diagram.

The laser transmitter housing is hermetically sealed and consists of a cover and a baseplate mounted on four steel rods terminating in Gaertner magnetic bases. All electronic and coolant connections are made through the baseplate. The transmitter contains the optical bed and interferometer, the radiation and synchronization control electronic packages, the Q-switch driver package and miscellaneous minor electronic components. The transmitter derives its electronic inputs from the power supply via a single primary cable and several BNC cables. A single BNC cable connects with the cooling system via inlet and outlet coolant hoses. The output of the transmitter will be a single subnanosecond pulse.

The Spaceborne Laser System power supply subsystem is mounted on a standard 19-in. enclosed chassis that is rack-mountable. The power supply contains the flashlamp power module, the pulse-forming networks (PFNs), pulse rate generator, prebase and Q-switch delay logic, Q-switch bias and driver voltage sources, and miscellaneous minor electronic components.

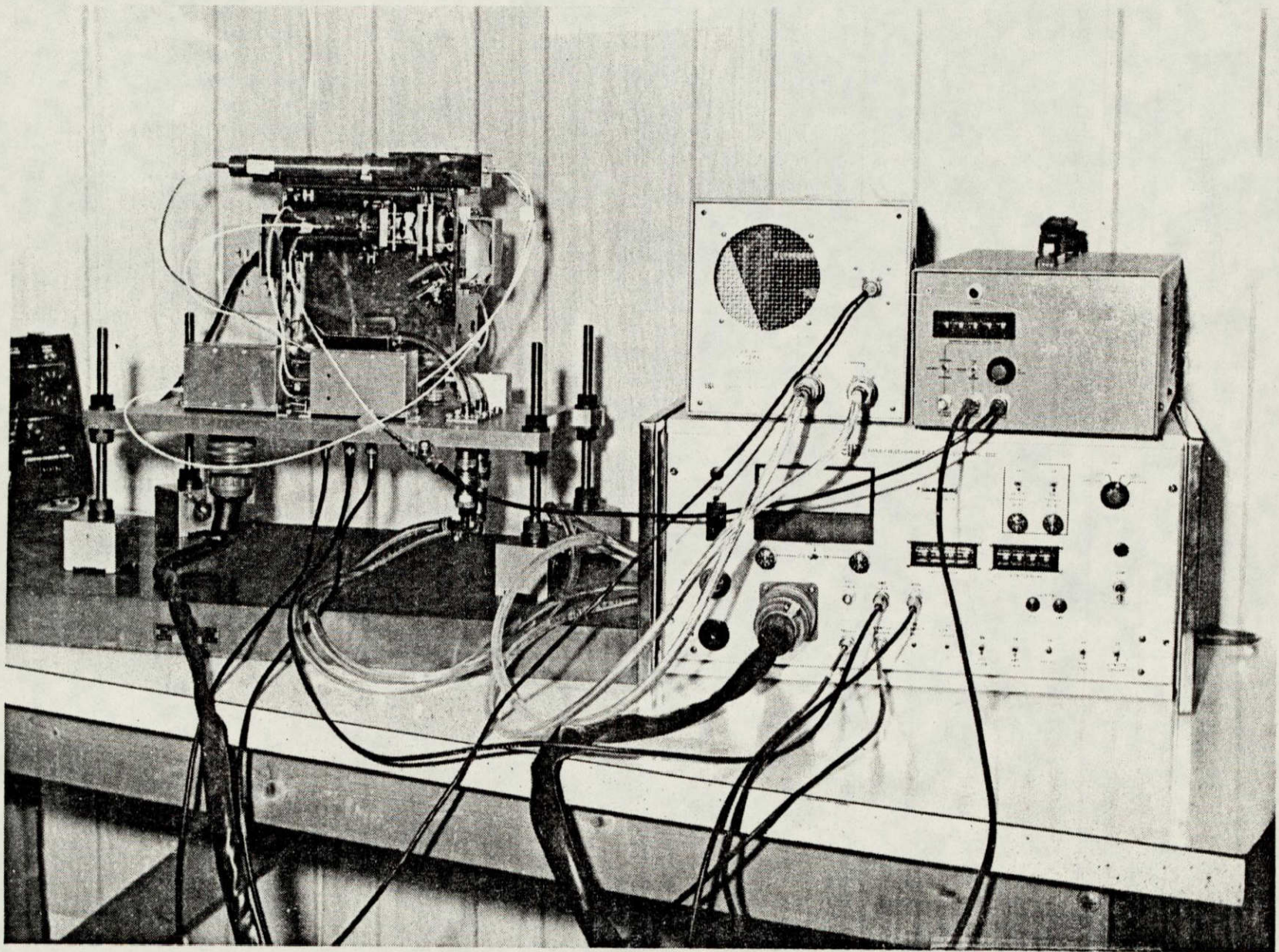
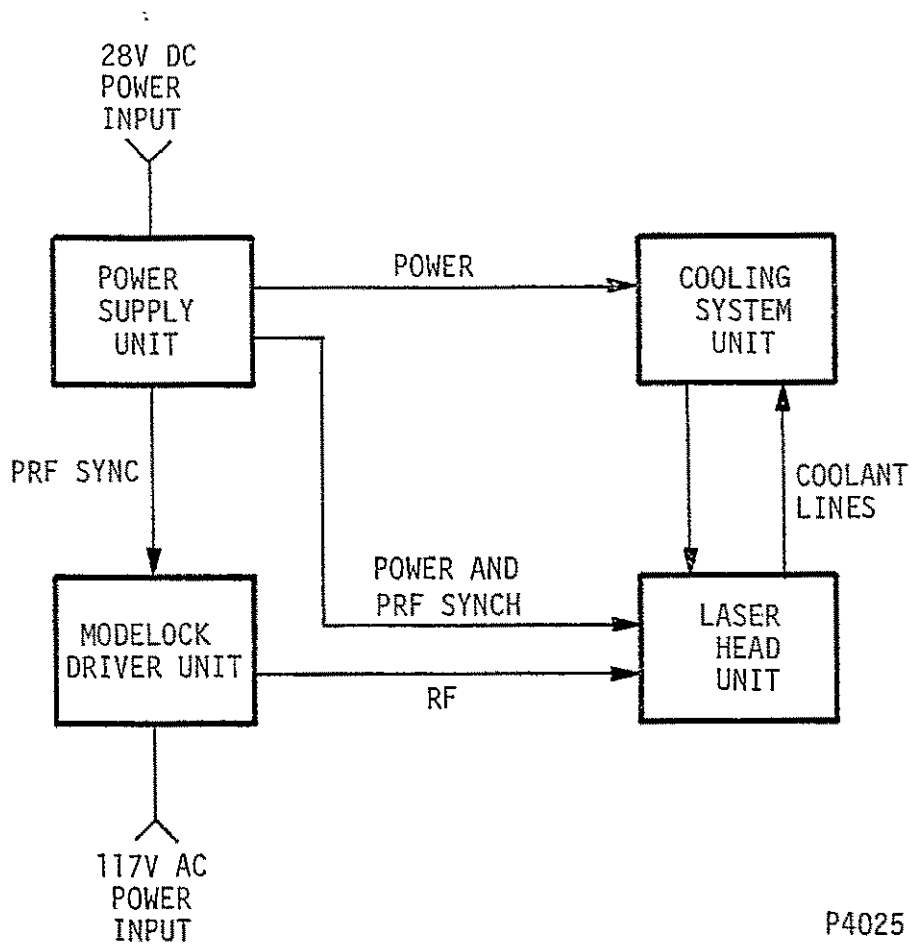


Figure 3-1. Hardware Subassemblies



P4025

Figure 3-2. System Block Diagram

All power supply connections are made through the front panel. The prime power input of 24-v dc to the system is made via the power supply. The power supply provides a logic input to the modelocker driver via a single BNC cable. All other power supply connections are with the laser transmitter. Essentially all the controls of the Spaceborne Laser System are accessible via the power supply front panel. These controls -- described in detail in the power supply design section -- are flexible and complex because of the experimental nature of this hardware.

The modelocker driver electronics are packaged in the housing of an Electronic Navigation Industries Model 310L RF amplifier. This housing contains, in addition to the RF amplifier, a precision crystal-oscillator frequency source and a frequency synthesizer. The power input required for this unit is 120 v, 60 Hz ac. The two BNC cables from this unit to the power supply and the transmitter connect to the front panel. The controls for this unit also are on the front panel. The prime power input will be modified to 28V-dc in Phase II of this program.

The cooling system for the Spaceborne Laser System is housed in a chassis and case. The system is a closed-cycle unit containing a fan, coolant pump, ion-exchange filter and liquid-to-air heat exchanger. The 24-v dc power required for this unit is obtained via a cable splitting from the main transmitter power supply cable. Quick-disconnect coolant fittings are provided for the inlet and outlet coolant hoses at both the transmitter and cooling system ends. All connections to this unit are made via the front panel. The cooling system will use a liquid-liquid heat exchanger in Phase II.

2. Mechanical Configuration

The mechanical design effort on the Spaceborne Laser System program was essentially the design of the laser transmitter. Existing packaging designs were used with minor modifications for the power supply and cooling system. The modelocker driver packaging was a minor modification to a purchased unit. The mechanical design of the Spaceborne Laser System transmitter is almost entirely new. This design effort involved designs of the optical bed, modulator housing and optical mounting, laser pump cavity, passive optics mounts, and the transmitter packaging.

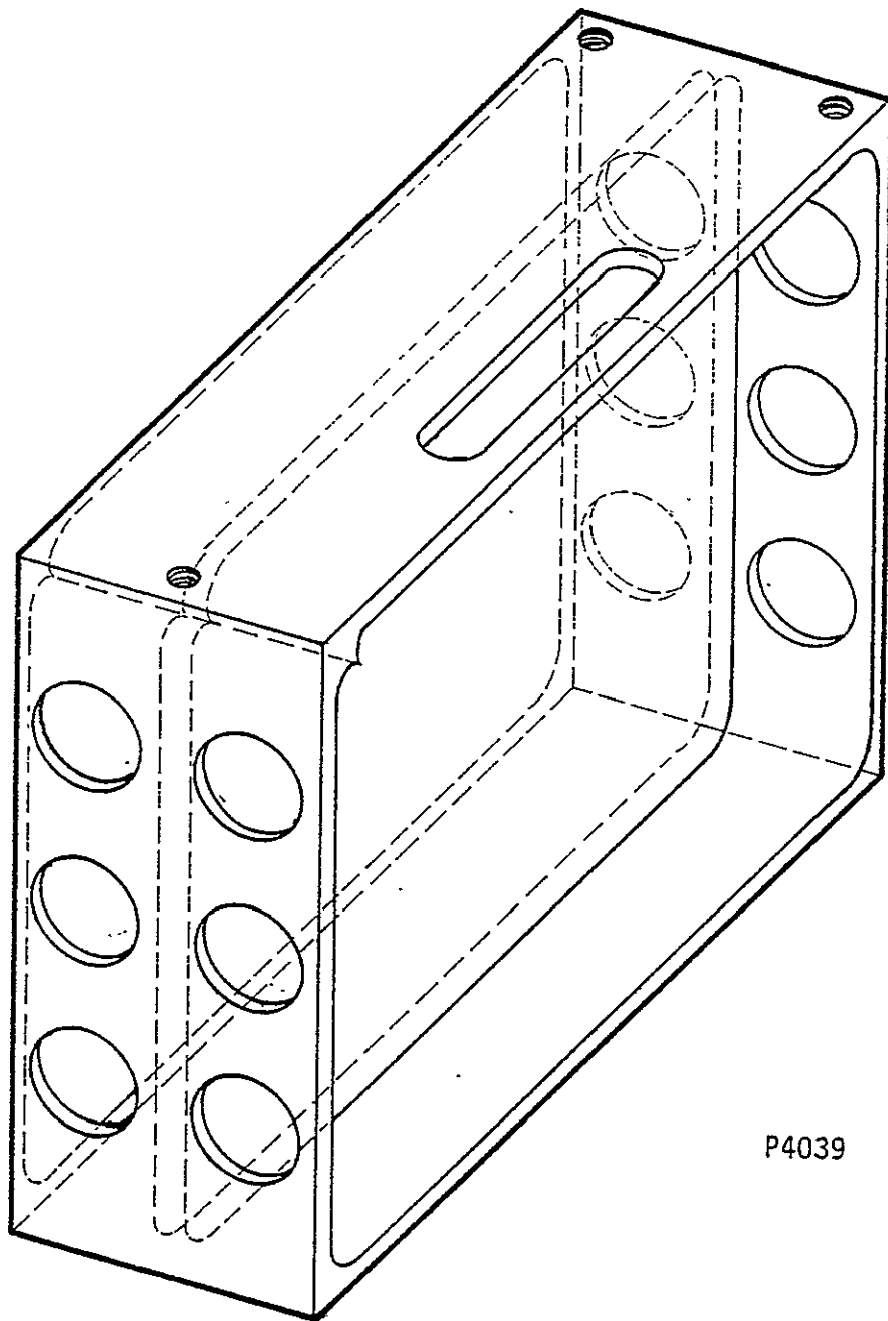
A major function of the mechanical design task involved the conception, analysis and design of the optical bed. The mechanical and thermal stability of this bed was an important parameter since the Spaceborne Laser System involves active modelocking. Modelocking of this type requires stringent control of the optical length of the laser resonator which depends substantially on optical bed dimensional stability.

Figure 3-3 is a sketch of the optical bed conceived on this program. The material used for this optical bed was Invar, a low thermal expansion material. A thermal and mechanical stress analysis was performed on this optical bed which indicated a dimensional and distortion stability approaching that of the Invar material. This optical bed concept is considered by ILS to be a near optimum one for the implementation of the Spaceborne Laser System concept. Appendix C gives the details of the optical bed analysis.

3. Electronic System Overview

The electronic system, as considered in the most elementary form, is depicted in Figure 3-2. Four component blocks comprise the system. These blocks are:

- The power supply unit;
- The laser head unit, or transmitter unit;
- The modelocker driver unit; and
- The cooling system unit.



P4039

Figure 3-3. Optical Bed Sketch

Figure 3-4 elaborates upon the major system circuit block to depict the subunits contained within.

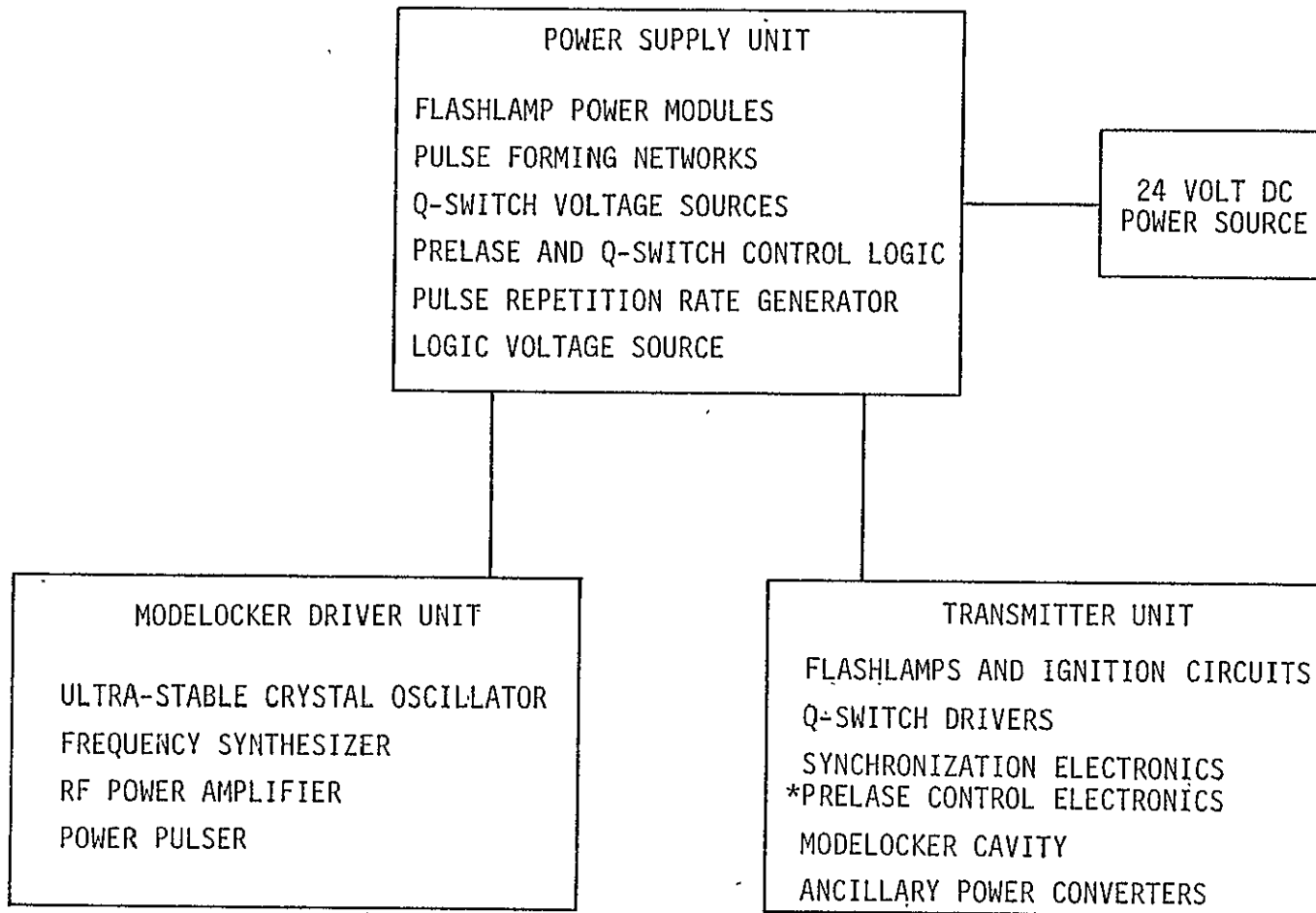
The power supply unit contains:

- The flashlamp power modules (two each);
- The pulse-forming networks (two each);
- The Q-switch voltage sources (two each);
- The prelude and Q-switch control logic;
- The pulse repetition rate/frequency (PRF) generator;
- The logic voltage source or power supply; and
- The simmer supplies (two each).

The prime power input is 24 to 28 V dc.

The transmitter unit contains:

- The Q-switch drivers and Pockels cell;
- The synchronization electronics;
- The prelude control electronics;
- The flashlamps and ignition transformers;
- The active modelock modulator; and
- Ancillary low-voltage power supplies.



P2789

Figure 3-4. Electronic System Block Diagram

All laser transmitter power is routed from the power unit, the exception being the modelock drive which originates from the modelocker driver unit. Figure 3-5 depicts the transmitter unit electrical system.

The remaining unit, the modelocker driver unit, contains:

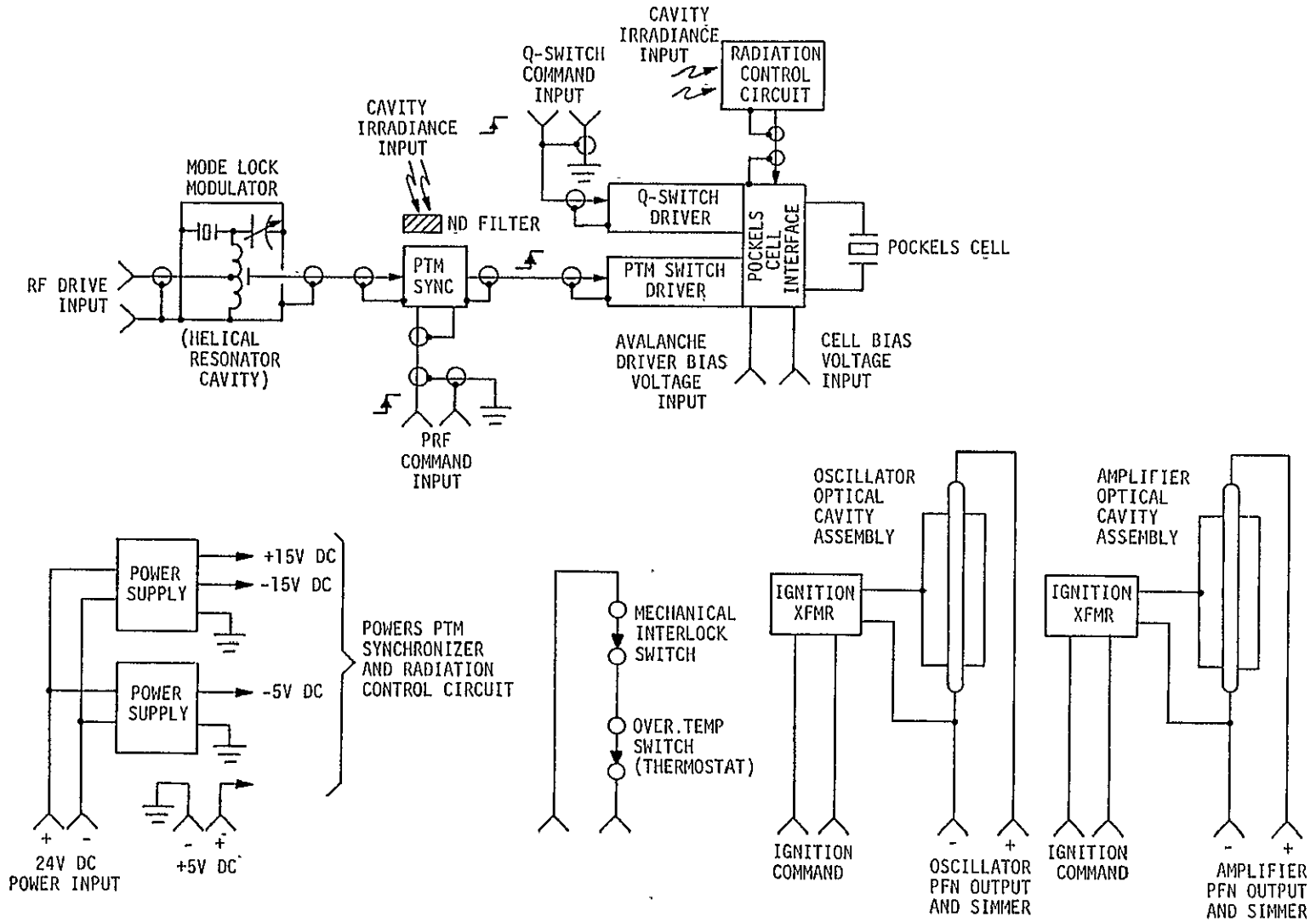
- An ultrastable crystal controlled oscillator;
- A frequency synthesizer;
- A radio frequency (RF) amplifier; and
- A power pulser.

Power for the modelocker driver is currently from the 117 V ac mains; however, the unit lends to modification for 24-V dc operation. Because the modelocker driver is only a bread-board, this modification was not considered necessary.

4. Optical Concepts

The primary optical concepts developed on the Spaceborne Laser System program are the common-mirror, crossed TIR prism resonator and the double-pass amplifier utilizing a Porro prism as both mirror and half-wave phase plate. Analysis involving these two concepts plus modulator, pump cavity and laser damage studies were the topics of the optical design performed on this program.

The common-mirror, crossed TIR prism resonator is the most important optical concept developed on this program. Figure 3-6 shows the optical elements of this resonator as employed in the Spaceborne Laser System. The importance of this concept stems from its relative insensitivity to misalignment with respect to small motions of the common mirror and TIR prisms and the compactness (low volume) provided by the four folds. Both of these properties are very important for laser hardware, the end goal of this development program. The design studies performed related to the Spaceborne Laser System resonator included resonator mirror design, resonator length and alignment sensitivity analysis, and the specific optical design of each resonator element. The goal of the latter design task was to avoid etalon effects within the resonator.



P3988

Figure 3-5. Transmitter Electronic System

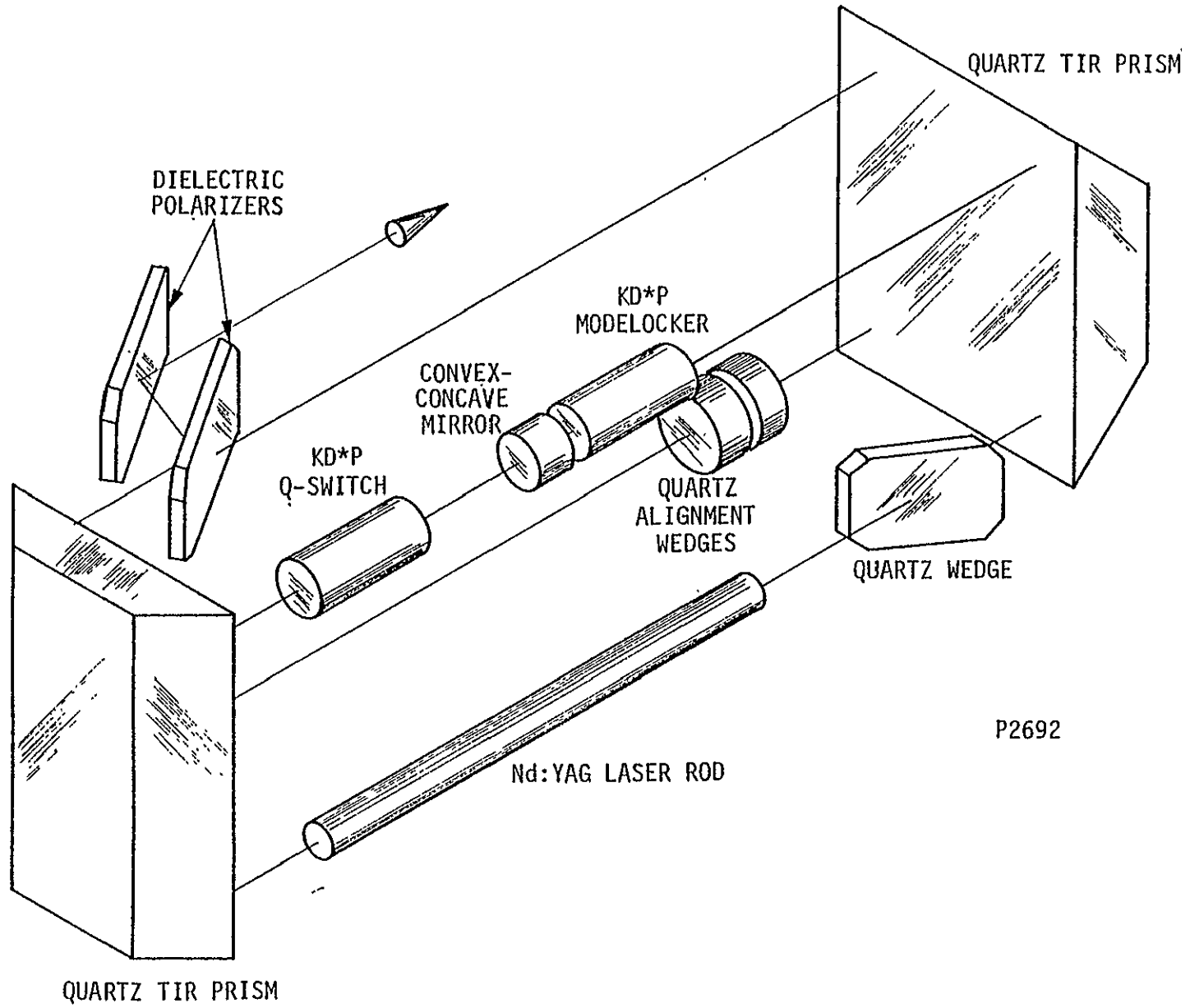


Figure 3-6. Spaceborne Oscillator Optical Configuration

The optical elements of the amplifier system are depicted in Figure 3-7. The optical designs of these elements were simple because etalon effects were not important as in the resonator system. The concept of using a Porro prism as Max R reflector and as a half-wave phase retarder was generated to avoid the use of crystalline quartz, a low damage threshold optical material. The roof line of the Porro prism actually is 45° to the polarization plane. It is shown vertical for ease of illustration.

All of the optical materials used in the Spaceborne Laser System were evaluated with respect to laser damage threshold via the published literature and discussions with vendors. The effects of nonlinear self-focusing also were evaluated. The latter phenomena was shown to be the primary limiting factor on the energy output of the Spaceborne Laser System.

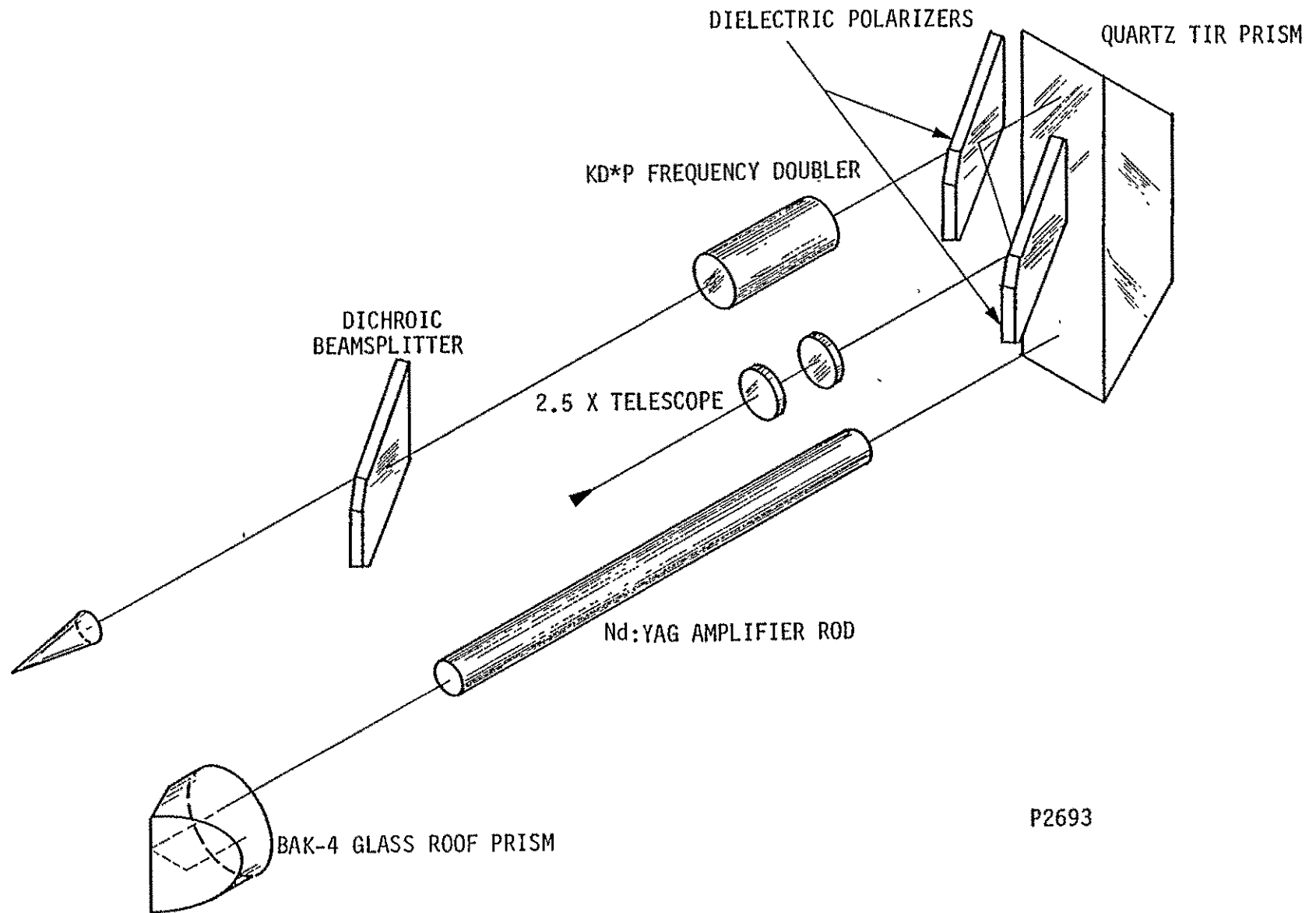
The modulator study determined the electronic drive requirements for the cylindrical ring electrode (CRE) KD*P crystals used as the Q-switch and modelocker modulators. The transmission uniformity, the quarter-wave voltage and the capacitance of the CRE KD*P crystals were reviewed. Also, the loss tangent reported for KD*P was utilized to analyze heating effects in the modelocker modulator.

The pump cavity design study involved a review of the literature on pump cavity design and consultation with ILS experts in this area. The design generated combined several ideas from the literature and ILS personnel in an attempt to improve pumping efficiency and uniformity.

B. OPTICAL DESIGN

1. Laser Damage Evaluation

Nonlinear self-focusing effects limit the attainable power density and thus the energy output of the Spaceborne Laser System. These effects limit the power density in two ways. Localized self-focusing induced by spatial intensity fluctuations of the laser beam can result in laser damage. Whole-beam self-focusing can limit the TEM₀₀-mode volume. The laser damage thresholds of the optical materials and dielectric thin films utilized in the Spaceborne Laser System are substantially higher than the limits imposed by self-focusing.



P2693

Figure 3-7. Spaceborne Amplifier Optical Configuration

The electric field intensity of a high-peak-power laser beam modulates the refractive index of optical materials through nonlinear effects. The variation of the index as a function of the electric field is given by:

$$n = n_0 + n_2 |E|^2 \quad (3-1)$$

where n_0 = the refractive index of the optical material;
 n_2 = the nonlinear index of refraction;
 and $|E|^2$ = the instantaneous value of the electric field squared.

The relationship between the latter parameter and the beam intensity, denoted by I , is:

$$I = \frac{n_0 |E|^2}{2\eta_0} \quad (3-2)$$

where η_0 = the characteristic impedance of free space.

The index of refraction of a material irradiated by a gaussian beam of intensity,

$$I = I_p \exp(-2r^2/w^2) \quad (3-3)$$

is thus given by

$$n(r) = n_0 + 2(n_2 n_0 / \eta_0) I_p \exp(-2r^2/w^2). \quad (3-4)$$

Clearly, the index of refraction is greatest at the center of the gaussian beam and falls gradually to n_0 as one moves from beam center. Thus, the beam propagates slower at the center of the beam than elsewhere and optical focusing results.

The effects of whole-beam self-focusing on the TEM₀₀-mode diameter in Nd:Glass lasers has been analyzed by Eckhardt⁹. A critical parameter in this analysis was the temporal regime in which the pulse has a high intensity. The degree of whole-beam self-focusing is inversely proportional to the duration of this temporal regime. The higher gain of Nd:YAG relative to Nd:Glass significantly reduces the extent of the temporal regime in which the power density is significant. A power density limit of ~ 1.0 GW/cm² was extrapolated from the results of Eckhardt's analysis for the Spaceborne Laser System resonator.

An optical beam with an intensity greater than the critical power of its propagation medium is unstable with respect to localized self-focusing. The critical power¹⁰ of an optical medium is defined by

$$P_c = 3.77 \frac{\epsilon_0 c \lambda_0^2}{8 \pi n_2} \quad (3-5)$$

Table 3-1 gives the critical power of several optical materials used in the Spaceborne Laser System.

Table 3-1 Critical Power of Selected Optical Media ^{11, 12}

Material	n_2 ($\times 10^{-22} \text{ m}^2/\text{V}^2$)	P_c ($\times 10^5 \text{ W}$)
YAG	4.5	10.01
QUARTZ	1.1	40.96
KDP	1.1	40.96
ED-4	2.1	21.46

Transverse spatial fluctuations in an optical beam of greater intensity than the critical intensity will, in general, grow exponentially and might eventually result in laser damage. Clearly, localized self-focusing can be controlled by obtaining a smooth spatial profile. However, inevitable optical defects will generate spatial fluctuations. It is difficult to obtain analytic power density limits for which localized self-focusing is not a problem. However, the literature does report operation of modelocked Nd:YAG laser oscillators at or slightly above 1.0 GW/cm^2 without incurring laser damage as the result of localized self-focusing.^{13, 14}

Tables 3-2 and 3-3 present the damage threshold at 1,064 nm of the optical materials and dielectric thin-films selected for use on the Spaceborne Laser System. Clearly, these power densities exceed considerably the limits set by self-focusing effects.

Table 3-2 TEM₀₀ Mode Laser Damage Thresholds ^{15, 16}

Material	Damage Threshold
KD*P	22 GW/cm ² *
ED-4	108 GW/cm ² *
Nd:YAG	>12 GW/cm ²
Quartz	>100 GW/cm ²

*Pulsewidth = 125 ± 25 psec

Table 3-3 TEM₀₀ Mode Laser Damage Threshold¹⁵
of Dielectric Coatings

Coating	Substrate	Average Damage Threshold
Anti-reflection	EY-1	3.7 J/cm ² (29.6 GW/cm ²)
Dielectric Polarizer	BK-7	3.6 J/cm ² (28.8 GW/cm ²)
Maximum Reflection	--	3.3 J/cm ² (26.4 GW/cm ²)

pulsewidth = 125 ± psec

Spot Diameter = 0.25 cm

2. Resonator Design

The design of the resonator mirrors for the Spaceborne Laser System took into consideration spot size sensitivity to thermal lensing and alignment sensitivity of the common-mirror resonator. A concave-convex resonator was chosen for implementation because of the absence of a beam waist within the resonator as well as other properties cited in the literature.

The spot size, w , of a gaussian TEM₀₀ laser beam is defined by the equation:

$$I(r) = I_p \exp [-2(r/w)^2] \quad (3-6)$$

where I_p = peak beam intensity and

r = distance from center of beam.

The spot sizes¹⁶ on the mirrors of a resonator with a thin internal lens are given by

$$w_{2,1} = \left(\frac{\lambda B}{\pi} \right)^{\frac{1}{2}} \left[\frac{g_{1,2} g_{2,1}}{1 - g_1 g_2} \right]^{\frac{1}{4}} \quad (3-7)$$

where

$$B = d_1 + d_2 - \frac{d_1 d_2}{f},$$

$$g_1 = 1 - \frac{d_2}{f} - \frac{B}{R_1},$$

$$g_2 = 1 - \frac{d_1}{f} - \frac{B}{R_2},$$

f = lens focal length,

$R_{1,2}$ = mirror radii of curvature, and

$d_{1,2}$ = distance from mirror 1, 2 to lens center.

In practice, the laser rod can be treated as a thin lens if the rod thermal focal length is long. This condition will be shown to be the case for the Spaceborne Laser System.

The sensitivity of the TEM₀₀-mode volume in the laser rod to fluctuations in thermal lensing can be expressed analytically. The derivative of the spot size on the mirror nearest to the laser rod with respect to the focal length of the rod can be derived as follows:

$$\frac{dw_2}{df} = \frac{w_2}{4f^2(1-g_1g_2)} \left\{ \frac{2d_1d_2(1-g_1g_2)}{B} + \frac{d_2}{g_1} \left(1 - \frac{d_1}{R_1} \right) + \frac{d_1(2g_1g_2-1)}{g_2} \left(1 - \frac{d_2}{R_2} \right) \right\} \quad (3-8)$$

This derivative can be calculated numerically given the mirror radii, mirror-rod optical distances and rod focal length.

The sensitivity of the common mirror resonator to misalignment can be determined analytically. The partial derivatives¹⁷ of the beam displacements on the laser mirrors with respect to mirror angular tilt, θ , are

$$\frac{\Delta d_1}{\Delta \theta} = \frac{R_1R_2(1-g_2)}{X} \quad \text{and} \quad \frac{\Delta d_2}{\Delta \theta} = \frac{R_1R_2(g_1-1)}{X} \quad (3-9)$$

where $X = g_1R_1 + R_2 + R_1R_2 \cdot \frac{f}{d_2} \frac{\partial g_1}{\partial f}$.

Δd_1 and Δd_2 are the lateral displacements of the beam center on mirrors 1 and 2, respectively, and $\Delta \theta$ is the mirror tilt.

The thermal focal length of a solid-state laser rod that is uniformly pumped and symmetrically cooled is given by the equation:¹⁸

$$f = \frac{K\pi r^2}{H \left[(1/2) \frac{dn}{dT} + Cn_o^3 \right]} = \frac{K}{H} \quad (3-10)$$

where

- f = focal length of laser rod thermal lens,
- K = thermal conductivity of laser material,
- r = laser rod radius,
- dn/dT = refractive index thermal coefficient,
- n_o = refractive index at lasing wavelength,

α = coefficient of linear expansion,
C = stress optic coefficient,
H = heat per unit time absorbed by laser rod.

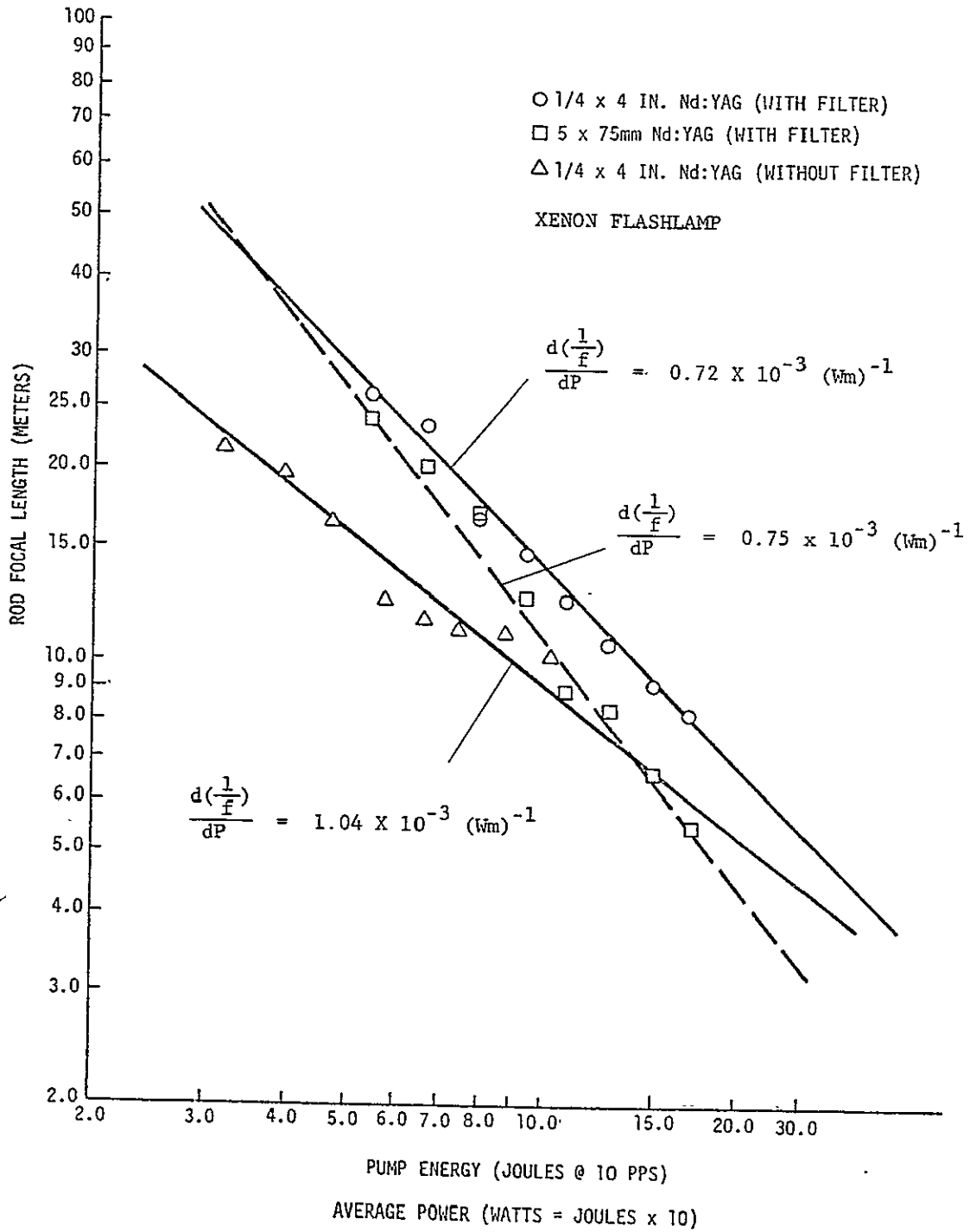
Typical thermal lensing of Nd:YAG laser rods is shown in Figure 3-8. The pump level of the Spaceborne Laser System ranges between 3 to 5J. Thus, a focal length of ~ 25 m is used in the calculations given below for the 5 x 101.6mm oscillator laser rod.

The equations given above permit calculation of the spot sizes on the laser mirrors as a function of rod focal length, the alignment sensitivity and the sensitivity to thermal lensing. Figure 3-9 gives these quantities for a laser resonator with parameters near those of the Spaceborne Laser System resonator.

3. Oscillator Optical Design

The optical design of the Spaceborne Laser System resonator shown in Figure 3-10 was generated with the paramount consideration of avoiding etalon effects. These effects would limit the spectral width of the laser radiation and then make the achievement of the desired pulsewidth difficult, if not impossible. Every element of the laser resonator was designed as a wedge except the laser mirror. Also, every optical surface was set 0.20° to 0.25° off every other optical surface. The one exception was two sets of optical surfaces of the TIR prisms. These surfaces however were tilted sufficiently and far enough apart to eliminate the interference effects of the established etalon. In practice, the establishment of this etalon was improbable because of the optical tolerance of intervening optical components.

The laser rod leg of the resonator was designed to include a quartz wedge which essentially compensated for the deviation and lateral offset introduced by the wedged laser rod. The KD*P Q-switch and modelock cells were designed to be identical and were mounted such that the deviation and lateral offset of one cell was compensated for by the other cell. The dielectric polarizer internal to the resonator also was designed as a wedge. The two quartz Risley wedges were designed to compensate for both the offset and deviation of the polarizer. These Risley wedges also were designed to have a range of deviation and offset sufficient to compensate for the cumulative fabrication tolerance of the optical elements. The quartz TIR prisms were designed with a pyramidal error so



P2209A

Figure 3-8. Dependence of Laser Rod Focal Length on Pump Level

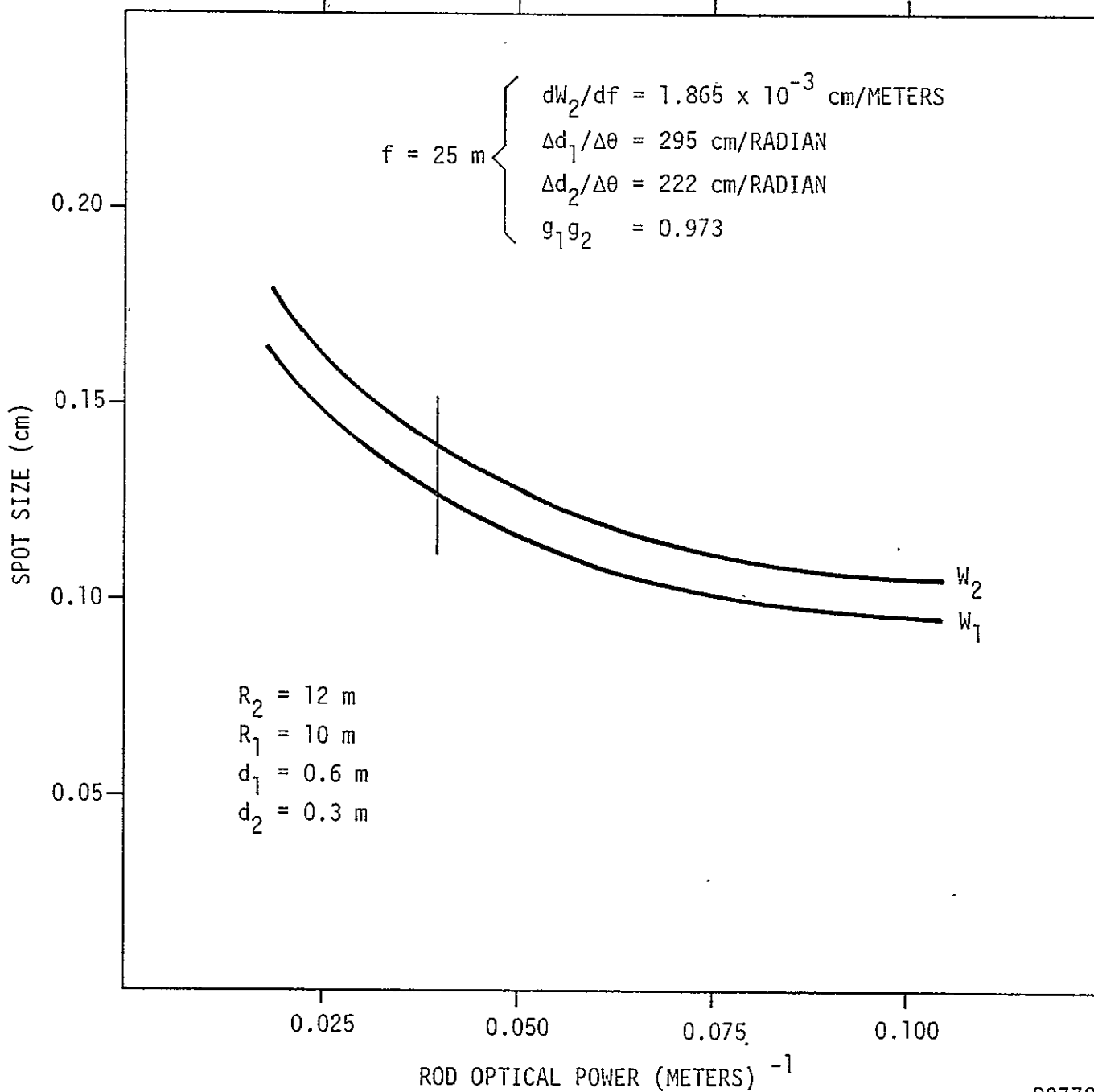
ROD FOCAL LENGTH - METERS

40

20

13.3

10



P2772

Figure 3-9. Spaceborne Resonator Spot Size Characteristics

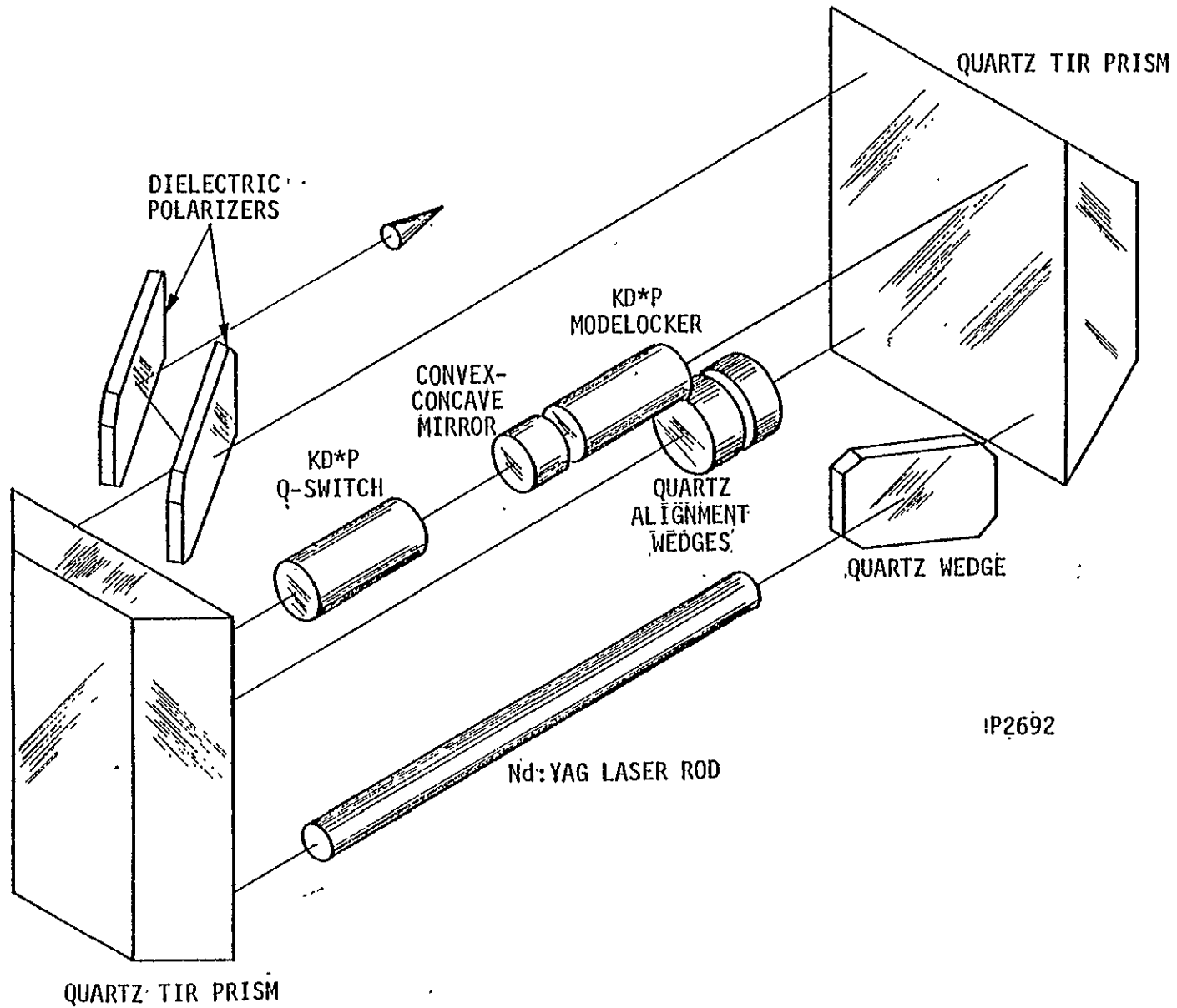


Figure 3-10. Spaceborne Oscillator Optical Configuration

that the entrance and exit faces were not parallel internal to the TIR prisms. The detailed description of all of the optical components is presented in the appendix containing the optical design drawings.

4. Modulator Analysis

The nonlinear crystal KD*P was used as the modelocking and Q-switching modulators. The cylindrical ring electrode (CRE) configuration for KD*P is employed. The transmission uniformity, the $\lambda/4$ voltage and the modulator capacitance are significant for both the modelocking and Q-switch KD*P cells. In addition, the loss tangent is significant for the mode-locking modulator. Table 3-4 summarizes the properties of KD*P crystals.

The $\lambda/4$ voltage for a CRE KD*P Pockels cell given by Lasermetrics literature is 3200 v. The $\lambda/4$ voltage is related to the nonlinear electro-optic coefficient r_{63} by

$$V_{\lambda/4} = (\lambda/4n_o)^3 r_{63} \quad (3-11)$$

where n_o is the ordinary index of refraction of KD*P. This index is reported by Harshaw to be 1.47.¹⁹ However, a close comparison of the ordinary index of refraction of KD*P and KDP reveals that n_o is probably closer to 1.49.

The electro-optic coefficient for 90% deuterated KD*P at high frequencies is 24.0×10^{-12} m/V at 500 nm for room temperature. Assuming r_{63} to be wavelength-independent, $V_{\lambda/4}$ at 1,064 nm for high-frequency modulation is calculated to be 3350 v. The corresponding static $\lambda/4$ voltage is ~ 3200 v.

Table 3-4 Properties of KD*P²⁰

<u>Thermal Conductivity</u>	$18 \frac{\text{mW}}{\text{cm}^\circ\text{K}}$ @ 300°K
<u>Electrical Conductivity</u>	$10^{-10} (\text{ohm-cm})^{-1}$
<u>Resistance</u>	1000 M Ω
<u>Maximum Safe Operating Temperature</u>	100°C
<u>Surface Resistivity</u>	$1.3 \times 10^{11} \text{ ohm/cm}^2$

Table 3-4 Properties of KD*P (continued)

<u>Dielectric Strength</u>	~70,000 V/cm
<u>Dielectric Constant</u> (ϵ_c)	45 @ 30°C @ 9.2 GHz 50 @ 24°C @ 1000 Hz
<u>Piezoelectric Constants</u> @ 30°C	$d_{36} = 52 \times 10^{-12}$ C/N, $d_{14} = 3.3 \times 10^{-12}$ C/N, $g_{36} = 0.13$ m ² /C @ 60 MHz
<u>Loss Tangent @ 24°C</u>	0.0012 @ 100 MHz 0.0072 @ 1000 MHz
<u>Dielectric Constant @ 24°C</u>	39.3 @ 100 MHz 41.3 @ 1000 MHz
<u>Electro-Optic Coefficient</u> @ 30°C	$r_{63}^t = 25.6 \times 10^{-12}$ m/V $r_{63}^s = 24.0 \times 10^{-12}$ m/V
<u>Refractive Index</u>	$n_o = 1.47$ @ $\lambda = 1.0\mu$ (E 1 to C axis)

The capacitance of a CRE KD*P Pockels cell is given according to Steinmetz²¹ by the equation

$$C = (\pi R^2 \epsilon_z \epsilon_o / 2) (L/W) \quad (3-12)$$

where R = the crystal radius;

$\epsilon_z \epsilon_o$ = the electrical permittivity of the crystal in the z direction;

2L = the length of the crystal; and

W = the electrode width.

The CRE configuration identified by Steinmetz as near optimum with respect to transmission uniformity for a 0.25-in. diameter beam had L = 12mm, W = 8mm, and R = 6mm. This configuration will be used in the Spaceborne Laser System and has a calculated capacitance of 6.4 pF. Measured capacitance of 7 to 10 pF for CRE cells of these dimensions are regularly obtained by Lasermetrics.

According to a McDonnell Douglas report²² the loss tangent of KD*P is 0.0012 at 100 MHz. Other sources (Cleveland Crystals²³ and the Handbook of Linear Electro-optic Materials²⁰) confirm that this value is fairly accurate. The loss tangent is almost certainly no greater than 0.002 for the driving frequency of ≈ 60 MHz. These values are for 30°C. Data in the handbook mentioned above indicate that the loss tangent decreases with increasing temperature. However, the data is not definitive for the proposed driving frequency.

The KD*P modelocking modulator is driven via a series resonant circuit. The voltage source for this series resonant circuit is a temperature stabilized crystal oscillator ($>1/10^6$ stability) amplified to 3V peak-to-peak by a commercial RF amplifier system.

The differential equation for a RLC circuit driven by a sinusoidal source is

$$L \frac{d^2 i}{dt^2} + R \frac{di}{dt} + \frac{i}{C} = V_m \omega \cos(\omega t) \quad (3-13)$$

where $v = V_m \sin(\omega t)$ is the driving voltage.

The steady-state solution to this equation is

$$i = \frac{V_m}{\sqrt{R^2 + (1/\omega C - \omega L)^2}} \sin \left[\omega t + \tan^{-1} \left(\frac{1/\omega C - \omega L}{R} \right) \right] \quad (3-14)$$

At the series resonant condition,

$$\frac{1}{\omega C} = \omega L \text{ and} \quad (3-15)$$

$$i = \frac{V_m}{R} \sin(\omega t). \quad (3-16)$$

The literature²² gives a value of 0.0012 for the loss tangent of KD*P at 100 MHz--that is, $\omega CR = 0.0012$. The capacitance of a typical cylindrical-ring-electrode (CRE) KD*P cell is no greater than 10 pF. The modelocking frequency that has been selected is 60 MHz. Assuming that the loss tangent for 60 MHz is approximately that at 100 MHz--say 0.002-- the effective resistance of the cell is $R \approx 0.53 \Omega$.

The resonant frequency of a series resonant circuit is given by

$$f = \frac{1}{2\pi} \frac{1}{\sqrt{LC}} \quad (3-17)$$

Thus, the ideal inductor required to produce series resonance in series with a KD*P cell with ~ 10 pf of capacitance at a frequency of 60 MHz is $L \approx 0.7 \mu\text{h}$. Recall that the current at series resonance is given by $i = (V_m/R) \sin(\omega t)$. Thus, the voltage across the KD*P cell is given by

$$V_c = \frac{i}{\omega C} = \frac{V_m}{\omega CR} \sin(\omega t). \quad (3-18)$$

Recalling that $v = V_m \sin(\omega t)$, it is clear that the voltage multiplication factor is given by

$$V_c/v = \frac{1}{\omega CR} \approx 500 \quad (3-19)$$

for $f = 60$ MHz, $C = 10$ pf, and $R = 0.53\Omega$. Thus for a voltage input of 6 v peak-to-peak, it should be possible to obtain a voltage of 3000 v peak-to-peak across the KD*P cell.

The equation for the average power dissipated in the RLC circuit at series resonance is

$$P = \frac{V_m I_m}{2} = \frac{V_m^2}{2R} \approx 34 \text{ W} \quad (3-20)$$

for $V_m = 6$ v and $R = 0.53\Omega$. For a duty cycle of 1000 of 1 the average power input to the modulator is 37 mW. Thus, crystal heating problems should not be encountered.

5. Pump Cavity Design

The pump cavity designs for the Spaceborne Laser System were guided by information obtained from a literature review and previous ILS experience. International Laser Systems has personnel who have been involved in pump cavity design and experimentation for the past 15 years. The emphasis in the studies performed has always been on increasing laser efficiency. As a result, ILS pump cavities now represent the state-of-the-art with regard to pumping efficiency.

Pumping and cooling uniformity also were goals of the final designs of the Spaceborne Laser System pump cavity. These latter two parameters are important for the efficient operation of a TEM₀₀-mode laser. The designs developed for the Spaceborne Laser System pump cavity were plural because an experimental approach was indicated by the reviews of pump cavity theory. At present, this theory analytically speaking is fragmented and only provides design guidelines.

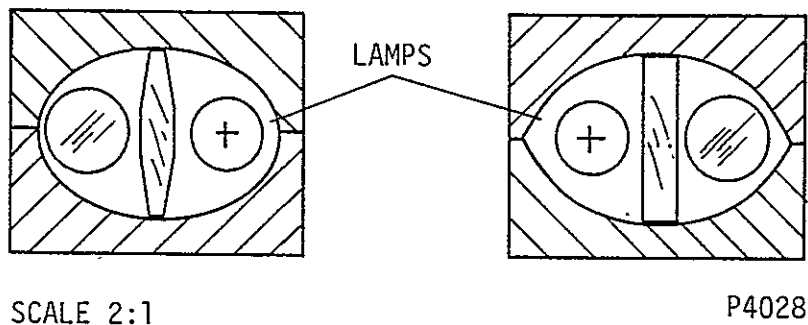


Figure 3-11. Typical ILS Pump Cavity

Figure 3-11 shows two typical ILS pump cavity cross sections on a two-to-one scale. The cavity reflectors are silver-plated for optimum reflectivity. Degradation of these reflectors is avoided by use of ultra-clean coolant and ion-exchange filters. The reflectors are approximately four times longer than the average cross-sectional dimension. Both of the pump cavities shown are nonfocal--that is, the flashlamp and

rod are not at the focal points or a precise focal point is not defined.

A color filter is indicated between the rod and lamp in Figure 3-11. These filters are essentially opaque below 3500 Å and thus reduce heating of the laser rod due to UV absorption. Shaping the filter into a wedge as shown in Figure 3-13 results in better laser efficiency in some cavity geometries.

A typical feature of ILS pump cavities not shown in Figure 3-11 is the use of silver baffles to direct coolant flow uniformly around the rod. This feature results in essentially uniform cooling and, as a consequence, uniform thermal lensing of the laser rod. Symmetrical thermal lensing is essential to the achievement of efficient TEM₀₀-mode operation. The flashlamp diameter for 6.35-mm (0.25-in.)-diameter laser rods that is near optimum for laser efficiency is 5 mm. The actual bore diameter is 3 mm because the quartz envelope is typically 1 mm thick.

The pump cavity design guidelines given in the literature^{24, 25, 26, 27} essentially mirror the present ILS designs. From several references the following guidelines have been established:

- A single elliptical cavity is more efficient than multiple ellipses;
- Long elliptical cavities are more efficient than short ones;
- Nonfocal pump cavities can be more efficient in small elliptical cavities because of enhanced multiple reflections through the laser rod; and
- The flashlamp should be the same diameter or smaller than the laser rod diameter.

All of the above guidelines are followed by present ILS pump cavity designs to the extent that is practically possible. Additionally, ILS has determined particular optimization of some of the above guidelines via experimentation as mentioned previously.

Information, not mentioned in the literature but discovered experimentally by ILS personnel, is that the pumping

enclosure need not be elliptical. Also, the effects of filters between the laser rod and flashlamp are not mentioned as a potential enhancement of efficiency. Thus, the major conclusion of the internal ILS experimentation and the literature review is that the two factors remaining to be investigated in pump cavity design are the shape of the pump cavity and the effects of an intra-cavity filter. A limited experimental effort was initiated on the Spaceborne Laser System program to investigate these two parameters. The pump cavity shapes shown in Figure 3-11 together with various filter shapes were chosen for investigation based on previous ILS experience. Experimentation with a diffuse filter also was planned in an attempt to improve pumping uniformity as described by Lewinberger and Herziger²⁸. The specific design details of the pump cavities are given in the mechanical design section of this report.

6. Amplifier Optical System

The Spaceborne Laser System double-pass amplifier optical system is shown in Figure 3-12. The elements of this system are a beam-expanding telescope, two dielectric polarizers, a Nd:YAG laser rod, and a Porro prism which functions as a mirror and a half-wave phase retarder. The design of this optical system was performed with two guidelines. First, to eliminate or reduce spurious reflections back into the oscillator and, second, to avoid damage-prone components. The first guideline resulted in the Nd:YAG laser rod and the TIR prism being wedged. The second guideline resulted in the use of a glass Porro prism as a phase retarder instead of a crystalline quartz phase plate.

The operation of the amplifier system is described with reference to Figure 3-12. Initially, the oscillator beam is vertically polarized with reference to the shown dielectric polarizers, expanded by the telescope and directed by the two dielectric polarizers through the TIR prism. When the beam has been amplified by the laser rod, it enters the anti-reflection-coated half of the Porro prism. Two reflections off the Porro prism TIR surfaces direct the beam to the maximum reflectance-coated half of the Porro prism. Proper alignment of this element directs the beam back on itself and two more TIR reflections are made. The four TIR reflections result in a half-wave phase retardation. The resultant horizontally polarized beam is amplified again, once more traverses the TIR prism and is transmitted by the second folding dielectric polarizer. The transmitted beam is the output of the Spaceborne Laser System.

The lenses are of quartz and were anti-reflection (AR) coated by Valtech. The telescope is designed to diverge any reflections from the lens surfaces to eliminate the danger of a reflection focus resulting in laser damage. Two sets of negative lenses were made. One gives a magnification of 1.499 and the other gives 1.587. These magnifications permit a beam diameter near 5 mm

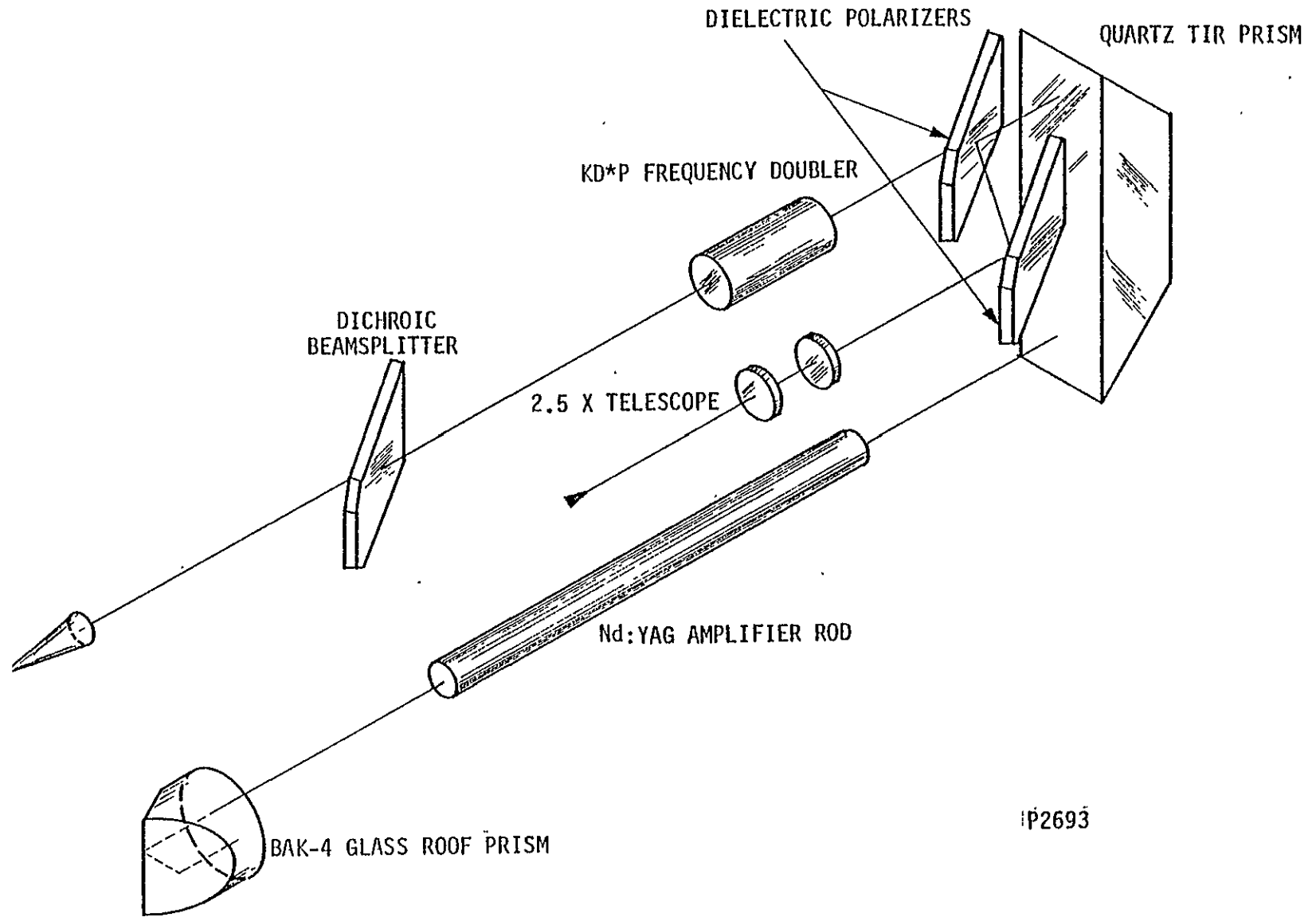


Figure 3-12. Spaceborne Amplifier Optical Configuration

with the oscillator beam diameter ranging from 3.0 to 3.5 mm.

The folding polarizers and the TIR prism were both fabricated of quartz. The polarizers were coated by Optical Coating Laboratory, Inc. (OCLI) and the prism was coated by Valtech. The TIR prism was fabricated with a pyramidal error which eliminates spurious reflection from the prism outer surfaces back into the oscillator.

The amplifier laser rod is a 1/4-in. by 4-in. Nd:YAG crystal. The rod is wedged on both ends in the same direction to eliminate reflections into the oscillator. The laser rod ends were AR-coated by Lambda-Airtron.

The Porro prism is the one special optical piece in the amplifier system. This element performs as both maximum reflectance mirror and phase retarder. The operation of the element as a mirror is clear. The beam enters the AR-coated side of the prism, reflects from the TIR surfaces and is returned on the same optical path by the Max R-coated side of the prism. Thus, the beam makes four TIR reflections on one pass through the prism. The fact that the two polarizations perpendicular and parallel to the TIR surfaces have different phase retardations after a TIR reflection is used to make the Porro prism a phase retarder. The following paragraph describes in detail how this was accomplished.

Define I_0 as the beam intensity incident on the Porro prism, I_{\perp} as the beam intensity polarized vertically, and I_{\parallel} as the intensity polarized horizontally. Before entering the Porro prism, the beam polarization is defined by $I_0 = I_{\perp}$. If the roof line of the Porro prism is placed 45° to the incident polarization, the beam reflected out of the Porro prism is defined in a polarization sense by

$$I_{\parallel}/I_0 = \sin^2(\theta/2). \quad (3-21)$$

θ is the total phase retardation (after four reflections) between the polarization components parallel and perpendicular to the plane of incidence of the TIR reflections. This relationship is expressed by

$$\theta = 8 \tan^{-1} \sqrt{1 - 2/n^2}. \quad (3-22)$$

Thus,

$$I_{\parallel}/I_0 = \sin^2 [4 \tan^{-1} \sqrt{1 - 2/n^2}] \quad (3-23)$$

defines the polarization state for the beam reflected from the Porro prism. If BAK-4 or ED-4 glass ($n \approx 1.55$) is used for this prism, $I_{\parallel}/I_0 \approx 1$ - that is - the polarization has been rotated 90° as desired.

C. ELECTRONIC DESIGN

This section of the report deals with the specific design concepts as dictated from the requirements established within the section devoted to the system overview. Specifically, the electronic design must provide the flashlamp excitations and the overall timing and control as constrained from and by the lase energy sequence and the lase command sequence. The reader is referred to Figure 3-13 and Figure 3-14 so he can acquire a concise view of the design requirement.

Slight departures from the depiction of Figure 3-14 will occur to provide ease of discussion of the various hardware groups. Three specific groupings are discussed, namely:

- The modelocker electronics;
- The switching and control electronics; and
- The power supply.

1. Modelocker Electronics

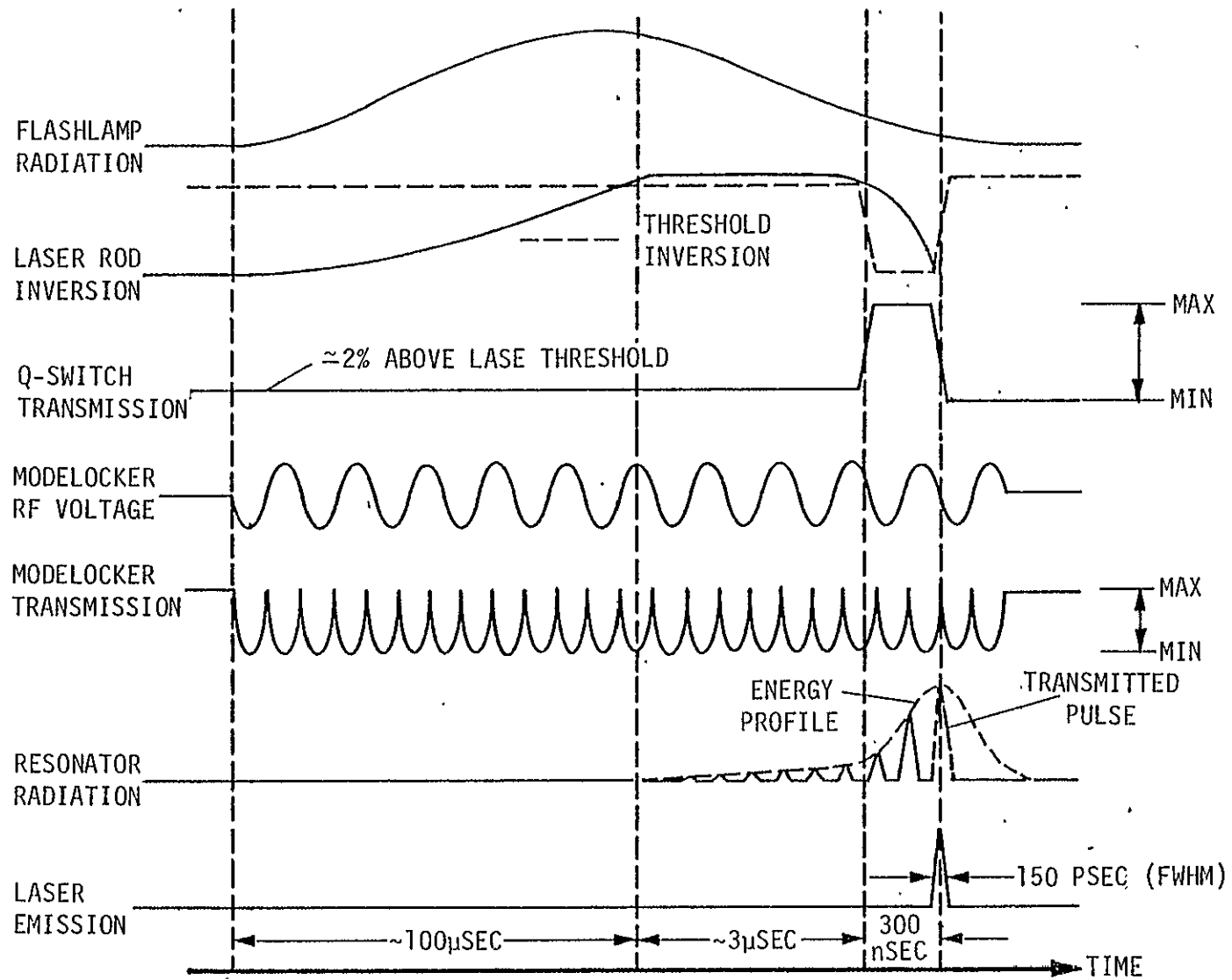
The modelocker electronics must generate a sinusoidal voltage across the modelocker Pockels cell to provide a variable transmission within the optical resonator at a rate synchronized to the optical resonator roundtrip transit time. The end result of this modulation is the compression of the resonator energy into a photon packet whose half-power pulsewidth is in the region of 200 psec duration. The compression is to occur prior to the Q-switch time.

a. Modelocker Subsystem

The modelocker subsystem consists of: the modulation Pockels cell and drive circuitry for impedance match, which is referred to as the helical resonator assembly; a precise crystal-controlled oscillator as a frequency reference; a frequency synthesizer; and a radio frequency (RF) power amplifier unit. The basic subsystem circuitry is depicted in Figure 3-15.

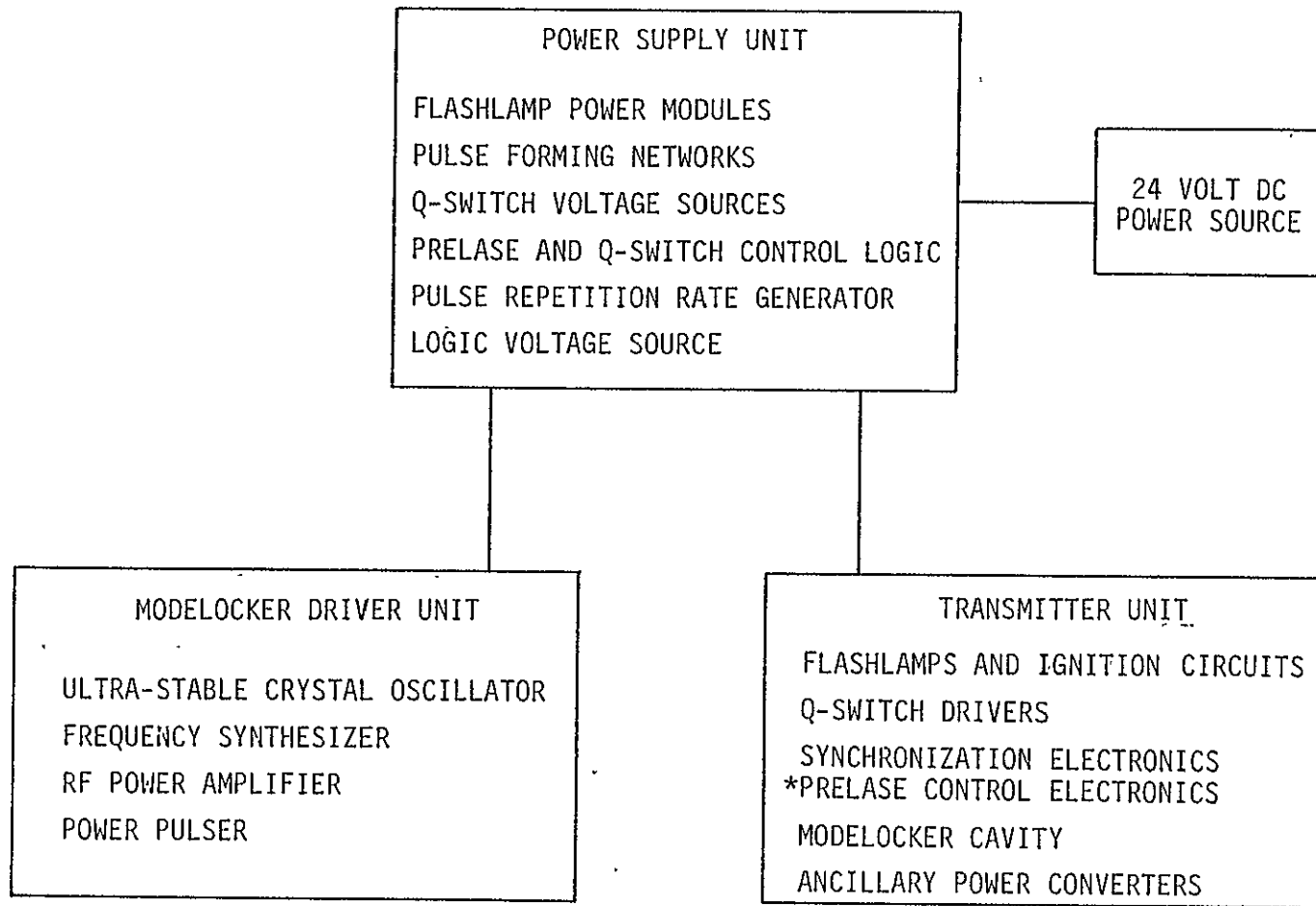
b. Frequency Source

The precision frequency source oscillator is a Vectron Model C0276 series unit, having an integral proportional temperature-stabilization oven. The frequency stability, as specified by Vectron, is $\pm 0.0001\%$ over temperatures from -40° to 50° C, following a stabilization period of 15 to 30 min. from turn-on.



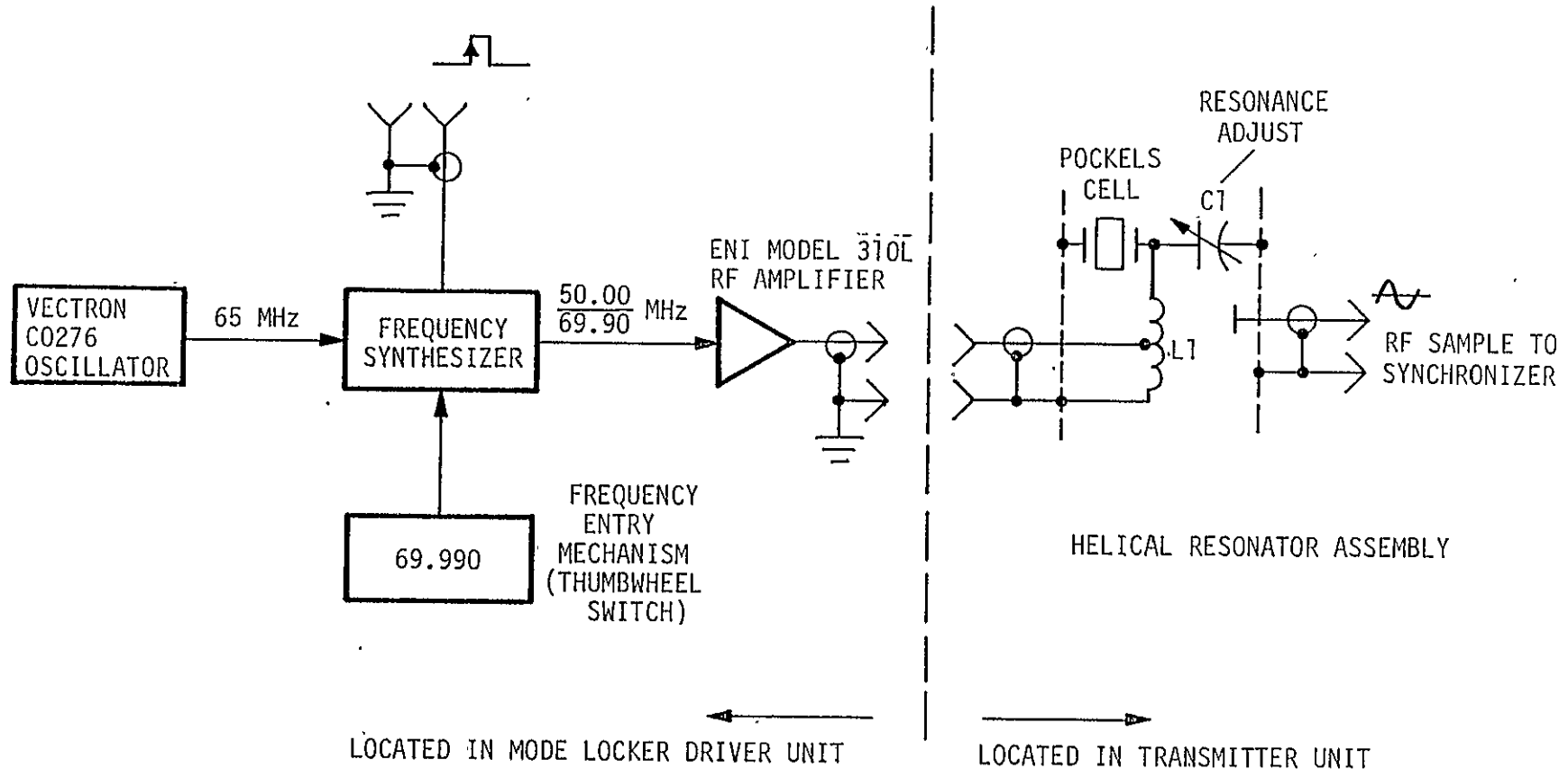
P4733'

Figure 3-13. Spaceborne Laser Command Sequence and Lase Energy Sequence



P2789

Figure 3-14. Electronic System Block Diagram



P3996

Figure 3-15. Modeløcker Electronics

c. RF Amplifier

The RF amplifier selected is an Electronic Navigation Industries Model 310L broadband unit. This unit is specified to produce an output power of 10 W at a distortion level of 7%; however, useful higher powers are available when this unit is operated in conjunction with a helical resonator load. This becomes true because of the inherent high Q-factor of the resonator. Powers in excess of 20 W are readily available as useful outputs. The high Q-factor of the helical resonator also results in the suppression of frequencies other than the resonant frequency. Thus, the harmonic distortion of the RF signal at the modelocker terminals should be less than 0.1%.

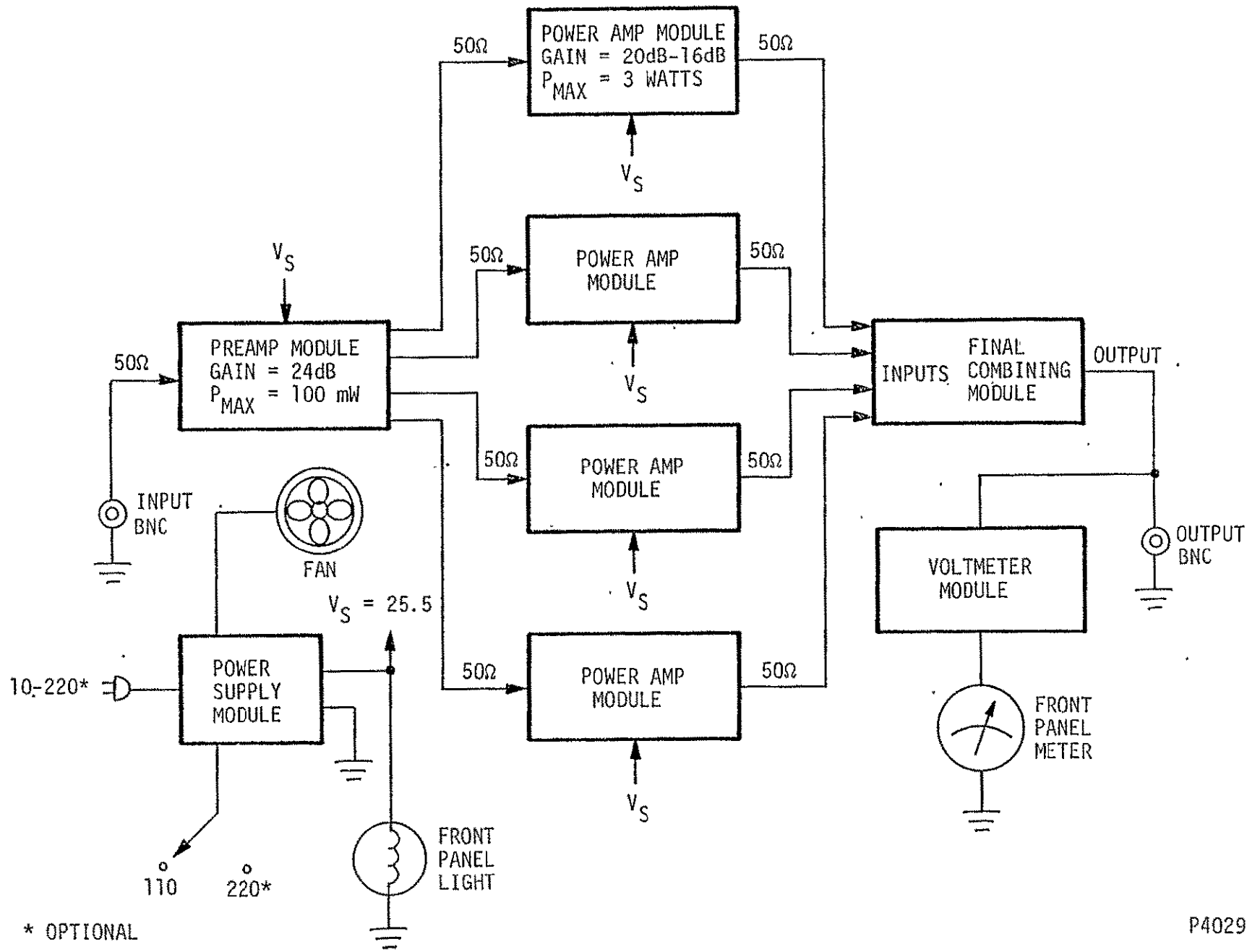
Figure 3-16 illustrates, in block form, the configuration of the amplifier. (Schematics are included in the appendices of this report.) It is to be noted that four power amplifier modules are driven through power splitters from a common preamplifier module. The outputs from the power modules are then combined to form the RF output. The final combining network also contains a directional coupler. This directional coupler feature is most valuable, since it renders the amplifier able to operate into any load without damage.

From examination of the supplied schematics, it should be noted that the basic power for the amplifier modules is $\sqrt{24}$ V dc. Thus, the unit would easily operate from the prime power source of 24/28 V dc with little modification. Presently, the power source is from the 117 V ac power mains, however the modification to 24/28 V dc prime power will be made in Phase II.

d. Frequency Synthesizer

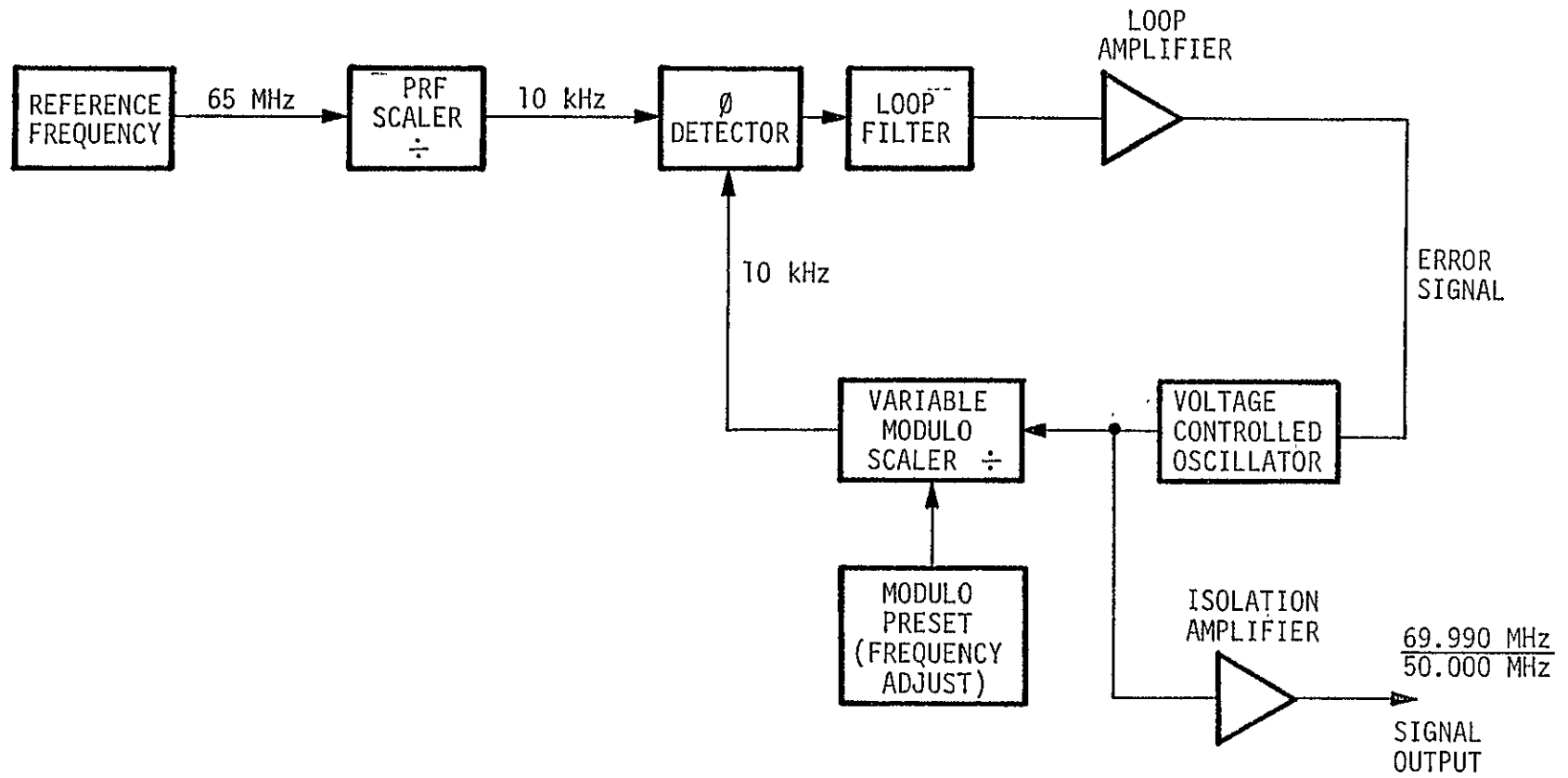
The necessity for the frequency synthesizer arises from the inability to precisely determine the roundtrip time within the optical resonator with sufficient accuracy to utilize a crystal-controlled oscillator alone. The design concept allows frequency adjustment increments of 10 kHz within the range of 50.000 to 69.990 MHz. The basic design is depicted in Figure 3-17. A voltage-controlled oscillator is compared to a precision oscillator through a phase detector. The phase detector is of the type one class which achieves lock with zero phase error. Schematics and circuit description are provided within the appendices. Experimental results of frequency stability of the combined frequency synthesizer and the reference oscillator are provided in Section IV.

3-37



P4029

Figure 3-16. RF Amplifier Block Diagram



P3995

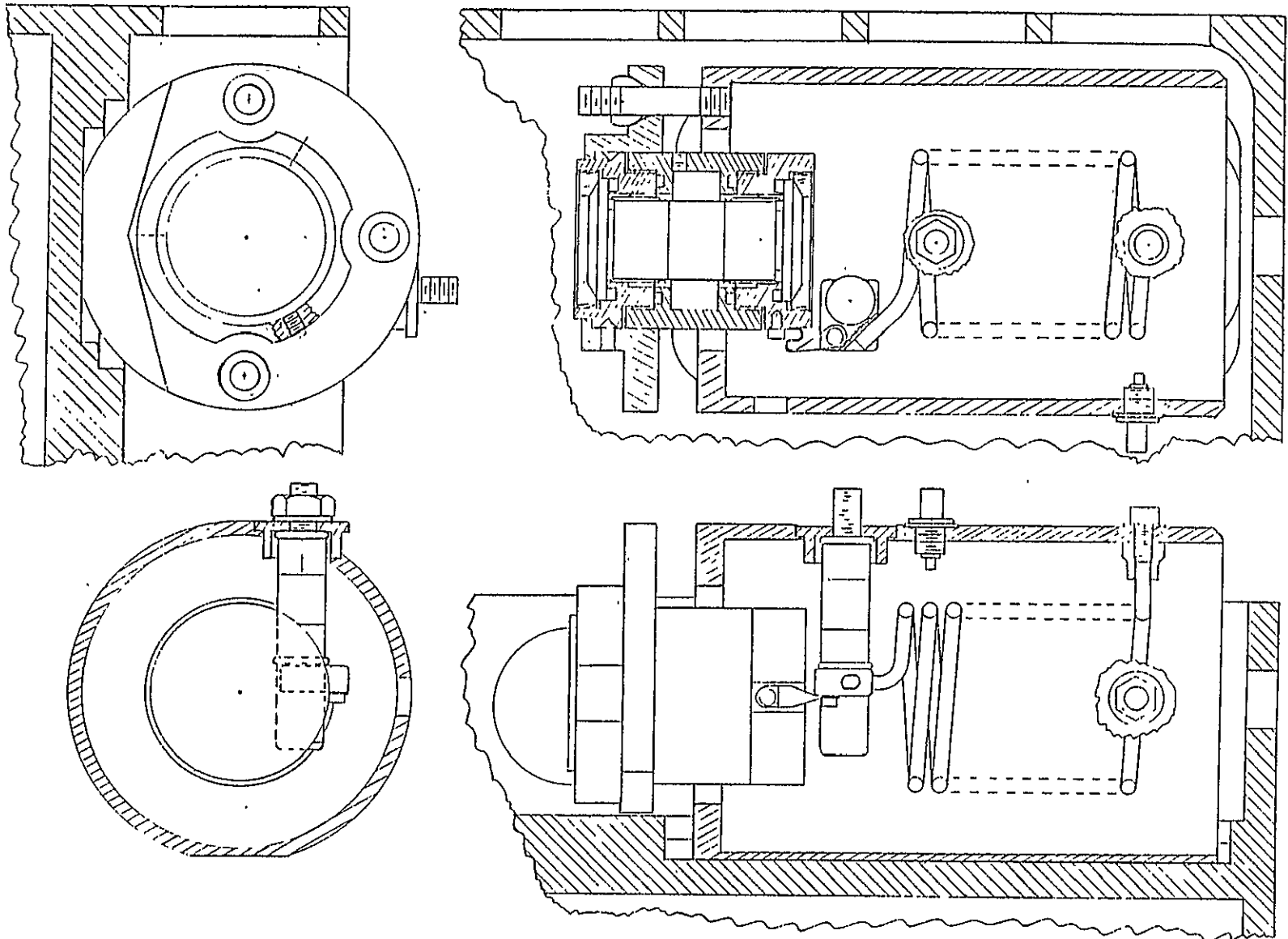
Figure 3-17. Frequency Synthesizer Diagram

e. Helical Resonator

The paramount function of the helical resonator assembly is the voltage transformation from the RF amplifier to the CRE Steinmetz cell. The basic design approach is the series-resonant-circuit Q multiplier which serves to increase the voltage amplitude. In this circuit configuration, the high impedance point is the junction of the resonating inductor and the resonating capacitor. The high-impedance point also is the point of greatest voltage. Thus, if the resonating capacitor were predominantly the Pockels cell the cell would experience the maximum voltage. Resonant circuits of this nature tend to become excessively lossy when conventional lumped constant inductors are utilized. The losses stem from various sources such as direct radiation, surface or skin resistance, driving source impedance and the like. The mechanism implemented utilizes a helical resonator which is fore-shortened to accommodate a high-end capacitive load which, in actuality, is the Pockels cell.

Figure 3-18 shows the construction of the modelocker RF cavity while Figure 3-19 depicts the circuit in schematic form. The mechanical construction is exceedingly critical to proper performance of the voltage multiplication action. The RF cavity wall must be of unitized construction. No mating mechanical interfaces are permissible because they tend to increase the resistivity of the cavity and because the circulating current in the cavity wall is reduced. Placement of the helix within the cavity also is critical. The low-voltage terminal of the helix must contact the inner wall of the cavity at a point placed from the cavity end by not less than the cavity diameter divided by four. Additionally, the helix must be reasonably well centered within the cavity and the turns spaced such that the high-voltage terminal is not closer to the cavity end than the cavity diameter divided by four. With these design criteria²⁹, the cavity ends may be open with little or no radiation loss.

The cavity is constructed of brass which is nickel plated, silver plated, nickel flashed (to prevent migration) and finally hard gold plated. This process assures high Q for an extended time because the plating enhances electrical conduction and prevents surface contamination. Typically, helical resonators of this nature and size exhibit Q_{μ} factors (unloaded quality factor) in the realm of 800 to 1,000. However, the introduction of the Pockels cell, with its inherent loss factor, reduces the circuit Q to $Q_{\mu} \sim 125$.

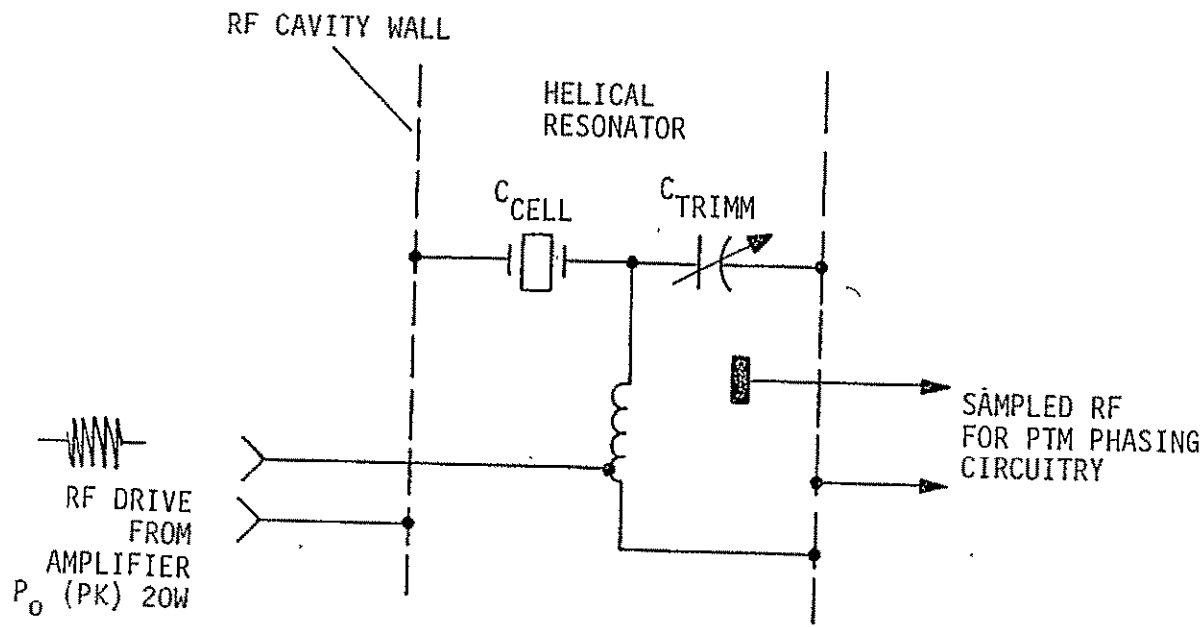


3-40

2

P2781

Figure 3-18. Modelocker RF Cavity Construction



P2688

Figure 3-19. RF Cavity Circuit

The electrical configuration includes a small trimmer capacitor, in parallel with the cell, which is utilized to bring the cell into resonance at the desired frequency. Drive to the helix occurs at the 50- Ω impedance point. A small probe is introduced into the cavity to extract a RF signal for use in the PTM command generation circuitry. This energy loss is of miniscule magnitude. Experimental data relating to the performance of the helical resonator modulator cell is supplied within Section IV.

2. Switching and Control Electronics

a. Q-switch/Dump Subsystem

The Q-switch and dump subsystem is depicted graphically as a portion of Figure 3-20. The subsystem consists of:

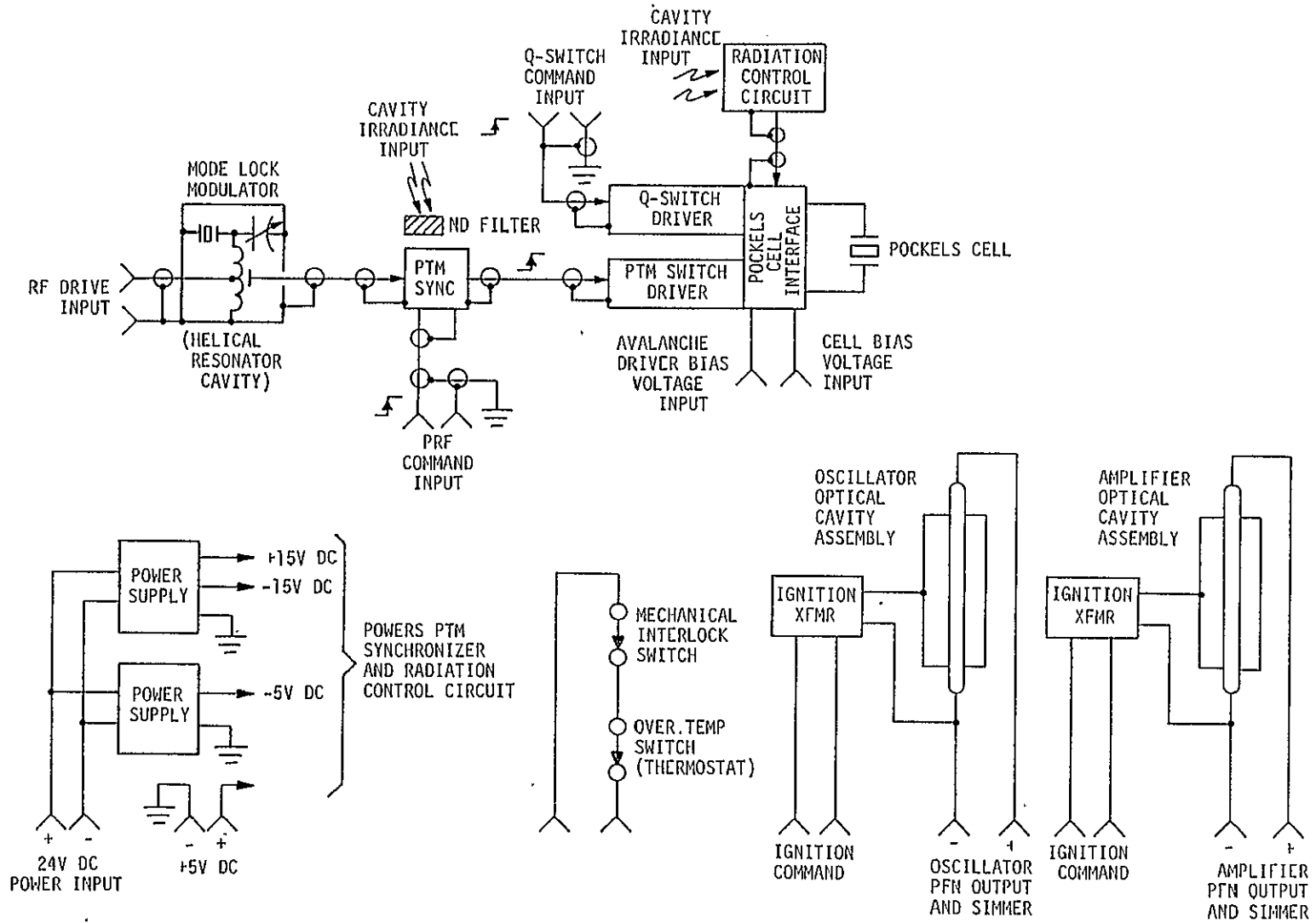
- The Pockels cell;
- The Pockels cell electronic interface;
- The Q-switch driver;
- The PTM or dump driver;
- The radiation control circuit; and
- The PTM/dump synchronizing circuit.

The most stringent requirement within the area of switching and control was to assure adequate switching speed. This requirement stems from the fact that most transitions must be completed before expiration of one round trip time interval within the optical resonator. This constraint dictates that the interval be not greater than 9.5 nsec.

The second stringent requirement was the implementation of the Pockels cell interface electronic circuitry to accommodate the Q-switch drive, the PTM drive and the radiation control drive without mutual interaction. Basically, this problem area was solved by implementing the circuit depicted in Figure 3-21. Voltage/drive input was at the point and in the sequence illustrated. Certain specific embellishments were incorporated to lessen mutual interaction. These will become apparent in the specific discussion to follow.

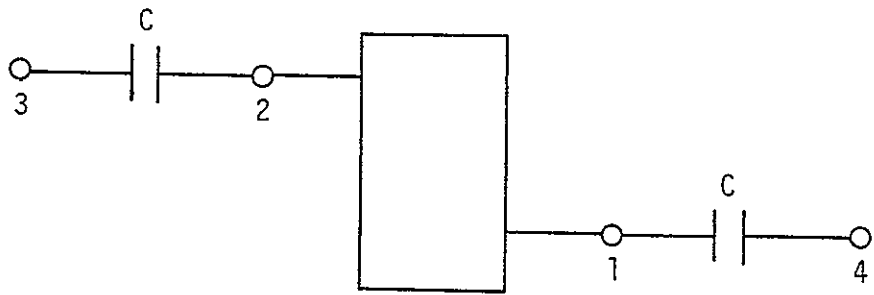
b. Q-switch/Dump Electronic Interface

Because of the multiplicity of drive requirements needed to satisfy the control event sequence, it became necessary to employ differential drive techniques for the Pockels cell. Furthermore, because the Pockels cell is essentially a capacitor when considered electrically, it became necessary to provide small capacitive loading to each side of the cell to achieve adequate voltage drop across the cell. Figure 3-22 depicts this basic differential drive circuit where capacitors C_A and C_B are the loading capacitors. Depending upon which side is driven, the cell capacity and either C_A or C_B form a voltage divider, which increases the driver voltage requirements and increases the switching time. Additionally, the remaining capacitor is shunted across the driver and serves only to reduce the switching time.



P3988

Figure 3-20. Transmitter Electronic System



P4030

Q-SWITCH INPUT BLOCK DIAGRAM

1. HOLDOFF VOLTAGE INPUT
2. PRELASE CONTROL INPUT
3. Q-SWITCH INPUT
4. PTM SWITCH INPUT

VOLTAGE INPUT SEQUENCES

Figure 3-21. Simplified Q-switch Interface

3-46

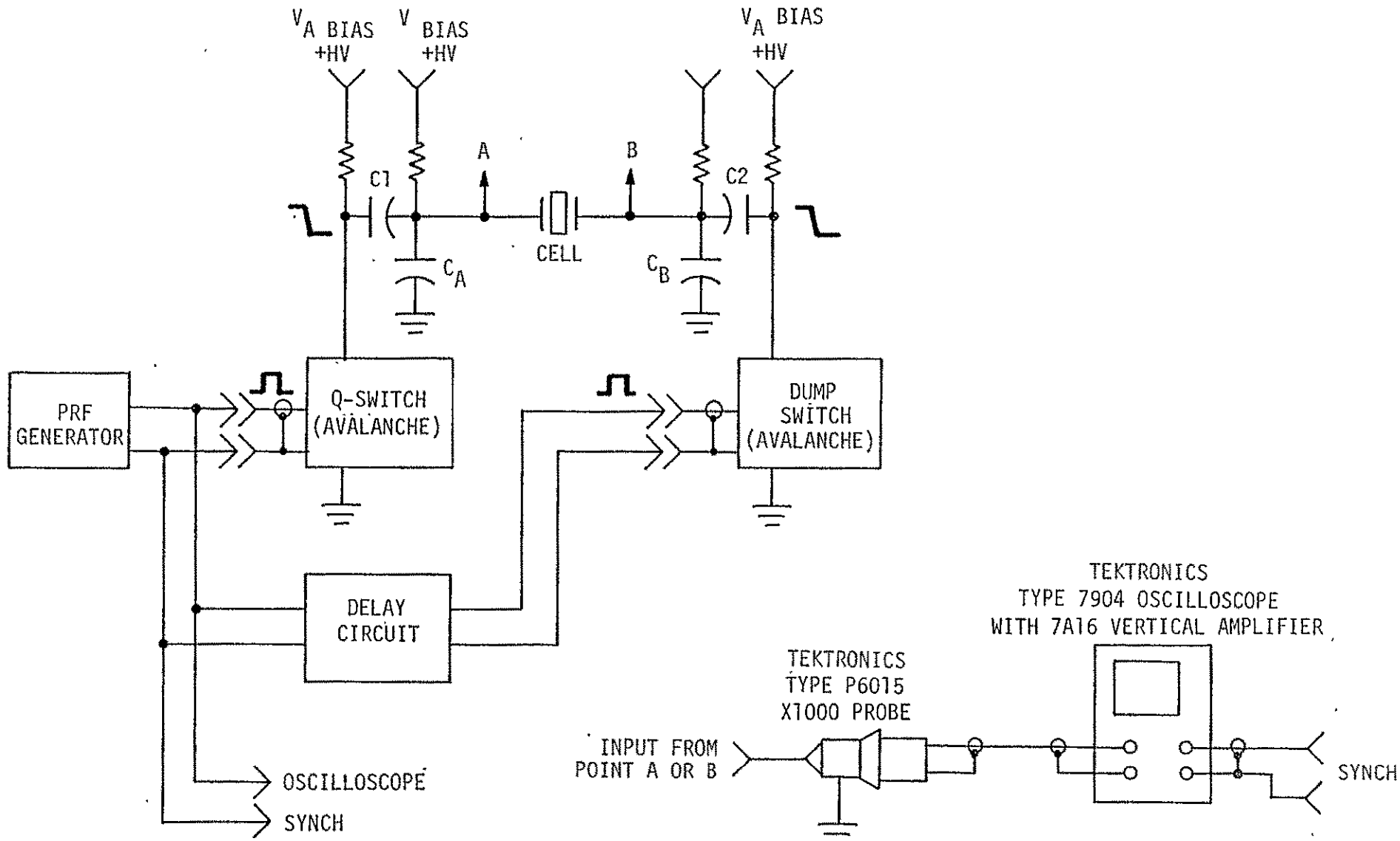


Figure 3-22. Simplified Pockels Cell Drive Configuration

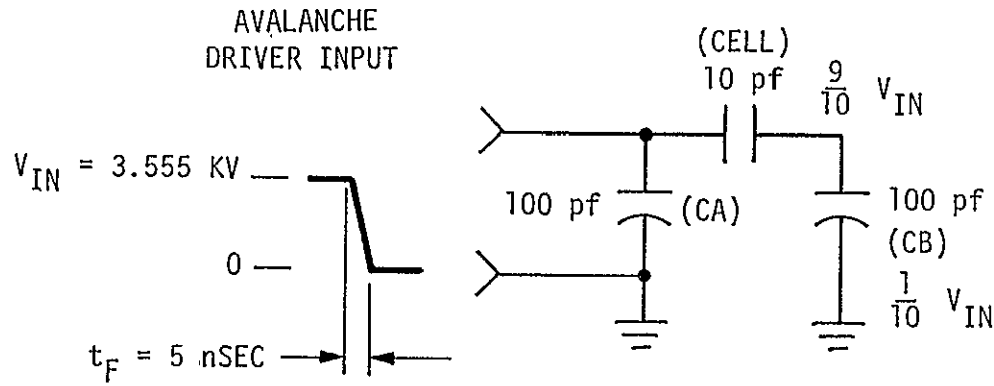
P3764

A trade off now becomes evident. The shunted capacitance can be made small which requires a much higher drive voltage, or the capacitance can be of moderate value which requires little additional drive voltage. The latter was selected in view of the need for introduction of the radiation control drive signal and the consideration of reliability when the driver voltage is increased significantly. Figure 3-23 illustrates the transform to determine the effective capacitance the driver is required to discharge when C_A and C_B are selected to be 100 pF. This arrangement results in a discharge current through the driver of approximately 77 A, which is well within the driver capability.

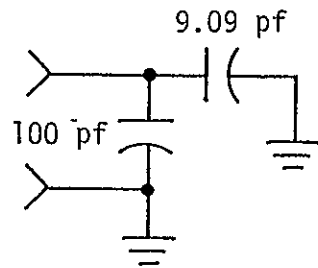
Figure 3-24 depicts in schematic form the actual interface circuit. Driver bias voltage is established to be 3.6 kV which affords 100 μ A dc quiescent current to each driver. The cell bias voltage could range from 1 kV dc to a maximum of 3.6 kV dc. Resistor R3 and the pre-lase radiation control establish a voltage of near +300 V dc at terminal B of the Pockels cell. Resistors R4 and R6 develop a potential of near +400 V dc at the cathode of diode CR3. The Q-switch driver is diode coupled to terminal A of the Pockels cell. The PTM driver is capacitively coupled to the cathode of diode CR3 and thence to terminal B of the Pockels cell. The operating sequence places the cell bias voltage below holdoff value, which is generally about +2,700 V dc. The radiation control electronics forces the terminal B of the Pockels cell to be in the region of +300 V dc, at the Q-switch event time.

When the Q-switch event occurs, the Q terminal voltage of the Pockels cell is discharged to near ground by the forward conduction of diodes CR1 and CR2. Simultaneously, the B terminal voltage of the Pockels cell is reduced to near ground potential by the voltage divider action of the cell capacitance and 100 pF capacitor C5. The cell differential voltage now is zero and HI O is assured within the resonator.

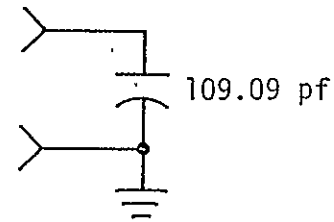
A brief time later the PTM or dump event is commanded. The PTM voltage excursion is 3.4 kV; thus, the cathode voltage of CR3 excursion is from +400 to -300 V dc. The diode CR3 did not become forward biased until the cathode potential reached 0 V. The cell voltage becomes -3.0 kV dc. An interesting and aiding phenomenon occurs at the A terminal of the Pockels cell. Diodes CR1, and CR2 exhibit long minority carrier storage time (in the region of 2 to 3 μ sec) following the Q-switch current surge. This effectively clamps the A terminal of the Pockels cell to the avalanche driver. The avalanche driver also is exhibiting a similar minority storage phenomena which effectively clamps the A terminal of the Pockels cell to ground. Thus, no voltage divider action occurs at the A terminal and the full PTM voltage is applied across the cell. Capacitor C4 cannot be omitted because it is the discharge current that this capacitor



EQUIVALENT CAPACITANCE LOAD FOR DRIVER, SHOWING INDEPENDENT CAPACITORS



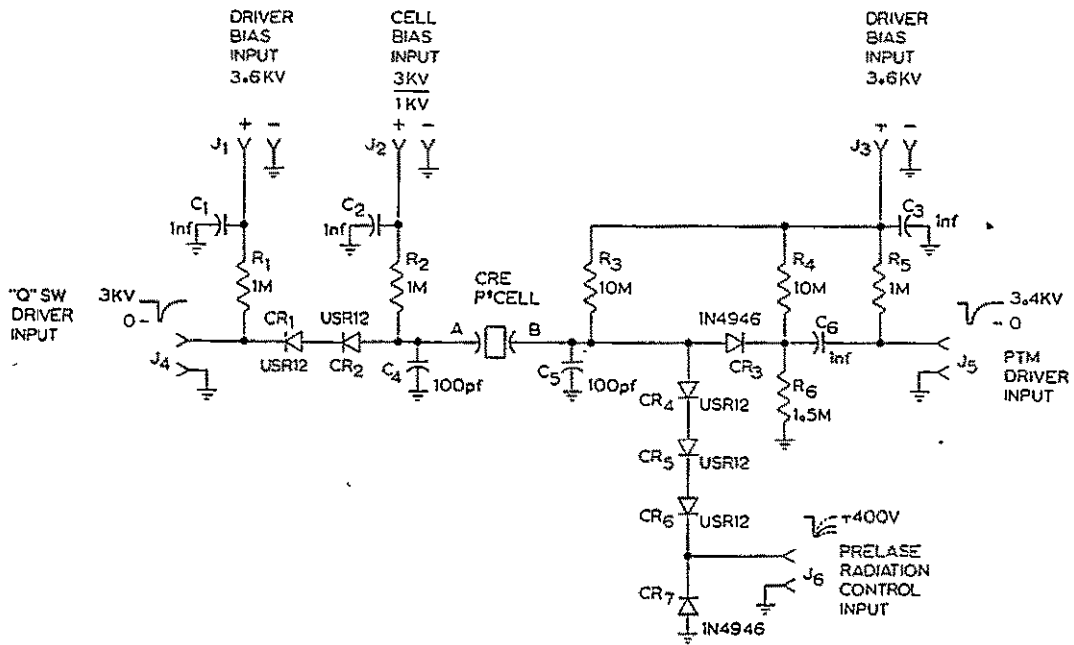
FIRST SIMPLIFICATION



EQUIVALENT CAPACITANCE

P3784

Figure 3-23. Effective Capacitance Load for Avalanche Driver



D1018736

Figure 3-24. Q-switch Interface Schematic

produces which induces the storage effect. Diodes CR4 to CR7 isolate the radiation control electronics from the PTM drive voltage.

Construction techniques are important for effective operation of the interface. The interface housing is nickel plated, silver plated, nickel flashed, and hard-gold flashed to achieve adequate surface conduction and, thereby, preserve switching speed. Additionally, this surface preparation assures reliable operation for extended time periods because surface contamination is unlikely. Interconnections are as direct as possible, heavy leads or straps are used to minimize stray inductance. Noninductive, high-voltage resistors are used throughout. Monolithic chip-type capacitors are employed wherever possible to minimize coupling loss and/or stray inductance. A specific circuit description and schematic of the interface circuit is included in the appendices of this report.

c. High-Voltage Avalanche Driver

The avalanche driver design is rather straight forward. The transistors utilized are selected 2N3019 devices. These devices are coaxially packaged end-to-end within a tubular shield enclosure. The packaging technique ensures low switching impedance, prevents false triggering from ambient noise, and prevents interaction by radiation from the driver at transition. Each transistor is selected for an avalanche holding voltage of > 250 V dc at $100 \mu\text{A}$ holding current. Thus, 14 devices will withstand 3,500 V dc and will provide a transition voltage of nearly 3,250 V. Quiescent power dissipation within each transistor string is equal to approximately 0.35 w.

Typical voltage transition time with a 10-pF load is 2 nsec. With additional capacitance, the switching time is degraded. Subsystem experimental data contained in Section IV illustrates the switching speed obtained. A specific circuit description and schematic of the driver are included in Section VI which contains the appendices of this report.

d. PTM/Dump Synchronization

The paramount function performed by the PTM synchronizer is the determination of the proper time to effect pulse emission from the resonator. This determination is accomplished by sensing the optical resonator energy level referenced to a predetermined threshold value. Whenever the threshold is exceeded, the PTM initiate command is generated. Additionally, a determination of the photon packet placement within the resonator is accomplished so that the PTM driver transition occurs before the energy pulse encounters the Pockels cell. This synchronization is accomplished by sampling the modelocker cavity signal and through signal conditioning of the sample.

The sinusoidal RF signal sample is squared at the centroid, or zero, level by a threshold voltage comparator. This signal then is used as a "clock" to initiate the PTM command whenever the PTM threshold is exceeded. Two stages of phase shift circuitry precede the squaring comparator which permit empirical adjustment to assure that pulse "slicing" of the photon packet is avoided. The phase adjustment range is $\pm 170^\circ$. The ECL logic family is utilized in all high-speed stages to assure speed and to minimize component count.

The PTM threshold circuit is windowed to the laser PRF command to assure that the PTM driver is not discharged prior to the event time. A detailed schematic and circuit description are provided in Section VI which contains the appendices of this report.

e. Radiation Control Loop

The purpose of the radiation control loop is to energy stabilize and pulse stretch the oscillator optical resonator energy during the prelude interval prior to Q-switching. Basically, the system consists of an optical detector, and an amplifier which controls the Pockels cell transmission. This system operates as a servo mechanism to effect a low-level radiation density within the oscillator optical resonator.

The photo detector is chosen to exhibit some integration for narrow-pulse inputs; thus, the average power within the oscillator resonator is maintained rather than the peak power. For very narrow laser pulses — approaching the 200-psec region — this integration action is necessary in view of the limited amplifier high-frequency limit.

The bandwidth of the preamplifier is established to be ~ 360 MHz, that is

$$\text{Observed } t_r = 1.5 \text{ nsec} \quad (3-24)$$

$$\text{Oscilloscope } \tau = 0.8 \text{ nsec}$$

$$\text{Ampl } t_r = \sqrt{1.5^2 - .8^2} = 1.26 \text{ nsec}$$

$$f = \frac{1}{2.2 t_r} \quad \sim 360 \text{ MHz}$$

The preamplifier low-end response is quite good, showing a droop of less than 1 dB over a pulsewidth of 3 μ sec. Maintaining proper amplifier bandwidth is essential for the prelude control to effectively stretch the normal-mode pulse to a usable value.

A high-voltage driver stage follows the preamplifier and must handle voltages in the region of 400V. Additionally, the voltage is predominately discharging; therefore, it is meaningful to consider slew times or attack time rather than bandwidth. Voltage slew time from the 400-V level to near 0 V is ~50 nsec or $8kV/\mu\text{sec}$. Because of the nature of the normal mode build-up, this slew rate is adequate to effect control.

Irradiance sensitivity is $\leq 100\mu\text{W}$ total illumination to the detector to achieve the total control voltage range. This apparent over-design was purposeful in that neutral-density filters easily reduce the gain of the servo loop.

A detailed circuit description together with a schematic are provided within Section VI, which contains the appendices of this report.

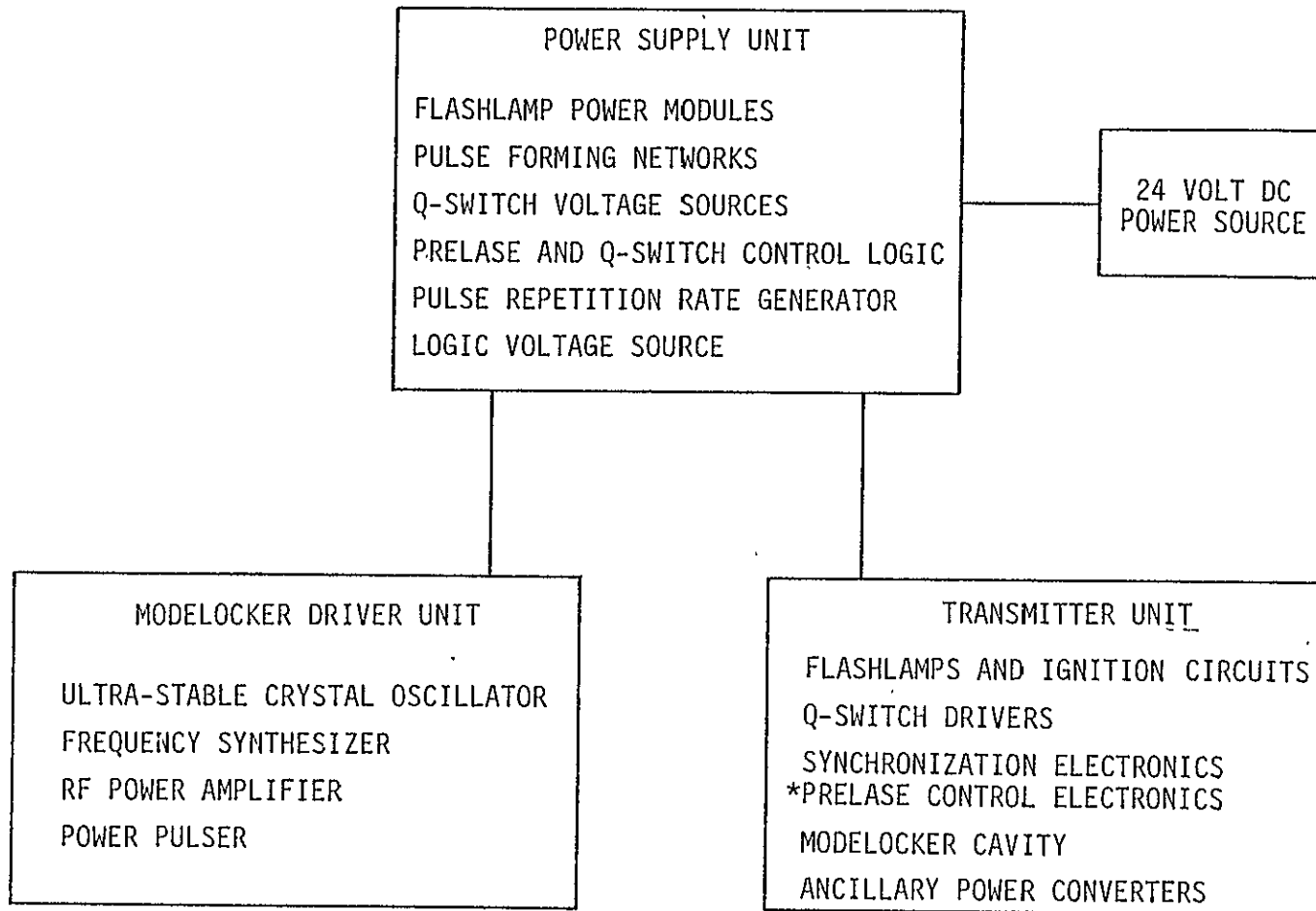
3. Power Supply

The power supply consists of various sub-unit circuit blocks which effect power input conversion or mode control for the Spaceborne laser. Figure 3-25 depicts the interface between the power supply unit and the remainder of the laser system. Additionally the subunit circuits are listed within the power supply block depiction. These subunits are designated:

- The flashlamp power modules;
- The pulse forming networks;
- The Q-switch driver voltage sources;
- The prelase and Q-switch control logic;
- The pulse repetition frequency (PRF) rate generator; and
- The logic voltage power supply.

Because the laser system design encompasses an oscillator and an amplifier, some of the subunits appear in duplicate. Specifically, this applies to the flashlamp power modules and the pulse-forming networks. In the case of the power modules, no differences exist relating to power output or charge time; however, the different power requirements between the oscillator and the amplifier necessitate a variation in voltage regulation level. This level change is accomplished by the front panel controls. Functionally, the pulse-forming networks are identical. The component values are optimized for the requirements of oscillator and/or amplifier pump.

Additionally, two simmer circuit subunits are required. Each circuit is identical and is of the full simmer type. The simmer current is adjusted for approximately 120 mA dc. Flashlamp ignition is automatic whenever the lamp current falls below a preset sense level in order that lamp ionization is maintained.



P2789

Figure 3-25. Electronic System Block Diagram

The choice of high-voltage, avalanche-type drivers for the Q-switch and PTM switch functions, necessitates two high-voltage supplies. One supply is utilized for quiescent avalanche holding current for the avalanche drivers, while the sole purpose of the second supply is the generation of the hold-off bias voltage for the Pockels cell. The two supplies are identical in regard to the output voltage and the output current capabilities. Design of these supplies employs the closed-loop voltage sense technique which ensures excellent stability with time and load. Voltage adjust of these supplies is accomplished from panel mounted controls.

A single logic card contains both the pulse repetition frequency (PRF) generator and the pre-lase and Q-switch control logic. These functions are derived from a 10-MHz crystal clock oscillator through digital counter technology. This assures excellent long-term as well as short-term stability. The timing resolution is limited to one clock pulse period which equates to 100 nsec. Operator control is accomplished as an enablement of the logic circuitry, rather than a direct-line switch function. Thus, timing accuracy is unimpaired and noise pickup is prevented. A single logic voltage power supply is incorporated to convert the prime power to an isolated 5-V level for operation of the logic circuitry.

Interface connections for the power supply unit are depicted in Figure 3-26. Figure 3-27 shows the overall laser system in pictorial format and serves to depict the front panel controls for the power unit. Prior to specific subunit circuit discussion, a brief description of controls, indicators, and connectors is provided.

Prime power enters the power supply unit via high-current jacks which are located on the left-rear corner of the panel. Polarity must be observed in this connection. The prime power source is 24 to 28 V dc. The prime power interrupt (circuit breaker) is located on the left side and immediately above the prime power input jacks. This switch engages the power source and arms the control circuit. An incandescent indicator immediately over the switch is illuminated for power engaged conditions. An armed/standby switch - located to the right side and about midway up the panel - controls power to the flashlamp charging circuits, the simmer circuits and the high-voltage driver circuits. The system is armed when the switch is in the elevated position. An incandescent indicator - located immediately above the switch - is illuminated when the power supply unit is armed. It is to be noted that the simmer circuits automatically ignite the flashlamps when the system is armed. However, the lamps are unable to discharge the PFN until each flash command is engaged by the operator. This characteristic will become evident from the following discussion.

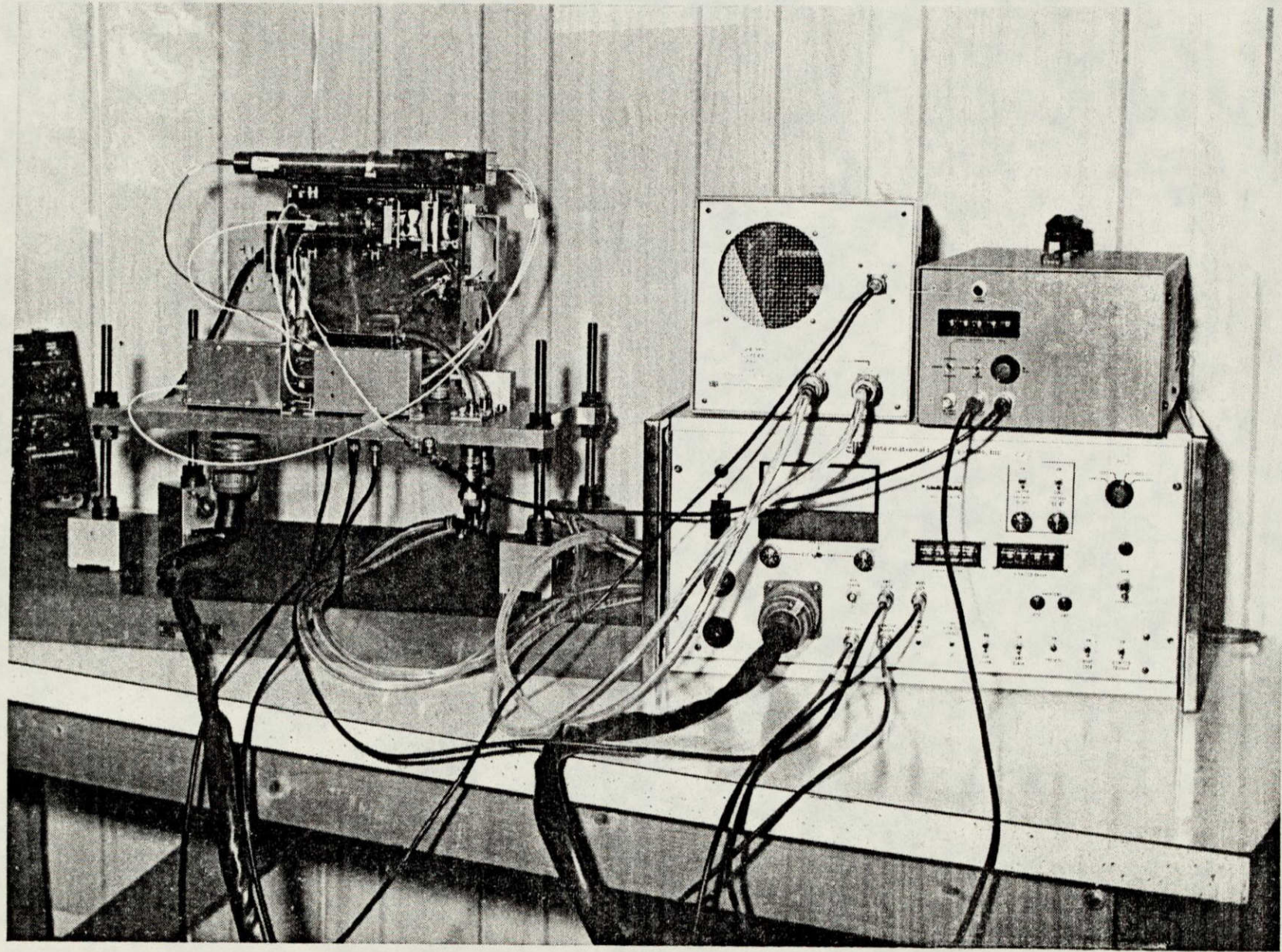


Figure 3-27. Hardware Subassemblies

The laser head/transmitter unit power is interfaced via the large MS type connector adjacent to the prime power input jacks. All power functions, with the exception of the driver high voltages and the modelock drive signal are transmitted through this connector to the transmitter unit. Typical power inputs are the cooling system 24 Vdc power, the oscillator flashlamp power, and the amplifier flashlamp power.

The analog meter and the associated selector switch are used to determine the voltage level of the PFNs. Either the oscillator PFN or the amplifier PFN can be monitored. Adjustment of the charge voltage for either the oscillator or the amplifier can be accomplished at the front panel. Adjustment of the knob potentiometers accomplishes the voltage change. These controls are located below the panel meter to either side of the meter select switch.

An electro-mechanical totalizer is located near the center top of the panel. Each ten flashes of the oscillator flashlamp results in the totalizer advancing one least-significant count. A mechanical reset is possible for the totalizer through an access port to the left side of the totalizer.

The high-voltage adjustments and enable switches are grouped together to the right top of the panel. Each high-voltage supply is independently adjustable in voltage via the potentiometer knob. Each high-voltage supply can be enabled (turned on) independently by the control switch located above each knob. The high-voltage output is scaled to equal approximately 50% of the dial reading times ten.

The pulse repetition frequency (PRF) is accomplished by the position of the rotary switch at the top right of the panel. The PRF may be operator selected as, 1, 5, 10, or 20 pulses per second (pps).

Two thumbwheel switch arrays allow operator programmed delays for the prease initiation and the Q-switch initiation. The thumbwheel entry is in the decimal format. The least significant digital resolution is 100 nsec. The maximum delay entry value is 399.9 μ sec which is established by mechanical limitation to the most-significant digit thumbwheel. These controls allow precise delay for the appropriate function. Typical indicated jitter at the command lines, referenced to the flashlamp command, is equal to or less than ± 2 nsec.

Two high-voltage connectors appear near the bottom center of the panel. These connectors interface to the laser head to supply bias to the drivers and the Pockels cell. They are labeled Q-switch driver and Q-switch bias respectively.

Five BNC type connectors are utilized for various command outputs. These are:

- The oscillator flash command;
- The amplifier flash command;
- The prelease command;
- The Q-switch command; and
- The modelock command.

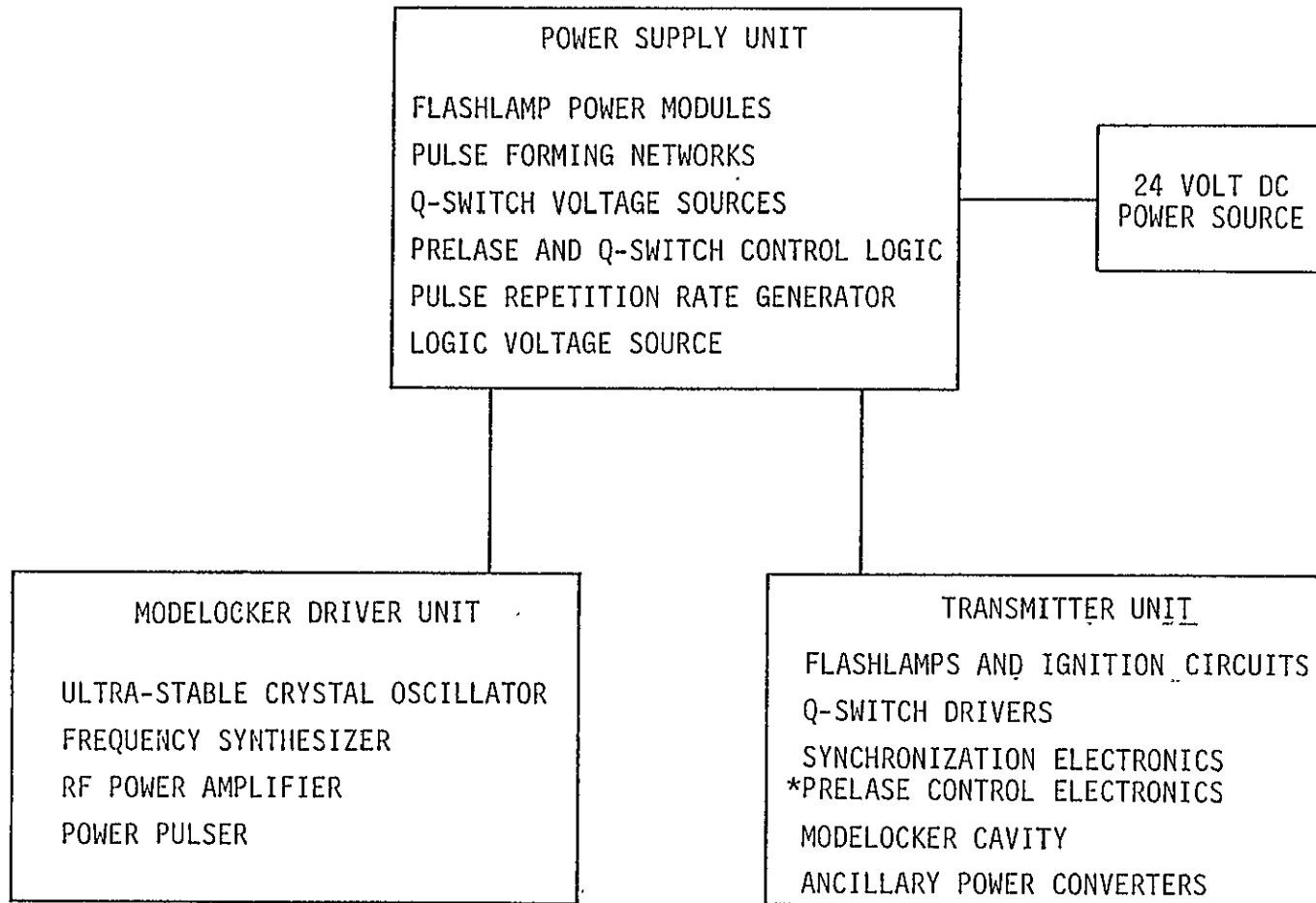
These outputs are essentially self-explanatory. The prelease command and the Q-switch command are routed to the laser transmitter unit for initiation of their respective functions. The modelock command is routed to the modelock driver unit to initiate the modelock pulse burst. The oscillator and amplifier flash commands are available as convenient reference synchronization signals for use with auxiliary instrumentation such as oscilloscopes. Each command function is controlled by an operator-selectable mode switch. These five selection switches appear at the lower right of the control panel. Each switch is designated for the control function. These functions are identical to the BNC outputs previously enumerated.

The remaining indicators pertain to over-temperature conditions within the laser system transmitter. Separate indication is provided for the laser oscillator and the laser amplifier. Direct control of these incandescent lamps is from snap action thermostats located upon each respective optical pump housing assembly within the laser transmitter.

a. Power Supply Subsystem

Organization of the power supply unit subsystem is illustrated in Figure 3-28. Figure 3-29 enumerates the subsystem circuits which comprise the power supply unit. This report section deals generally with the components and the component interface. A detailed description and associated circuit schematic material for each subsystem is provided within the appendices.

Flashlamp power is provided by two circuit groupings. Each circuit grouping consists of: a pulse-forming network (PFN), consisting of an inductor and an energy storage capacitor; a voltage-charging power module assembly; a simmer supply; and a discharge switch, consisting of a silicon-controlled rectifier (SCR).



P2789

Figure 3-29. Electronic System Block Diagram

The simmer supply voltage initially rises to the kilovolt level when the laser system is armed and the automatic flashlamp ignition circuit - located within the simmer supply circuitry - energizes the lamp ignition transformer. The lamp ignites and draws current from the simmer supply. The output voltage of the simmer supply reduces to a level which maintains a current ≈ 100 mA dc through the flashlamp. The automatic ignition circuit is disabled so long as the simmer current is maintained. The simmer supply design is essentially a constant-current type; thus, no problem arises when the terminal voltage varies. Flashlamp arc wander and minute variations within the flashlamp plasma result in rapid voltage fluctuations at the flashlamp terminals. For this reason, inductive ballasting is provided.

Simultaneously, beginning at laser system arm time, the PFN capacitor charging power modules produce a voltage across the PFN capacitor. These modules are of the inductive "fly-back" type which perform as constant-current-charging generators. When the voltage of the PFN capacitor reaches a predetermined level, the charging current is removed. The charging circuitry is designed to maintain the voltage level within $\pm 0.5\%$ of the preset value.

The flashlamp is ignited and simmered, and the PFN now is charged. An output from the pulse-repetition-frequency (PRF) generator commands the SCR to dump the PFN through the flashlamp. Transformer isolation allows the SCR to be placed in series with the flashlamp and the PFN. A quench circuit senses the flashlamp current pulse and inhibits the charging circuit for a time ≈ 2 msec. Interaction between the charging circuit, the dump circuit and the simmer circuit is avoided by diode isolation to the simmer power modules.

The arming circuit is enabled by closure of two case interlock switches and by the temperature monitors of each optical pump cavity assembly. Interruption of any one circuit results in disarming, and both the simmer current and the PFN voltage are removed. One case switch is located within the transmitter unit, while the other switch is within the power unit.

The PRF generator outputs the delayed commands at the appropriate delayed time(s). These commands, with the exception of the flash commands, are utilized within the laser transmitter unit and the modelock unit.

The operation of the remaining power supply submodules is completely straight forward. Each power supply is a stand-alone assembly. Only the logic power unit - the 5-V dc supply - is powered external to the interlocked arm/standby control.

b. Flashlamp High-Voltage Supplies

Two completely independent power supplies are required. One supply charges the oscillator PFN capacitor, while the other supply charges the amplifier PFN capacitor. The charging supplies are of the fly-back type which produce constant-current charging of the capacitors. In the interest of predictable operation, these units are configured as driving mechanisms.

A modular approach has been applied to the implementation of the supplies. The basic power capability of a single power module is ≈ 250 W. Two power modules are slaved for each charging circuit to achieve the necessary output charging capability. Module slaving is at 180° phasing to minimize power current peaking and electrical noise. Operating efficiency is in the 80% region; thus, heat sinking and convection cooling are more than adequate to maintain the component temperatures below 60°C . Voltage regulation is equal to or better than 0.5% as the result of the voltage regulation implementation chosen.

c. Flashlamp Simmer Supplies

The paramount requirements for the flashlamp simmer supplies are:

- The commanding of the trigger transformer to achieve lamp ignition; and
- Supplying a small keep-alive current, referred to as simmer current, within the lamp to stabilize the arc and to maintain ionization.

Flashlamps with varying lengths, varying arc bore diameters and varying fill pressures exhibit widely diverse requirements from the standpoint of simmer voltage and/or simmer current. Ideally, the supply should furnish constant current to the lamp and should possess excellent voltage tracking with the lamp.

The present implementation is considered adequate even through the circuit is of the constant-energy type, which produces a nominal simmer current of 125 mA dc. Voltage tracking speed is enhanced by the use of an inductive ballast. Complete circuit schematics and circuit operation descriptions appear within the appendices.

A separate simmer supply is required for each flashlamp. For this reason, two identical supplies are incorporated into the Spaceborne Laser System. One supply serves to ignite and simmer the oscillator flashlamp, while the second supply performs for the amplifier flashlamp.

d. Flashlamp PFN

The current density near optimum for krypton flashlamps is near $3,500 \text{ A/cm}^2$. This current density results in a good spectral match between the krypton emission lines and the Nd:YAG absorption lines.³⁰ The following calculation determines the inductor and capacitor resulting in critical damping for the oscillator and amplifier pulse-forming networks (PFN) to generate a current density near the optimum at the necessary pump energy levels.

The flashlamp selected for use in the Spaceborne Laser System is a 3-mm bore, 3.375-in. arc length krypton flashlamp manufactured by ILC, Inc. The gas pressure was 450 Torr. The damping parameter for flashlamp discharges is given by³⁰

$$X = \frac{K_0}{\sqrt{V_0} \sqrt{L/C}} \quad (3-25)$$

where V_0 = voltage across capacitor,

L = PFN inductor value,

C = PFN capacitor value,

and K_0 = flashlamp parameter.

K_0 is 33 for the particular flashlamp selected. For critical damping, X should be approximately 0.8.³⁰

The equation relating the pump energy, the PFN capacitor and PFN voltage is

$$E = (1/2) CV^2 \quad (3-26)$$

This equation and the equation resulting from setting $X = 0.8$ can be used to calculate the remainder of the PFN characteristics given the pump energies. The average pump energy for the Spaceborne Laser System oscillator is 4J/pulse and that for the amplifier is 8 J/pulse. Table 3-5 gives the results of the PFN calculations.

Table 3-5. PFN Parameters

Characteristic	Oscillator	Amplifier
Pump Energy (J/pulse)	4	8
Voltage (V)	886	948
Capacitance (μF)	10.2	17.8
Inductance (μH)	37.6	57.0
Pulsewidth (μsec)	69	111
Current Density (A/cm^2)	3268	3746

e. PRF and Delay Generator

The PRF and delay generator circuitry establishes the laser emission rate and provides precise, delayed initiate commands for activation of the Q-switch driver and the prelase control. Various enable gating circuits are provided for ease of laser control. These are:

- Q-switch enablement;
- Prelase enablement;
- Mode lock enablement;
- Oscillator lamp flash; and
- Amplifier lamp flash.

The PRF can be operator selected for 1, 5, 10 and 20 pps. Additionally, a divide-by-10 scaler is incorporated to drive the flash shots counter.

The Q-switch delay and the prelase delay are entered from thumb wheel switch arrays. The maximum delay is 399.9 μsec , while the minimum delay is $\pm 0 \mu\text{sec}$. The minimum program increment of delay is 100 nsec. The entry format is decimal. High-speed TTL logic is utilized in the interest of timing accuracy. A detailed circuit description and circuit schematic are provided in Section VI, of this report which contains the appendices.

f. High-Voltage, Low-Current Supplies

Two high-voltage power units are provided. One supply is utilized to establish the Pockels cell hold-off bias voltage. The other power supply supplies the bias voltage for the avalanche drivers.

Design care was exercised to assure good regulation, minimum ripple voltage and ease of adjustment. Each supply is capable of producing voltage output within the range of +800 V to +4.0 kV dc. Each supply is capable of furnishing current in excess of 500 mA dc. A concise circuit description and schematic are provided in Section VI of this report which contains the appendices.

D. MECHANICAL DESIGN

1. Transmitter Packaging

Figures 3-30 and 3-31 show the transmitter mechanical assembly. The optical bed is mounted to an aluminum base plate by a three-point kinematic suspension. One point of this suspension is shown in Figure 3-30 as item 20. The kinematic suspension of the bed allows free relative thermal expansion between the Invar bed and aluminum base plate without inducing mechanical stress in the optical bed. Each point of the suspension consists of a ball spring-loaded into a conical-like aperture with Belleville washers. Two of these apertures are elongated to permit motion in orthogonal directions and one is a perfect cone which constrains that point in all three dimensions.


The electrical and cooling hose interfaces of the transmitter with the other three modules of the laser system are made through the aluminum base plate from below. The base plate is suspended on four steel rods terminated by Gaertner magnetic bases to permit space for these interface connections. The transmitter subsystem is sealed by an aluminum cover which fastens to the base plate via a hermetic o-ring seal. This cover has a dry-gas fill port, a pressure relief valve, and a sealed beam output window.

The major subsystems within the transmitter are the optical bed assembly, the Q-switch driver assembly, the Q-switch and PTM dump synchronization electronic assemblies, and minor electronic components. The following descriptions of the mechanical design center on the optical bed and its component optical mounts.

	3	24	79NE-048	NUT, KINEMATIC MOUNT		
	3	23	A1015109-1	BALL, KINEMATIC MOUNT		
	2	22	3/8-16X1" LG.	SCREW, SOC. HD. CAP	ST, STL.	
	4	21	.093 X 1/2 LG.	PIN, DOWEL		
	1	20	C1016822	BLOCK, DUAL SUPPORT		
	1	19	C1016823	BLOCK, SINGLE SUPPORT		
	5	18		CONNECTOR		
	2	17		CONNECTOR		
	1	16	2-277	O-RING, CONNECTOR PLATE	PARKER-SILICONE RUBBER	
	10	15	#6-32X3/8 LG.	SCREW, SOC. HD. CAP	ST STL,	
	1	14	C1016824-1	CONNECTOR PLATE		
	4	13	#6-32X5/16 LG.	SCREW, SOC. HD. CAP	ST, STL.	
	1	12	#10-32X3/8 LG.	SCREW, SOC. HD. CAP	ST, STL.	
	4	11	#8-32X3/16 LG.	SCREW, SOC. HD. CAP	ST, STL.	
	8	10	#10-24X7/16 LG.	SCREW, SOC. HD. CAP	ST, STL.	
	2	9	C-1016885-9	BOX, ELECTRICAL COMPONENT		
	2	8	B1016820-1	ADAPTER, COOLING LINE		
	8	7	HNC-5	NUT, SUPPORT PLATE	REID TOOL	
	8	6	FW-4	WASHER, SUPPORT PLATE	REID TOOL	
	1	5	D1016816-9	PLATE, SUPPORT		
	4	4	A1016821-1	STUD, SUPPORT PLATE		
	1	3	A1016818-1	NUT, F.O. HOLDER		
	1	2	A1016817-1	SLEEVE, F.O. HOLDER		
	1	1	J1016270-9	OPTICAL BED, MACHINING		

ORIGINAL PAGE IS OF POOR QUALITY

QUANTITY REQD	ITEM	PART NO.	DESCRIPTION	CODE IDENT	REV
-9	←	ASSY.	LIST OF PARTS		

TITLE LASER RANGEFINDER ASSEMBLY		USED ON	 International Laser Systems, Inc.		ORLANDO, FLORIDA
		SIZE	CODE IDENT NO.	DRAWING NO.	REV
		A	34860	D 1016815	-
		0739A			

3-69

3-70

				2	48	4-40 X 5/16 LG.	SCREW, SOC. HD, CAP		ST, STL		
				1	47	C1016085-9	APERTURE ASS'Y				
				8	46	6-32 X 1/4 LG.	SCREW, BINDING HD.		PIC# Y4-6-U	ST, STL	
				1	45	C1014760-9	CAVITY ASS'Y, AMPLIFIER				
				1	44	C1014760-19	CAVITY ASS'Y, OSCILLATOR				
				2	43	#8 SCREW	WASHER, FLAT		ST, STL,		
				3	42	D6-23	BELLEVILLE WASHER		PIC		
				6	41	B1016012-1	LOCATOR, PRISM SHOULDER				
			AVR	40	LV-45		EPOXY, ECCOBOND		TRA-CON		
				4	39		BASE, MAGNETIC		GAERTNER		
				1	38	D1016884-9	COVER ASS'Y, RANGEFINDER				
				1	37	2-HIL15 1/4"NPT	CONN, HYDR, QUICK-DISCONN.		HANSEN MFG. CO.		
				1	36	2-KIL15 1/4"NPT	CONN, HYDR, QUICK-DISCONN.		HANSEN MFG. CO.		
				1	35	B1016825-1	SUPP. BLOCK, AV. DR.				
				2	34	6-32 X 5/8 LG	SCREW, SOC. HD. CAP		ST, STL,		
				1	33	D1015794-9	AVALANCHE DRIVER ASS'Y				
				2	32	B1003316-7	FITTINGS, COOLANT				
				2	31	2-023	O-RING, COOLING LINE ADAPT.		PARKER-SILICONE RUBBER		
				1	30	A1016819-1	GASKET, CONNECTOR				
				1	29	MS-3102	CONNECTOR		BENDIX		
				3	28	B1015108-3	SOCKET, BALL				
				3	27	1/4" SCREW	WASHER, FLAT		ST, STL,		
				15	26	D6-24	BELLEVILLE WASHER		PIC		
				3	25	A1015110-1	STUD, KINEMATIC MOUNT				

QUANTITY REQD	ITEM	PART NO.	DESCRIPTION	CODE IDENT	REV
---------------	------	----------	-------------	------------	-----

-9 ← ASSY. LIST OF PARTS


TITLE LASER RANGEFINDER ASSEMBLY		USED ON	ILS International Laser Systems, Inc. ORLANDO, FLORIDA	
		SIZE	CODE IDENT NO.	DRAWING NO.
		A	34860	D 1016 115
		0739A		REV -

	2	72	C1015240-9	FOLDING POLARIZER ASS'Y.		
	4	71	B1016888-1	STANDOFF		
	2	70	4-40X 1/2 LG.	SCREW, SOC. HD. CAP		ST. STL.
	2	69	A1012406-3	ADJUSTER FOLDING MIRROR		
	1	68	A1016904-9	COMPENSATING WEDGE ASS'Y.		
	1	67	B1016889-1	INSULATING SHEET, OSC.		
	6	66	B1015834-1	BRACKET, CORNER		
	1	65	J6S275X48.260	O-RING, COVER		CONOVER SILICONE RUBBER
	1	64	B1016887-1	INSULATING SHEET, AMPL.		
	A/R	63	5722-18-4A	LAMINATED WASHER		SEASTROM
	30	62	8-32X5/8 LG	SCREW, SOC. HD. CAP		ST. STL.
	1	61	B1015854-9	RETAINER ASS'Y, PRISM 3		
	1	60	C1015462-1	PRISM 3		
	1	59	C1015460-1	PRISM 1		
	1	58	C1015461-1	PRISM 2		
	2	57	B1015853-9	RETAINER ASS'Y, PRISM 1+2		
	8	56	10-32X 1/2 LG	SCREW, SOC. HD. CAP		ST. STL.
	A/R	55	5722-56-4A	LAMINATED WASHER		SEASTROM
	1	54	C1015591	WEDGED RISLEY PRISM ASS'Y.		
	1	53	C1016191	PORRO PRISM SUB ASS'Y.		
	1	52	C1014772-9	KD*P INDEX MATCHED CELL		
	1	51	C1012710-39	CRYSTAL OVEN ASS'Y		
	1	50	B1014651-9	SCOPE, COMPENSATING		
	1	49	D1016343-9	MODEL LOCKER ASSEMBLY		

3-71

QUANTITY REQD	ITEM	PART NO.	DESCRIPTION	CODE IDENT	REV
---------------	------	----------	-------------	------------	-----

-9 ← ASSY. LIST OF PARTS

TITLE LASER RANGE FINDER ASSEMBLY		USED ON	 International Laser Systems, Inc.		ORLANDO, FLORIDA
		SIZE	CODE IDENT NO.	DRAWING NO.	REV
		A	34860	D1016815	-
		0739A			

Following the discussion of the optical bed design, the subassemblies attached to the bed will be discussed in the following order:

- Beam-folding TIR prisms;
- KD*P Q-switch;
- KD*P modelocker;
- Pump cavities;
- Resonator mirror;
- Double polarizer;
- Rislely prisms;
- Folding polarizers;
- Porro prism reflector;
- Expanding telescope;
- Compensating wedge;
- Aperture assembly; and
- Q-switch drivers.

Three optical bed subassemblies are shown in Figure 3-30 which were not implemented in Phase I of this program. These are the frequency doubler, dichroic mirror, and a diffuser and are existing ILS designs.

2. Optical Bed

The stability of the optical path length of the laser resonator is of paramount criticality to keep the optical transit time matched to modelocker frequency. Accordingly, early consideration was given to environmentally induced distortions of the optical bed during operation. A goal of 0.001% bed length stability was established with temperature control to $\pm 5^{\circ}\text{F}$ and in a one "g" ground checkout condition. Bed length control methods considered were:

- Use of materials of differing and offsetting thermal expansion. While feasible, certain problem areas were recognized. Accurate knowledge of both steady-state and transient temperature gradients throughout the bed would be required. These probably could not be adequately determined until a prototype system was fabricated and tested. Additionally, with a bed structure of discrete parts bolted together, minute positional shifting of parts with respect to each other during temperature cycling was considered a detrimental possibility;

- Control of modelocker frequency to compensate for bed length changes caused by temperature variations. Temperature sensing would be required with attendant uncertain effects of steady-state and transient temperature gradients throughout the bed which would have to be compensated. Modelocker frequency control, while feasible, would require additional electronic circuitry complexity;
- Use of stable, low-expansion alloy such as Invar. Thermal and stress analysis showed thermal effects to exceed gravity distortion by $\approx 10:1$. Therefore, use of Invar (Temperature expansion coefficient $0.9 \times 10^6/^\circ\text{F}$) would approach the above goal (0.001% stability). This was selected as a direct, practical approach.

The configuration selected for the Invar optical bed is an integral structure as shown in Figure 3-30. The bed thickness is 0.5-inch and the walls are 0.1875-inch thick by 1.25-inches high. The optical mounts fasten to the sides of the bed such that the beam height off the bed is 0.75 inch. Three TIR prisms are mounted to the ends of the bed to fold the beam along the desired paths through the optical components.

The bed was fabricated from a block of free-machining Invar 36. The substantial machining required to fabricate the bed dictated stress-relief heat treatments. Two in-process, stress-relief treatments were performed prior to the final machining of the bed. The Invar block was first machined to 0.06-inch oversize in its major dimensions, then heat-treated for one hour at 1200°F and cooled slowly. Machining of the bed to 0.03-inch oversize in the major dimensions was performed next followed by heat treatment as above. The bed was then machined to its final dimensions with the inclusion of all detail machining. A final heat treatment was as described above but at a temperature of 600°F . An acid treatment of the bed was performed to remove oxidation elements resulting from the final heat treatment. The bed was then nickel-plated to prevent future oxidation. The bed fabrication procedure described above was developed in consultation with a metallurgist at Carpenter Technology, the Invar vendor.

3. TIR Prism Mounting

The three beam-folding TIR prisms attach to the bed via metal clamps with rubber pads between the clamp and prism as shown in Figure 3-30. The prisms are held against Invar pads attached to the bed. These pads are located to avoid mechanically-induced stress in the prisms at the beam paths through them. The purpose of the Invar pads is to align the prisms in their sensitive plane. The machining of these pads was a two-stage precision process. The result desired and achieved was a non-adjustable optically precise mounting of the TIR prisms.

The TIR prisms were designed to have a 1.5° pyramidal error to avoid etalon effects. Thus, it was necessary to tilt the entrance surface of the prism 2.175° to the required optical paths in order to achieve alignment. This implies a requirement that the Invar pads be fabricated as wedges with an angle of 2.175° with the assumption that the bed ends are perpendicular to the required optical paths. In practice, fabrication errors of both the prisms and the optical bed dictated a slightly different angle that could be determined only through an optical measurement to be described in the laser alignment section of this report. An optical polish of both sides of the Invar pads and the optical bed ends to $\lambda/4$ flatness using sodium light was performed to ensure the accuracy of the above-outlined alignment technique. It is implied above that a second machining operation is required for the Invar pads. This machining and subsequent repolishing was achieved to an accuracy of better than 10 arc-seconds.

Proper location of the TIR prisms relative to the optical axes was also necessary. This was also achieved via a precision mechanical reference surface. Each prism was mounted with one side flush against an Invar bar attached to the optical bed. These metal bars were mounted to the bed and then the reference surface was machined to be either parallel or perpendicular to the optical bed surface on which the remaining optical mounts were attached. The particular beam-folding direction of each prism dictated the correct reference plane. Slippage of the prisms parallel to the pads mounting surfaces was constrained by Noryl blocks attached to the bed.

4. Q-Switch Modulator Mounting

A KD*P crystal, 0.5-in. in diameter and 1-in. long is mounted in a sealed cell with quartz end windows and partly filled with a refractive-index-matching fluid (FC-77). Both the crystal and windows were fabricated with small, carefully selected, precise wedge angles to avoid etalon effects. Fluid thickness between the crystal and windows was kept thin (0.040 in. Max) by Teflon spacers which also provide some resilience at assembly. The index-matching fluid was selected for high surface tension to inhibit formation of small air bubbles which might occur between the crystal and windows. A bubble-trap is provided to collect larger air bubbles out of the optical path. A second purpose of the bubble trap is to provide a built-in air volume to compress and accommodate liquid thermal expansion. A high-voltage drive (3,250 V) applied to each end of the crystal accomplishes Q-switching. Thus, an electrically insulating cell body with conductive end caps isolated from ground to serve as crystal electrodes was indicated. The cell end caps also serve as window retainers. The cell body is made of Macor, a machinable ceramic, and the end electrodes of gold-plated brass with flexible fingers about the periphery of the crystal. The cell is supported by a three-ball kinematic mount which allows 2° adjustment of the cell axis in pitch and yaw attitude. Full 360° rotational adjustment and locking of the cell is provided by set screws riding in an annular V-groove in the Macor cell body.

5. Modelocker Cell and RF Cavity

The crystal cell is internally the same as the Q-switch (KD*P crystal, index-matching fluid, quartz windows). External parts were modified for modelocker application where only one end of the crystal is driven by high voltage, the other end being at ground potential. The metal end caps serving as crystal electrodes were modified as follows:

- A screw attachment is provided for an electrical lead to the high-voltage electrode; and
- The ground electrode is modified to provide the annular V-groove for rotational adjustment of the cell, thus providing a ground electrical contact.

Again a three-ball kinematic mount supports the cell on the modelocker RF cavity. The range of adjustment of cell position are:

5.

- Pitch and Yaw $\pm 1.50^\circ$
- Rotation $\pm 0.50^\circ$

The cell is oriented so that its optical axis nominally is on the centerline of the RF cavity. Layout studies were made of methods to mount the cell transverse to the RF cavity, but none promised as compact an assembly as the coaxial configuration.

The RF cavity provides a high-efficiency, RF, LC circuit (3 kV at 60 MHz) to drive the modelocked cell. It consists of a coil, a capacitor, and a ground tube with electrical connections to excite and monitor the circuit. The coil consists of 10 turns of 0.1-in. diameter wire wound to a 1.0-in. ID with a pitch of 0.15 in. One end of the coil is attached to the external ground tube of the cavity. The other end is connected to an adjustable piston capacitor mounted in the ground tube wall and to the high-voltage electrode of the KD*P crystal. The ground tube has a 2.0-in. ID, and a 0.1-in. wall thickness and is 3.35 in. long. As the result of high circulating currents, both the coil and ground tube are gold plated and minimum interruptions of material are allowed in approximately 2.5 in. of the tube spanning the coil. The ground tube provides attachments for:

- A coil ground connection;
- A piston capacitor;
- A coil excitation connector;
- A voltage sensing connector (no electrical connection to the coil is required);
- A support for the cell kinematic mount;
- Three-ball adjustable kinematic attachment to the optical bed.

6. Pump Cavity

An important system objective was to optimize optical coupling between the flashlamp and the laser rod. The pump cavity was designed to allow acquisition of comparative test data on the following configuration variables:

- Elliptical versus intersecting-circle cavity cross sections (two sizes of each);

- Two diameters of laser rod; and
- Optical filters between the lamp and rod with five different wedge angles.

It was considered that by trial of these variables, optical coupling from the lamp to the laser rod could be optimized.

The cavities are water/glycol cooled and contain the Nd:YAG rod and krypton flashlamp. Coolant is circulated first through the rod side of the cavity and then through the flashlamp side to optimize rod cooling. The coolant path is baffled to enhance turbulent flow for more uniform cooling. Cavities were designed to accept 0.25-in. x 4-in. and 5-mm x 101.6-mm rods. Cavities are of brass with all internal surfaces highly polished and silver plated. Rod ends were fabricated at wedge angles to avoid etalon effects.

7. Passive Optical Mounts

a. Concave/Convex Resonator Terminating Mirror

A single double-faced concave/convex mirror is used to terminate both ends of the resonator optical path. It is a 0.5-in. diameter x 0.312-in. thick glass mirror with high reflectivity coatings. The mirror is bonded into a stainless steel holder which is in turn clamped into an adjustable mount. This arrangement was provided to facilitate changing mirrors during Phase I testing. Six mirrors of differing face radii were provided. The adjustable mount has a three-ball kinematic support providing a pitch and yaw range of 10 mr with 0.4-mr resolution.

b. Double Polarizer Assembly

The function of this component is to direct the resonator beam either into the resonator path or, with a parallel offset (0.8-mr limit to deviation from parallel) out to the amplifier path depending upon the direction of polarization of the beam). Two matched polarizers are cut from the same dielectric-coated glass blank so that the optimum angle of incidence of both will be the same. These are bonded to a special holder which, in turn, is supported on a special adaptation of standard ILS polarizer mounts with screw adjustment for tilt and rotation.

c. Wedge Risley Prisms

These components provide beam corrections either angularly or laterally offset. They consist of two prisms 0.5-in. in diameter

x 0.25-in. thick with faces polished at wedge angles. The prisms are bonded into holders in which one roller only can be rolled or both rollers can be rolled in unison. The mount is an adaptation of standard ILS designs with a screw adjustment on the optical axis for pitch and yaw. Roll adjustment and locking of the prism holders is achieved through set screws riding in annular V-grooves.

d. Folding Polarizers

The function of these two items is to provide a lateral offset of the output beam from the telescope to the laser amplifier via a folding prism. Two matched polarizers are cut from the same dielectric-coated glass blank so that the optimum angle of incidence of both will be the same. Each is bonded to identical special holders with rotational and tilt capability. The pivot-points for rotation of the holders is selected so that regardless of the angle of incidence of the beam on the polarizers (within $\pm 6^\circ$), the beam lateral offset remains constant. It is required, however, that both polarizers have the same optimum incidence angle.

e. Porro Prism Subassembly

This is a conventional Porro prism with half of the front face coated so that the incident beam can be reflected back exactly on the same path. A three-ball kinematic suspension is provided so that the prism axis can be directed precisely into the incident beam. The prism is bonded into a sleeve which, by virtue of three set screws riding in an annular slot, can be rotated and locked.

f. Expanding Telescope

A 1.5X telescope is provided to expand the output beam diameter. Although redesigned for this application as the result of space limitations, it is a direct adaptation of a standard ILS design.

g. Compensating Wedge

This component provides beam path angular and lateral offset correction. The glass, with a $2^\circ 1'$ wedge angle is bonded to a standard ILS polarizer mount. The base of the mount is attached to the bed by a shoulder screw and Belleville washer to allow mount rotation. The holder is shaft mounted to the base with screw adjustment for tilt.

h. Aperture Assembly

Beam diameter can be controlled by this item. It consists of an adjustable holder into which varied sizes of aperture can be inserted. Screw adjustment of aperture position in both transverse directions for aperture diameters of 0.118, 0.138 and .158 in. was provided.

i. Avalanche Driver

Two units of an existing ILS design are used to drive the Q-switch high-voltage electrodes. Particular attention was paid to mounting these in proximity to the Q-switch with low-impedance circuitry.

SECTION IV

EXPERIMENTAL RESULTS

A. ELECTRONIC SUBSYSTEM TESTS (Modelock Cell Evaluation)

The test configuration for this measurement is illustrated in Figure 4-1.

The helical resonator is intolerant to either capacitance loading or energy radiation loading; therefore, direct measurement of cell voltage becomes a problem. Attachment of a probe to the voltage side of the helix adds capacitance to the circuit and conducts energy from the circuit to effectively reduce the circuit Q . Adjustment of the resonant circuit to compensate for the additional capacitance does nothing to restore the circuit Q ; thus, it is apparent that any probe technique is unacceptable and an alternate approach must be attempted.

Meaningful measurements require that the actual Pockels cell be part of the resonant circuit. It is to be noted that one terminal of the Pockels cell is at ground reference in the normal configuration. Now consider the insertion of a series capacitor of large value between the cell terminal and the ground reference to form a capacitance type of voltage divider. This is the technique used to accomplish cell voltage measurement and is an indirect method. It also is to be noted that the series capacitor value must be in the order of 10,000 to 20,000 times the cell capacitance to prevent excessive energy loss from the cavity assembly and the resultant degradation of the circuit Q . Additionally, the series capacitor must possess low-lead inductance; thus, "chip"-type (leadless) capacitors were selected.

The assembled cell was measured to exhibit a total capacitance of 9.9 pF. The series capacitor was chosen to be 200 nF (200,000 pF) approximately 20,000 times greater than the cell capacitance. Multiple capacitors were distributed around the low side terminal of the cell assembly to ground. These capacitors were trimmed to provide a measured value of 199,000 pF. The additional capacitance of the cable from the test capacitor to the oscilloscope attached is ~ 120 pF.

The frequency synthesizer/amplifier was adjusted to operate in a gated or burst mode and to furnish a peak power output of nearly

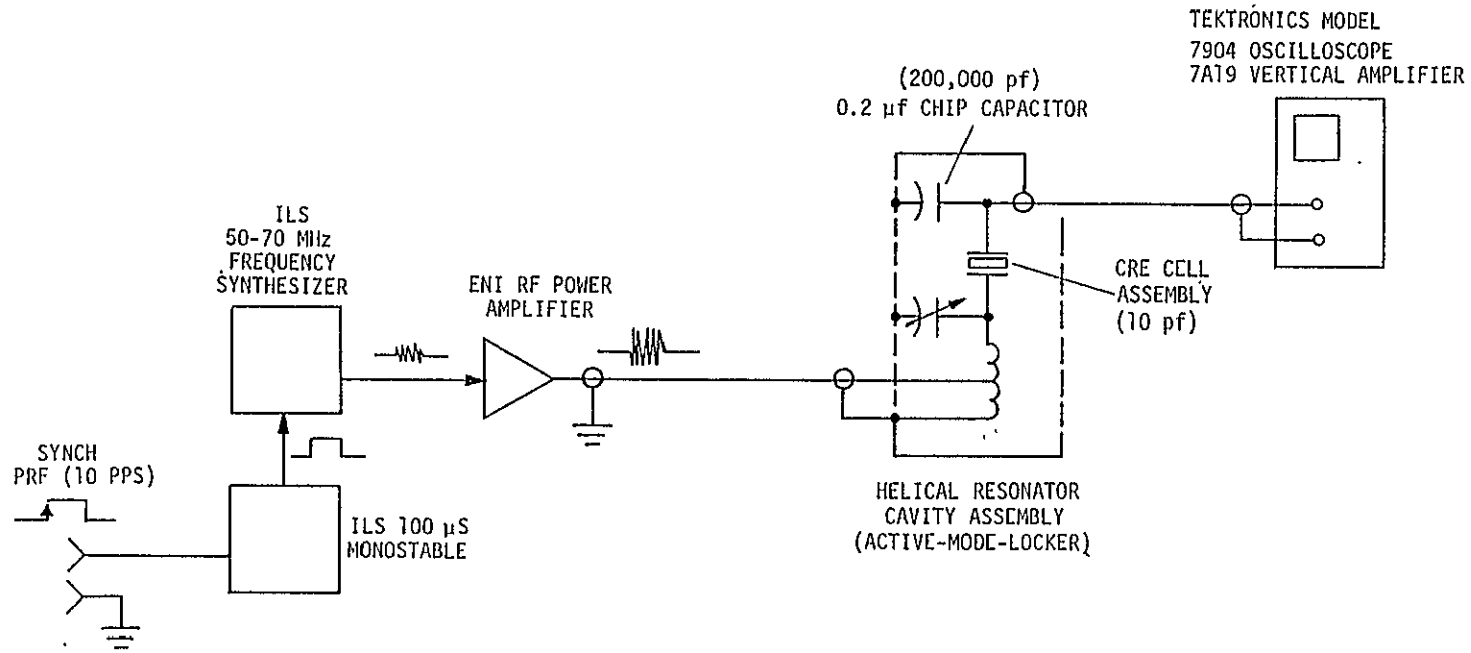


Figure 4-1. Modelock Cell Voltage Measurement Setup

30 W during the pulse. The pulse repetition rate was 10 pulses per second. The RF output was adjusted to 69,860 MHz. The cell was connected and peaked to proper resonance. Figure 4-2 presents scope traces of voltage waveforms obtained to assess modelock cell performance.

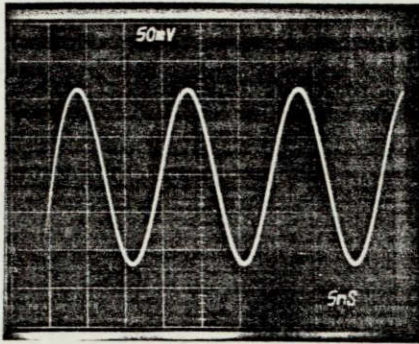
Oscilloscope photo no. 1 in Figure 4-2 illustrates the voltage available across the cell at resonance. It is to be noted that approximately 4.8 divisions of the vertical range are distended by the peak-to-peak excursions of the sine wave. For a given sensitivity of 50 mV/division, this relationship equates to a peak-to-peak voltage of 24 mV. The capacitive voltage divider ratio is approximately equal to $20,000 \times 24 \text{ mV}$ or 4,800 V peak-to-peak. This figure equates to a peak cell voltage deviation of 2,400 V from 0 V, which corresponds to 75% of the quarter-wave voltage of the Pockels cell and a modulation depth of 1.178.

The measurements were deliberately taken at the maximum expected operating frequency expected to illustrate the worst-case conditions. The worst-case condition arises from the fact that the helical resonator is foreshortened by capacitive loading (the Pockels cell capacitance). Obviously, the higher the frequency the more severe the capacitance loading becomes for a fixed helix length.

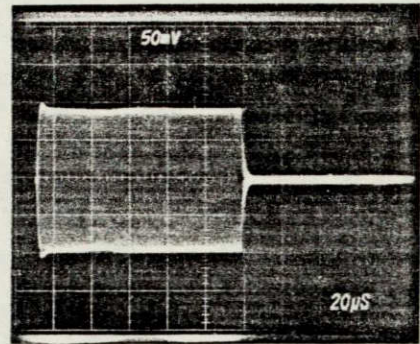
The approximate RF frequency the Spaceborne Laser System will operate at is 60 MHz. The resonant cavity Q is a function of frequency; lower frequencies yield higher Q and, thus, higher voltage amplitude. The extrapolated voltage amplitude excursion from 0 V at 60 MHz is $\sim 2,600 \text{ V}$.

1. RF Burst Envelope

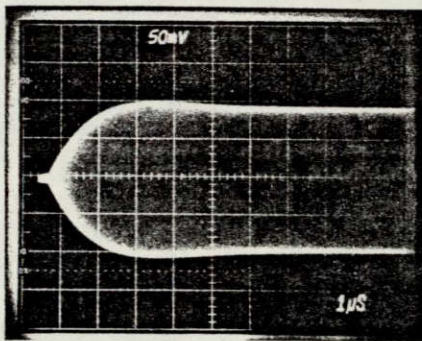
The RF burst envelope is obtained with the test configuration depicted in Figure 4-1. Oscilloscope photograph no. 2 serves to illustrate the burst. It is to be noted that a slight envelope "over-shoot" occurs at the leading edge. Apparently, this characteristic is produced by the Pockels cell material response to the pulse because it is not present whenever a high-quality capacitor is substituted for the cell. In addition, photograph no. 2 illustrates the overall flatness of the pulse for the pulse interval, which is approximately 110 μsec . Oscilloscope photograph no. 3 shows the pulse burst leading edge which illustrate the pulse burst envelope build-up time of $\sim 2.5 \mu\text{sec}$. Oscilloscope photograph no. 4 shows the pulse burst trailing edge decay time. The time trailing edges of the pulse burst are indicative of the high Q of the resonant cavity.



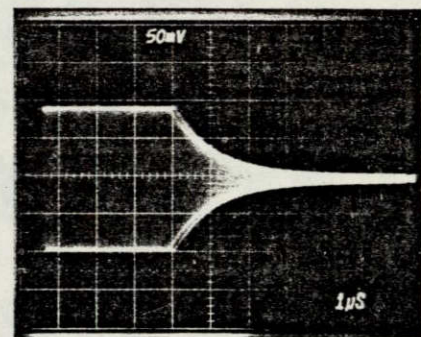
OSCILLOSCOPE PHOTO NO. 1



OSCILLOSCOPE PHOTO NO. 2



OSCILLOSCOPE PHOTO NO. 3



OSCILLOSCOPE PHOTO NO. 4

F803

Figure 4-2. Modelock Cell Voltage Waveforms

Clearly, the pulse burst amplitude envelope is temporarily sufficiently long and reaches stability rapidly enough to provide the desired modulation and, thus, the pulse compression required in the prelude period ($\sim 3 \mu\text{sec}$) of the Spaceborne Laser System device.

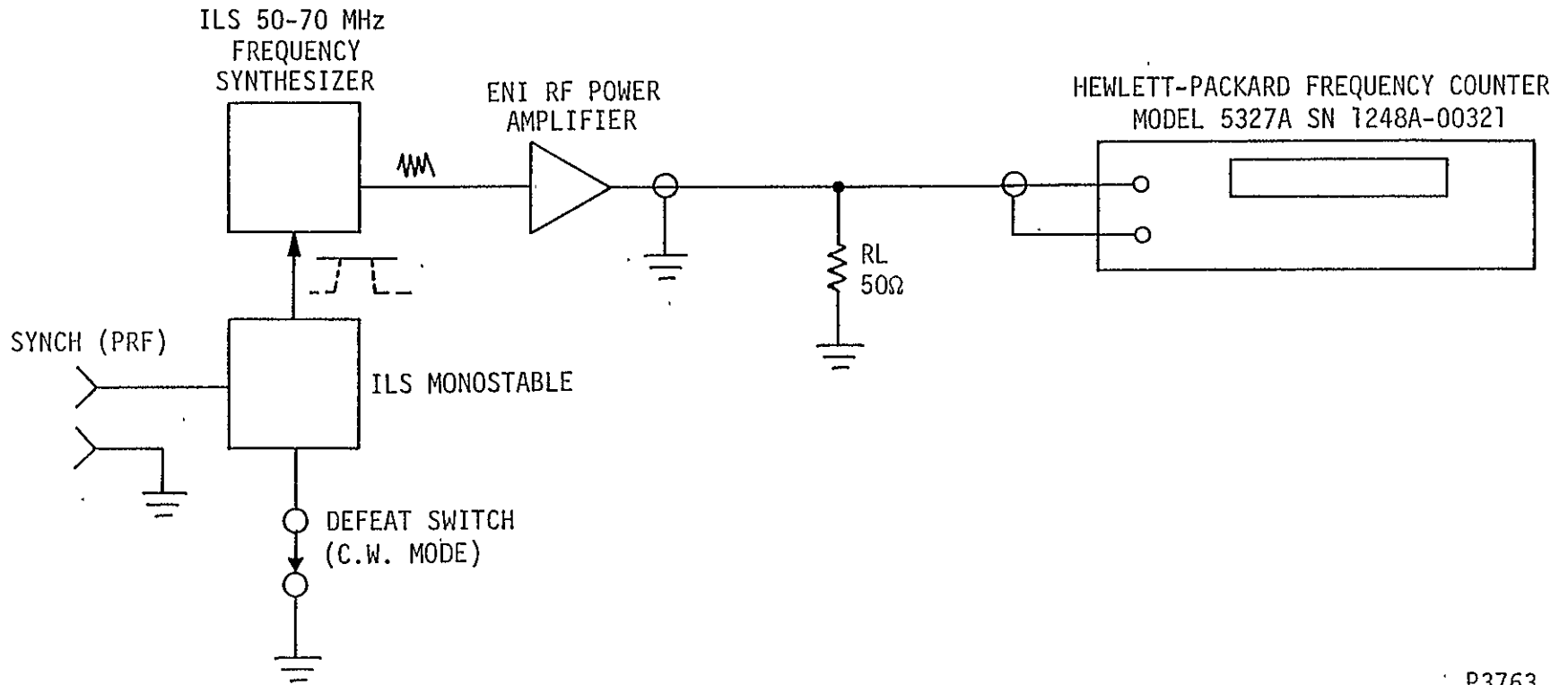
2. Frequency Synthesizer Stability Measurement

The test configuration of this measurement is illustrated in Figure 4-3. Test data are tabulated and attached.

It is to be noted that the modelocker cell could not be utilized in this test because the output signal of the synthesizer must be of the continuous-wave (CW) mode. Under CW excitation, the crystal would be required to dissipate excessive heat and crystal damage would probably occur. The modelocker cell was replaced with a 50 Ω resistive load and the amplifier was operated at the maximum power output to simulate the worst-case thermal loading of the ENI RF power amplifier. It is to be noted that replacement of the cell with the load resistor in no way affects the frequency stability measurement accuracy because the unidirectional signal isolation afforded by the RF amplifier circuitry provides excellent isolation of the frequency synthesizer from the load. Test conditions are tabulated with the test data.

The frequency synthesizer/amplifier assembly was tested from a cold start--that is, the test is begun with the reference crystal oven at ambient temperature. The test data show that the reference crystal frequency drifted sufficiently during the first 20 min. of the test to create an output frequency change equating to $\sim 6,155$ Hz. This drift is not serious since the manufacturer of the reference crystal specifies the oven stabilization time to be approximately 15 to 30 min. Therefore, the stability data occurs following crystal oven stabilization. The initial data are included only to illustrate that the reference crystal oscillator exhibits no wild frequency excursion during the stabilization time.

At an elapsed time of 60 min. into the test, the synthesizer output frequency is 60,000,024 Hz. The test data show that a gradual increase in frequency of 68 Hz has occurred from the data taken at an elapsed test time of 25 min. Thus, the drift during this period is equal to approximately one part per million. An additional 7 Hz of drift occurs to an elapsed test time of 90 min. The test data indicates a total drift during the second hour of the test interval to be ~ 16 Hz, which equates to a sta-



P3763

Figure 4-3. Frequency Synthesizer Stability Measurement Setup

Frequency Synthesizer Frequency Stability Test Data

REFERENCE: Figure 4-3 for Test Configuration

TEST EQUIPMENT: HP Model 5327A
 Frequency Counter S. No. 1248A-00321
 Calibration Date 6/13/77

TEST CONDUCTED BY: _____

SPECIAL CONDITIONS:

1. Model 5327A Counter in operation 1 hr minimum prior to test start.
2. Ambient temperature ~ 25°C.
3. Device under test (frequency synthesizer) measured from cold-start to illustrate stabilization time.
4. Test frequency 60 MHz.

TEST DATA:

<u>ELAPSED TIME</u> (MIN)	<u>FREQUENCY (Hz)</u>	<u>COMMENTS</u>
0	60,006,107	ΔF=6,155 Hz ΔF=68 Hz ~ 1.0 part in 10 ⁶ stability Reasonable stability achieved after 1 hr operating time.
5	60,002,589	
10	60,000,340	
15	60,000,002	
20	59,999,952	
25	59,999,956	
30	59,999,962	
35	59,999,979	
40	60,000,003	
45	60,000,017	
50	60,000,024	Synthesizer and crystal oscillator oven warm-up
55	60,000,026	
60	60,000,028	
65	60,000,029	
70	60,000,032	
75	60,000,031	
80	60,000,032	
85	60,000,032	
95	60,000,032	

TEST DATA: (continued)

<u>ELAPSED TIME</u> <u>(MIN)</u>	<u>FREQUENCY (Hz)</u>	<u>COMMENTS</u>
96	60,000,031.8	Data taken each minute to illustrate settle- time of frequency output
97	60,000,032.3	
98	60,000,032.3	
99	60,000,032.8	
100	60,000,033.0	
101	60,000,033.7	
102	60,000,033.9	
103	60,000,034.0	
104	60,000,034.5	
105	60,000,034.5	
106	60,000,034.7	F = 16 Hz over second hr period (2.6 parts in 10 ⁷ stability)
107	60,000,035.0	
108	60,000,035.4	
109	60,000,035.6	
110	60,000,035.8	
111	60,000,035.8	
112	60,000,036.6	
113	60,000,037.0	
114	60,000,036.9	
115	60,000,037.5	
116	60,000,037.6	Thermal roll-over point
117	60,000,037.9	
118	60,000,037.9	
119	60,000,038.3	
120	60,000,038.9	
121	60,000,039.1	
122	60,000,039.9	
123	60,000,040.1	
124	60,000,040.9	
125	60,000,040.5	
126	60,000,040.0	
127	60,000,040.1	
128	60,000,039.5	
129	60,000,039.5	
130	60,000,039.2	
131	60,000,039.2	
132	60,000,039.0	
133	60,000,039.0	

bility of 2.6 parts in 10^7 . The test data indicates further that the frequency drift/temperature roll-over occurs at 123 min. into the test. The required drive signal stability for satisfactory modelocking is 1 part in 10^5 . The ILS modelocker driver system exhibits a stability exceeding this level after stabilization of the crystal oscillator.

Operation of the ILS modelocker driver system in a pulsed mode will result in a frequency stability equal to that exhibited in the CW mode. The crystal oscillator is operated continuously in either the pulsed or CW mode and pulsing of the modelocker driver system is achieved by pulsing the RF amplifier. Because the frequency stability is dependent primarily on the crystal oscillator as illustrated in the reported experiment, the required or better frequency stability can be achieved in the pulsed mode by allowing 30 min. of warming time prior to system operation.

3. Q-Switch/Dump Switch Waveform Measurements

The Q-switch/dump switch measurement configuration is depicted, in simplified form, in Figure 4-4. It is to be noted that the cell is excited in the differential drive configuration. Prior to discussion and presentation of voltage waveforms of the cell drives, a brief discussion of the basic circuit configuration is appropriate.

The Pockels cell voltage conditions will be defined for each phase of the laser performance so that a systematic description of the required driver performance can be presented. Initially, the driver and Pockels cell are required to develop a very low Q within the optical resonator. This condition, or hold-off, allows energy storage to the laser rod for a determined time interval. The input, termed the V bias (+HV), establishes a voltage potential across the cell effecting the low Q condition. When the energy storage is accomplished, it becomes necessary to effect a rapid increase in the Q of the optical resonator to achieve lase action. The block in Figure 4-4, termed Q-switch avalanche, effects this change by reducing the applied voltage of the cell to near zero potential. It is to be noted that the greatest "Q" is obtained within the optical resonator when no potential is impressed upon the cell. The output voltage from the "Q" switch avalanche driver is conducted to the cell through the action of capacitor C_A . The high "Q" condition causes rapid lase action to occur.

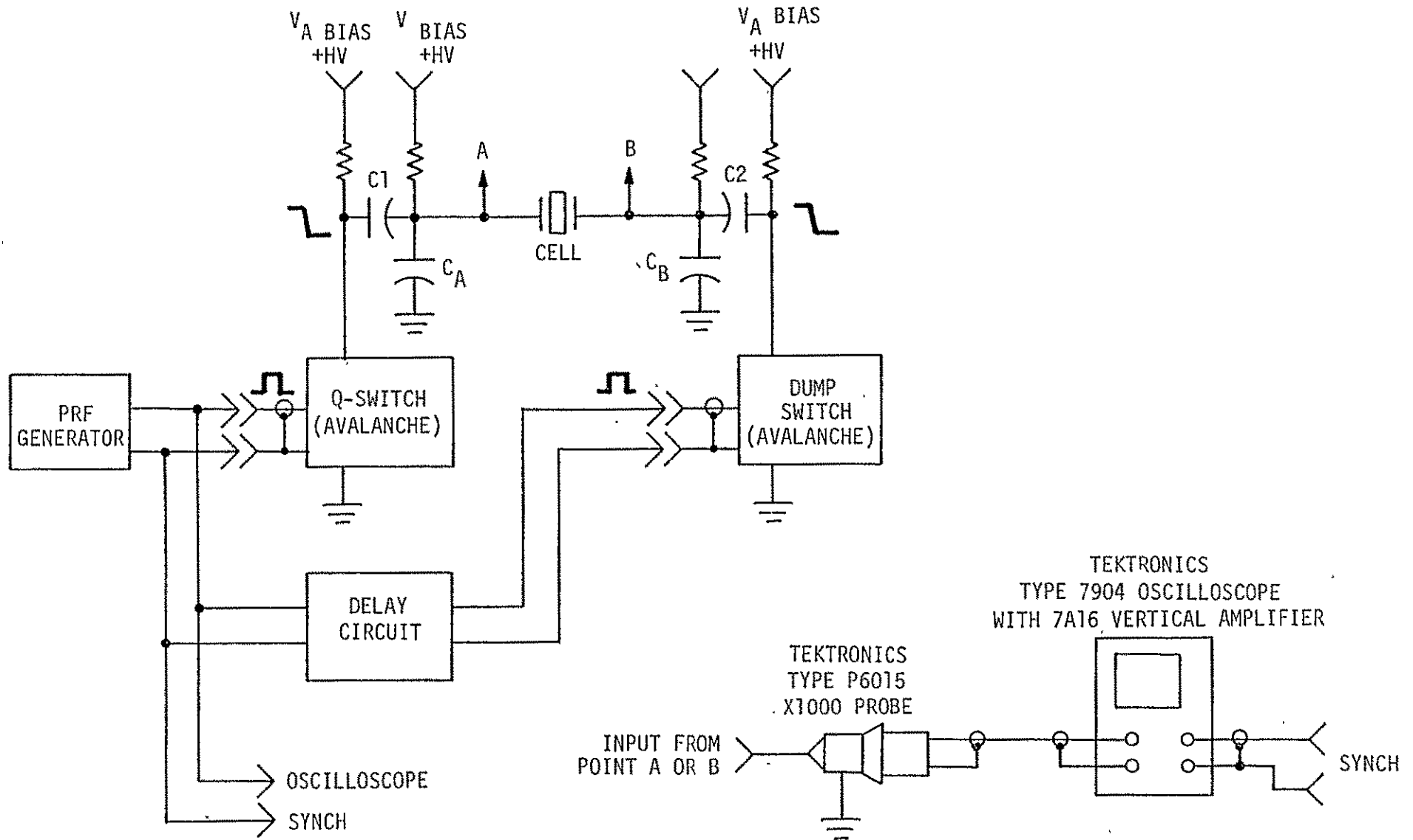


Figure 4-4. Simplified Pockels Cell Drive Configuration

In actuality, the low "Q", or hold-off state of the laser, is altered by varying the cell bias voltage in such a manner as to produce coherent radiation, slightly above laser threshold, just prior to the Q-switch time. The simple depiction of Figure 4-4 does not provide for this detail.

Energy rise within the optical resonator following Q-switching occurs rather slowly as referenced to the modelocked pulse interval because many reflections within the resonator are required to deplete the stored energy within the rod. This point is significant as it dictates the required interval for the removal of voltage from the cell. A voltage fall time of approximately 15 nsec is quite adequate for this Q-switching operation.

As energy is depleted from the rod, the active resonator energy increases. When the energy reaches a critical magnitude, it is necessary to direct the energy from the optical resonator. This process -- that is, the cavity dumping of the modelocked pulse must occur very rapidly. Thus, the necessity for the dump avalanche driver. The requirement for this driver is the generation of a differential cell voltage of 3200 V. It is to be noted that the dump voltage is not equivalent to the initial bias voltage, but is a greater voltage. Furthermore, the dump avalanche drive circuitry must successfully apply the cell voltage within one round-trip time of the optical resonator. This condition dictates the switching speed required which is a total elapsed time of approximately 9 nsec. Additionally, the initiation of this action must be synchronous to the modelocked pulse within the resonator. Thus, synchronization jitter must be maintained at the lowest possible level. A jitter of ± 1 nsec is achievable which dictates a maximum dump switching time of 6 nsec. The action of the dump avalanche switch is conducted to the cell by the action of capacitor C_B . Dumping of the modelocked pulse from the optical resonator completes the voltage switching sequence.

As pointed out earlier, the drive to the Pockels cell is of the differential mode which creates some problem in achieving the required performance. Thus, the need for capacitors C_A and C_B is realized. Application of a very abrupt voltage step to either point A or point B, with the shunt capacitors omitted, would result in virtually no voltage impressed across the cell because basically the cell appears as a capacitor. Any impressed voltage would be caused by stray capacitive coupling to the cell terminal not being excited directly. The addition of capacitors C_A and C_B , forms a

capacitance voltage divider, regardless of excitation from source A or B. Obviously, the greater the capacitance value used for capacitors C_A and C_B , the greater the percentage of the applied voltage which will be impressed upon the cell. The remainder of the impressed voltage will be impressed on either C_A or C_B as dictated from the excitation source. It is to be noted that the capacitors C_A and C_B appear in parallel with the avalanche drivers. Each driver must either charge or discharge its appropriate capacitor simultaneously with driving the cell. For this reason, it becomes quite apparent that capacitors C_A and C_B must be of the minimum capacitance value possible to achieve adequately rapid cell excitation. Previous experience has dictated a ratio of one to ten between the cell capacitance and the shunt capacitance. This relationship assures that roughly 90% of the applied voltage is impressed upon the cell, while the remaining voltage appears across the shunt capacitor.

Figure 4-5 lends some clarification of the voltage sharing across the various capacitors involved. Cell capacitance, cell holder capacitance, and stray wiring capacitance total in the order of 10 pF. Thus, the shunt capacitors are selected to exhibit 100 pF of capacitance. Figure 4-5 additionally illustrates the effective capacitance load to either avalanche driver, which simplifies to a value of 109.09 pF, the total effective capacitance load. Optimum switching action occurs for an impressed voltage of 3200 V across the cell. This voltage represents 90% of the input voltage; thus, 355 V appears across the shunt capacitor, and the applied voltage must be 3,555 V.

To allow some small time margin in the dump switching operation, the required cell voltage risetime will be reduced to 5 nsec as measured from the 10 to 90% points. This condition allows the avalanche pulse current to be calculated as follows:

$$I = \frac{CV}{t} \tag{3-26}$$

where

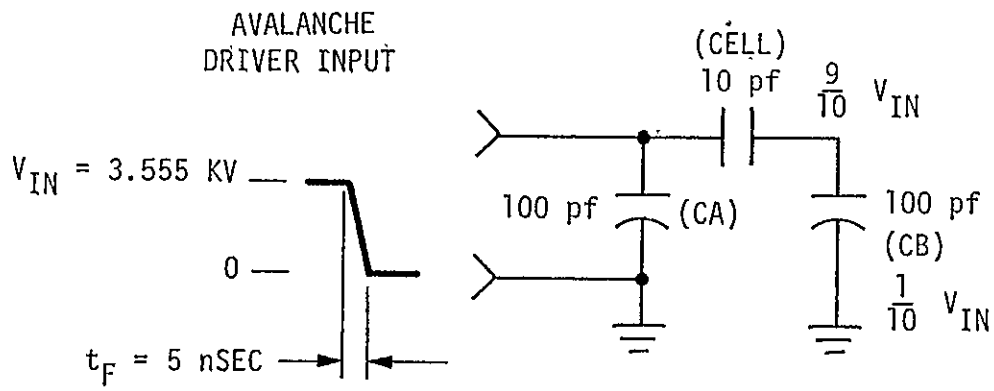
$$C = 109.09 \times 10^{-12} \text{ F}$$

$$V = 3,555 \text{ V}$$

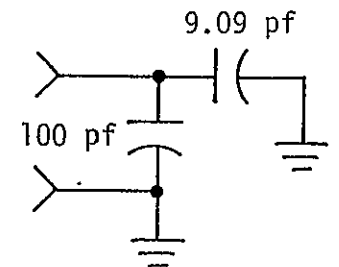
$$t = 5 \times 10^{-9} \text{ sec}$$

$$I = \frac{(109.09 \times 10^{-12})(3,555)}{5 \times 10^{-9}}$$

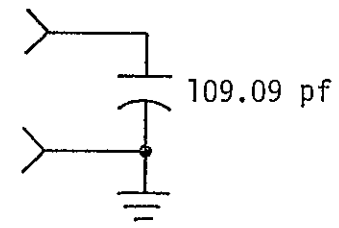
$$I = 77.56 \text{ A}$$



EQUIVALENT CAPACITANCE LOAD FOR DRIVER, SHOWING INDEPENDENT CAPACITORS



FIRST SIMPLIFICATION



EQUIVALENT CAPACITANCE

P3784

Figure 4-5. Effective Capacitance Load for Avalanche Driver

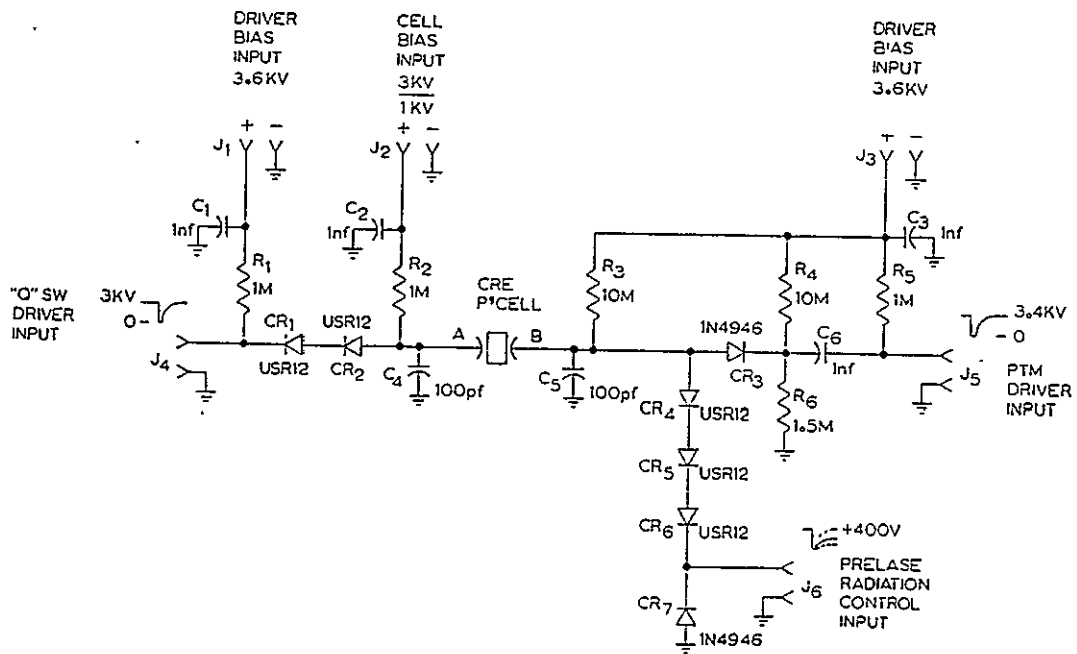
This value of pulse current is quite acceptable from a standpoint of reliable avalanche driver operation. Additionally, this current peak is required only for the dump driver. The Q-switch driver is required to discharge only the bias voltage upon the cell, which is lower than the 3,555 V seen at the dump driver, and the fall time requirements also are less stringent for the Q-switch driver.

Conclusions which are drawn to this point are: Initially, the 100 pF shunt capacitor is acceptable from a standpoint of voltage risetime and avalanche current; the differential drive technique is acceptable; and, finally, good avalanche driver isolation can be maintained, with regard to false triggering.

Now that the description of the basic Pockels cell interface is complete together with the definition of the required sequence of operation, the actual hardware operation will be presented. Variation from the elementary configuration will be noted, and reasoning for the departure in technique will be presented.

The schematic shown in Figure 4-6 details the actual hardware from which the exhibit oscilloscope trace photographs were recorded. Inspection of Figure 4-6 immediately reveals, the departure in the coupling circuitry for the Q-switch driver input. A series diode string (CR_1 and CR_2) is used for this coupling. This coupling technique is used because: Excellent isolation is achieved between the driver output and the cell bias voltage; the driver is required only to reduce the differential cell voltage to near zero potential; and the diode string assists in maintaining the appropriate differential cell voltage for the Q-switch function whenever the cell bias voltage is adjusted. It is to be noted that were capacitive coupling used only one value of bias voltage would be possible to achieve the optimum Q-switch condition of zero cell voltage. This bias voltage would be essentially the Q-switch hold-off voltage. Were a lower bias voltage utilized, the differential cell voltage would be driven below zero volts. Conversely, a higher voltage would result in a lack of achieving zero volts.

Further inspection of Figure 4-6, reveals that the dump driver is capacitively coupled and also diode isolated. This technique is necessary so that the prelude radiation control can be effected. Resistor R5 is the bias resistor for the dump avalanche driver. Capacitor C6 is the output coupling capacitor.



D1018736

Figure 4-6. Q-switch Interface Schematic

Resistors R4 and R6 form a voltage divider to achieve a position potential of approximately 460 V at the cathode of diode CR3. Obviously, the output from the dump driver is referenced to this voltage as a start potential when coupled through capacitor C6. Resistor R3 provides current to the prelude radiation control circuitry through diodes CR4, CR5, and CR6 by way of connector J6.

The voltage of the radiation control circuitry is limited to a maximum positive value of 400 V whenever an absence of radiation exists to the control circuitry optical detector. Normally, the bias voltage is adjusted to allow a "leakage" which affords a lase action in the region of 1 to 3% above threshold during the prelude interval. The prelude control electronics removes voltage from the dump side of the cell (point B) and increases the differential cell voltage which increases optical hold-off to achieve control.

It is to be noted that diode CR3 is reverse biased for all conditions other than the dump function. It is to be further noted that the prelude electronics always reduces the point B cell voltage prior to the Q-switch interval, and that the Q-switch function additionally reduces the point B voltage resulting from the capacitor C5. Cell bias voltage input of 1.5 kV, results in a voltage division to reduce the C5 voltage by 177 V. This voltage together with the reduction afforded by the prelude radiation control electronics, results in a point B voltage which is approximately ± 100 V, as referenced to ground, at the completion of the Q-switch action, and the cell voltage is, indeed, near zero differential voltage. Initiation of the dump driver, produces a voltage transition of approximately 3.4 kV. Diode CR3 conducts when the voltage excursion has reached the 460 V point, and capacitor C5 is charged to roughly 3.0 kV.

An interesting phenomenon occurs when the delay from Q-switch to PTM switch is less than 100 nsec. The Q-switch avalanche driver is still in the high-current-conducting state. Diodes CR1 and CR2 also are unable to recover because of the large minority carrier concentration resulting from Q-switch discharge current. Thus, the dump driver voltage is impressed almost in its entirety across the cell because the point A side of the cell is clamped to ground. It is to be noted that the differential cell voltage is 3.0 kV ± 100 V when the dump driver output occurs.

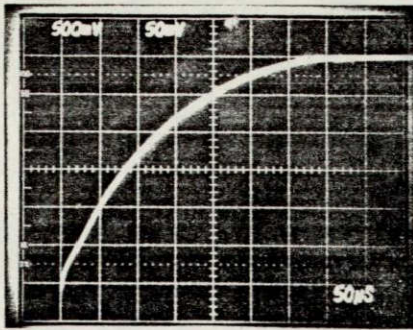
At the occurrence of the dump event, diodes CR4, CR5, and CR6 are reverse biased, and the pre-lase radiation control electronics is effectively removed from the circuit. The remainder of the discussion and presentation deals specifically with the measurements taken of the actual hardware.

Figure 4-6 depicts the actual circuitry which comprises the Q-switch/dump-switch/radiation-control interface. For these tests the radiation control voltage was fixed at a value of +400 V. The Q-switch was driven directly from the pulse repetition frequency (PRF) generator at a 10 pps rate. A delay generator was utilized to drive the dump avalanche switch. Voltage waveforms highlighting switching response in the Q-switch and PTM dump modes are illustrated in Figure 4-7. The delay time was adjusted initially to roughly 40 nsec; however, clarity was somewhat impaired in the scope photographs obtained, and the delay time was increased to 100 nsec to obtain better trace clarity.

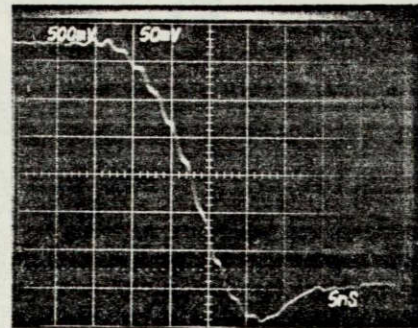
It is to be noted that all photographs are realtime exposures with no superposition of either graticule or scope nomenclature. A Tektronix model 7904 oscilloscope with a model 7A16 vertical amplifier was used in conjunction with a type P6016 highvoltage probe to acquire the oscilloscope trace photographs.

Oscilloscope trace photograph (OTP) no. 6 is presented to illustrate the Q-switch voltage magnitude. The probe attachment was at point A and measurement was made of the switch recovery waveform. Cell bias voltage was adjusted to 3.2 kvdc. It is to be noted that the full 3.2 kvdc is switched. OTP no. 7 illustrates the leading edge fall time of the Q-switch. Note that some slight ringing occurs at the transition time which is inevitable when a lead/probe attachment is provided. It also is to be noted that the indicated response always is slower than the actual circuit response. This condition is caused by: first, the probe possesses an input capacitance of roughly 18 pF; and, second, the probe response time is finite because of probe inductance. Thus, the probe causes degradation of pulse rise/fall presentations which are 1 to 5 nsec greater than reality when the oscilloscope sweep speed is 5 nsec/division.

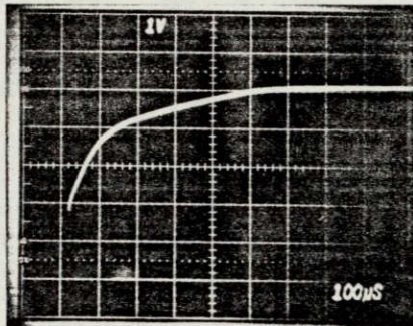
OTP no. 8 depicts the voltage at point B, the dump drive. This trace is taken with a vertical sensitivity of 1,000 V/division. Once again, measurement is made of the switch recovery waveform to show the voltage excursion and the recovery characteristics. OTP no. 9 shows the leading edge with the 300-V step



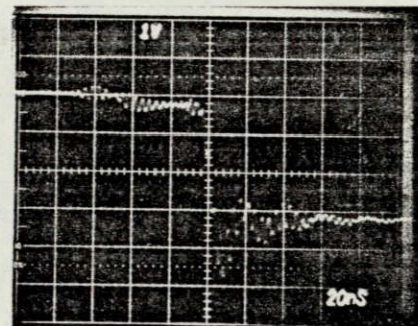
OSCILLOSCOPE PHOTO NO. 6



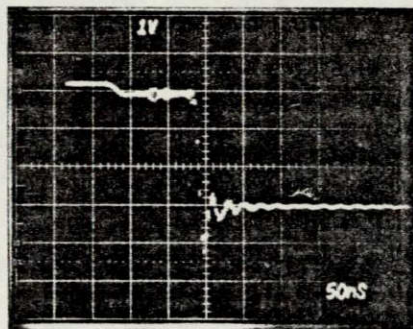
OSCILLOSCOPE PHOTO NO. 7



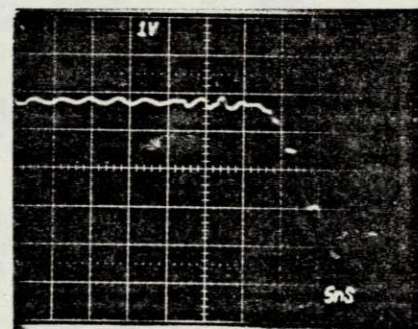
OSCILLOSCOPE PHOTO NO. 8



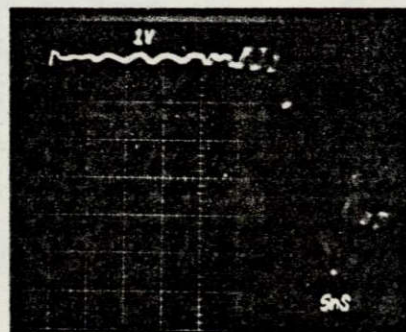
OSCILLOSCOPE PHOTO NO. 9



OSCILLOSCOPE PHOTO NO. 10



OSCILLOSCOPE PHOTO NO. 11



OSCILLOSCOPE PHOTO NO. 12

F804

Figure 4-7. Q-switch and PTM Dump Switching Voltage Waveforms

which is induced by the Q-switch excitation. The Q-switch activation time is 40 nsec prior to the dump output. The ringing is induced from the probe attachment. The OTP no. 10 is a repeat of the previous photograph with the exception that the PTM switch time has been extended 100 nsec from the Q-switch time.

OTP no. 11 shows the fall time of the dump avalanche drive. In reality, this is the rise time of the cell voltage for the dump action. Probe attachment is at point B. Again, the ringing is because of the probe attachment. It is to be noted that the risetime, as indicated on OTP no. 11, is considerably more than 5 nsec. Thus, OTP no. 12 is provided in an attempt to depict a more realistic presentation of the true risetime of the dump drive pulse. These photo data depart from that produced from the previous test configuration. A capacitance probe is provided by placing a VHF x 10 probe in proximity to the driven electrode of the cell. Thus, the response degradation of the type P6015 probe is avoided. As indicated, the response of dump drive to the cell occurs well before 4 nsec of elapsed time.

B. SYSTEM OPTICAL ALIGNMENT

1. Alignment Overview

The alignment of the Spaceborne laser oscillator is a complex task because of the use of wedged optical elements to avoid etalon effects on pulsewidth. The basic problem is that the correct optical path through the resonator lacks an optical reference normal to this path prior to alignment of the laser mirror. The precision machining of the optical bed allows the use of the mechanical centers of the beam exit holes to establish correct reference optical paths. The alignment of the optical components to these reference paths achieves the resonator mirror alignment and oscillator alignment to an accuracy which permits lasing. Dynamic tweaking of particular optical elements while operating the laser then achieves optimum laser alignment.

The amplifier subsystem alignment is a simple and straightforward procedure since the optical components are not wedged. Therefore, this procedure will not be discussed. The description of the detailed alignment procedures for the oscillator subsystem are given in the following paragraphs of this report section. Figures 4-8 and 4-9 show the oscillator optical diagram and an optical bed sketch as references for understanding of the oscillator alignment procedure. The steps in this procedure are:

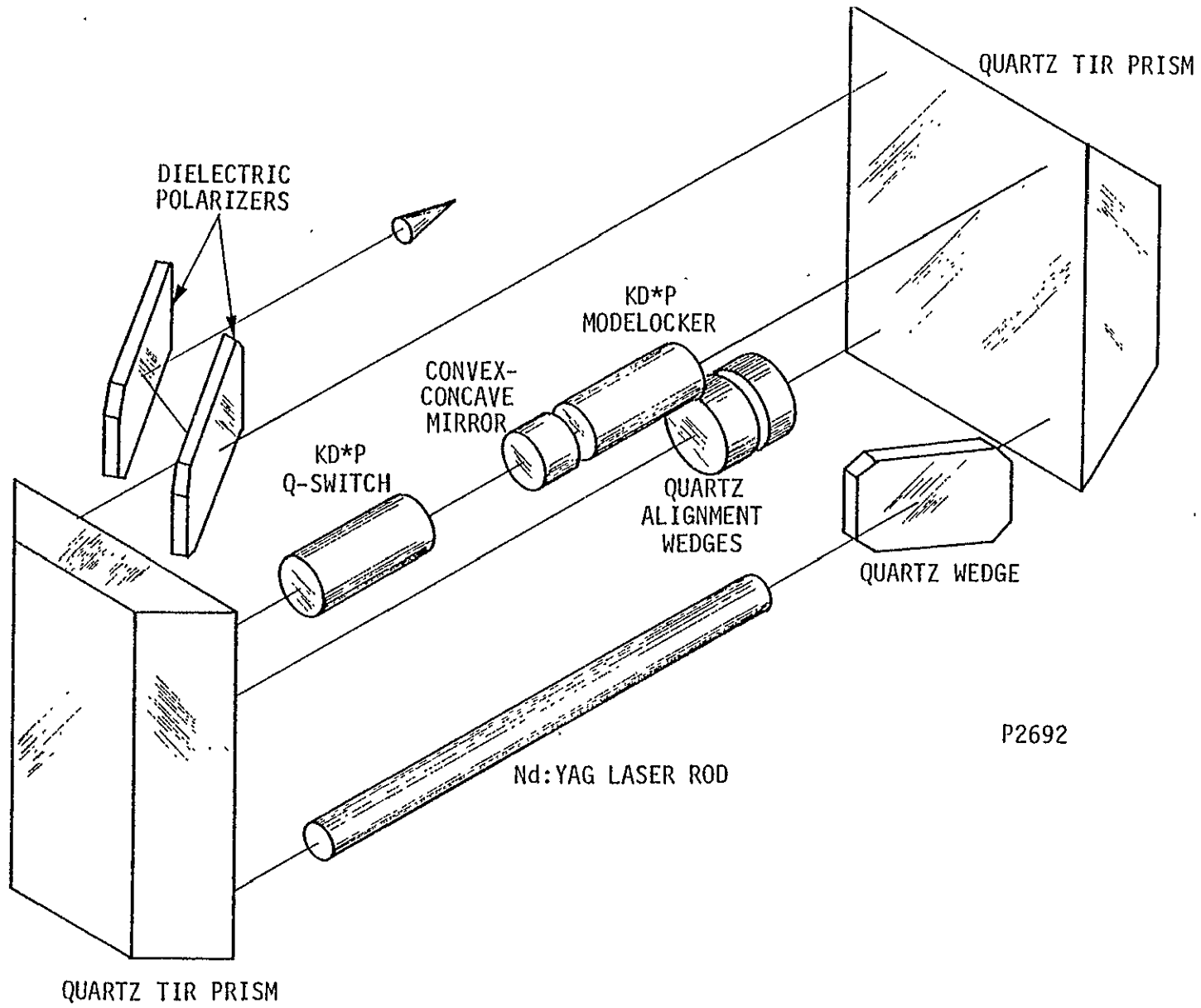
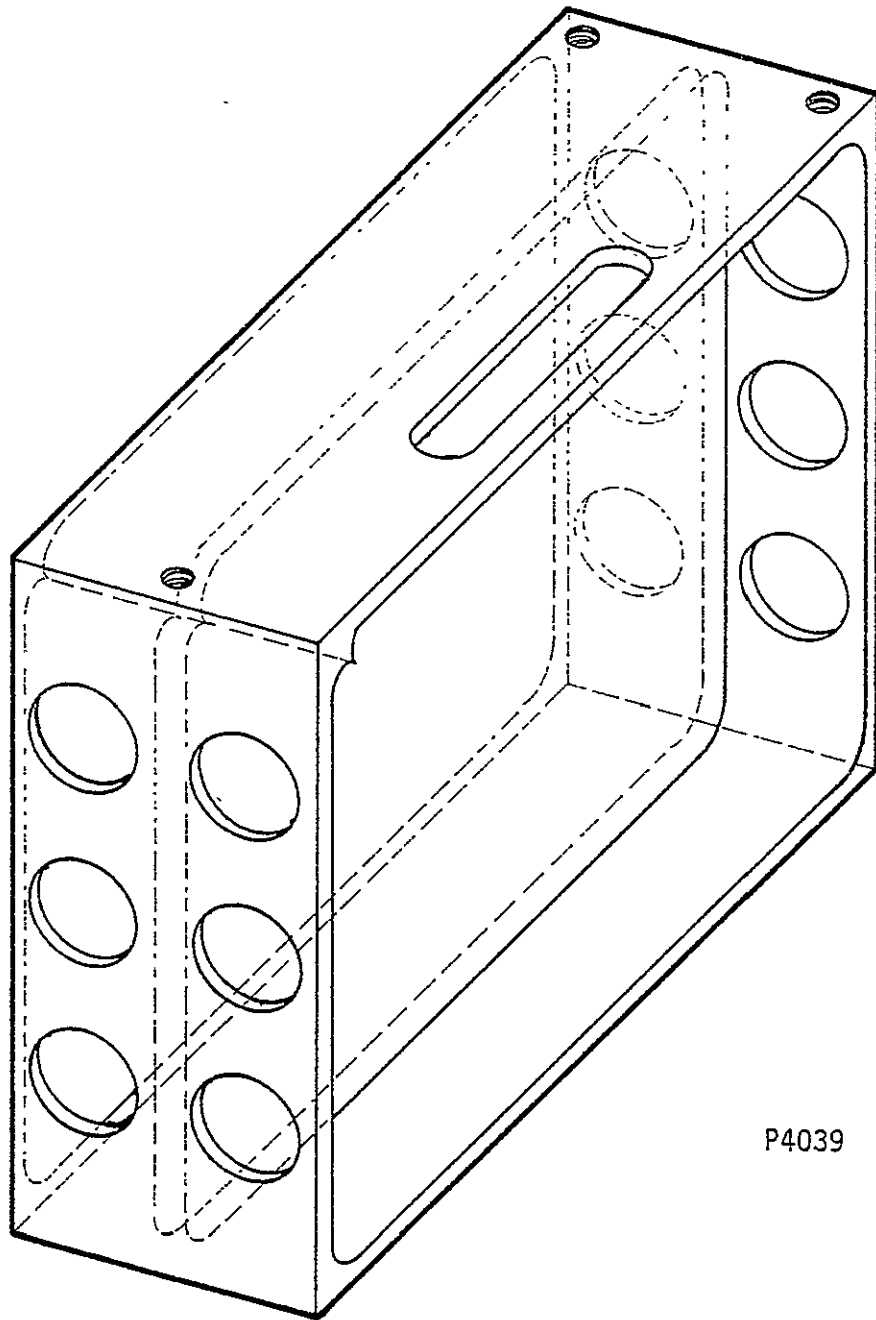


Figure 4-8. Oscillator Optical Diagram



P4039

Figure 4-9. Optical Bed Sketch

- TIR prism alignment;
- Rod-wedge leg alignment;
- KD*P cell leg alignment;
- Mirror-rod alignment;
- Risley prism-polarizer alignment; and
- Dynamic laser alignment.

A He-Ne beam was used in all the following alignment techniques. The alignment error introduced by the difference in optical indices of the oscillator components was calculated and proved in practice to be negligible.

2. TIR Prism Alignment

Each of the three TIR prisms is designed to have a pyramidal error of 1.5° . One of these is illustrated in Figure 4-10. The pyramidal error results in the entrance and exit faces of the prism to be non-parallel. Thereby, etalon effects are avoided. The 1.5° pyramidal error of the prisms dictates, via Snell's Law, that they be tilted 2.175° to the required optical paths so that the entrance and exit beams be parallel. The orientation of the TIR prisms is governed by the Invar pads that they are clamped to, as discussed in the mechanical design section. Perfect fabrication of the Invar bed and pads and the TIR prism would result in correct prism alignment simply by attachment to the bed. However, in practice, fabrication to better than 10 arc-seconds, as required, is not achievable. Thus, the precision mounting of the TIR prisms to the bed is a two-stage process involving a second machining of the Invar pads. A description of this process follows which is identical for each TIR prism.

First, the prism is clamped to the Invar pads attached to the optical bed. A He-Ne beam is then aligned through the center of the appropriate beam exit holes using mechanical apertures with 0.04 inch holes. In general, the He-Ne exit beam is not parallel to the beam entering the prism. A measurement of the angle between the entrance and exit He-Ne beams is then made. By elementary optics, the orientation of the prism is defined then to be in error by half the measured angle. The TIR prism is then removed along with the Invar pad. The Invar pad is then remachined and optically polished to a new wedge whose angle differs from the initial fabrication angle by the angular error (either positive or negative) of the initial prism orientation. This was proved to be achievable to an accuracy of better than 10 arc-seconds. Following the above procedure, the prism was

remounted to the optical bed and the optical alignment remeasured for verification. With correct measurements, the above-described procedure resulted in the alignment of all three TIR prisms to within 10 arc-seconds of the correct optical paths of both the oscillator and amplifier subsystems.

3. Rod-Wedge Leg Alignment

The optical drawings of the oscillator laser rod and the compensating wedge are shown in Figure 4-11 and 4-12. The compensating wedge corrects for both the angular and lateral displacements from the correct optical path produced by the wedged oscillator rod. As before, the first step in the alignment is to direct a He-Ne beam through the centers of the beam exit holes using mechanical apertures in order to establish the correct reference optical path. The second step is to mount and orient the laser rod so that its deflection is parallel to the optical bed. The laser rod is also positioned by moving the pump cavity mounting so that the He-Ne beam enters and exits the laser rod at the center of the rod ends. The final step is to mount and orient the compensating wedge so that the He-Ne traverses the same path after exit as it did before mounting the laser rod and compensating wedge. Figure 4-13 illustrates the He-Ne beam propagation through the rod-wedge leg after alignment completion. The angles are exaggerated for clarity of illustration.

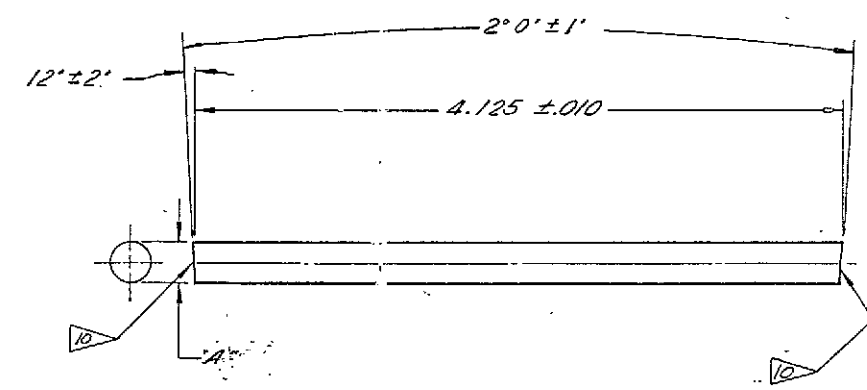
4. KD*P Cell-Mirror Leg Alignment

The KD*P modelocker cell, the common laser mirror, and the KD*P Q-switch are the specific optical elements of this oscillator leg. The modelocker and Q-switch cells are designed identically. Figures 4-14, 4-15 and 4-16 are optical drawings of the KD*P crystal, the cell windows, and the laser mirror respectively. Figure 4-17 is an optical diagram of this oscillator leg when correctly aligned to the illustrated reference optical path. The modelocker and Q-switch cells are aligned to give equal and opposite angular deviations and a net lateral displacement of 0.002 inches. The cells must actually be individually aligned as well, so the the He-Ne beam propagates along the KD*P optical axes. Rotation of the cells so that the X or Y axes of the crystals are parallel to the optical bed — the oscillator polarizer transmission plane — is also necessary. This rotation is necessary to achieve maximum phase retardation by the KD*P cells when voltage is applied.

NOTES:

1. MATL: MATERIAL TO BE Nd:YAG WITH A NEODYMIUM DOPING LEVEL OF $1.0\% \pm 0.1\%$ UNIFORMLY DISTRIBUTED ALONG ROD LENGTH WITHIN $\pm 0.05\%$. CRYSTAL ORIENTATION TO BE \parallel WITH ROD AXIS PARALLEL TO \parallel .
2. CHAMFER: $45^\circ \pm 5^\circ \times .005 \pm .002$. (FINE GRIND, DO NOT POLISH CHAMFER)
3. THERE SHALL BE NO VISIBLE VOIDS, INCLUSIONS, OR SCATTERING CENTERS; THE ROD SHALL EXHIBIT AN EXTINCTION RATIO $> 1000:1$ (30dB) BETWEEN CROSSED POLARIZERS @ $\lambda = 0.6328\mu$
4. WAVEFRONT DISTORTION TO BE LESS THAN $1/8$ WAVE PER 1.0" OF LENGTH FOR SINGLE PASS OF 0.6328μ LIGHT (= $1/4$ THYMAN-GREEN FRINGE PER 1.0 LENGTH).
5. END FACES OF ROD TO BE FLAT WITHIN $1/10$ WAVELENGTH AT 0.6328μ .
6. SCRATCHES AND DIGS ON END SURFACES NOT TO EXCEED SCRATCH 10, DIG 5 PER MIL-0-13830, WITH NO SCRATCHES, DIGS, OR PITS VISIBLE @ $20\times$ IN THE CENTRAL 80% DIAMETER.
7. EDGE CHIPS NOT TO EXCEED 0.127mm .
8. SIDE OF ROD TO BE FINE GRIND.
9. PACKAGE ROD IN A REUSABLE CONTAINER PERMANENTLY MARKED WITH ROD SERIAL AND PURCHASE ORDER (P.O.) NUMBERS.
10. TWO GEOMETRIC PLANES - CONTAINING THE ROD AXIS AND A LINE BOTH PERPENDICULAR TO THIS AXIS AND PARALLEL TO A ROD FACE - EXIST CORRESPONDING TO EACH ROD FACE. THESE TWO PLANES ARE TO INTERSECT AT AN ANGLE OF $0^\circ \pm 3'$.

REVISIONS				
ZONE	LTR	DESCRIPTION	DATE	APPROVED
A		REVISED NOTE 10	6/20/78	
B		WAS $3^\circ 0' \pm 1'$	11/9/74	BY



DASH #	
-1	250 ± .000 DIA -003
-3	197 ± .000 DIA -003

1 FOLDOUT FRAME 1

2 FOLDOUT FRAME 2

P4794

Figure 4-11. Oscillator Laser Rod

QTY REQD	ITEM	PART NUMBER	SYM	DESCRIPTION	CODE IDENT NO	MATERIAL AND SPECIFICATIONS
				← ASSY		
				LIST OF PARTS		
				TOLERANCE UNLESS SPECIFIED	SIGNATURES	DATES
				.XX ± .XX FINISH	DRAWERMAN	2/15/78
				.XXX ± .XX ANGLE	CHECKER	
				MATERIAL	APPROV	2/17/78
				See Note 1	APPROV	2/17/78
				FINISH	APPROV	
				See Notes	APPROV	
				NEXT ASSY USED ON		
				APPLICATION		

INTERNATIONAL LASER SYSTEMS INC. ORLANDO, FLORIDA

TITLE LASER ROD OSCILLATOR

SIZE CODE IDENT NO DRAWING NO REV
C 34860 1015342 B

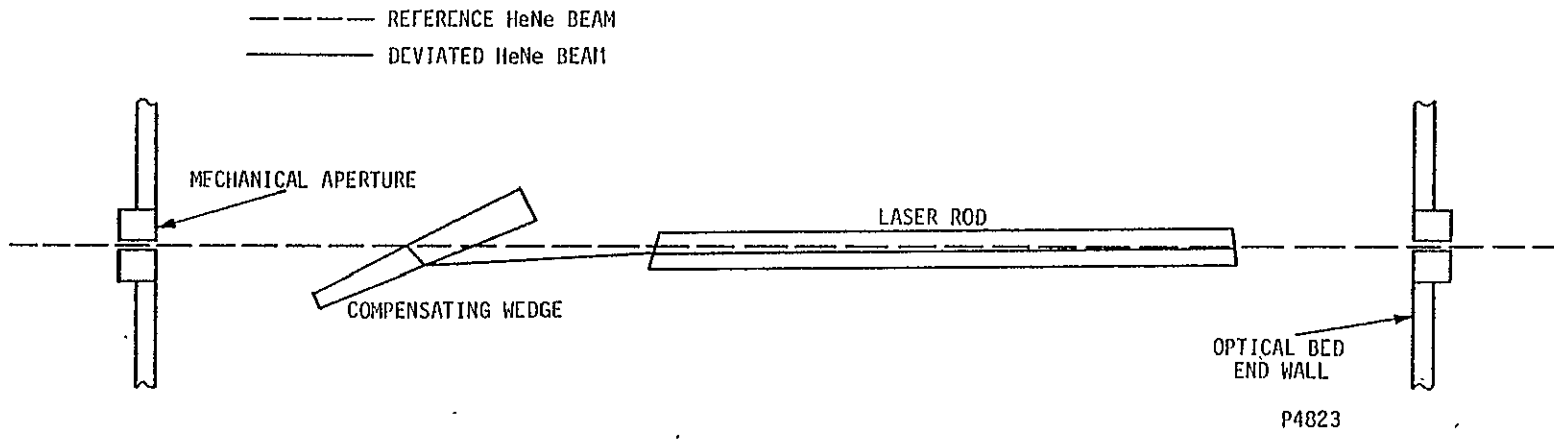


Figure 4-13. Rod-Wedge Leg Alignment

REVISIONS				
ZONE	LTR	DESCRIPTION	DATE	APPROVED
	A	REV NOTE 1	6-20-78	10/3 6-12-78

NOTES:

1. MATL: MATERIAL TO BE KD*P HAVING A DEUTERIATION LEVEL $\approx 98\%$.
2. THE CRYSTAL IS TO BE CLEARLY MARKED TO INDICATE WEDGE END, i.e., SURFACE ②
3. SURFACES ① AND ② SHALL BE POLISHED TO A FLATNESS OF $1/10 \lambda$ AT 0.6328μ , AND A SCRATCH DIG OF (10-5) OR BETTER. (MIL-0-13830).
4. SURFACE ③ OF CYLINDER TO BE ROUGH GROUND WITH SILVER AND .005 THK INDIUM ELECTRODES DEPOSITED ON CROSS HATCHED AREA INDICATED.
5. THE CRYSTAL ELEMENT IS TO EXHIBIT A QUARTER WAVE VOLTAGE AT 1.0641μ OF 3200-3250 VOLTS OR LESS.
6. THE CRYSTAL TO HAVE A DEMONSTRATED EXTINCTION RATIO OF 500:1 AT 0.6328μ . ITS CONTRAST RATIO SHALL NOT VARY MORE THAN $\pm .5\%$ OVER THE CENTRAL (90%) REGION OF THE CRYSTAL FACES.
7. THERE ARE TO BE NO VISIBLE VOIDS, INCLUSIONS, OR DEFECTS IN THE CRYSTAL. EDGE CHIPS NOT TO EXCEED 0.1mm MAX DIA.
8. THE CRYSTAL TO BE CLEARLY MARKED TO INDICATE THE ORIENTATION OF EITHER THE X OR Y AXIS, WHICHEVER LIES IN PLANE OF WEDGE.
9. SURFACE ② WEDGE TO BE IN KZ PLANE OR YZ PLANE OF CRYSTAL AS INDICATED.
10. OPTIC AXIS TO BE $33 \pm 2^\circ$ TO CYLINDER AXIS OF CRYSTAL AXIS AS SHOWN.
11. EACH CRYSTAL TO BE PACKAGED IN A SEPARATE REUSABLE CONTAINER AND PLAINLY MARKED AS FOLLOWS.

WARNING: DELICATE ELECTRO-OPTICAL CRYSTAL
DO NOT OPEN UNTIL CONTAINER HAS REACHED AMBIENT TEMPERATURE
CRYSTAL MATERIAL IS HYGROSCOPIC

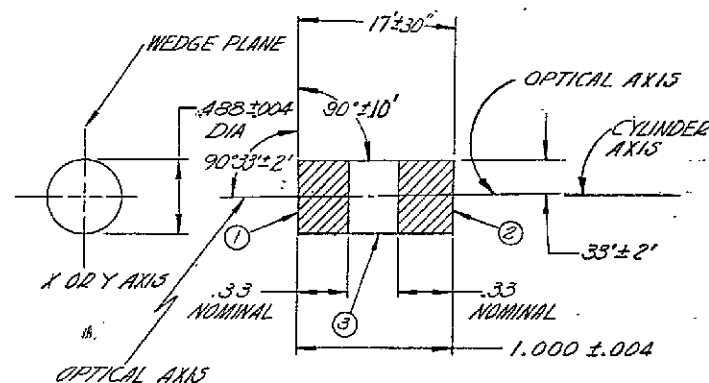


Figure 4-14. KD*P Crystal

QTY REQD	ITEM	PART NUMBER	SYM	DESCRIPTION	CODE IDENT NO	MATERIAL AND SPECIFICATIONS
LIST OF PARTS						
← ASSY				TOLERANCE UNLESS SPECIFIED	SIGNATURES	DATES
				DRAFTSMAN	9/15/76	
				CHECKER		
				MATERIAL		
				SEE NOTE 1		
				FINISH		
				SEE NOTES		
DASH NO	QTY REQD	NEXT ASSY	USED ON	APPLICATION	SIZE	CODE IDENT NO
					C	34860
					DRAWING NO	1015341
					REV	A
					SCALE	2x1
						A-29
					SHEET	1 OF 1

P4784

INTERNATIONAL LASER SYSTEMS INC.
ORLANDO, FLORIDA

TITLE
KD*P
MODULATOR CRYSTAL

SIZE CODE IDENT NO DRAWING NO REV
C 34860 1015341 A

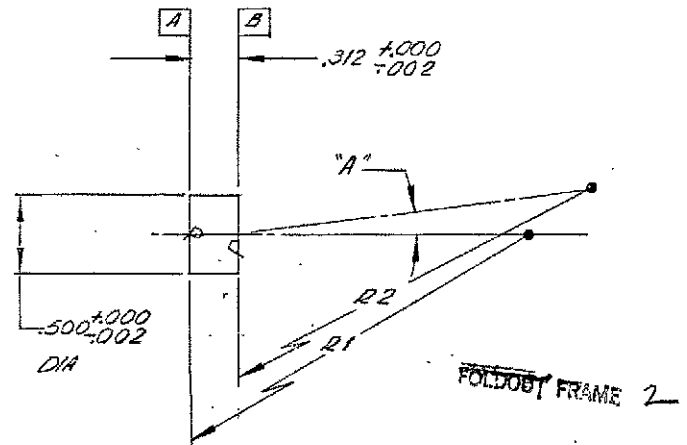
SCALE 2x1 A-29 SHEET 1 OF 1

NOTES:

UNLESS OTHERWISE SPECIFIED MANUFACTURE PER ILIS SPEC 11001772B

1. SURFACE QUALITY: (SCBATCH-DNB) 10-5 ON POLISHED SURFACES.
2. SURFACES A & B TO BE COATED WITH HARD HIGHLY REFLECTING COATING SO THAT:
 - a. REFLECTIVITY = 99.8% AT 1.064μ.
 - b. COATINGS MUST WITHSTAND FIELDS UP TO 10 GW/cm², NOMINAL PULSEWIDTH, 100psec.
 - c. COATINGS PASS DURABILITY TEST PER MIL-C-675 AND MIL-M-1350B.
3. MIDDLE SHALL BE PERMANENTLY MARKED ON ROUGH GROUND SURFACES FOR IDENTIFICATION OF R1, R2, AND WEDGE APEX (WHERE APPLICABLE).

REVISIONS				
ZONE	LTR	DESCRIPTION	DATE	APPROVED
A		ADDED - 15 AND REVISED NOTE - 2, B.		



FOLDOUT FRAME 1

DASH#	R1	R2	"A"
-1	-10.000m	11.352m	0° 0' 0"
-3	-4.000m	5.000m	0° 0' 0"
-5	-2.050m	2.9464m	0° 0' 0"
-7	-10.000m	11.352m	0° 30' 0" ± 2"
-11	-4.000m	5.000m	0° 30' 0" ± 2"
-13	-2.0501m	2.9464m	0° 30' 0" ± 2"
-15	-7.000m	5.000m	0° 0' 0"

QTY REQD	ITEM	PART NUMBER	SYM	DESCRIPTION	CODE IDENT NO	MATERIAL AND SPECIFICATIONS
				← ASSY		
				LIST OF PARTS		
-13	1	1015764	0-739A	TOLERANCE UNLESS SPECIFIED		
-11	1	1015764	0-739A	FINISH		
-7	1	1015764	0-739A	ANGLE 2		
-5	1	1015764	0-739A	MATERIAL		
-3	1	1015764	0-739A	Monasil Quartz		
-1	1	1015764	0-739A	FINISH		
				As Specified		
				← NEXT ASSY		
				USED ON		
				APPLICATION		

SIGNATURES	DATES	TITLE
DESIGNER		
DRAFTSMAN	10-11-76	
CHECKER		
APPROVED	11-1-76	MIRROR
APPROVED	11-3-76	
APPROVED	11-1-76	
APPROVED	11-1-76	

SIZE	CODE IDENT NO	DRAWING NO	REV
C	34860	1015765	

Figure 4-16. Laser Mirror

P4792

DRAWING NO 1015765

A

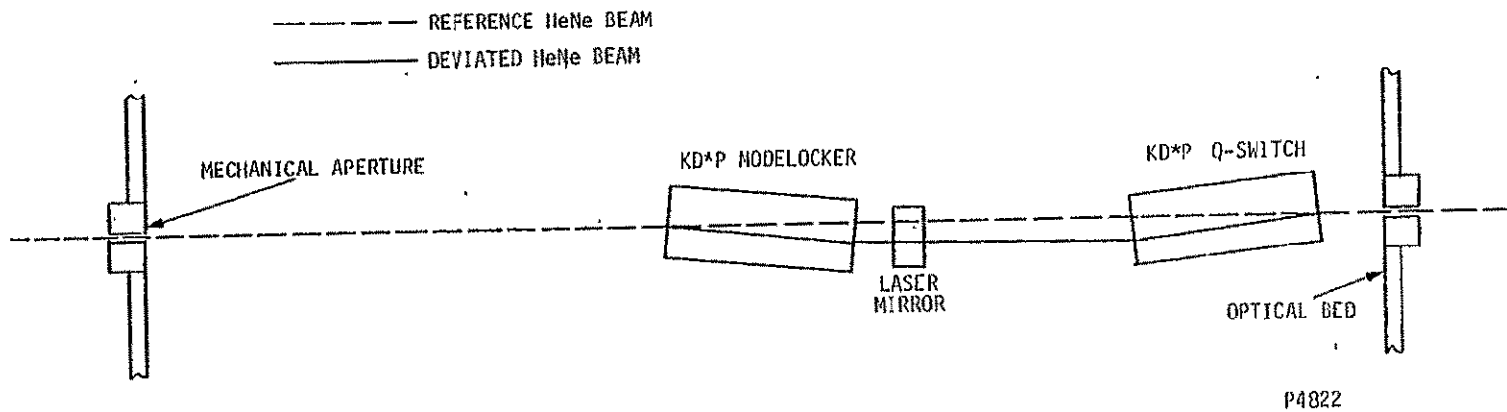
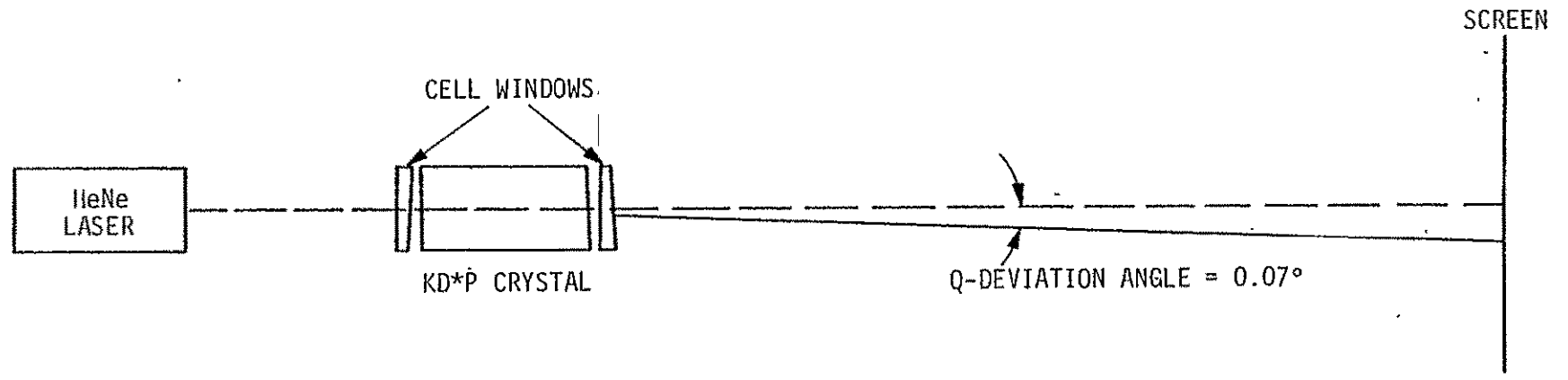


Figure 4-17. KD*P Cell-Mirror Leg Alignment
(Angles Exaggerated for Clarity)

The initial step in this complex alignment procedure is to verify the achievement of the optical specifications of the KD*P cells. The angular deviations of the cell windows and KD*P crystals are first measured. The cells are then assembled and their net angular deviations are measured. The latter measurement setup is illustrated in Figure 4-18. The planned cell deviation was achieved to within 30 arc-seconds for each cell.

The precision alignments of the KD*P crystal axes as discussed above was accomplished using a mechanically referenced He-Ne beam as before. A brief discussion of the electro-optical properties of KD*P crystals is necessary before describing the alignment technique. The application of voltage along the Z-axis or optical axis of KD*P results in the originally uniaxial crystal becoming biaxial. The birefringent axes of the crystal as viewed along the optical axis are 45° to the X- and Y- axes of the crystal. A He-Ne beam polarized parallel to one of these birefringent axes will traverse the KD*P crystal with its polarization unchanged. These observations form the basis of the technique for correctly aligning the optical axes of the KD*P crystals to the reference He-Ne beam.

After establishing the He-Ne beam reference path, a calcite polarizer mechanically referenced to the optical bed is mounted to transmit the polarization plane parallel to the optical bed. The purpose is to establish a reference polarization plane parallel to the oscillator polarizer transmission plane. Two film polarizers mounted in precision rotation assemblies are then placed external to each end of the bed in a sequence that results in these polarizers being crossed with one transmitting the same polarization plane as the reference polarizer. One of these polarizers is then rotated 45° and the other is rotated to null the He-Ne beam. The point of this procedure is that the correct mounting of the KD*P modelocker and Q-switch cells between these polarizers will now introduce zero phase retardation with voltage on or off the crystals. To elaborate, the He-Ne beam remains nulled by the crossed polarizers when the KD*P cells — with voltage applied — are aligned such that one birefringent axis is parallel to a polarization plane 45° to the optical bed plane and the optical axis of the crystals are aligned to the He-Ne reference beam. This corresponds to the correct alignment of the KD*P cells as discussed earlier in this section.



P4826

Figure 4-18. KD*P Cell Deviation Measurement

The specific procedure to align the KD*P cells is now apparent. The mechanical apertures in the optical bed beam exit holes are removed and each cell is sequentially mounted to the optical bed with no voltage applied. A rough alignment of the optical axis of each KD*P crystal is then performed after mounting each cell by placing a lens tissue between the He-Ne beam and cell and centering the resulting isogyre pattern. This pattern is observed by placing a white card behind each cell. The second nulling polarizer is not used in these observations. Following these procedures, each KD*P cell is fine-tweaked to null the He-Ne beam. This results in the alignment of the KD*P crystals optical axes to the reference He-Ne beam. Voltage is then applied in sequence to each crystal which is rotated to once more achieve nulling of the He-Ne beam by the crossed polarizers. These procedures result in the alignment of one of the birefringent axes of each crystal to the polarization plane of the He-Ne beam. Thus, the X- or Y-axis of each crystal is aligned parallel to the optical bed plane as required. A verification of the cancellation of the angular and lateral deviations of the KD*P cells is then made by re-installing the mechanical apertures in the beam exit holes of the optical bed. A positive result of this verification is achieved in practice, but is essentially assured via the verification of the correct fabrication and assembly of each cell discussed earlier. This completes the description of the alignment of the KD*P cells.

The final step of the alignment of the KD*P cell-mirror oscillator leg is to mount the laser mirror bed to the optical bed and to align the mirror so that its He-Ne reflection falls on the He-Ne laser exit aperture. To recapitulate, the above-described procedures resulted in the alignment of the KD*P crystal axes and the laser mirror normal axis precisely referenced to both the optical bed plane and to a He-Ne beam correctly referenced to the planned optical path for this oscillator leg.

5. Mirror-Rod Alignment

The alignment of the laser rod axis and the laser mirror axis should be achieved by simply mounting the TIR prism adjacent to the quartz wedge (See Figure 4-8). This is the result in practice if the TIR prism, rod-wedge leg, and KD*P cell-mirror leg alignments are correctly performed. However, a verification of this result is necessary.

The verification procedure consists of installing the above-mentioned TIR prism; mounting a partially reflective laser mirror external to the bed which is aligned to the oscillator mirror; and establish lasing. The achievement of a round beam pattern for the normal mode radiation generated by tweaking only the external mirror verifies correct mirror-rod alignment. Figure 4-19 illustrates the experimental arrangement for the alignment of the external mirror via a He-Ne laser.

6. Risley Prism-Polarizer Alignment

The rod-wedge and KD*P cell-mirror leg alignments are necessarily performed with the oscillator TIR prisms removed from the bed. The risley prism-polarizer alignment involves two oscillator legs as illustrated in Figure 4-8. The TIR prism adjacent to the compensating wedge remains on the bed to establish the risley prism - polarizer alignment. Figures 4-20 and 4-21 are optical drawings of the polarizer and one risley prism. The two risley prisms are identical and are initially set to yield zero angular optical deviation via an experiment using a He-Ne beam which is performed external to the optical bed. The plane-parallel polarizer produces only a lateral deviation and the pair of prisms are tilted to compensate for this deviation which occurs in a plane parallel to the optical bed.

Figure 4-22 illustrates the risley prism-polarizer alignment. The first step in this alignment after establishing the He-Ne reference path is to mount and orient the dielectric polarizer. The criteria for the proper orientation are that the angle of incidence of the He-Ne beam must be $56 \pm 2^\circ$ and that the polarizer be perpendicular to the optical bed. This orientation is performed by simply adjusting the polarizer so that the He-Ne beam reflection from the polarizer is incident on the inner wall of the optical bed at a pre-calculated point. Adjustment of the risley prism tilt to yield parallelism of the entrance and exit He-Ne beams through the bed completes this alignment.

7. Dynamic Laser Alignment

The preceding alignment procedures result in the alignment of all four legs of the oscillator. The next step is to mount

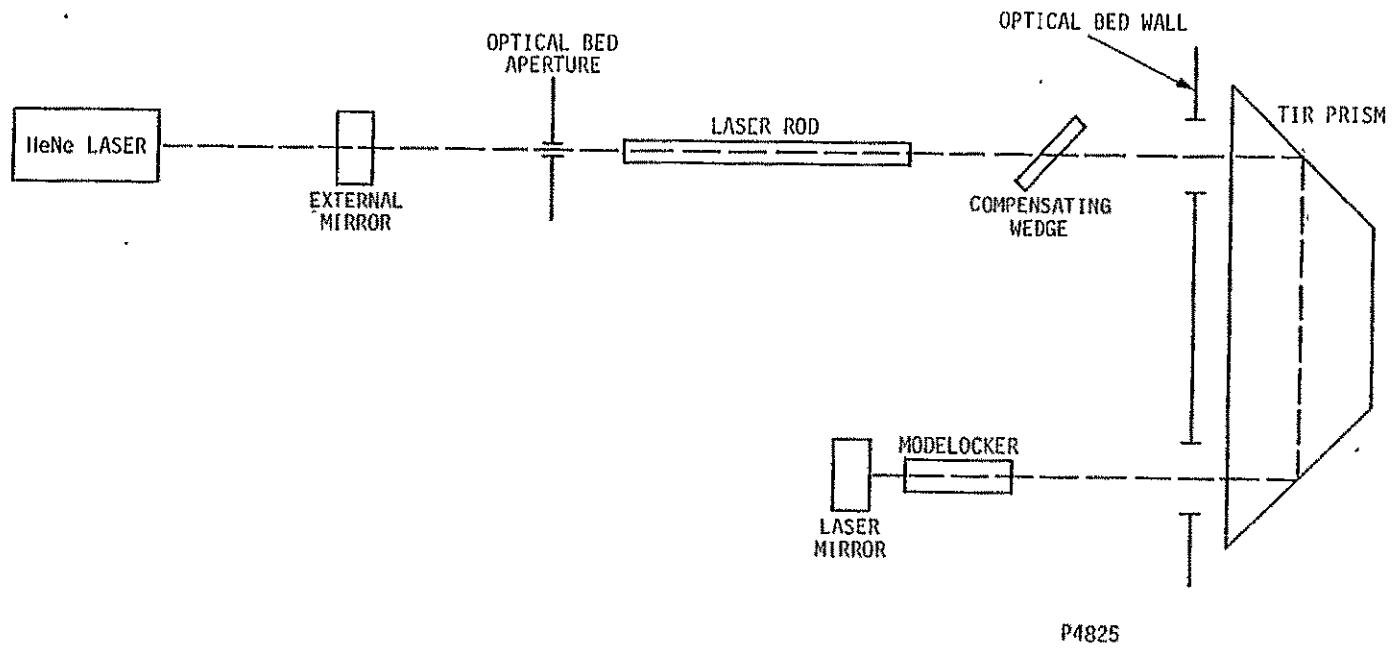
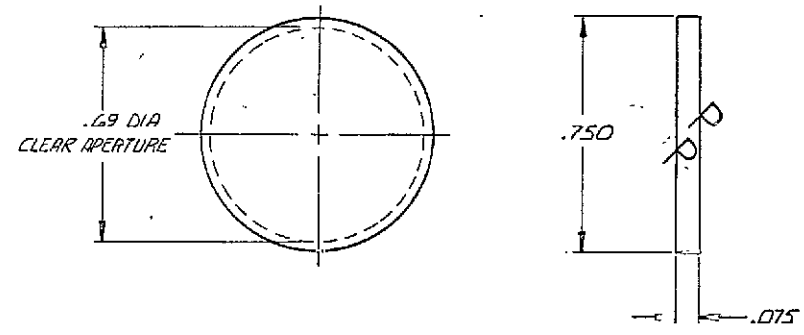


Figure 4-19. Mirror-Rod Alignment Verification

REVISIONS				
ZONE	LTR	DESCRIPTION	DATE	APPROVED

NOTES: UNLESS OTHERWISE SPECIFIED, MANUFACTURE PER ILS SPEC A1010290.

1. SURFACE QUALITY: (SCRATCH-DIG) 10-5 ON POLISHED SURFACES.
 2. POLISHED SURFACES TO BE FLAT WITHIN 1/4 WAVELENGTH OF SODIUM LIGHT AND PARALLEL TO 30 ARC SECONDS.
 3. POLARIZER MUST WITHSTAND FIELDS OF UP TO 10 GW/CM² AT PULSE RATES UP TO 10 PPS AT A PULSEWIDTH OF 100 PSEC. COATING MUST MEET DURABILITY TEST PER MIL-C-675 AND MIL-M-1350B.
- △4 MATERIAL: HOMOSIL QUARTZ
- △5 FINISH: SURFACES MARKED P. POLISH ALL OTHERS FINE GRIND.



FOLDOUT FRAME 1

FOLDOUT FRAME 2

Figure 4-20. Oscillator Polarizer

QTY REQD	ITEM NO.	CODE IDENT NO.	PART OR IDENTIFYING NO.	SPECIFICATION OR DOCUMENT NO.	NOMENCLATURE OR DESCRIPTION	MATERIAL DESCRIPTION						
← ASSEMBLY →												
LIST OF PARTS												
UNLESS OTHERWISE SPECIFIED DIMENSIONS ARE AFTER PLATING AND ARE IN INCHES/MM						REV	REV STATUS OF SHEETS					
						4	3	2	1	MP	PL	SHEET
TOLERANCES						ADDITIONAL APPROVALS		CONF. NO. A/ASIS-22916		INTERNATIONAL LASER SYSTEMS INC. ORLANDO, FLORIDA		
± .01 ± .005 ANGLES ±						FCTN SIGNATURE DATE P. MITCHER 11/16/78		DATE		TITLE POLARIZER		
MATERIAL						DESIGN		CHECK		SIZE CODE IDENT NO DRAWING NO REV C 34860 1022638 -		
FINISH						ENGR		PRGDR		SCALE 4/1 SHEET OF		
PART DASH NO.						DWC				OUTSTANDING NORS <input type="checkbox"/> <input type="checkbox"/> <input type="checkbox"/> 4-37		
NEXT FINAL NEXT ASSY USED ON APPLICATION												
1						G0229						

SIZE DRAWING NO
 C 1022638

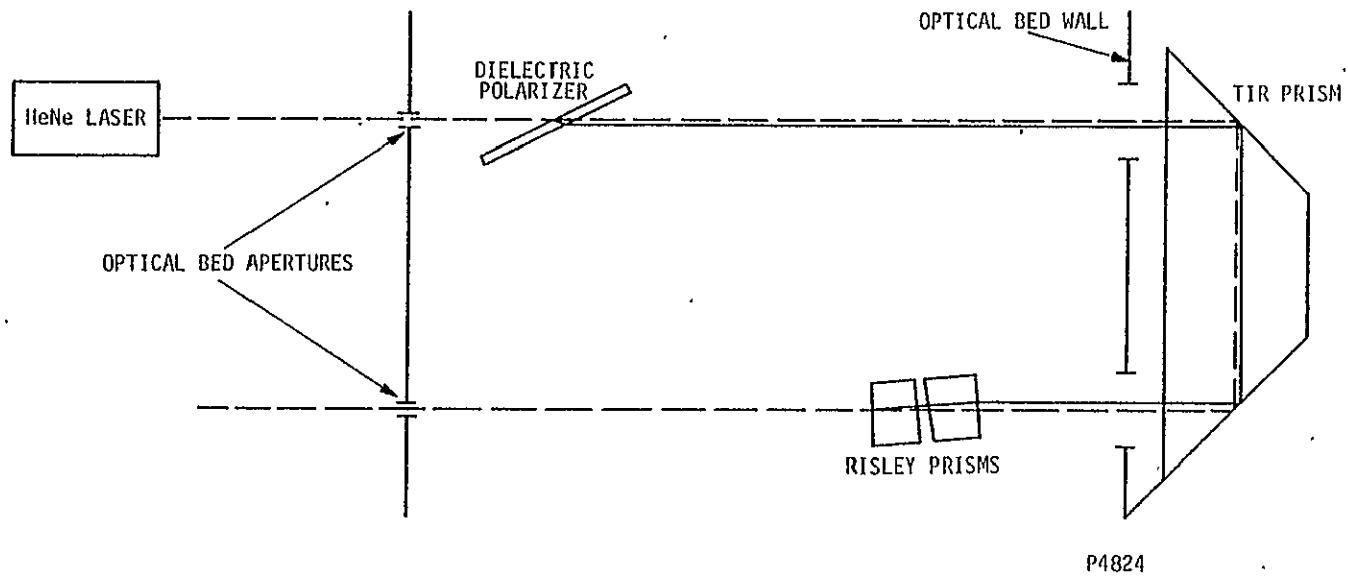


Figure 4-22. Risley Prism-Polarizer Alignment
(TIR Fold shown in orthogonal plane
to actual case for clarity)

the second oscillator TIR prism on the optical bed. The laser is then operated with the modelocker and Q-switch being passive. Slight rotational and/or tilt tweaks of the risley prisms results in low-level lasing which is detected using an infrared viewer. An $\lambda/8$ voltage bias is then applied to the Q-switch so that a laser output is obtained via the polarizer. Further tweaking of the risley prisms leads to energy output optimization via monitoring of the laser output. The following report section covers further dynamic tweaking of the laser to optimize PTM Q-switching and active modelocking.

Appendix E gives all optical drawings for the amplifier subsystem except the KD*P doubler.

C. LASER PERFORMANCE EVALUATION

1. Introduction

The experimental evaluation of the Spaceborne laser system has shown the basic soundness of its concept and design. Extensive testing has been performed on the oscillator subsystem and essential tests have been performed on the amplifier subsystem. The results of the tests show essential agreement with the theoretical predictions given in Section II of this report. The following paragraphs report the results of:

- Normal mode testing;
- PTM Q-switch testing;
- Modelocking tests;
- Amplifier testing

The parameters evaluated in these tests, where appropriate, are pulse energy, beam divergence, laser efficiency, TEM₀₀ beam spot size, pulse amplitude stability, pulsewidth or laser temporal profile, and pre-and post-pulse suppression.

2. Normal Mode Testing

Normal mode testing of the Spaceborne oscillator was performed to verify good pump cavity efficiency and the achievement of optimum oscillator alignment. Figure 4-23 is an input/output curve illustrating the best normal mode performance achieved. Laser output was obtained by placing a dc voltage bias on the Q-switch. This voltage was set to optimize the output coupling to achieve maximum laser energy at the 10-15 mJ level. The low pump threshold of 1.3 Joules and the slope efficiency of 1.25% indicate a high effective reflectivity in the 70-80% R range. Correlation of the normal mode performance observed with previous ILS parametric studies on input/output curves versus reflectivity demonstrate a pump cavity efficiency equivalent to the best results previously obtained at ILS. The normal mode beam patterns obtained were uniform and round which verifies optimum oscillator alignment.

3. PTM Q-switch Testing

PTM Q-switch testing was performed in two operational modes. One of these was to utilize electronically-based timing for both

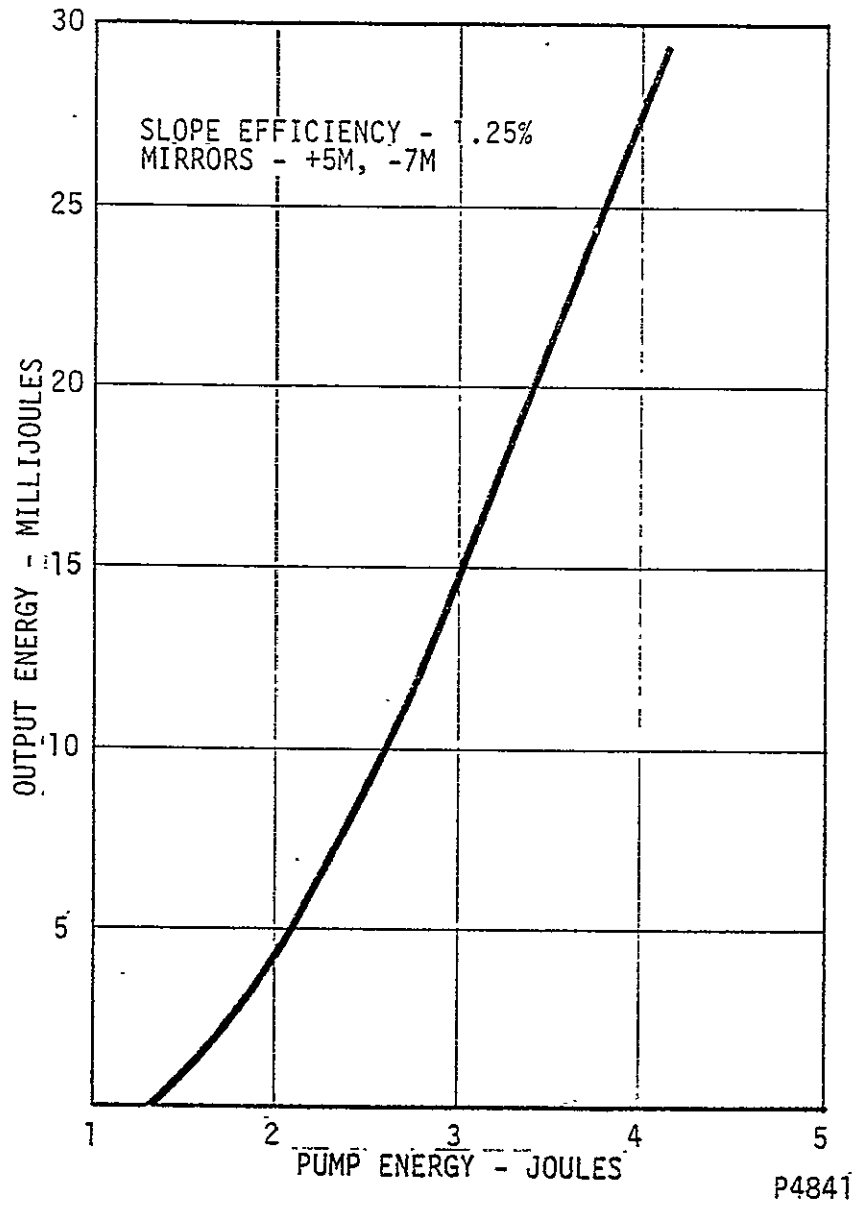


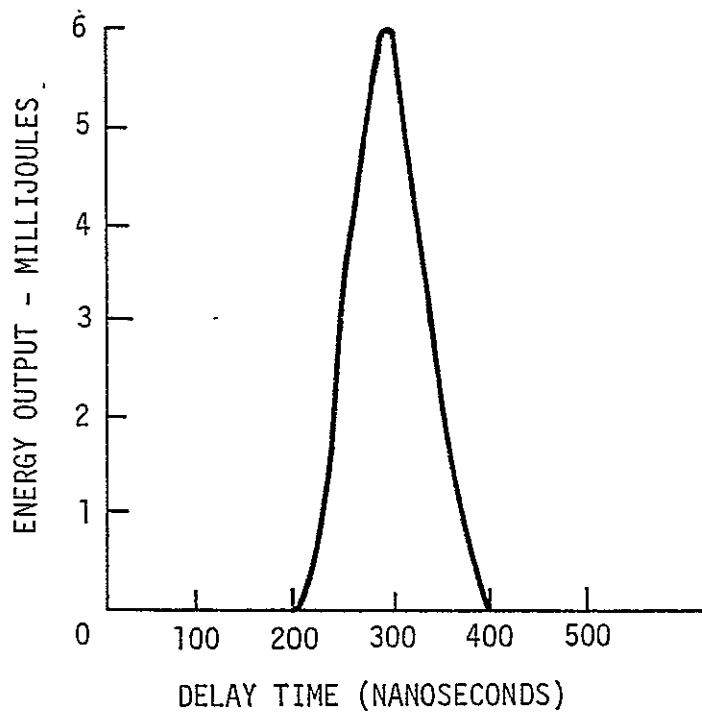
Figure 4-23. Normal Mode Performance Curve

the Q-switch and dump switching operations. This test provided information concerning the sensitivity of the dump synchronization with respect to the time at which the internal resonator radiation achieves its peak. Figure 4-24 illustrates this synchronization sensitivity via a graph of the PTM pulse energy output versus the delay time between the Q-switch and dump events. The energy input/output performance curve for this PTM Q-switching mode is shown in Figure 4-25. This curve shows lower efficiency than the normal mode performance curve due to a non-optimum oscillator alignment.

The second operational mode for PTM Q-switching utilized pre-lase and active synchronization of the Q-switch and dump events via direct lase detection. The specific techniques used to implement these concepts were previously described in the design section of this report. Figure 4-26 shows the energy input/output curves for this operational mode both with and without the 3 millimeter aperture used to achieve TEM₀₀ mode. The TEM₀₀ curve generated correlated well with the theoretical curve shown in Figure 2-5 for a loss/pass value of 50%. This curve was generated previous to the achievement of an optimum oscillator alignment. Later normal mode data (Figure 4-23) indicates a 25% loss/pass value. Figure 4-27 is a photograph of the pulse profile of a typical PTM Q-switched laser pulse.

TEM₀₀ mode operation in the PTM Q-switched mode using pre-lase was verified in two ways. The beam divergence and spot size of the beam was measured and shown to correlate, within experimental error, via the gaussian beam equation. Film burn patterns were also generated which indicate TEM₀₀ mode operation. These burn patterns were made at distances ranging from directly adjacent to the laser to the limit at which the film would burn. The burn patterns increased in diameter and decreased in intensity monotonically with increasing distance from the laser. The patterns also exhibited greatest intensity in the center with a smooth burn intensity decrease with increasing radius. This latter result strongly indicates TEM₀₀ mode operation. Together with the previous correlation of beam divergence and beam spot size, TEM₀₀ mode operation is verified. The above results are summarized in Figure 4-28.

Initial problems were encountered in the achievement of the TEM₀₀ mode. An annular film burn pattern was observed with the initial -10m, +11.35m radii common laser mirror. A second mirror with radii of -7m and +5m was installed and successful TEM₀₀ mode operation was achieved. The measured oscillator spot size⁰⁰ of 2mm (3 ω diameter) did not correspond with a theoretical prediction of 3mm. This phenomena is probably explained by pre-lase effects and a possible radial variation in the oscillator rod optical gain.



P4033

Figure 4-24. PTM Timing Synchronization

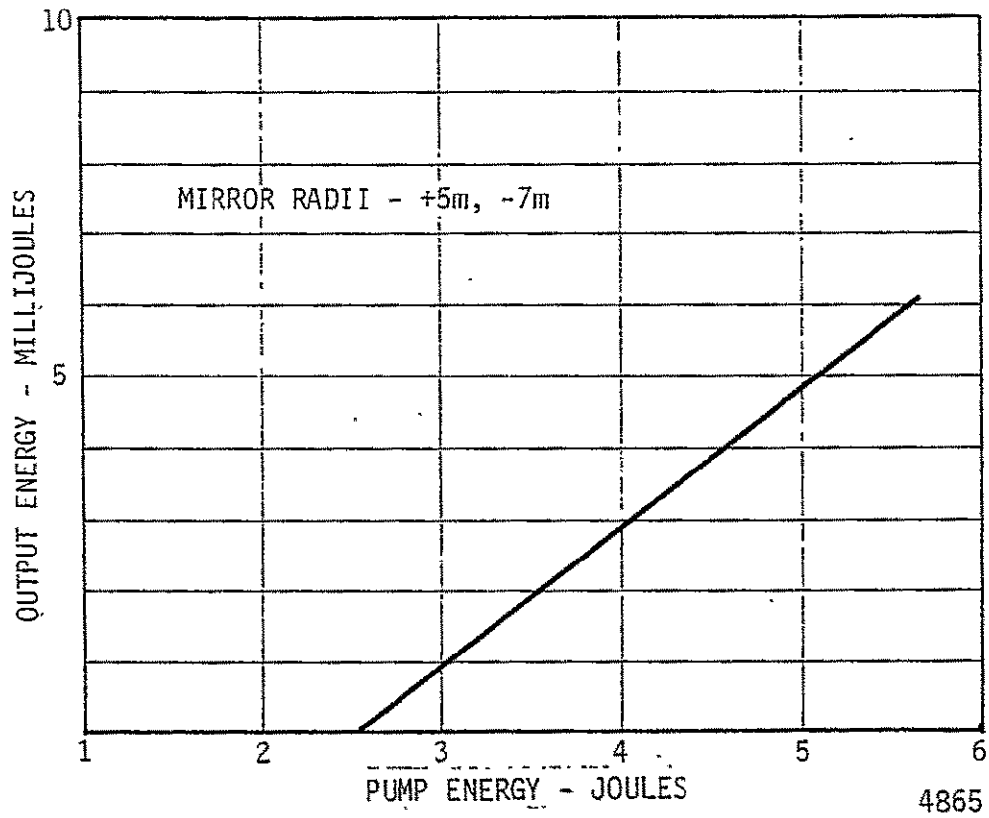


Figure 4-25. PTM Q-Switched Performance Curves
(Electronic Timing)

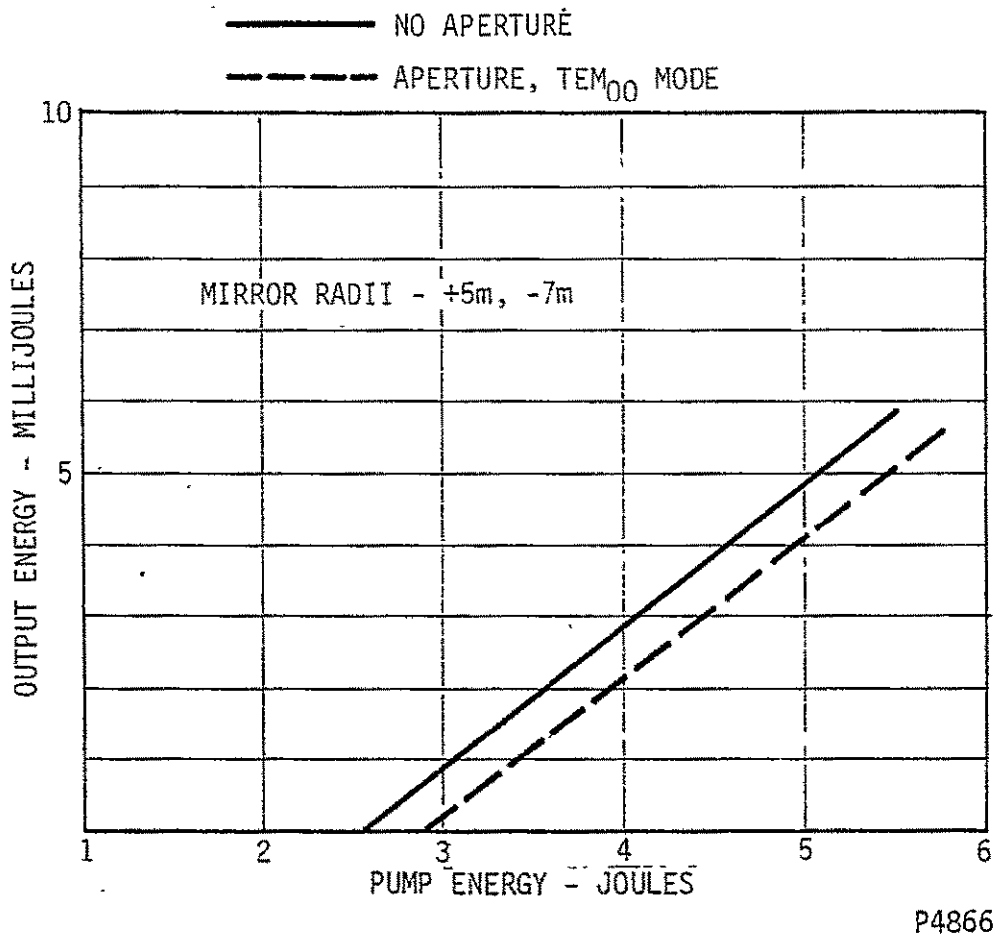
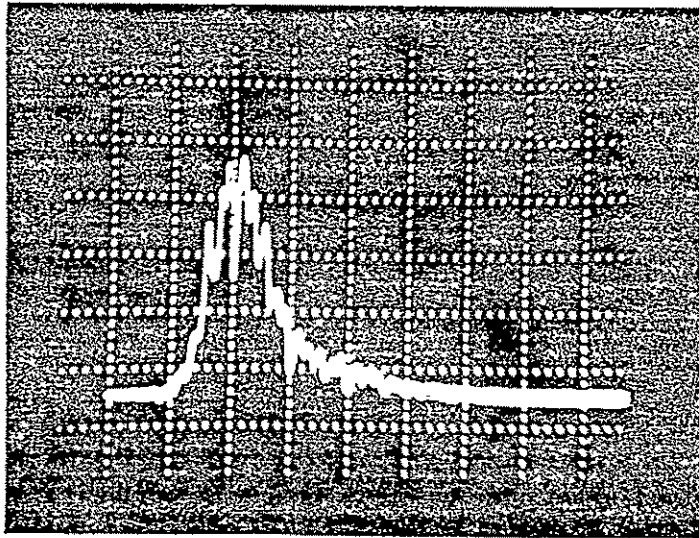


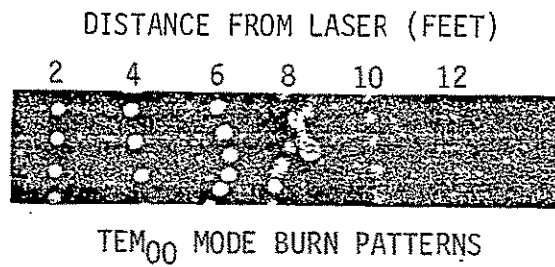
Figure 4-26. PTM Q-Switched Performance Curve
(Pre-lase and Active Timing)



TIME SCALE - 10 NSEC/DIVISION

P4867

Figure 4-27. Typical PTM Q-Switched Pulse



BEAM DIVERGENCE (90 POINTS) = 0.98 mr
 SPOT SIZE (w_0) = 0.64 mm

$$\sigma = \frac{2\lambda}{\pi w_0} = \frac{2(1.064 \times 10^{-9} \text{ mm})}{\pi(0.64 \text{ mm})} = 1.06 \text{ mr}$$

GAUSSIAN BEAM EQUATION CORRELATION

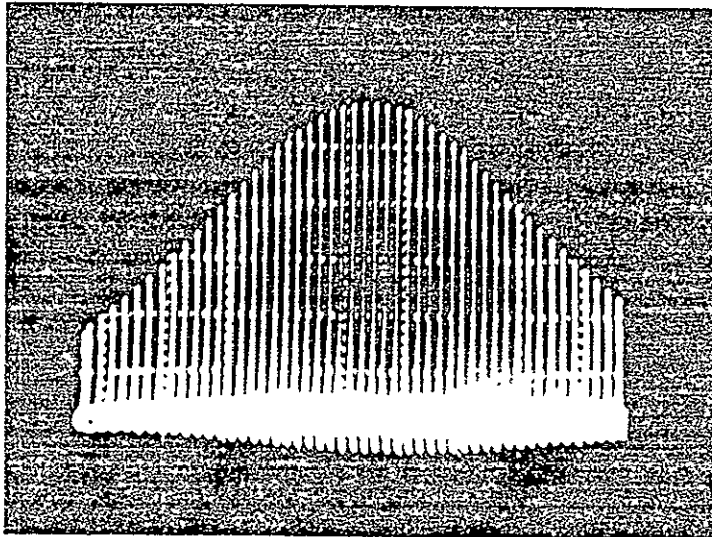
Figure 4-28. TEM₀₀ Mode Verification

4. Modelocking Tests

The objective of the initial modelocking tests was to establish the correct RF modelocking frequency. These tests were performed via normal mode lasing with the modelocker active and a voltage bias applied to the Q-switch to generate a laser output via the polarizer. Initial testing failed to establish stable 100% modulation of the normal mode pulse profile. The problem was traced to an insufficient RF voltage level and was solved by adding an RF amplifier stage to the modelocker RF drive electronics. The design and operation of this RF amplifier is described in Appendix D. Modelocking of the normal mode pulse was then achieved and a photo of the oscilloscope trace of the pulse profile is shown in Figure 4-29. Figure 4-30 is a photo of an expanded trace of this profile. The modelocking RF frequency determined to be near optimum was 52.63 Mhz.

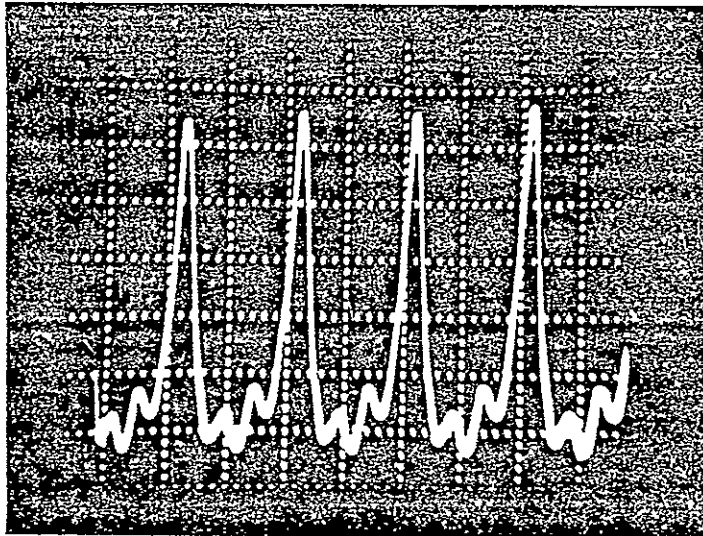
Extensive testing of the Spaceborne laser oscillator was performed for the actively modelocked, PTM Q-switched operational mode using pre-lase. The initial attempts to establish operation in this mode failed due to the unsuccessful attempts to achieve active feedback control of the pre-lase radiation. These efforts are described in the following report section. The actual pre-lase technique successfully implemented is fully described in a previous report section.

Figures 4-31 through 4-34 illustrate some essential results of the modelocking tests performed at ILS. Figure 4-31 is a photo of the oscilloscope trace of the intra-cavity radiation while simultaneously modelocking and PTM Q-switching. This photo indicates optimum single modelocked pulse selection via PTM Q-switching by the complete truncation of the intra-cavity Q-switch pulse profile. Figure 4-32 illustrates a typical oscilloscope trace of the single picosecond pulse emitted from the oscillator. The indicated pulsewidth is 800 picoseconds. However, the response time of the pulse detection equipment utilized was only 0.7 nanoseconds so that the actual pulsewidth is near 400 psec. Figure 4-33 indicates the pre- and post-pulse suppression achieved via the PTM Q-switch pulse selection. Expansion of the amplitude scale of the oscilloscope display showed a pre- and post-pulse suppression of 30 dB. Figure 4-34 illustrates the occurrence of both pre- and



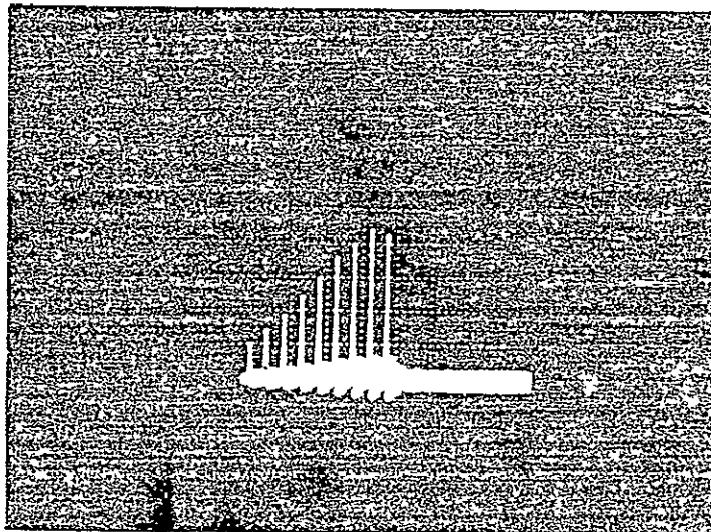
TIME SCALE - 50 NSEC/DIVISION P4870

Figure 4-29. Modelocked Normal Mode Pulse



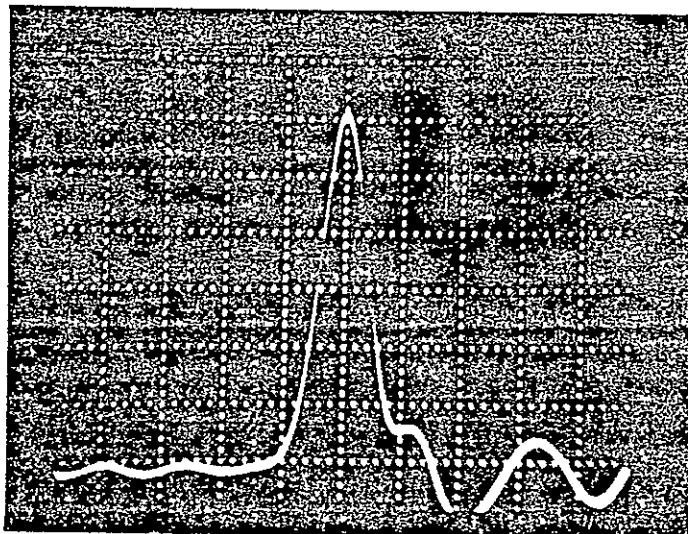
TIME SCALE - 5 NSEC/DIVISION P4869

Figure 4-30. Normal Mode Modelocked Pulses



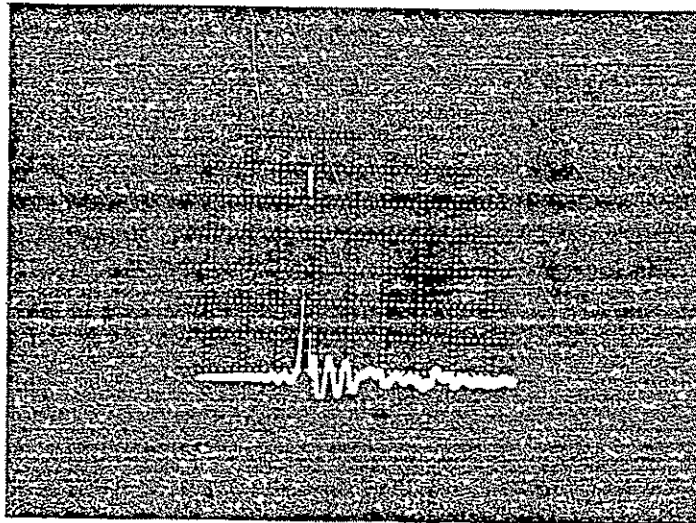
TIME SCALE - 20 NSEC/DIVISION P4871

Figure 4-31. Intracavity Radiation for PTM Q-Switched, Modelocked Operation



TIME SCALE - 1 NSEC/DIVISION P4872

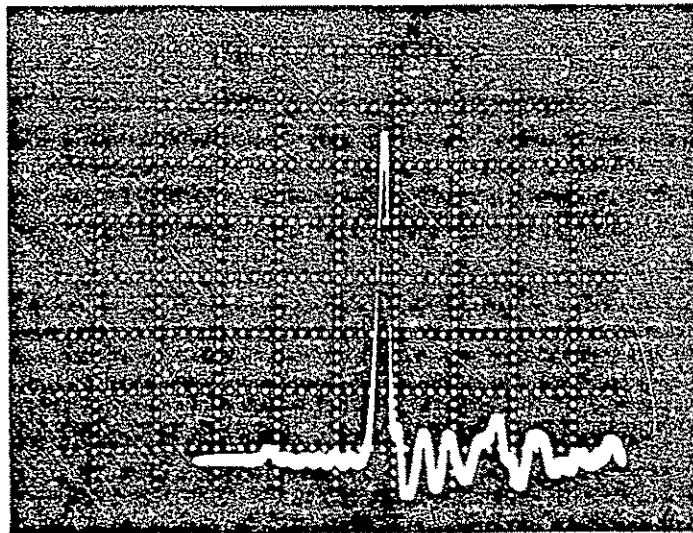
Figure 4-32. Typical Picosecond Pulse (Temporal Resolution - 700 psec)



P4873

TIME SCALE - 5 NSEC/DIVISION

Figure 4-33. Picosecond Pulse Showing Pre- and Post-Pulse Suppression



P4874

TIME SCALE - 5 NSEC/DIVISION

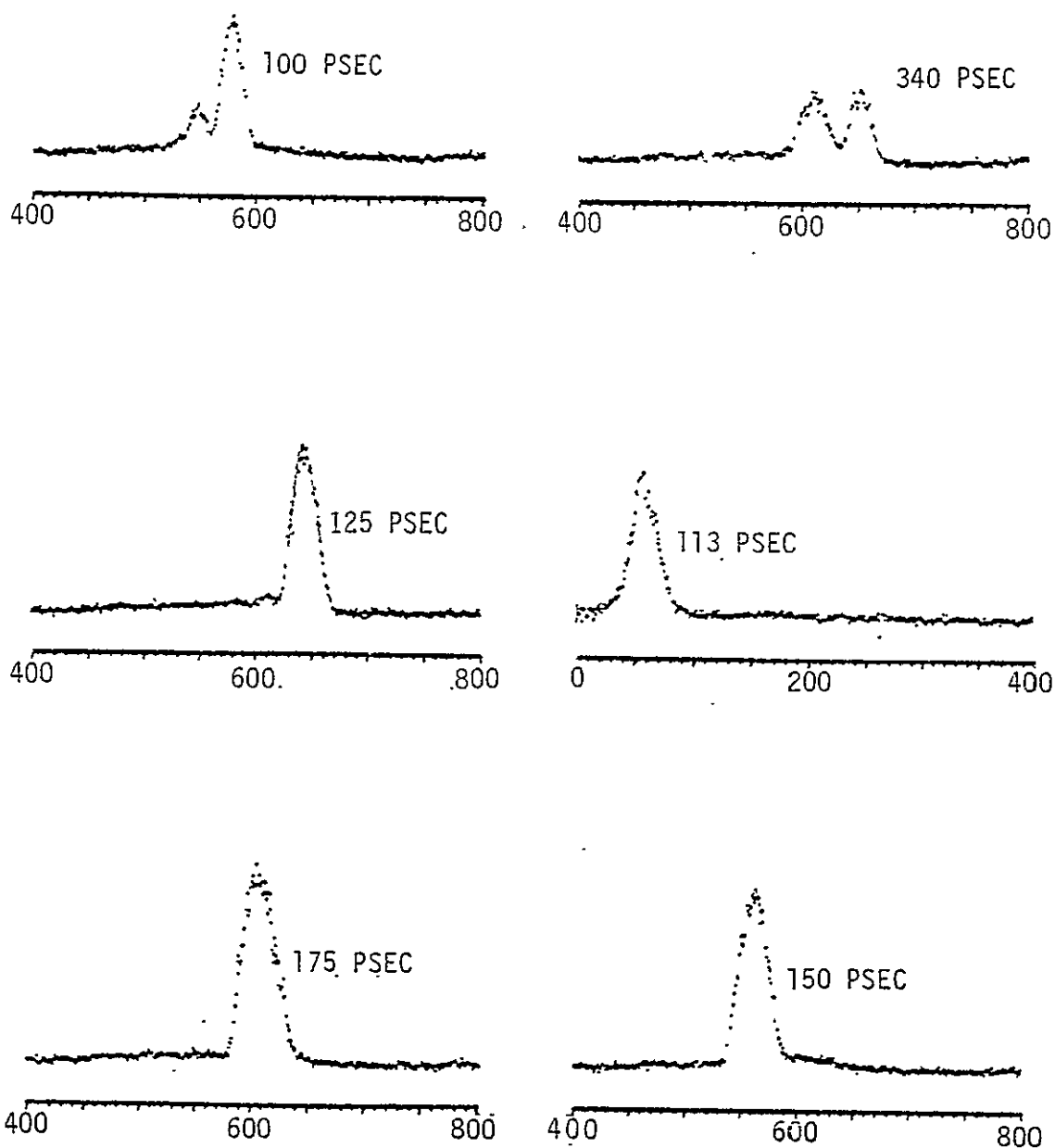
Figure 4-34. Picosecond Pulse Showing Pre- and Post-Pulses

post-pulses approximately 9.5 nsec from the primary pulse. These resulted primarily from non-optimum dump switch phasing. TEM₀₀ mode verification of the modelocked oscillator output was performed as described previously with nearly identical results.

The pulse energies generated via the PTM Q-switched, mode-locked operation of the oscillator were in the 0.5 to 5.0 millijoule range. Laser damage to the oscillator laser rod and one KD*P crystal eventually occurred at approximately the 5.0 mJ level. Testing was resumed following the replacement of these elements and operation was subsequently maintained below 1.0 mJ. Other problems that occurred during experimentation were chronic leakage of the fluid-filled KD*P cells and KD*P modelocker crystal damage due to excessive contact resistance at the crystal electrodes. The first problem necessitated several cycles of refilling and re-aligning the KD*P cells. Careful attention to the O-ring seals at the cell windows and seal port essentially solved this problem. The second problem was solved by a new KD*P crystal electrode which used indium, an extremely malleable metal, to achieve low electrode contact resistance.

Modelocking experimentation at ILS was performed using instrumentation which locked the response time to clearly define modelocking performance. The instrumentation employed consisted of a bi-planar photo-diode, a Tektronix Model 7912 Transient Digitizer, and a Tektronix Model 605 Oscilloscope. This pulse detection system had a temporal response time of 700 psec. Definition of the pulsewidth and pulse profile of the modelocked pulse was essential to determine the efficacy of these pulses for ultra-precision ranging. Thus, a computer-controlled streak camera instrument developed within the Electro-Optics Branch of the NASA Goddard Space Flight Center was employed. The temporal resolution of this instrument was 10 psec.

Following the transfer of the Spaceborne breadboard to NASA, extensive modelocking experimentation was performed. The pulse profile characteristics were observed as a function of the critical theoretical parameters of pre-lase duration, pulse energy, RF modelocker drive amplitude, and RF frequency variations. Figure 4-35 shows four typical pulse profiles obtained for the optimum modelocking achieved. The pulse profile varied from shot-to-shot with 75% single pulses for optimum operation. The optimum modelocking was achieved for minimum pre-lase normal mode amplitude



TYPICAL PULSE PROFILES

P4725

Figure 4-35. Typical Pulse Profiles for Optimum Modelocking
(Time Base: 200 = 1 nsec)

(maximum pre-lase duration) and maximum RF modelocked drive at a RF frequency of 52.676 Mhz. The maximum frequency detuning of the RF drive while maintaining optimum performance was observed to be 500 Hz. Theory predicts and the experimentation confirmed that the modelocked pulse increases in width with decreasing pre-lase duration on RF drive amplitude. The pulse energy level was observed to have little effect on pulsewidth as expected via theoretical analysis presented in this report. Table 4-1. summarizes the experimental results for the Spaceborne modelocked oscillator. The variation of the pulse profiles observed from pulse-to-pulse was impossible to eliminate in the experimentation performed. The cause of these fluctuations is explained theoretically via the variation of modelocked pulsewidth with pre-lase duration and the statistical characteristics of the initial intra-cavity radiation.³¹ The pre-lase duration (the normal mode pulse buildup time) fluctuates from pulse-to-pulse due to fluctuations in the normal mode pre-lase pulse amplitude. The latter fluctuations are caused by very small flashlamp-rod coupling efficiency variations from pulse-to-pulse. The above observations demonstrate that the Spaceborne laser operates as theoretically planned.

Table 4-1.

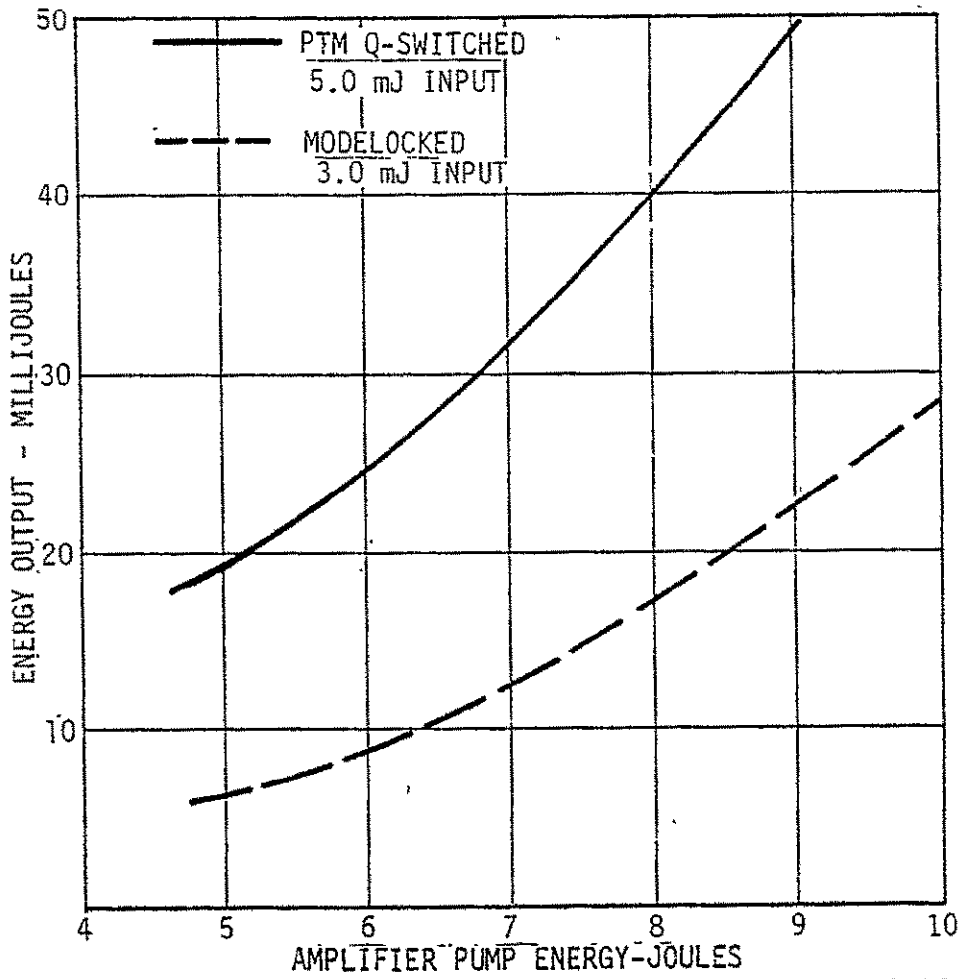
OSCILLATOR PERFORMANCE

Parameter	Value
Pulse Energy	1.0 mJ
Efficiency	0.05%
Pulsewidth	150 psec (FWHM)
Beam Divergence	0.98 mr
Mode Diameter (3 ω)	1.92 mm
Pulse Rate	10 pps
Pre- and Post-Pulse Suppression	30 dB
Pulse Amplitude Stability	\pm 10%

However, the pulse profiles fluctuations caused by the statistics of the initial intra-cavity radiation was not foreseen. A computer evaluation of the suitability of the present pulses generated by the Spaceborne breadboard is in progress. However, an approach to eliminating pulsewidth and pulse profile fluctuations is planned. This approach, defined in the Theory section of this report, is to utilize a quasi-CW, pulsed flashlamp power supply to extend the pre-lase duration to 150 μ sec. Normal moding of the pre-lase radiation will damp out with this pre-lase duration and the achievement of stable pulse profiles from pulse-to-pulse should be achieved. The feasibility of this pre-lase technique has been demonstrated with the SHIVA modelocked oscillator at Lawrence Livermore Laboratories.³²

5. Amplifier Testing

The amplifier subsystem testing established the pulse energy output levels possible with the double-pass Nd:YAG amplifier for both PTM Q-switched and modelocked pulse inputs. Figure 4-36 illustrates the optimum performance achieved. All amplifier testing was performed at ILS. The maximum modelocked pulse energy achieved was 28-mJ with an approximate pulsewidth of 300 psec. Pre- and post-pulse suppression following the amplifier was measured to be 25 dB. The beam divergence measured for the optimized oscillator/amplifier system was 1.0 mr.



P4726

DOUBLE-PASS AMPLIFIER PERFORMANCE

Figure 4-36. Oscillator/Amplifier Performance

C-3

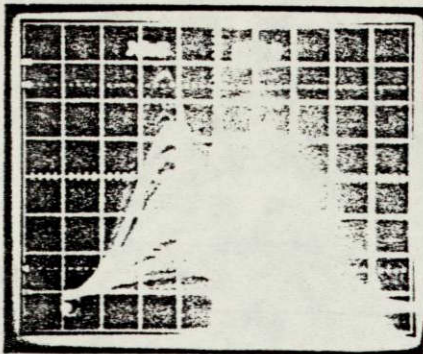
D. RADIATION CONTROL EVALUATION

This report section describes the attempts to achieve a feedback control of the normal mode pre-lase energy as discussed earlier. The basic approach was an energy control servo mechanism utilized to increase the Pockels cell voltage toward the holdoff value as the cavity energy rises. This negative feedback system was chosen to be linear, in order that the maximum energy stability might be achieved. Negative feedback affects the normal mode output pulse width by reducing the pulse amplitude and increasing the pulse width. It is reasonable to expect that a reduced detection threshold, or increased sensitivity, will result in a greater temporal stretching of the pulse. The pulse stretching technique has been successfully employed in the past^{33, 34}.

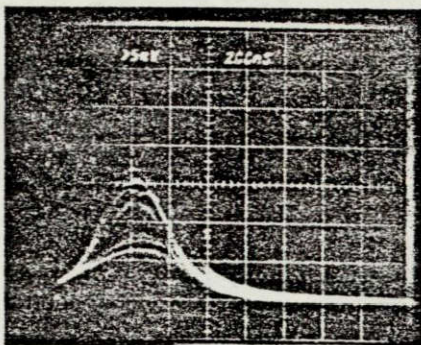
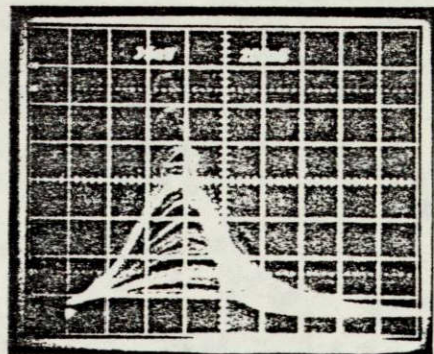
Investigations have shown that low values of reflectivity, and therefore low cavity gain, normal mode spiking occurs as a relatively broad pulse which tends to have rather poor temporal stability and poor amplitude stability. Normal mode spike separation was in the region of 2 to 6 μ sec.

Figure 4-37 illustrates Oscilloscope Trace Photographs (OTP) which were taken from normal mode output. Three series of OTPs are presented. The first OTPs show the laser action when the KD*P Pockels cell voltage was adjusted 340 V below the holdoff value of 3,250 V or a bias voltage of 2,910 V. The second set of OTPs illustrate the output when the bias voltage was adjusted to 2,850 V, a departure of 400 V below holdoff. The third set of OTPs illustrate the output when the bias voltage was adjusted to 2,800 V, a departure of 450 V below holdoff.

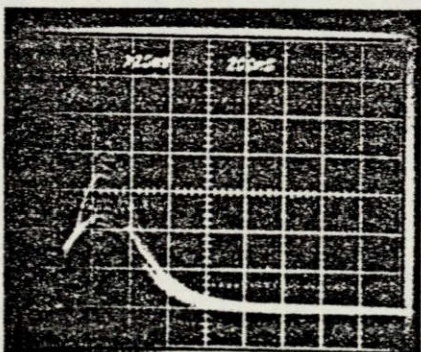
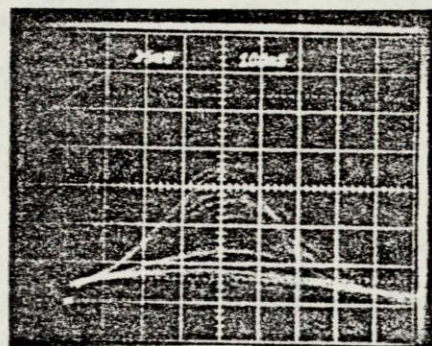
It is significant to note that these sets of OTPs were taken while using the external synchronization feature of the oscilloscope; therefore, the temporal jitter characteristics are excluded, in the interest of clarity of the photographs. Additionally, the combined energy of all normal mode spikes grouped was equivalent to the microjoule regime.



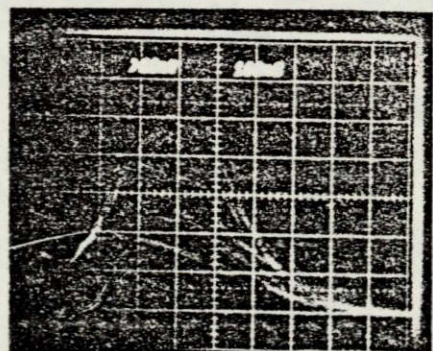
Series 1



Series 2



Series 3



F804-4

Figure 4-37. Normal Mode Single Pulse Profile

The OTPs disclose several pertinent characteristics:

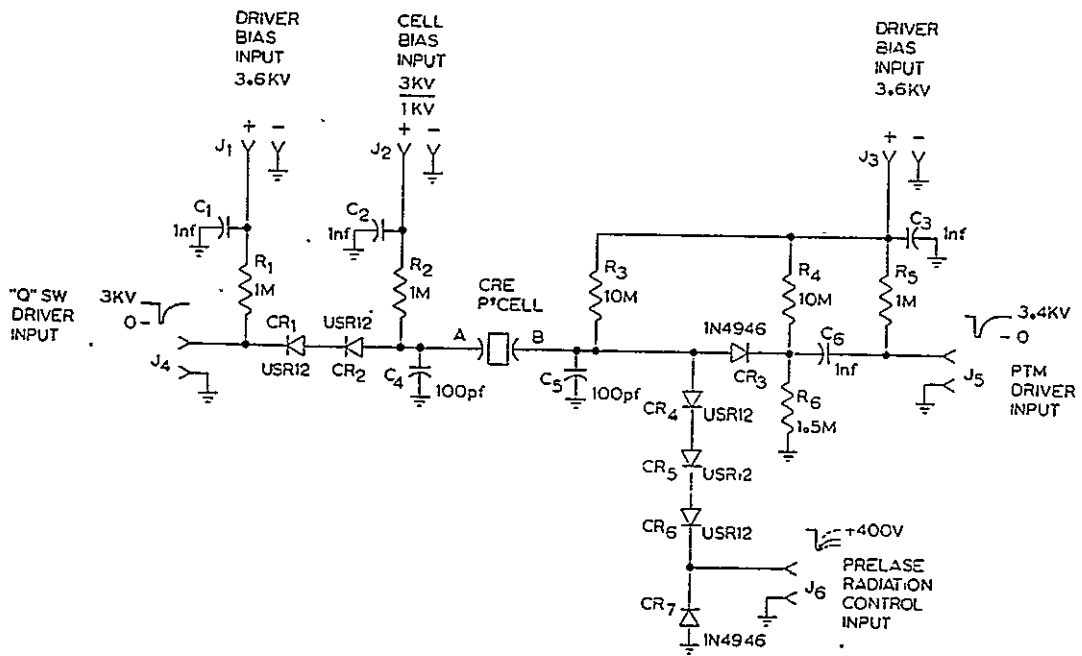
- The average normal mode spike half power pulse width is ≈ 400 nsec.
- The average normal mode spike pulse rise time is ≈ 400 nsec, as measured from the 10% to 90% points; and
- The pulse is essentially gaussian in shape.

Several conclusions concerning the energy control servo requirements may be drawn from these characteristics.

- The prelude may be obtained when the Pockels cell voltage is reduced less than 400 V; thus, a 400-V control range is adequate to achieve holdoff and cause laser action to cease;
- The laser action initial buildup is quite slow (i.e., the energy increase per unit time exhibits a low-slope near the leading edge). Therefore, provided that adequate sensitivity is achieved within the energy control servo, the Pockels cell voltage slew rate need never become excessive; and
- The energy control servo must exhibit good low-frequency response - ideally the response should be near dc, since the initial pulse width of ~ 400 nsec indicates a stretched pulse width of well into the microseconds is to be achieved.

These conclusions led to the hardware implementation depicted in Figure 4-38 and Figure 4-39, the Pockels cell interface, and the energy (i.e. radiation) control electronics respectively. The hardware was constructed and tested as a subsystem. The performance was considered to be satisfactory. The prime characteristics observed were:

- The frequency response of the detector and preamplifier was observed to be flat from 200 KHz to ~ 400 MHz;
- The attack time of the 400-V output driver was observed to require ~ 50 nsec when loaded into the Pockels cell interface;
- The output-driver voltage-level was observed to be linear relative to input irradiance;
- The output-driver voltage-level was observed to track pulsating input to the preamplifier, to achieve a mean-level as required, when the mode structure input change over occurs; and
- The output-driver voltage slew of 400 V was observed to occur for irradiance input of less than $10 \mu\text{W}$.



D1018736

Figure 4-38. Q-switch Interface Schematic

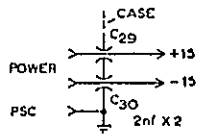
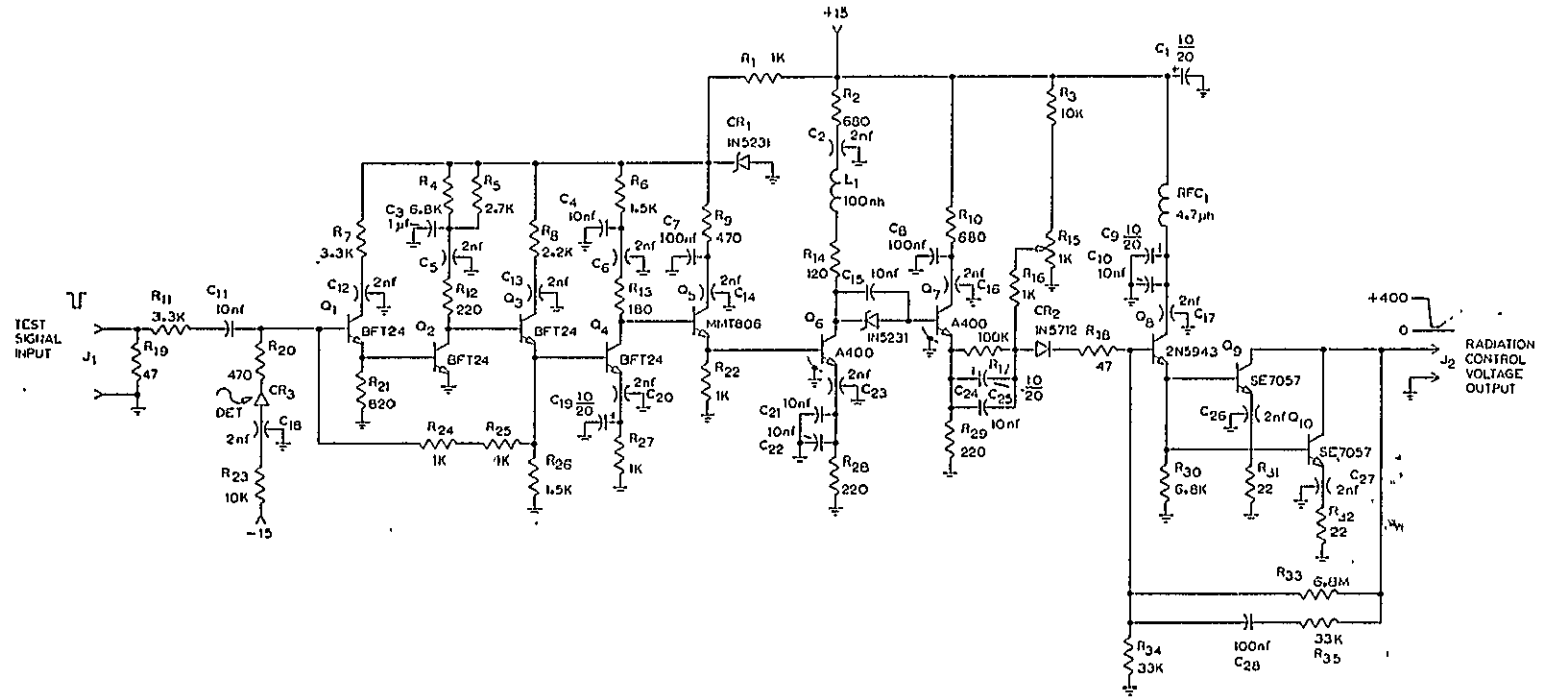


Figure 4-39. Radiation Control Schematic

D1018738

Based upon the subsystem tests, the energy control electronics assembly was integrated to the laser system. The Pockels cell voltage was reduced to 2,950 V to achieve pre-lase action. Little or no observable change occurred to the pre-lase normal mode spike. Careful investigation revealed that:

- The threshold is quite high - in other words the lase action is well developed before the control electronics responds;
- The driver output-voltage essentially follows the response curve of the pre-lase pulse; however, at this high radiation level within the resonator, insufficient control voltage range is available to the Pockels cell. Thus, the control driver saturates; and
- The control-driver output lags the energy-input change by some 55 to 60 nsec during the control trial period. This tends to indicate that about 20 nsec of response time is inherent within the control loop.

Of the observed integration performance, the most significant shortcoming is the lack of sensitivity. The through-put or response time is considered to be the second significant problem area.

The first problem was attacked by reducing the losses of the interfaces of the fiber optical bundle which transmits lase energy leaked through the oscillator polarizer to the detector circuit. Experimentation with the radiation control electronics revealed that the majority of the through-put delay occurs within the post amplifier or the driver portion of this circuit. This circuit was revised and fabricated as shown in Figure 4-40. Both bipolar transistors and VMOS devices are utilized within the circuit design.

Experimentation with the revised radiation control unit integrated to the laser system gave results that were unsuccessful as described for the initial design. The essential problems identified were insufficient input radiation to the control circuit and a too slow recovery time for the electronic post-amplifier. Experimentation with this concept was terminated and the pre-lase technique described earlier in this report was employed.

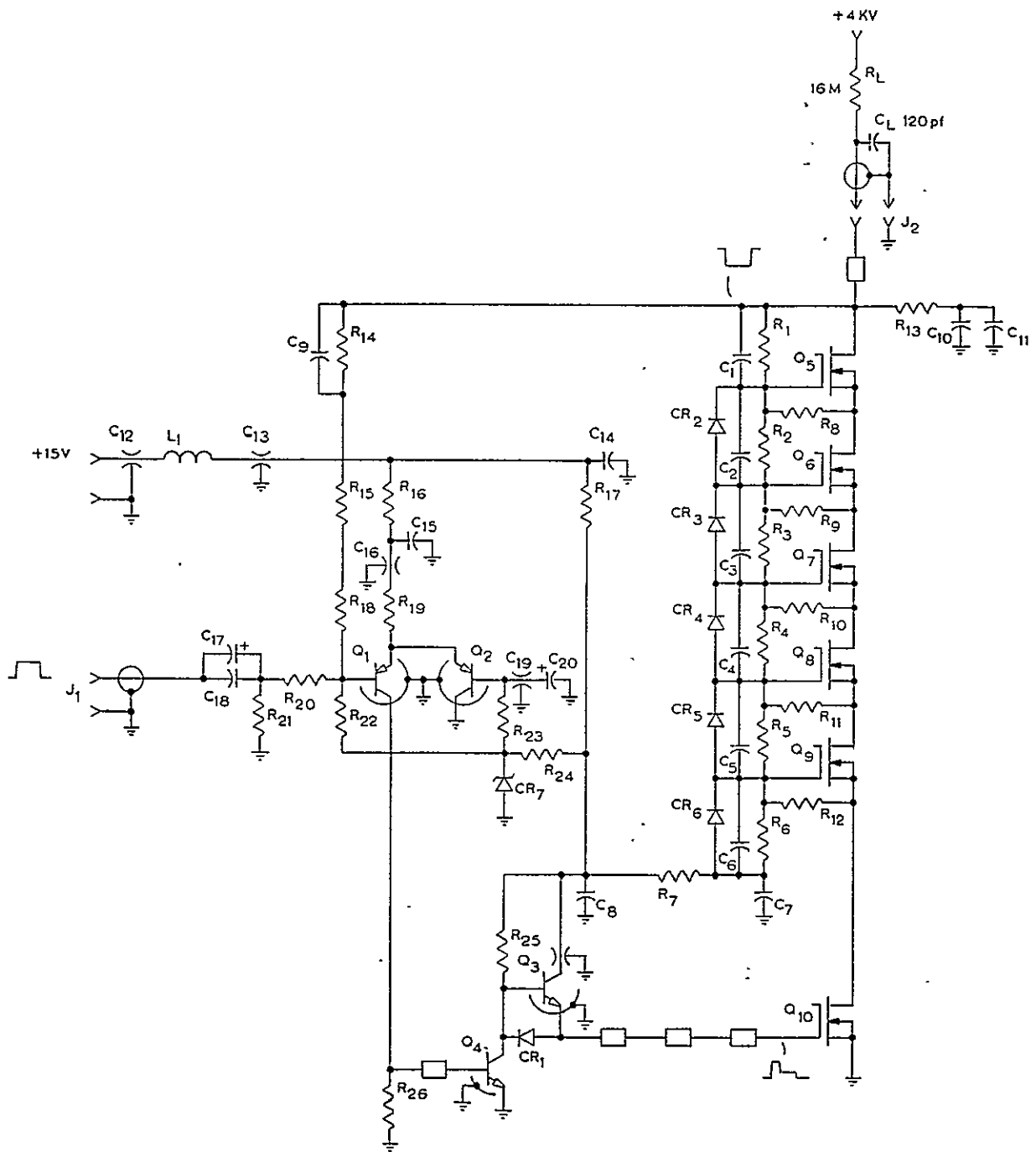


Figure 4-40. Radiation Control Schematic - Revised

Section V

CONCLUSIONS AND RECOMMENDATIONS

The Nd:YAG laser system developed by ILS for the Spaceborne Laser Ranging System has been shown to satisfy the essential objectives of Contract NAS5-22916. The engineering breadboard constructed proved the feasibility of the pulsed, actively modelocked, PTM Q-switched Nd:YAG laser concept for the generation of subnanosecond pulses suitable for ultra-precision ranging. The specific technical accomplishment was the generation of single 150 psec, 20-mJ pulses at 10 pps at a wavelength of 1.064 micrometers with 25 dB suppression of pre- and post-pulses.

The significant hardware implementations within the engineering breadboard were the rugged crossed TIR prism, Invar optical bed subsystem, the pulsed electro-optical KD*P modelocker, and the pre-lase and switching synchronization control circuits. The success of these subsystems establishes the engineering breadboard as the actual foundation for the planned engineering prototype development.

The reconfiguration and improvement of the existing breadboard into a prototype unit suitable for its planned use on the Spacelab Geodynamics Ranging System consists of the following tasks:

- Repackaging of the system into the following subsystems: control unit, power supply, laser transmitter, and cooling system;
- Implementation of a Quasi-CW power supply to stabilize and extend pre-lase and thus achieve stable pulse profiles;
- Temperature control of the transmitter to eliminate all operational temperature sensitivity;
- Reconfiguration of the cooling system to use liquid-to-liquid heat exchanger;
- Reconfiguration of all electronics for 28 V-dc prime power; and
- Extension of experimentation to identify and correct any existing problems related to overall system long-term stability and to perform frequency-doubling.

The engineering prototype developed in accordance with the above outlined tasks will be a reliable, rugged, compact, subnanosecond pulse laser system with extensive applications for space-based ultra-precision laser ranging systems.

REFERENCES

1. W. G. Wagner and B. A. Lengyel, "Evolution of the Giant Pulse in a Laser," J. of Appl. Phys., 34, No. 7 (July 1963).
2. J. A. Koningstein and J. E. Geusic, "Energy Levels and Crystal Field Calculations of Neodymium in Yttrium Aluminum Garnet," Phys. Rev., 136, 3A (Nov. 1964).
3. M. J. Weber and M. Bass, "Research and Development of Yttrium Aluminate Laser," AFML Technical Report TR-72-32, (June 1972).
4. G. A. Slack, et al, "Optical Absorption of $Y_3Al_5O_{12}$ from 10 - to 55000 cm^{-1} Wave Numbers," Phys. Rev., 177, no. 3, (15 Jan. 1969).
5. C. C. Wang "Optical Giant Pulses from a Q-Switched Laser," Proceedings of the IEEE, (1963).
6. D. J. Kuizenga and A. E. Siegman, "FM and AM Mode Locking of the Homogeneous Laser - Part I: Theory and Part II: Experiment," IEEE J. of Quant. Elect. QE-6, (1970).
7. D. J. Kuizenga, et al, "Simultaneous Q-Switching and Mode Locking in the CW Nd:YAG Laser," Optics Comm. 9, (1973).
8. L. M. Frantz and J. S. Nodvick, "Theory of Pulse Propagation in a Laser Amplifier," Journal of Applied Physics, Vol. 34, No. 8, (August 1963).
9. R. C. Eckhardt, "Self-Focusing in Mode-Locked Neodymium: Glass Laser Oscillators," IEEE J. of Quant. Elect. QE-10
10. J. H. Marburger, Prog. Quantum Electronics, 4, 35 (1975).
11. A. J. Glass, "Refractive Index Nonlinearity," LLL Laser Program Annual Report, 1974, p. 256.
12. D. Milam and M. J. Weber, J. Appl. Phys., 47, 2497 (1976).

13. A. N. Zherikhin, et al, "Sov. J. of Quant. Electron. 4, No. 2, (August 1974).
14. R. Wilbrandt and H. Weber, "Fluctuations in Mode-Locking Threshold Due to Statistics of Spontaneous Emission," IEEE J. of Quant. Electron. QE-11, No. 5, (May 1975).
15. Lawrence Livermore Laboratory Laser Program Annual Report - 1974, p. 165, 166.
16. W. D. Fountain, private communication
16. H. Kogelnik, "Imaging of Optical Modes - Resonator with Internal Lenses," The Bell System Technical Journal XLIV, No. 3 (March 1965).
17. D. R. Whitehouse, "Mode Control Technology for High Performance Solid State Laser," Technical Report ECOM-0269-F (Nov. 1973).
18. J. D. Foster and L. M. Osterink, "Thermal Effects in a Nd:YAG Laser," J. of Appl. Phys. 41, No. 9 (August 1970).
19. Harshaw Chemical, private communication
20. J. T. Milek and M. Neuberger, "Linear Electrooptical Modular Materials," Handbook of Electronic Materials, Vol. 8, (1972)
21. L. L. Steinmetz, et al, "Cylindrical Ring - Electrode KD*P Electrooptics Modulator," Applied Optics 12, No. 7, (July 1973).
22. McDonnell Douglas Modulator Report.
23. Cleveland Crystals, private communication.
24. K. Kamiryo, et al, "Optimum Design of Elliptical Pumping Chambers for Solid Lasers," Jap. J. of Appl. Phys. 5, No. 12, (Dec. 1966).
25. D. Roess, "Exfocal Pumping of Optical Masers in Elliptical Mirrors," Applied Optics 3, No. 2, (Feb. 1964).

26. D. Lekete, "Effect of Multiple Reflections on the Design of an Elliptic Cavity for Solid State Lasers," Applied Optics 5, No. 4, (April 1966).
27. C. Bowness, "On the Efficiency of Single and Multiple Elliptical Laser Cavities," Applied Optics 4, No. 1, (Jan. 1965).
28. H. U. Leuenberger and G. Herziger, "Optical Pump System for Mode-Controlled Laser Operations," Applied Optics 14, No. 5, (May 1975).
29. Reference Data for Radio Engineers, ITT (1970).
30. L. Noble, et al, "Optical Pumps for Lasers," Technical Report ECOM-0239-F, (Oct. 1973).
31. Fleck, J. A., "Evolution of a Q-Switched Laser Pulse from Noise," Applied Physics Letters 13 365, 1968.
32. Lawrence Livermore Laboratory Laser Program Annual Report - 1975.
33. R. V. Lovberg et al, "Pulse Stretching and Shape Control by Compound Feedback in a Q-Switched Ruby Laser," IEEE J. of Quant. Elec. QE-11, No. 1, (Jan. 1975).
34. D. C. Hanna, et al, "Single Longitudinal Mode Selection of High Power Actively Q-Switched Lasers," Opto-Electronics 4, (1972), 249-256.

Appendix A

SPACEBORNE ELECTRONIC DESCRIPTIONS

1. Flashlamp High-Voltage Supplies

Each flashlamp high-voltage supply is composed of four circuit assemblies. These assemblies are:

- The low voltage regulator and driver;
- The power converter module;
- The high voltage assembly module; and
- The high voltage regulator circuitry.

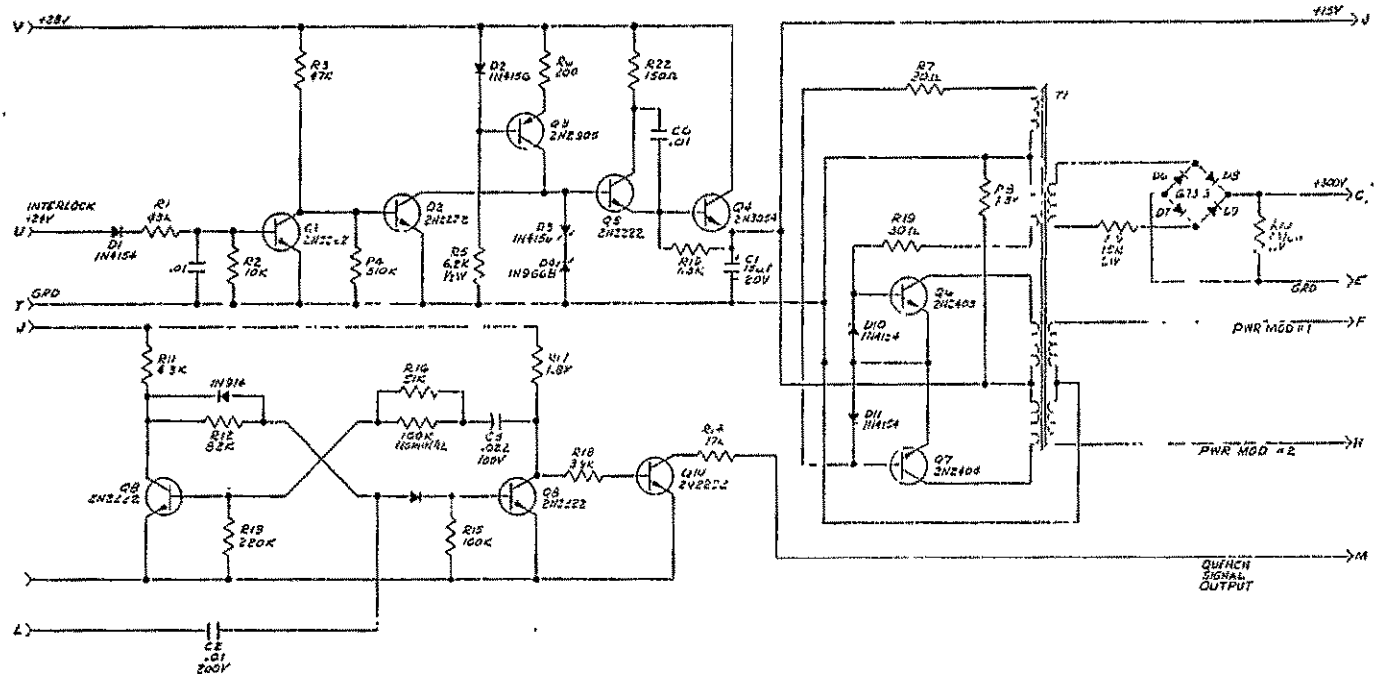
Drawings, numbers C1008876 through C1008879, depict the circuitry in schematic form. These drawings will be the reference for the detailed circuit operation description which follows.

Basically, the power conversion mechanism is in the form of a driven fly-back capacitor charging transformer. Energy is stored within a transformer, and is then transferred to the capacitive load. The energy imparted is a function of the allowed storage time and the transfer rate. Many charge cycles or steps are necessary to establish the desired capacitor terminal voltage. This method of charging imparts a precise energy pulse to the capacitor each time the fly-back action occurs, regardless of the instantaneous capacitor voltage, and given that a uniform energy storage is accomplished for each charge cycle. Thus the capacitor voltage increases in stair-step fashion.

In order that the charging action occurs in a systematic fashion, the power switching to/from the fly-back transformer is commanded by preliminary circuitry. This circuitry is the low voltage regulator and driver assembly, which is illustrated on drawing C1008876. The circuitry consists of a voltage regulator (low voltage \approx 16 Vdc), and an oscillator. Transistors Q3, Q4, and Q5 form the voltage control circuitry, with D3 and D4 providing the reference voltage. Transistors Q1 and Q2 interface the interlock circuitry to the voltage regulator. Regulated voltage appears at the emitter of Q4 when the interlock circuit is intact. Interruption of the interlock removes base drive to Q1, the collector voltage of Q1 rises and Q2 saturates. Q2 effectively shorts D3 and D4 to ground. Thus the reference voltage is now zero and the regulator performs to produce zero output voltage.

Under normal operation the input voltage is nominally 28 Vdc, which is regulated to 16 V.

REVISIONS		DATE	APPROVED
1	REVISED		

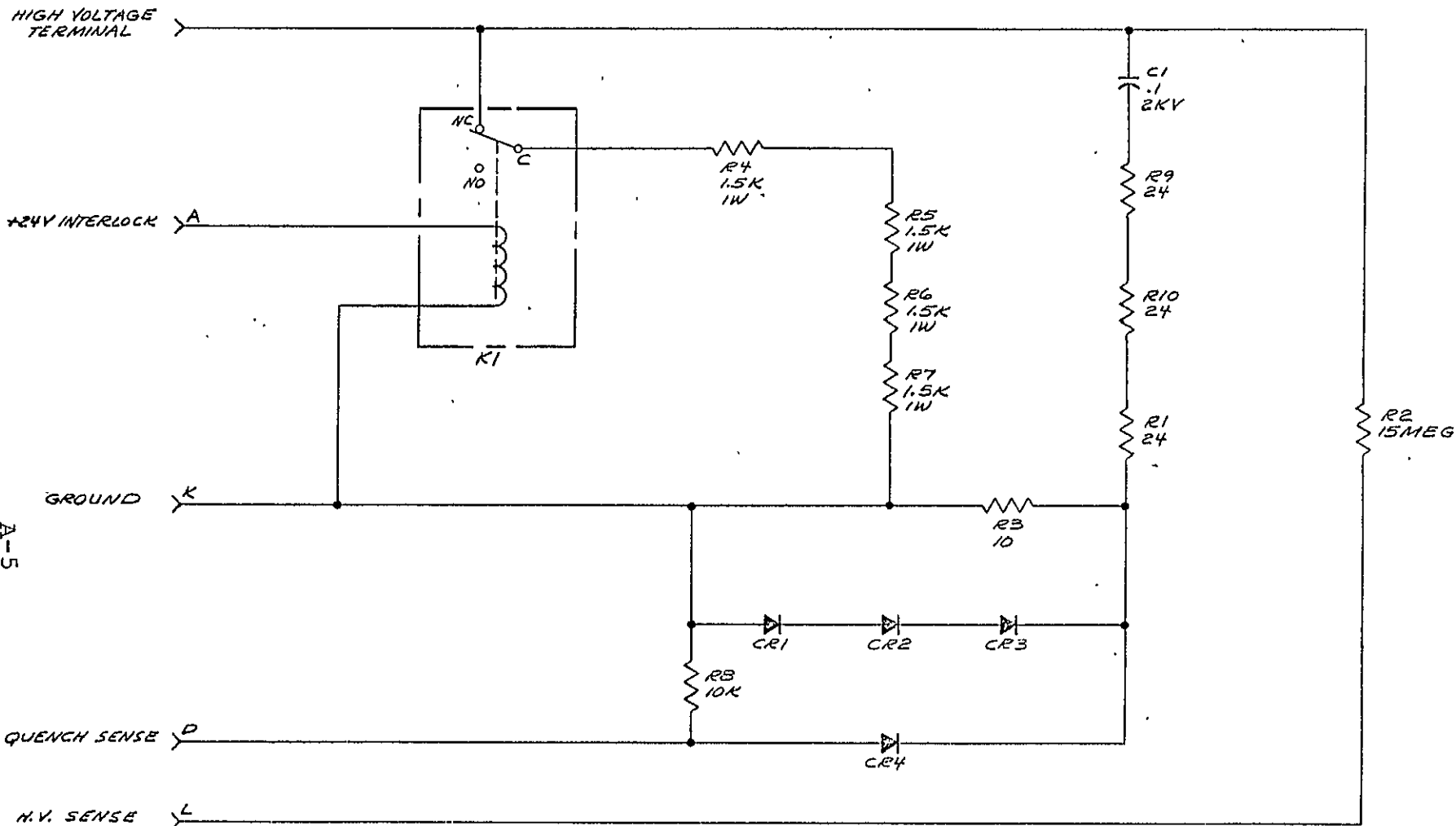


A-3

1008876

QTY	REQD	ITEM	PART NUMBER	SYM	DESCRIPTION	CODE IDENT NO	MATERIAL AND SPECIFICATIONS
					LIST OF PARTS		
					TOLERANCE UNLESS OTHERWISE SPECIFIED		
					FINISH		
					ASSEMBLY		
					WELD ON		
					APPLICATION		

INTERNATIONAL LASER SYSTEMS INC ORLANDO FLORIDA	DATE	SCALE	SHEET	DI
LOW VOLTAGE REGULATOR & DRIVER SCHEMATIC				
D 34860	1008876			



NOTES:

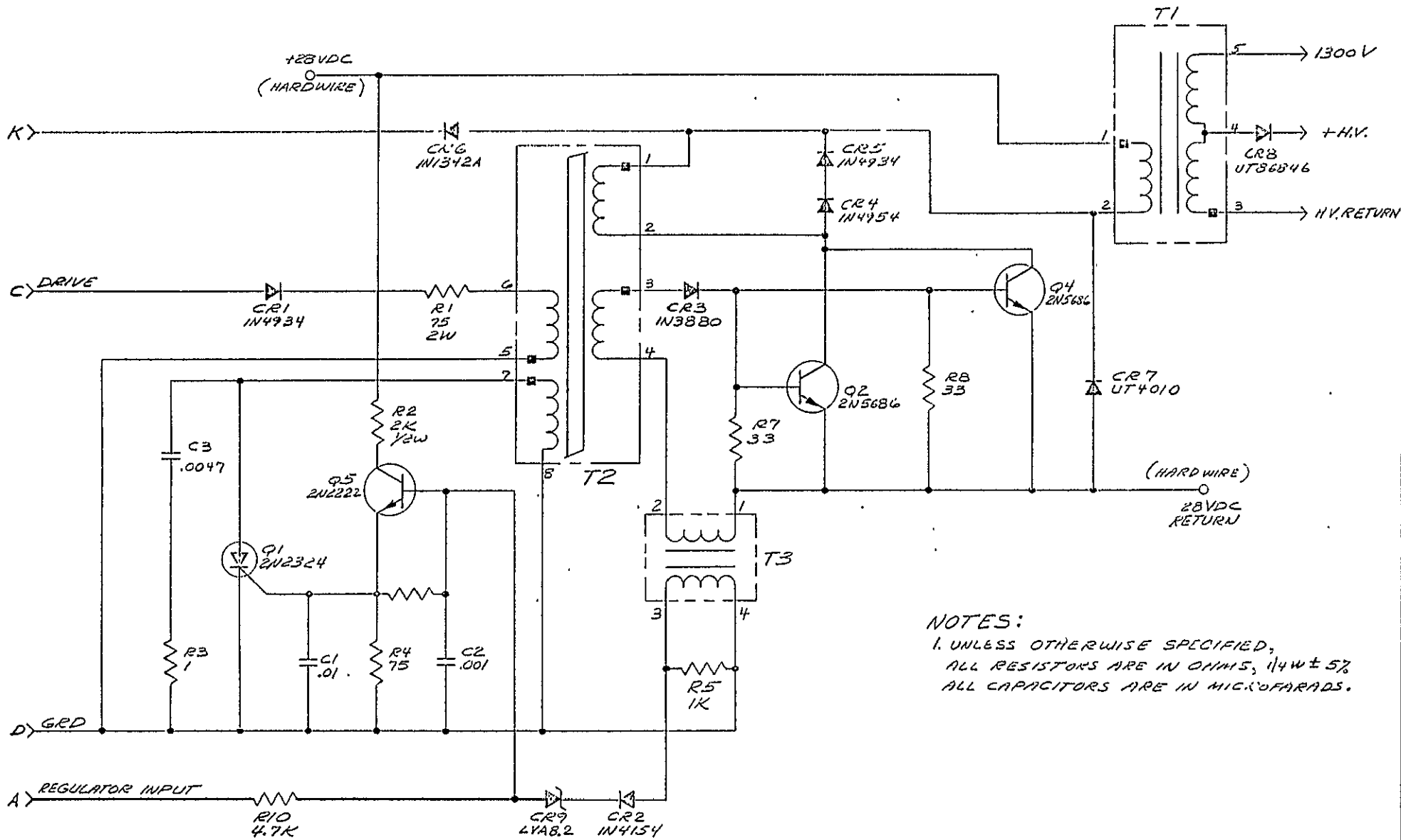
- 1. UNLESS OTHERWISE SPECIFIED;
- ALL RESISTANCE IS IN OHMS, 1/4W, ±5%
- ALL CAPACITANCE IS IN MICROPARADS (UF).

QTY REQD	ITEM	PART NUMBER	SYM	DESCRIPTION	CODE IDENT NO	MATERIAL AND SPECIFICATIONS
				← ASSY		
				LIST OF PARTS		
			TOLERANCE UNLESS SPECIFIED	SIGNATURES	DATE	INTERNATIONAL LASER SYSTEMS INC. ORLANDO, FLORIDA
			XX FINISH ✓	DRAFTER	11/30/74	
			XXX ANGLES*	CHECKER		
			MATERIAL	APPD	1/2/74	
			0-653	APPD	11/29/74	TITLE SCHEMATIC DIAGRAM HIGH VOLTAGE ASSEMBLY
			FINISH	ILL APPD	11/29/74	SIZE CODE IDENT NO DRAWING NO C 34860 1008878
			NEXT ASSY USED ON	CUSTOMER APPD		REV
DASH NO	REQD	APPLICATION		SCALE		SHEET OF

P4772

REV C 1008878

A



NOTES:
 1. UNLESS OTHERWISE SPECIFIED,
 ALL RESISTORS ARE IN OHMS, 1/4W ± 5%
 ALL CAPACITORS ARE IN MICROFARADS.

ORIGINAL PAGE IS
 OF POOR QUALITY

ORIGINAL PAGE IS
 OF POOR QUALITY

P4770

QTY REQD	ITEM	PART NUMBER	SYM	DESCRIPTION	CODE IDENT NO	MATERIAL AND SPECIFICATIONS
				← ASSY		
LIST OF PARTS						
				TOLERANCE UNLESS SPECIFIED	SIGNATURES	DATE
				FINISH ✓	DRAFTERMAN	11-574
				ANGLES*	CHECKER	
				MATERIAL	APPD	
					APPD	
					IL'S APPD	
				FINISH	CUSTOMER APPD	
DASH NO	REQD	APPLICATION				
				NEXT ASSY	USED ON	
				0-653		

INTERNATIONAL LASER SYSTEMS INC ORLANDO, FLORIDA			
TITLE SCHEMATIC			
POWER CONVERTER MODULE			
SIC	CODE IDENT NO	DRAWING NO	REV
C	34860	1008879	
SCALE ✓		SHEET OF	

The oscillator is of the square-loop saturated transistor inverter type, which produces a square wave output. Q6, Q7 and T1 form the oscillator. Oscillator start-up is assured by R8 and the inherent imbalance in beta (β) of the drive transistors. Base drive is taken from the feedback windings on T1. The feedback phase is positive. R7 and R19 limit base drive current.

This oscillator exhibits good frequency stability, since the power input is regulated. Thus, the predominant frequency determining mechanism is the core saturation time.

Two output windings are evident on T1. The bridge rectified output, marked +300 v, is of no concern since it is unused within the Spaceborne laser system. The remaining output, termed power module 1 and power module 2, are of interest. This output is the synchronization command for the power fly-back circuit.

It is to be noted that this output is center-tapped to the 28 V ground, which splits the phase of the output and generates two command signals of 180 degree phase relation. This alternate output signal allows use of two power modules to effectively double the capacitor charge slope, since the charge current is doubled.

The remaining circuitry, of the low voltage regulator and driver assembly, is the quench signal generator. This signal is required, during and for a brief time following the PFN discharge, to prevent CW excitation of the flashlamp from continued operation of the power charging circuit. Thus, this signal is an inhibit command to the power module. The inhibit duration is on the order of 2-3 msec.

Q8 and Q9 form a monostable multivibrator (MSMV). Q10 is an output driver. The flashlamp current pulse is sensed and appears at the base of Q9. C2 provides the necessary signal interjection path. The input signal is negative going, which removes base drive from Q9. The collector voltage of Q9 rises, Q8 is driven to saturation, and base drive to Q9 via R12 is removed. Capacitor charging occurs over a period of time for C3, which establishes the output pulse duration. When C3 is charged, Q8 is base current starved and can no longer maintain saturation. The collector voltage of Q8 rises. Current flows in R12 to the base of Q9. Q9 quickly saturates terminating the quench signal pulse. Q10 faithfully outputs the quench signal by operating as a current sink to external circuitry.

Schematic C1008879 depicts the circuitry of the power converter module. Input power to this circuitry is non-regulated, but filtered, 28 Vdc. Q2 and Q4 are the power switching transistors. Q1 and Q5 are current and voltage actuated turn-off mechanisms to the power switches.

In normal operation, the drive command, the synchronization command from the driver circuitry, appears at input point C. This signal is transformer coupled, via T2, into the base circuit of Q2 and Q4. Q2 and Q4 conduct, the collector voltage falls to produce a current in the primary of T1 and to produce positive feedback through T2 to the base of Q2 and Q4. Current rises linearly in time in the primary of T1 and in the feedback winding of T2. After a precise time interval, T2 saturates, base drive is abruptly removed from Q2 and Q4, and the fly-back action is initiated. The secondary of T1 is loaded into the capacitive load via CR8, and the stored energy is transferred to the capacitor.

Transformer T3 terminates the base drive of Q2 and Q4 when fault conditions occur in the output circuitry. This occurs by forward biasing the base of Q5 which initiates turn on of SCR, Q1. Q1 shorts one winding of T2; thus, no drive can reach Q2 or Q4, and any drive which was present was removed.

When the capacitor voltage is increased to the desired level, the regulator circuit outputs a positive pulse to input terminal A. Again Q5 activates Q1, drive to Q2 and Q4 is removed, and no additional charge is imparted to the capacitor.

Each power converter module is conservatively rated at 250 W; thus, it is generally necessary to operate two or more modules, slaved to a single driver, to charge a reasonably sized PFN capacitor. A maximum of 4 modules usually suffices for the most stringent requirements. Two modules, slaved at 180 degree phasing, are utilized in the Spaceborne laser system, one group each, for both the oscillator and the amplifier PFNs. The 180 degree phasing is essential to limit current peaking from the 28-V power source.

The high-voltage assembly monitors the output of the PFN capacitor, which is really the output of the power converter modules, to provide;

- The voltage regulation sense;
- The generator of the quench signal; and

- The power down discharging of the PFN capacitor in the interest of safety.

K1 is the discharge relay. 28-V excitation of the relay positions the armature to open the normally closed contacts. Interruption of the interlock circuit allows contact closure and the capacitor is discharged through R4, R5; R6 and R7.

The PFN discharge is sensed through the network comprised of C1, R9, R10, R1 R3 and CR1-4. Discharge of the PFN creates a steep voltage decline at the capacitor. This voltage step is capacitively coupled to forward bias CR1-3. CR4 is also forward biased to produce a negative pulse output at the quench sense, terminal S. This pulse activates the MSMV of the low voltage regulator and driver board, to produce the timed quench signal output.

R22, a high voltage 22 MΩ resistor, senses the output voltage. The voltage drop across the resistor equates to nearly the capacitor charge voltage. This voltage drop results in a current flow which is sensed within the final circuit group which comprises the power supply subassembly.

The high-voltage regulator is illustrated in schematic drawing C1008877. This circuit consists of:

- A voltage reference mechanism;
- A voltage comparator mechanism; and
- An error signal amplifier.

The paramount function of this circuitry is to disable the power converter module at the time the capacitor voltage is at a preset magnitude.

CR1 is the voltage reference diode. R7 maintains the Zener current at the minimum drift magnitude.

Q1 and Q2 are the voltage comparator. Q2 is taped across the reference voltage by the voltage divider produced by R5 and R6.

Q3, Q4, Q5 and Q6 comprise the error signal amplifier. The individual power modules are disabled via CR4 and CR5.

The high-voltage sense, from the high-voltage assembly, is applied to the input terminal 5. Generally a high-voltage adjustment potentiometer is connected from terminal T to ground, terminal V. Thus, the current from the high-voltage sense produces a voltage drop across the high voltage adjustment potentiometer. When the sensed voltage slightly exceeds the reference voltage, Q6 saturates and the charge current for the PFN capacitor is removed.

Voltage regulation is assured, since gradual voltage decay at the capacitor results in deactivation of Q6 which reinitiates charging to the capacitor until the voltage again is at the preset/controlled value.

Voltage regulation accuracy for this system is better than 0.5%. Control is therefore not limited to the granularity afforded by the driver oscillator..

2. High Voltage Low Current Supply

Drawing, ILS B1008210-S, Revision B, details the specific circuitry which comprises the power unit.

A power pass transistor pair, Q1 and Q2 serve to energize Z1, a tracking dc to dc converter unit. The power pass stages are controlled by a gain stage Z2. CR1 is a voltage reference unit. Resistive divider, R9, R10, R11 and R12 sample the high-voltage output to compare to the voltage reference.. The input voltage to Z1, is served to achieve equality between the reference voltage and the feedback voltage. The 5K external potentiometer is utilized to vary the effective voltage reference and consequently the high voltage output. Capacitor C2 and resistor R5 stabilize the loop response.

Input power is 24 to 28 Vdc. Input current at full load is \leq 400 mA dc.

3. Flashlamp Simmer Supply

The flashlamp simmer supply is schematically depicted in ILS drawing D1013775. The primary subsystems which comprise the supply are;

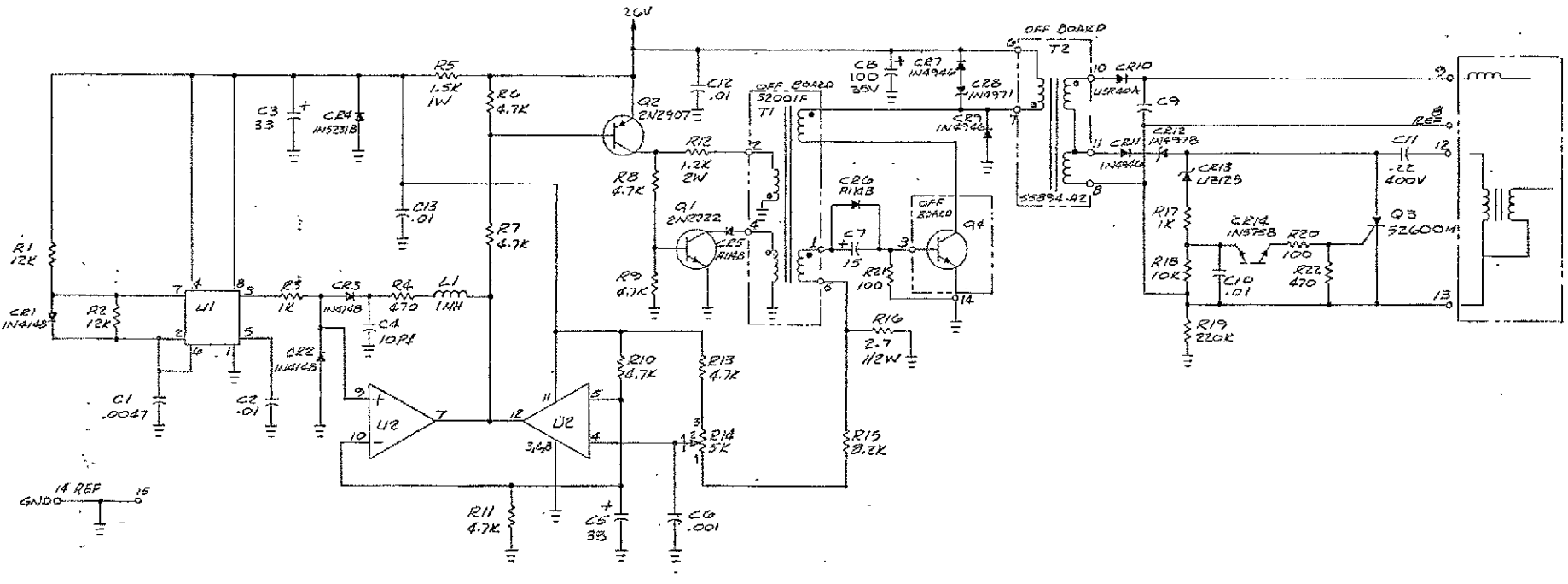
- A high rate clock or oscillator;
- An energy output sense mechanism;

NOT SUPPLIED

B1008210-S RB

FOLDOUT FRAME 1

FOLDOUT FRAME 2



NOTES: UNLESS OTHERWISE SPECIFIED,
 1. ALL RESISTORS ARE IN OHMS, 1/8W ±5%
 2. ALL CAPACITORS ARE IN MICROFARADS

REVISIONS			
JONE	DATE	DESCRIPTION	APPROVED
1	10-1-77	REV. CR. S.	10-1-77

DRAWN BY D/C/5775

OFF REGR	ITEM	PART NUMBER	SYM	DESCRIPTION	CODE IDENT NO	MATERIAL AND SPECIFICATIONS
				LIST OF PARTS		
VARIANCE UNLESS SPECIFIED				SIGNATURE		
SIZE	1/8"	1/4"	3/8"	DATE	INTERNATIONAL LASER SYSTEMS INC. ORLANDO, FLORIDA	
ANGLE	1"	1"	1"		TITL SCHEMATIC	
MATERIAL					SIMMER SUPPLY	
DASH NO					REV	
					D 34860 1013775 B	
					SCALE 1 SHEET 2 OF 3	

- A dc to dc converter; and
- A flashlamp ignition circuit.

The high rate oscillator is configured by V1 and the associated circuit components. The frequency of oscillation is 20 KHz.

One half of U2, together with L1, and associated circuitry shape the oscillator output signal to drive Q2. The drive signal is transformer coupled to the base of Q4.

T1, T2 and Q4 comprise the SC to SC converter. This implementation is of the inductive fly-back type in order to accommodate widely varying lamp voltage excursions and to afford good conversion efficiency.

Drive to the base of Q4 causes a reduction in collector voltage, to produce a voltage drop across the primary of T2 and the feedback winding of T1. Q4 rapidly reaches saturation, due to the positive feedback through T1. R16 senses the base drive to Q4. Resistors R13-15 couple the base drive sample to comparator V2, causes the comparator to react, and Q2 and Q1 are activated. Q1 clamps a winding of T1 and effectively removes drive from Q4.

R14 is the energy control adjustment. The voltage at pin 4 of V2 is a ramp type signal; thus, adjustment of R14 determines the on time Q4 and determines the energy stored in T2. Abrupt removal of base drive from Q4 results in a swift fly-back response in T2.

CR10 and CR11 are forward biased so that charging current is supplied to C9 and C11. Initially, no simmer current flows in the flashlamp, as the lamp is deionized. Voltage rise on C9 is quite high - in the KVdc region. CR11 and CR12 serve a dual purpose. For one thing they provide a portion of the over voltage fly-back transient snubber. Additionally, they provide a voltage depletion region which prevents activation of the ignition circuitry when normal simmer exists since no charge exists on C10 and C11 during this operation. C11 is charged through CR12. When the voltage rises sufficiently on C11, C10 charges through CR13 and R17. At a charge voltage, in the area of 15 to 20 V upon C10, CR14 enter conduction to activate the gate of SCR, Q3. Q3 discharges abruptly the stores charge of C11 through the primary of the ignition transformer, to ionize the flashlamp.

C9 is charged quite high and aids in initial lamp ignition. C9 discharges to a nominal holding voltage equating to the average lamp simmer voltage. During PFN discharge, the inductive ballast prevents activation of the ignition circuit.

In the event "simmer" is lost, due to deionization, a re-ignition sequence is initiated.

4. PRF and Delay Generator

The PRF and delay generator circuitry establishes the laser emission rate and provides precisely delayed initiate output commands for Q-switch and pre-lase control.

Additionally, a divide-by-10 prescaler is incorporated to drive the shots counter.

Various enablement features are incorporated for laser mode control.

The circuit is depicted in schematic format in ILS drawing number D1018733. The counter chain comprised of U9-15 establishes the laser emission PRF and serves also to provide the precise timing delay function. The system clock, U16, is selected to be 10MHz in order to afford a minimum timing interval of 100 nsec.

At initial power-up the counter chain is active at a random count. The counters accumulate content synchronously at the 10 MHz rate. When the counter content is equivalent to the programmed period, the J input of U4 pin 3 is enabled. The next sequential clock transition causes U4 to toggle. Pin 5 becomes a logic high state to enable to U4 pin 11 and the delay comparators U20-22 and U28-30. Simultaneously U9-11 are disabled by the \bar{Q} output of U4 pin 6. U9-11 are preset to zero content, while U11 is preset to a content of one, which equates to a time of 1 msec.

It is significant to note that counters U12-15 are naturally at a count content of zero because of the detection implementation technique for the PRF generation.

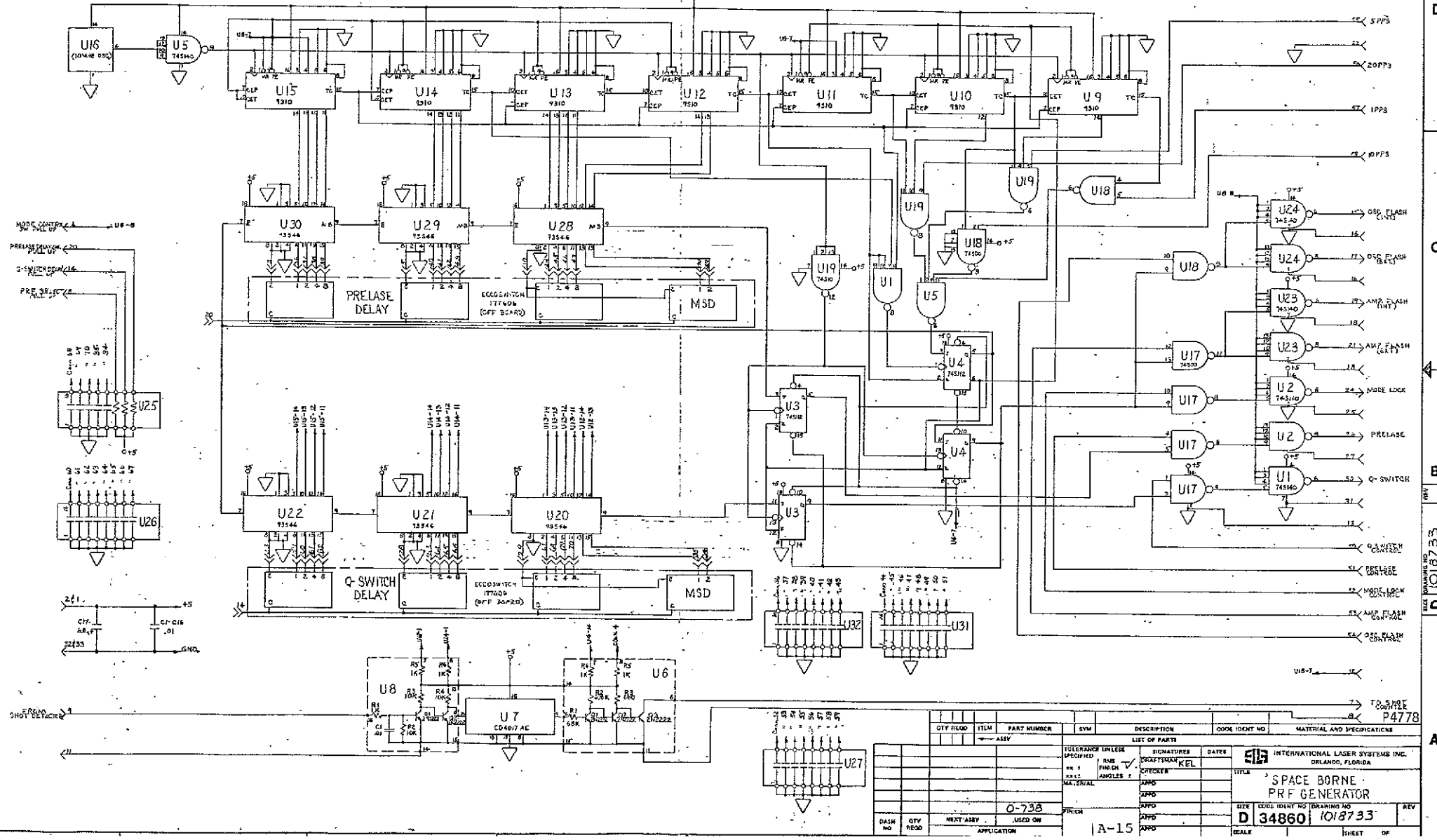
The delay comparators are programmed from digital decimal thumb wheel switches.

For a program delay input of zero to the delay comparator/comparators the J input/inputs to U3 are now also enabled. For programmed delay ≥ 1 the J inputs of U3 are held at a logic low level.

FOLDOUT FRAME

ORIGINAL PAGE IS OF POOR QUALITY

FOLDOUT FRAME 2



QTY REQD	ITEM	PART NUMBER	SYN	DESCRIPTION	COOK IDENT NO	MATERIAL AND SPECIFICATIONS
			→ ASSY			
LIST OF PARTS						
TOLERANCE UNLESS SPECIFIED				SIGNATURES		
FRS FINISH		CHECKER		DATE		
HOLE ANGLE		KEL				
MATERIAL						
PRF GENERATOR						
DASH NO		QTY REQD		REV		
		NEXT ASSY		DATE		
		MFGD ON		TITLE		
		APPLICATION		SPACE BORNE PRF GENERATOR		
0-738				SIZE		
A-15				DRAWING NO		
				D 34860 1018733		
				DEALE		
				SHEET OF		

The next sequential clock pulse toggles U4 pin 9 to generate the basic flash command. The counters continue to accumulate content. As the content agrees with the programmed delay content U3 is enabled and toggles at the appropriate time, to produce the preflash command and the Q-switch command. When counters U12-15 reach a content of 999.9 μ sec, the K input of U4 pin 2 is enabled. U4 toggles at the elapsed time of 1,000.0 μ sec. The preset strobe is removed from counter U9-11 and the enable is removed from the digital comparators. All output commands are removed.

It is significant to note that counters U12-15 are now naturally at a content of zero, counter U9 and U10 are preset to zero, and counter U11 is at a content of 1 which equates to 1,000.0 sec, which is the proper count sequence state.

The counter content accumulation continues until again the selected PRF decodes the content to re-initiate the sequence.

To this point in the discussion no output commands have actually been generated. U1, U2, U23 and U24 comprise output drivers. U17 and U18 serve as gated signal sources to generate and control the various outputs as commanded from operator adjustable front panel control switches.

The remaining area for discussion is the shots counter scaler U7. Transistors Q1 and Q2 comprise an input signal conditioner for U7. Transistors Q1-3 comprise a driver circuit to allow U7 to drive the shots counter. The scale factor of U7 is division by 10.

5. Frequency Synthesizer Circuit Description

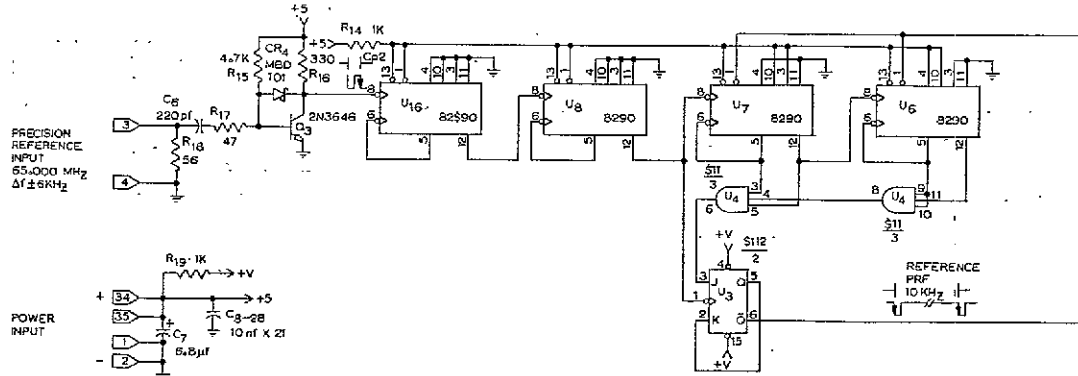
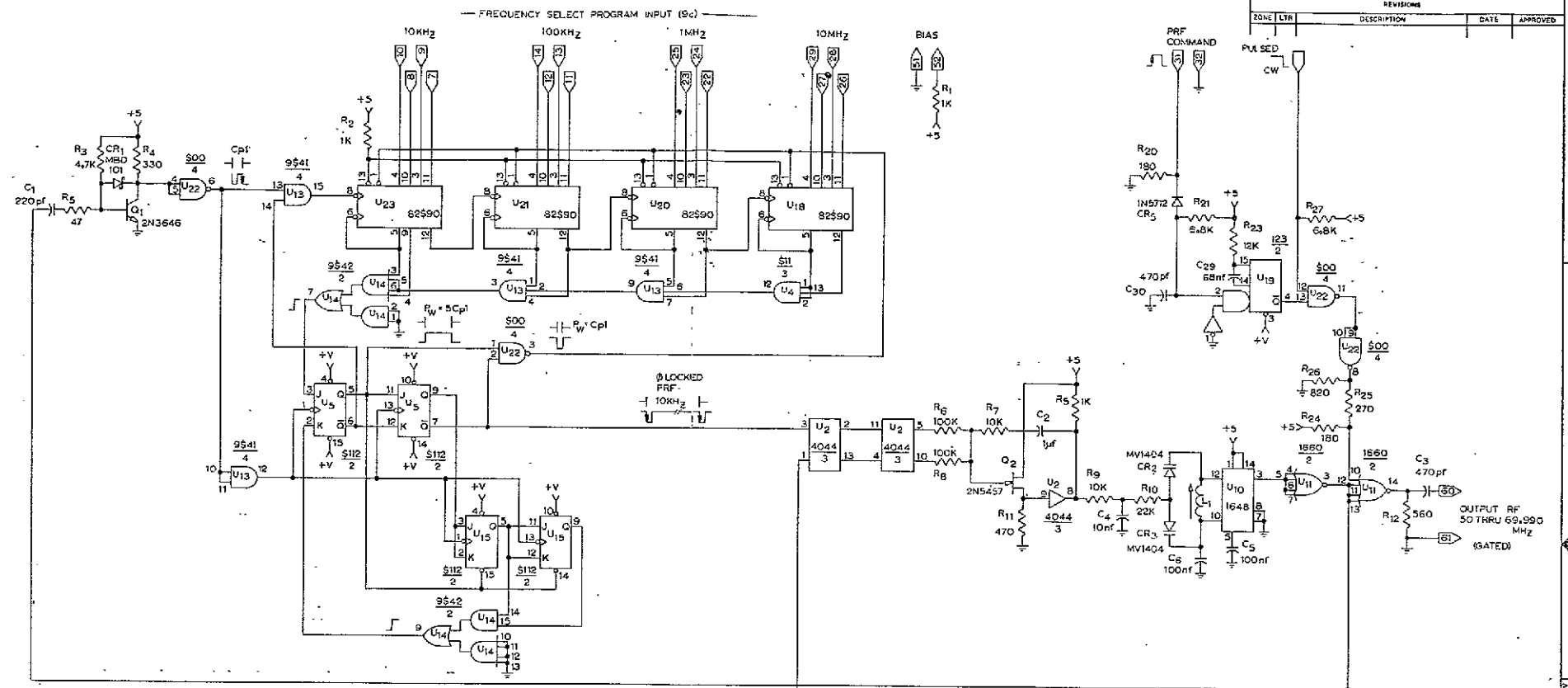
The following circuit description details the signal flow in step by step fashion within the frequency synthesizer.

Previous discussion from Section 3 of this report, has outlined the basic circuit concept and operation.

Schematic, ILS D1018735 shows the circuit in schematic format.

Signal output from the precision reference oscillator is 65 MHz and is in the emitter coupled logic (ECL) format. This signal enters the frequency synthesizer board at pin number 3.

REVISIONS			
22NC LTR	DESCRIPTION	DATE	APPROVED



FOLDOUT FRAME 1

FOLDOUT FRAME 2

REV	DATE	BY	DESCRIPTION
D	10/17/35		

QTY	REQD	ITEM	PART NUMBER	SYM	DESCRIPTION	CODE IDENT NO	MATERIAL AND SPECIFICATIONS
					TOLERANCE UNLESS SPECIFIED		
					FINISH		
					DRILL		
					PLATING		
					FINISH		
					USED ON		

SIGNATURE	DATE	TITLE
DESIGNER	3/20/77	FREQUENCY SYNTHESIZER
CHECKER		
APPD		
APPD		
APPD		

DRAWN	CITY	NEXT ASSY	USED ON	SIZE	CODE IDENT NO	DRAWING NO	REV
				D	34860	1018735	

D

C

B

REV
DATE
BY
DESCRIPTION

A

Resistor, R18, provides the proper termination for the input signal.

Transistor Q3 and associated circuitry comprise an ECL to TTL level shift function, to generate the signal referenced CP2.

U16 reduces the signal frequency by a factor of 10 such that the output of pin 12 is 6.5 MHz.

U8 reduces this signal frequency by a factor of 10 to produce an output at pin 12 of 650 kHz.

U3, U4, U6 and U7 operate in concert to reduce the 650 kHz signal to a frequency of 10 kHz, which appears at pin 6 of U3. This signal, of negative attitude, is the reference signal to the phase detector/comparator U2. This signal pulsewidth is 1,538.4 nsec.

The voltage controlled oscillator, U10 is of the ECL family. The output, pin 3, drives U11. The output of U11, pin 3 drives U11 pins 11, 12 and 13. Additionally, this signal drives Q1. Q1 and associated circuitry perform an ECL to TTL voltage translation, which drives pins 4 and 5 of U22. The output signal from pin 6 to U22 is designated CPL and is the modulo prescaler clock signal.

U4, U5, U13, U14, U18, U20, U21, U23 comprise the modulo prescaler. Initially, the prescaler is preset with the 9 complement of the desired output frequency. This preset is generated from thumbwheel switches which are operator programmable. The switch input range is limited to values which fall within the range of 50.000 MHz to 69.990 MHz through mechanical stops installed at the most significant digit thumbwheel. The least significant digit is the 10 kHz thumbwheel.

Once the counters are loaded the counters may accumulate content at the CPL rate, which is the VCO rate. When the least significant digit counter, U23, has reached a content of 3 and all other counter contents are equal to 9, coincidence detection occurs and the J input, pin 3, of U5 is enabled. The next sequential transition of CP 1 toggles U5 and pin 5 becomes a logic high level. Pins 1 and 2 of U22 are both a high level, and pin 3 of U22 becomes a logic low level to again load the counters. Simultaneously, pins 11 and 12 of U5 are enabled, and the clock to the counter string is disabled. The second clock

pulse following coincidence toggles U5. Pin 9 becomes a logic high level to enable U15 pins 2 and 3. Pin 7 becomes a logic low level to remove the counter preset command. The third and fourth clock pulses, following coincidence detection, toggle U15 to preset the K input, pin 2 of U5. The fifth clock pulse returns U5 to the original state and removes the clock inhibit command from the counter string. The sequence may now repeat.

The phase locked PRF pulsewidth is the $CP1 P_w \times 4$; thus, adequate pulsewidth is available to drive U2.

It is to be noted that the unusual coincidence detection deviation from true 9 complement logic is necessary to achieve adequate clear time through the coincidence detector, U4, U13 and U14.

U2 is the phase comparator. The comparator is connected to form a type 1 phase detector to provide an in-phase lock.

Assume that the VCO frequency is above the reference frequency for the sake of circuit explanation. U2 pin 5 becomes a logic high-level which drives pin 8 of U2 to a more negative value. This reduces the bias voltage upon the varactor diodes CR2 and CR3 to increase the effective capacitance to the VCO tank circuit, and the frequency is reduced. This action continues until lock is obtained. When lock is obtained, no current flows from or into U2 and varactor voltage stabilizes, as does the VCO frequency.

For conditions where the VCO frequency is less than the reference frequency the reverse occurs. U2 pin 10 becomes a logic low-level, the varactor voltage and the VCO frequency increase until lock is again achieved.

R7 and C2 are the predominant loop filter components. R9 and C4 form a additional filter for high frequencies in order to improve the spectral line of the VCO.

R10 decouples and VCO radio frequency energy from the control loop.

U11 is the output buffer amplifier. The output occurs at pin 60 of the frequency synthesizer.

U19 is a monostable multivibrator (MSMV). This circuit conditions the PRF input command signal to a precise pulse duration, in order to establish the emission burst duration. Gate, U22,

pin 12 is controlled to effect either the pulsed emission or continuous wave (CW) emission.

6. PTM Synchronizer

The PTM synchronizer determines the appropriate time to initiate the laser emission. This determination is accomplished in the following sequence:

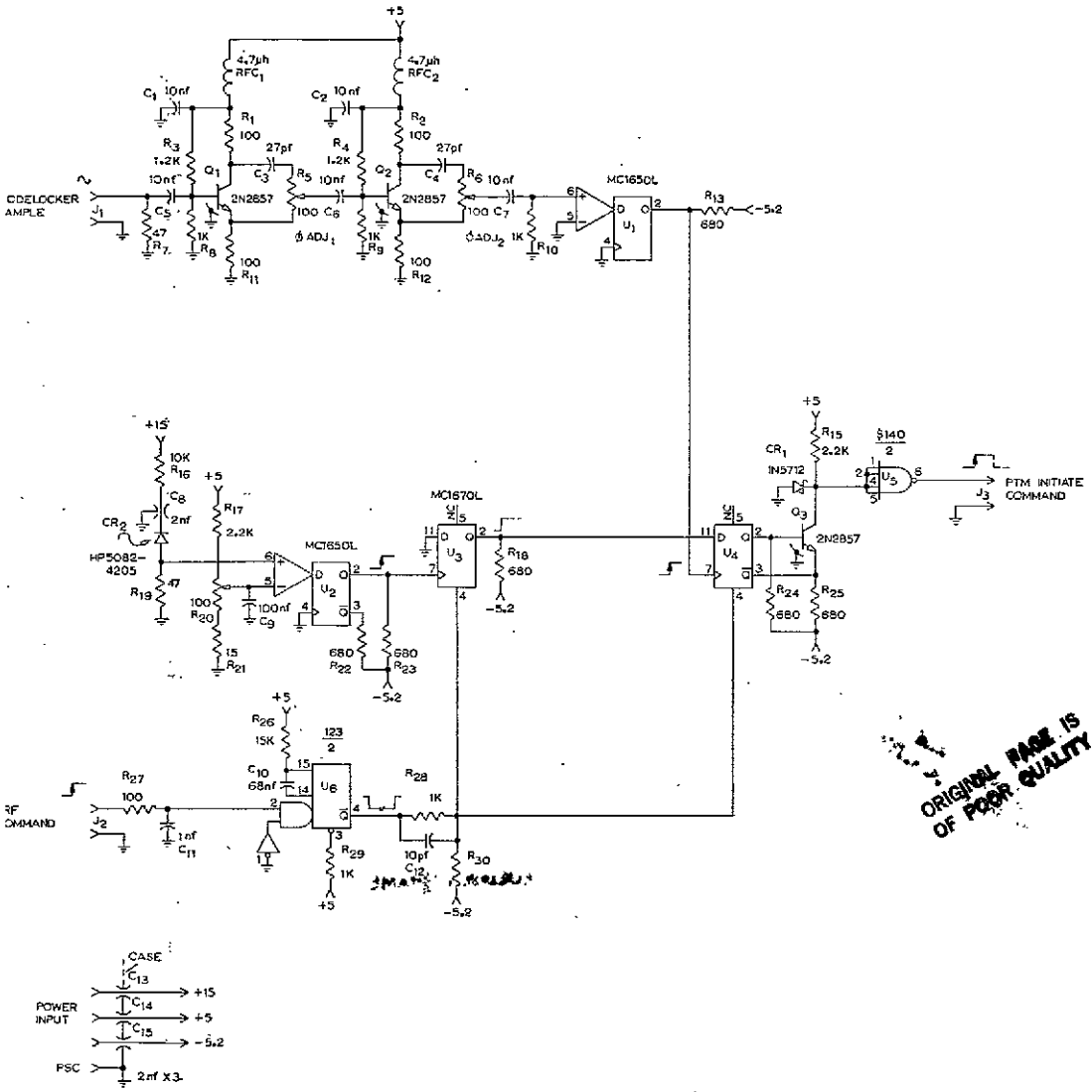
- The laser PRF command (flash) enables the sensor with a window aperture of approximately 200 microseconds duration.
- The optical resonator energy level is monitored against a reference level comparator.
- The laser energy packet position is determined by sampling of the modelocker drive voltage through a squaring circuit.
- The PTM/Dump command is generated whenever the laser energy exceeds threshold and the modelock voltage squarer provides a transition. Drawing ILS D1018737 depicts the circuit in Schematic format.

The PRF (flash) command is utilized to activate monistable multivibrator (MSMV) V6, at input pin 2. Triggering occurs at the low to high transition. The MSMV output occurs at pin 4. This output exists for a period of 200 μ sec following the leading edge of the PRF signal. During this time, the circuitry is active to accomplish the determination.

Photo detector CR2 senses the optical resonator energy. Energy pick-off is from the polarizer. Circuit V2 is the comparator. The photo detector converts the optical energy output into a corresponding current flow. This current flow produces a voltage drop across resistor R19.

The resistive voltage divider comprised of R17, R20 and R21 establish the reference for the threshold comparator. Resistor R20 allows adjustment of the threshold magnitude, Circuit V2 is operated as comparator only, the output of pin 2 is utilized to clock V3, a storage "D" flop. Whenever the energy level within the optical resonator exceeds threshold, the output at pin 2 of V3 latches in the logic high-state. The D input of V4 is now enabled.

REVISIONS				
ZONE	LTR	DESCRIPTION	DATE	APPROVED



FOLDOUT FRAME 1

ORIGINAL NAME IS OF POOR QUALITY

FOLDOUT FRAME 2

DATE		QTY	RECD	BY	RECD

QTY	RECD	ITEM	PART NUMBER	SYM	DESCRIPTION	CODE IDENT NO	MATERIAL AND SPECIFICATIONS

TOLERANCE UNLESS SPECIFIED	SIGNATURES	DATE	TITLE	
			PTM SYNCHRONIZER	

DATE	QTY	RECD	BY	RECD

P4776

INTERNATIONAL LASER SYSTEMS INC.
ORLANDO, FLORIDA

SIZE CODE IDENT NO DRAWING NO

D 34860 1018737

REV

Transistor Q1 and associated circuitry form the first phase shifter for the sampled modelocker R.F. signal. Resistor R5 allows phasing adjustment.

Transistor Q2 and associated circuitry form the second phase shifter. Resistor R6 allows phasing adjustment.

Circuit V1 is the signal squarer. It is to be noted that the reference for this comparator is at ground potential; therefore the sine wave signal input is sliced at the centroid of the excursion or at ground.

The low to high transition of the output of V1 at pin 2 clocks V4. The Q output of V4 becomes a logic-one level, and the \bar{Q} output of V4 becomes a logic zero level whenever the D input of V4 is a logic high level. This action forward biases the base/emitter junction of transistor Q3, the collector voltage of Q3 falls, and the output of V5 at pin 6 is generated. This signal is the PTM/Dump initiate command.

At the expiration of the timing interval of MSMV V6, the direct set inputs of V3 and V4 are activated and the PTM initiate command is terminated.

The sequence repeats at the next PRF command input.

7. Radiation Control Loop

The radiation control loop has only one function to perform for the laser system, the stabilization of the oscillator optical resonator energy during the prelude interval. Roughly 600 to 800 round trip intervals are required within the resonator to achieve active modelocking. This equates to an elapsed time of $\sim 6 \mu\text{sec}$ that the loop must remain active. The control function must effect a pulse stretching for this $6 \mu\text{sec}$ interval.

During the interval the active modelocker is compressing the resonator energy into a shorter pulse, so that the control system must respond at a reasonable rate to the decreasing pulse width.

A control tradeoff is effected whereby the response is good to a specific frequency or pulse width for peak energy control. The loop then effects a reduced performance whereby the average resonator energy is controlled. By the time the average

energy control is in effect the pulse shaping is well under way and the energy stabilization is quite effective. The photo detector affords the integration for average control.

The complete circuit is depicted in ILS drawing D1018738. Diode CR3 is the photo detector. Transistors Q1-3 and associated circuitry form a transimpedance preamplifier, to convert the diode current into an analog voltage. Resistors R24 and R25 form the transresistance.

Transistors Q407 and associated circuitry comprise a post amplifier. The output of the post amplifier is positive in attitude, and saturates at 600 to 800 mV.

Transistors Q8-10, and associated circuitry comprise the final voltage amplifier to drive the Pockels cell.

Resistor R15 provides some control of the energy threshold, by determining the point of voltage drive where the final voltage amplifier becomes active.

8. Revised Energy Control Output Driver

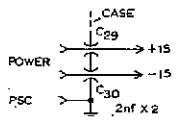
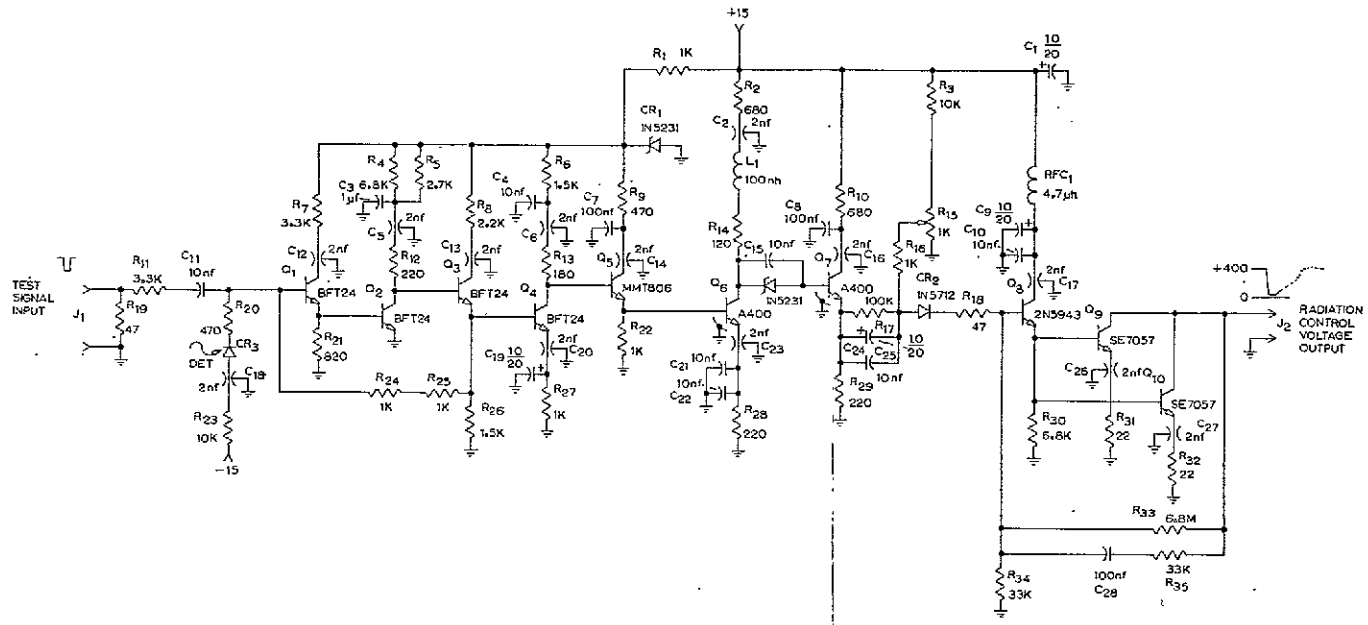
The discussion specifically details the revised/re-engineered output-driver for the energy control loop for the Spaceborne Laser System.

Schematic 1018738A depicts the revised energy control driver in schematic form. Basically, the circuitry is a very-very fast operational amplifier of the inverting configuration. Because of the need for proportionality, within the control loop, some means for loop gain adjustment is desired. Additionally, since the control loop is closed through the optical paths, all the classical problems of closed loop servos must be considered. Usually, a lag or lead/lag stabilization network must be provided. An operational amplifier concept lends ease for the loop stabilization network insertion. For this discussion, the network will be omitted other than to illustrate the awareness for the inclusion of the circuitry.

Specific Circuit Description

The circuit is a closed-loop operation amplifier. As implemented, only the inverting input terminal is utilized. True current mode summation is employed in the design.

REVIEWS				
ZONE	LTR	DESCRIPTION	DATE	APPROVED



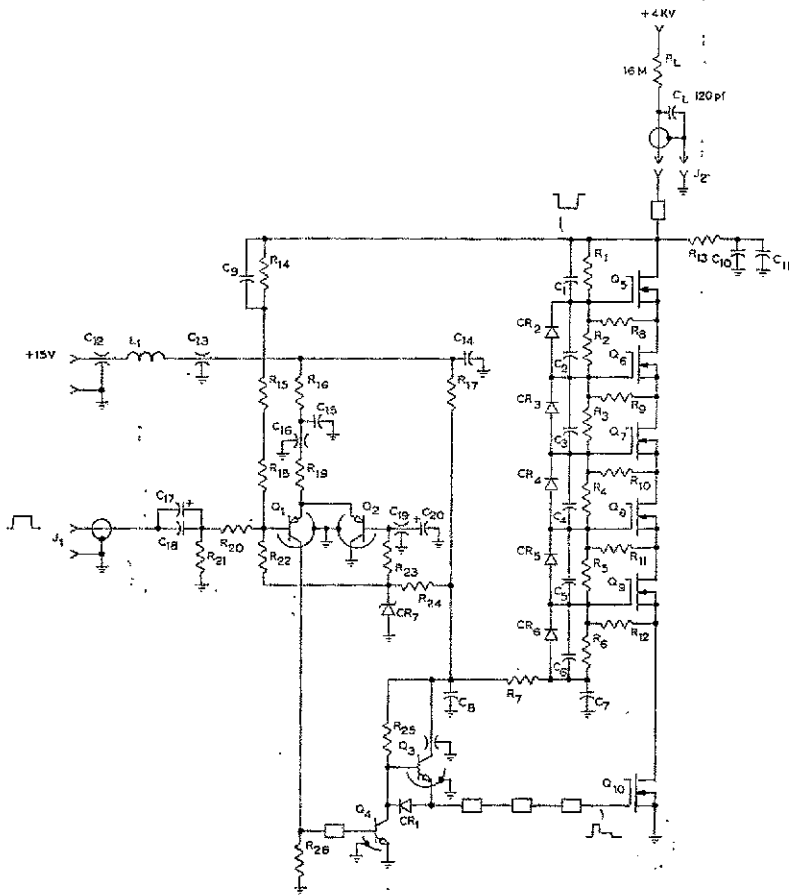
FOLDOUT FRAME

FOLDOUT FRAME 2

QTY RECD		ITEM	PART NUMBER	SYM	DESCRIPTION	CODE IDENT NO	MATERIAL AND SPECIFICATIONS
		← ASBY		LIST OF PARTS			
				SIGNATURES		DATE	INTERNATIONAL LASER SYSTEMS INC. ORLANDO, FLORIDA
				DRAFTSMAN		2-9/77	
				CHECKER			TITLE
				MATERIAL			RADIATION CONTROL
				APPROV			SIZE
				APPROV			CODE IDENT NO
				APPROV			DRAWING NO
				APPROV			1018738
				APPROV			REV
DASH NO	QTY RECD	NEXT ASBY	USED ON	APPLICATION	A-24	SCALE	SHEET OF

P4775

PART 1018738



FOLDOUT FRAME 1

FOLDOUT FRAME 2

QTY REQD	ITEM	PART NUMBER	SYM	DESCRIPTION	CODE IDENT NO	MATERIAL AND SPECIFICATIONS
				INTERNATIONAL LASER SYSTEMS INC.		ORLANDO, FLORIDA
				ENERGY CONTROL DRIVER		
				34860	1018738-A	

REV D
REV C
REV B
REV A

The design emphasis was placed upon:

- The circuit must possess a 400 V output voltage excursion range;
- The circuit must be of the linear type;
- The through-put time delay must be minimized at all costs;
- The output slew rate must be in the order of ≈ 10 kV/sec; and
- The circuit must not possess instability when capacitively loaded.

Using this criterion the circuit depicted in Schematic 1018738A evolved. Transistors Q1 and Q2 form a differential amplifier. The base of Q2 is referenced to an interval reference, while the input signal is applied to the base of Q1. Transistors Q3, Q4 and Q10 furnish the excess gain needed in addition to the gain afforded by the differential pair.

Transistors Q5-9 furnish no gain, rather they operate as voltage range extenders, to enable an output voltage swing of 400 V. Power for the output stage is derived from the Pockels cell bias supply, which is depicted as RL. The capacitive load is denoted as CL.

Resistive-divider network R14, R15, R18, R20, and R21, determines the quiescent dc voltage which appears at output jack, J2, by virtue of the fact that the summation node (the base of Q1) is connected to the divider. Network weighting of the feedback network shapes the desired ac response.

Considerable care was exercised in the device selection. Bipolar transistors were chosen for the differential pair, and the predriver (Q3 and Q4) because good gain bandwidth product (F_t) devices are readily available, which operate at the necessarily low current. The F_t of the differential amplifier devices, at $I_C=15$ ma dc, is specified to $b\beta \geq 1,600$ MHz. The F_t of the pre-driver devices, at $I_C =30$ ma dc, is specified to $b\beta \geq 5,000$ MHz. Thus, the response and delay time of this circuitry is ≤ 4 nsec.

The capacitive load, plus the necessity to swing 400 V, places quite a limitation on device selection for the output drivers.

In the interest of determination of the current required to discharge a capacitive load of 120 pF in 20 nsec, the following calculation is included.

$$I = \frac{CV}{t}$$

$$I = \frac{(120 \times 10^{-12}) (400)}{20 \times 10^{-9}} = 2.4 \text{ A}$$

Obviously, this current requirement precludes any small geometry devices not already excluded on the basis of low collector/emitter voltage ratings.

Additionally, in the interest of circuit efficiency, bipolar transistors are not desirable from the inordinately high base drive current requirements necessary to achieve collector currents of 2.5 A at the needed response speed.

A recent development within the field effect transistor (FET) family of devices has yielded the power FET, or the VMOS. This device is of the enhancement gate drive variety, which requires virtually no gate drive current. Excellent current capabilities, coupled with extreme speed, make this device attractive. Typical switching speed at the drain current level of 2 A, is 4 nsec. This time includes both delay and fall time. Obviously, the device is much faster than present bipolar selections.

At present the device voltage rating, the source to drain sustaining voltage, is 90-V maximum. This is not a serious problem. The devices permit an ease of series operation, since the gate drive current is miniscule.

VMOS devices are used for Q5-10. The gate voltage source is clamped to +15 Vdc for devices Q5-9 in order to preserve good low end voltage response. The bipolar driver actuates the gate of Q10. The preamplifier/detector unit, positive attitude output, voltage drives the base of Q1 toward cutoff. The Q1 collector current reduces and the collector voltage moves toward ground potential. The base current of Q4 is reduced, causing the collector voltage of Q4 to advance toward the 15-V source. Diode, CR1, is reverse biased and the base of Q3 is driven positively. Emitter current flows in Q3 to charge the gate capacitance of Q10. The gate voltage of Q10 becomes positive.

The voltage divider string of R1-6, and C1-6, establishes a fixed distributed gate potential of Q5-9.

The drain current increases in Q10, which causes the drain voltage to decrease. This decrease produces gate drive to Q9 since the source voltage of Q9 becomes less than the gate voltage.

This ripple process continues up the string, until Q5 is energized. The drain voltage of Q5 falls toward ground potential.

It is to be noted that the capacitor and resistor divider string are driven from the drain terminal of Q5. As the applied voltage of the Q5-10 amplifier string is reduced, the individual gate voltage potential of Q5-9 are proportionately reduced, and each device shares the instantaneous remaining applied voltage.

As the drain voltage falls, less current flows through R15 and R18. When the reduction current is equivalent to the injected current through R20, the differential pair is again brought into balance, and drive voltage is reduced to Q10, and the output voltage stabilizes.

Capacitors, C10-11, and R13 afford current pullup when the input pulse is no longer present, since energy was stored in the capacitors.

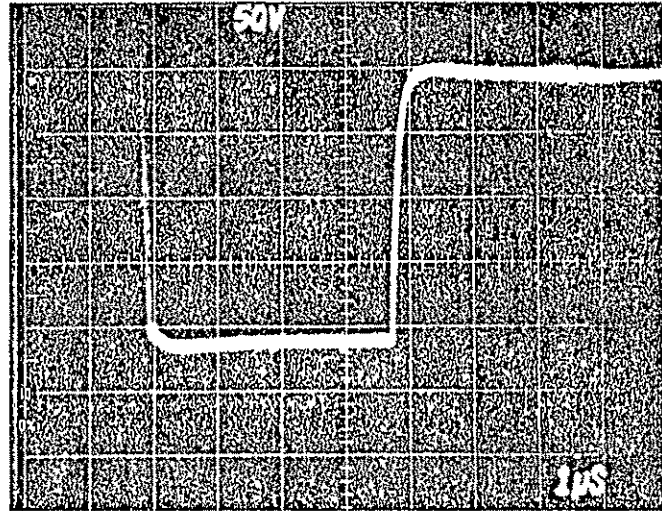
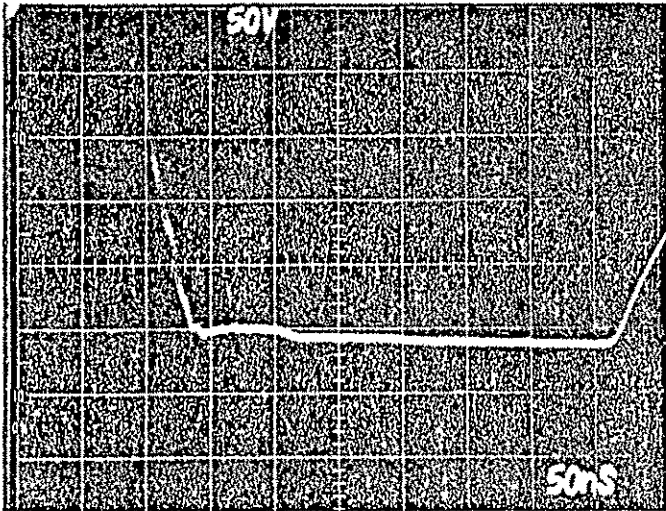
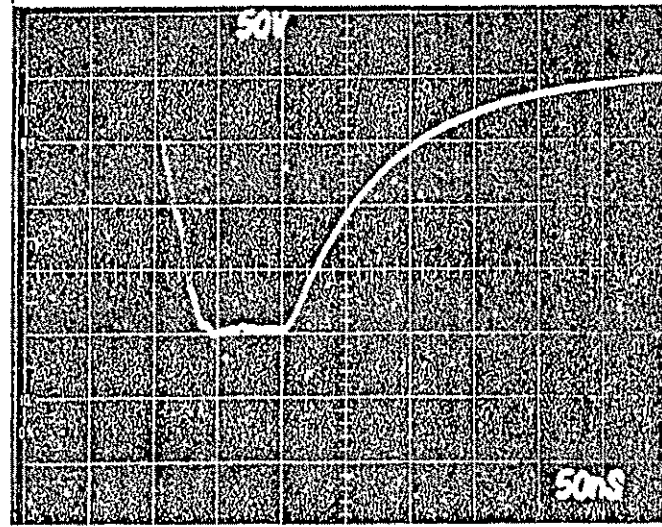
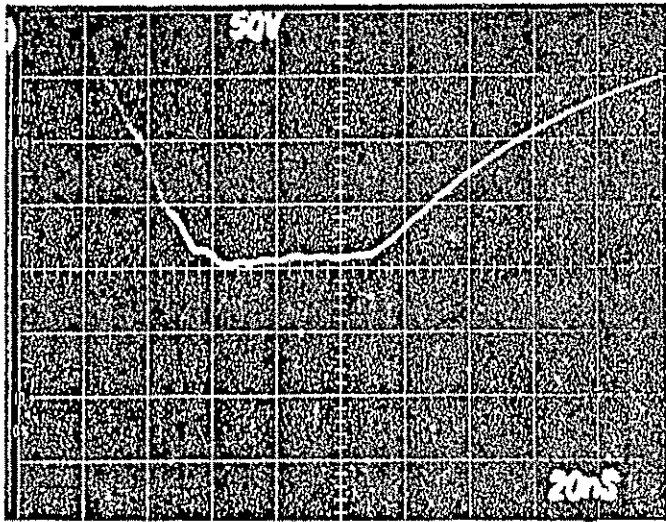
The performance of this circuit is well illustrated from the oscilloscope trace photographs of Figure A-1 and Figure A-2. Figure A-1 illustrates complete stability with the capacitive load. Figure A-2 was taken with only the resistive load and illustrates the lack of stability in the loop response. This is no great problem since normal operation includes the capacitive load.

The present loop gain of the driver is $\approx 2,000$. Tests indicate that this value may be altered, in order to adjust the overall control loop servo gain, with no great problems arising.

9. Avalanche Transistor Pockels Cell Driver

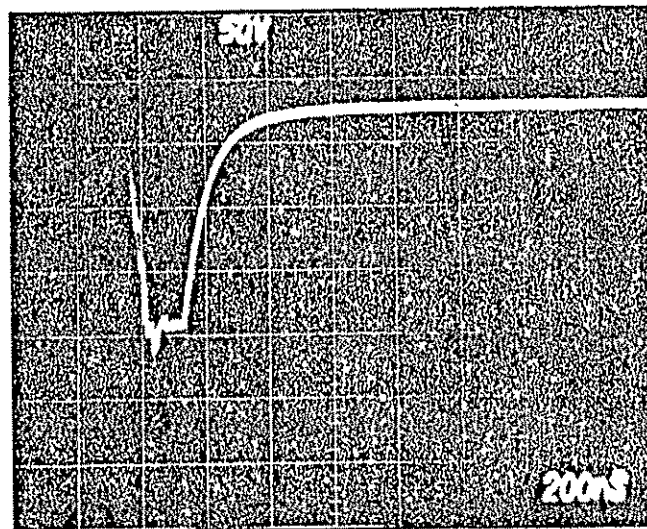
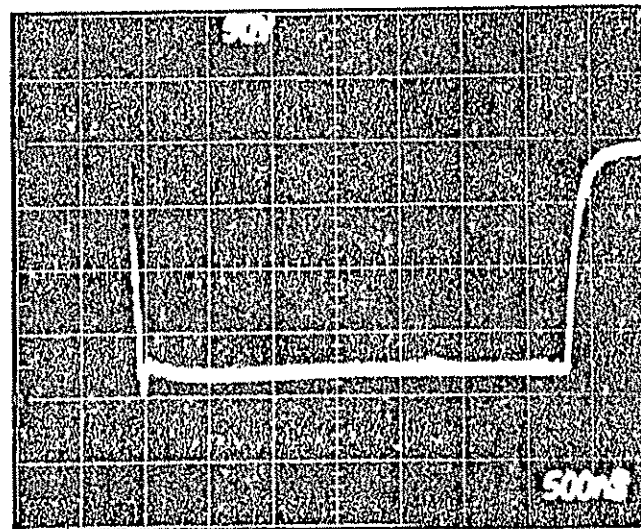
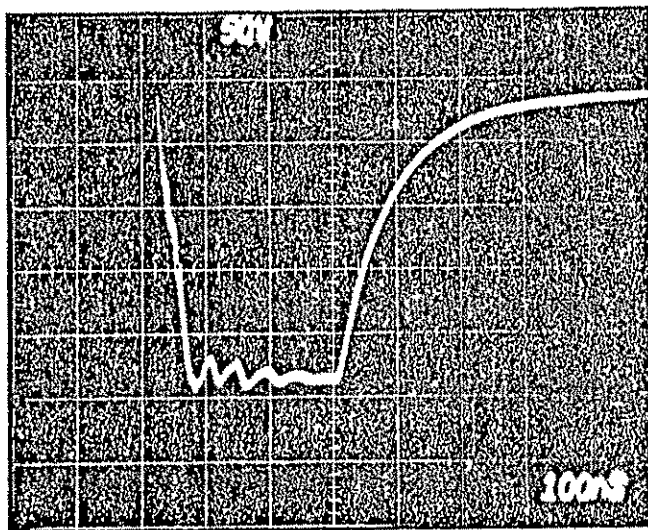
a. Introduction

Prior to the discussion of specific Pockels cell driver circuitry, it is necessary to characterize the avalanche action of the transistor. The discussion is concerned with the external properties of avalanche transistor switches, such as bias current and bias voltage, and is intended to illustrate usage of the device rather than design of the transistor junction.



F804-2

Figure A-1. Revised Driver Output Wave Forms C_L Terminated



F804-3

Figure A-2. Revised Driver Output Wave Forms Output Terminated R_T Only

b. Breakdown Characteristics

Because avalanche transistors operate in breakdown, a brief description of breakdown characteristics is in order. Figure A-3 depicts the avalanche transistor collector breakdown characteristics. BV_{CER} is the collector-emitter breakdown voltage for a specified external resistance from base to emitter of the transistor. Increasing the voltage across the transistor above the breakdown potential causes the collector current to increase until it reaches the level termed I_{HOR} , or the hold-off current. After I_{HOR} is reached, the transistor appears as a negative resistance element -- that is, for voltages between the value of BV_{CER} and BV_{CEO} -- and the breakdown avalanches to a value near BV_{CEO} . If the collector current is further increased beyond I_{HEO} , the open-base breakdown characteristics will further drop the collector voltage to a low-voltage level equivalent to $V_{CE(sat)}$.

The first avalanche -- that is, from BV_{CER} to BV_{CEO} -- is termed low-current-mode avalanche. If the collector current supplied by the low-current-mode avalanche is sufficient to overcome I_{HEO} , the device enters the high-current-avalanche state. When I_{HEO} is small, only the high-current avalanche is detectable.

Figure A-4 illustrates the relationships of BV_{CER} and the base emitter resistance R_{BE} . It should be noted that the choice of R_{BE} is limited to reasonable low values to maintain the maximum voltage differential between BV_{CER} and BV_{CEO} . If R_{BE} is chosen too large in value, the difference between BV_{CER} and BV_{CEO} will be too small to generate sufficient collector current to exceed I_{HEO} and the high-current-mode-avalanche state will not occur.

Hold-off current versus R_{BE} obeys a curve similar to that shown in Figure A-5. As can be seen, hold-off current can be changed merely by alteration of the external R_{BE} resistance value.

Two types of collector bias arrangements are used in avalanche transistor circuits -- current biasing and voltage biasing. Each has advantages and disadvantages.

A device is current-biased if V_{CC} is greater than BV_{CER} . The quiescent collector current is limited by R_L and must be less than I_{HOR} . In a voltage-biased circuit, V_{CC} is slightly less than BV_{CER} , but sufficiently greater than BV_{CEO} to ensure high-current-mode-avalanche operation.

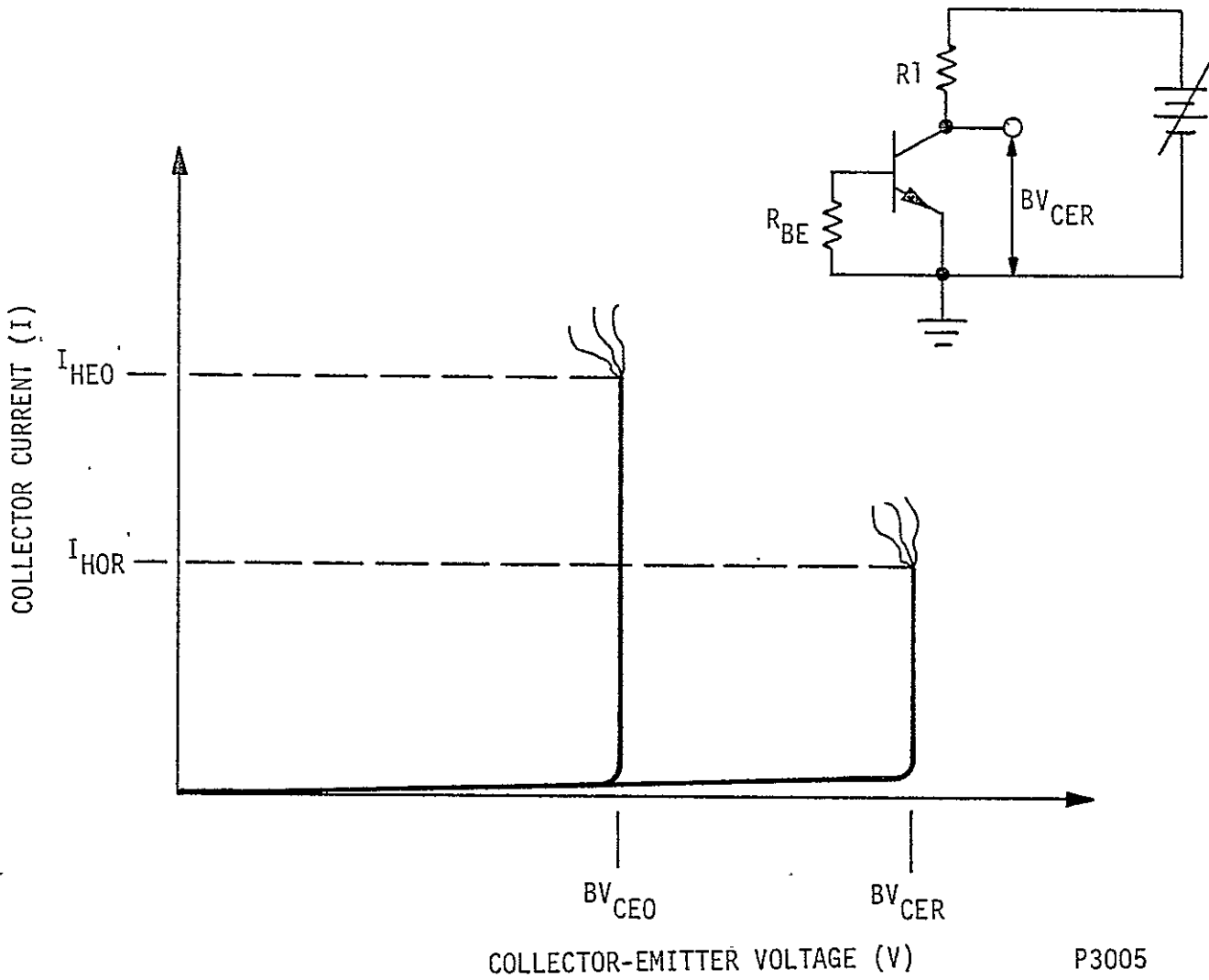
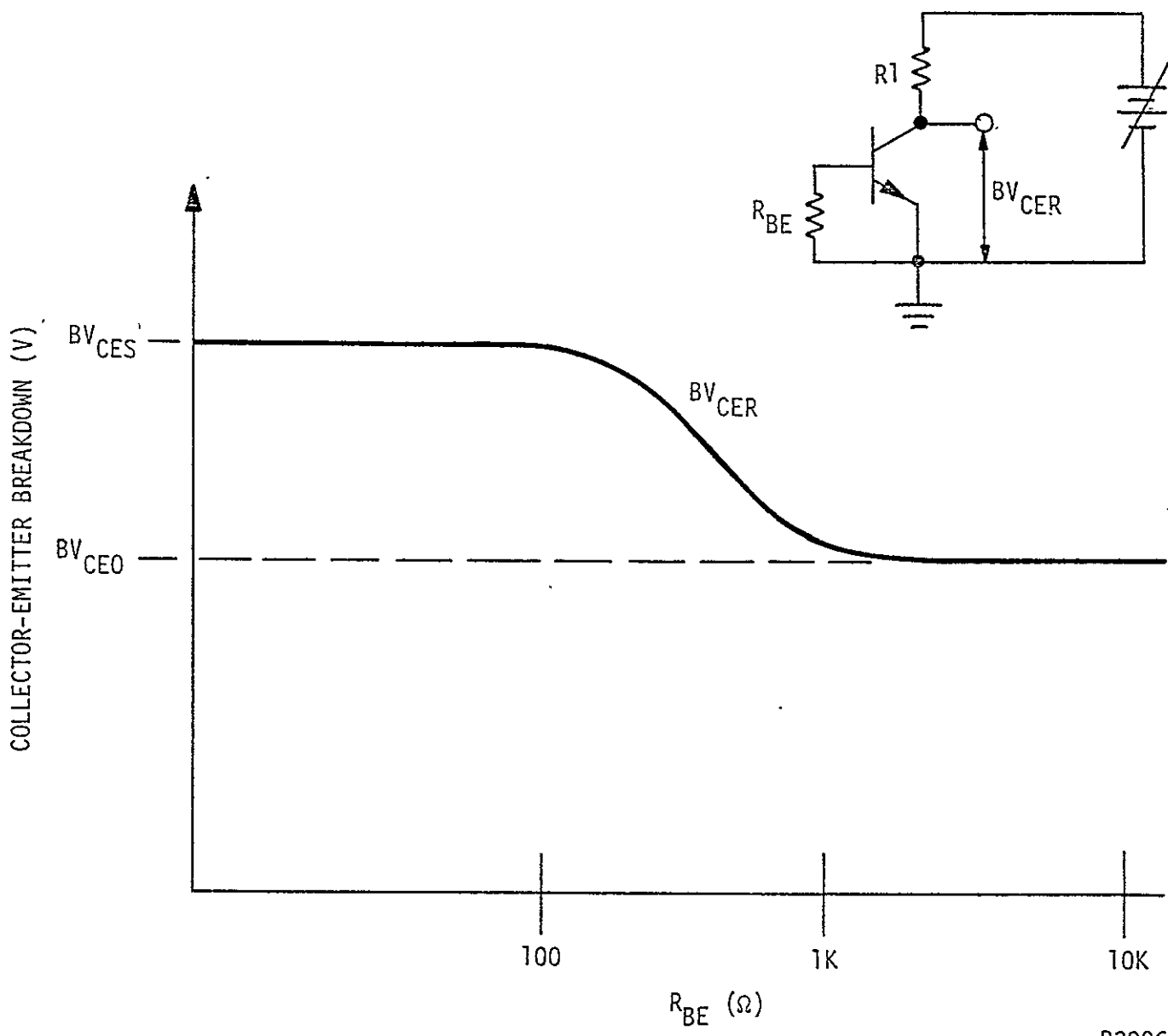
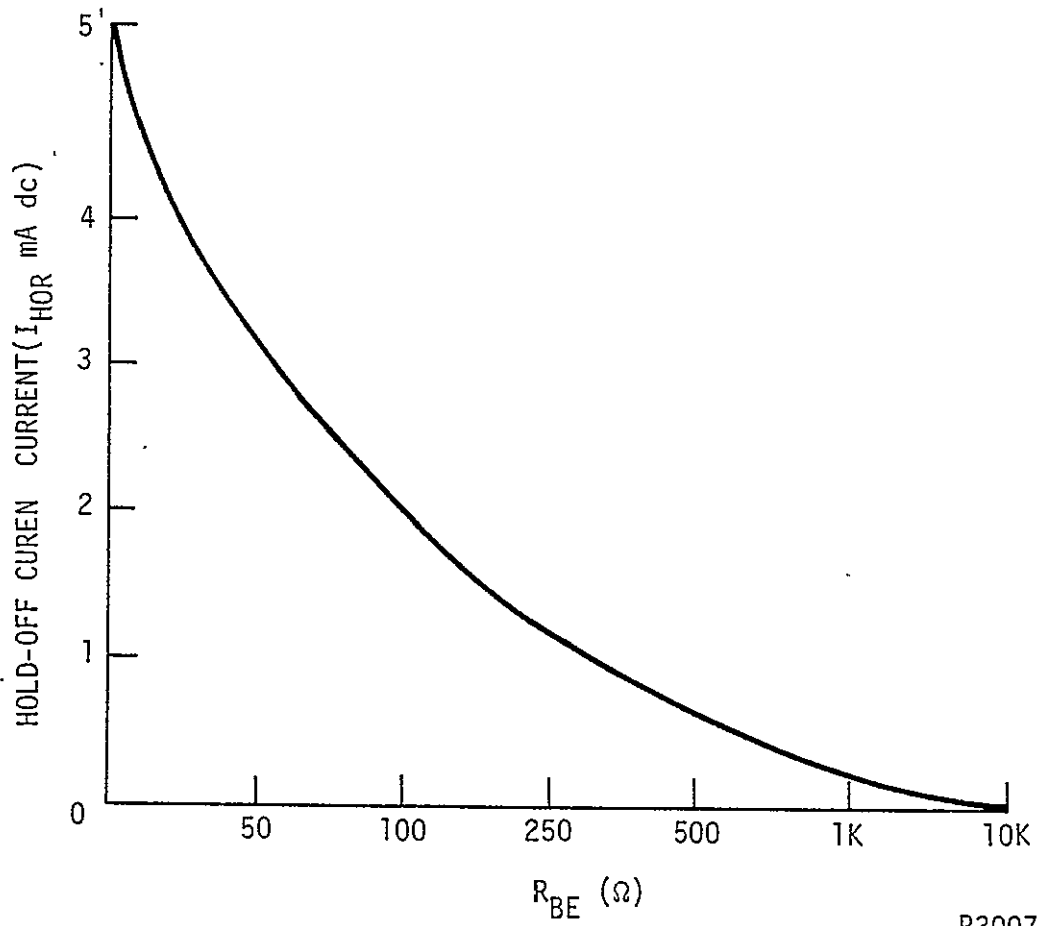


Figure A-3. Avalanche Transistor Collector Breakdown Characteristics



P3006

Figure A-4. BV_{CER} versus R_{BE}



P3007

Figure A-5. I_{HOR} versus R_{BE} (typical)

Generally, the voltage-bias technique is used where the power budget and/or dissipation limits preclude current biasing. Obviously, the voltage-biasing technique imposes a moderate voltage stability requirement, whereas the current-biasing technique removes the stability requirement to the extent that the quiescent R_L current must not exceed the I_{HOR} value. The current-biasing technique generally provides shorter delays and risetimes associated with increased voltage and current outputs.

c. Typical Avalanche Transistor Circuit

A typical avalanche transistor circuit is depicted in Figure A-6. A discussion of the circuit operation will clarify some of the previous voltage and current related parameters.

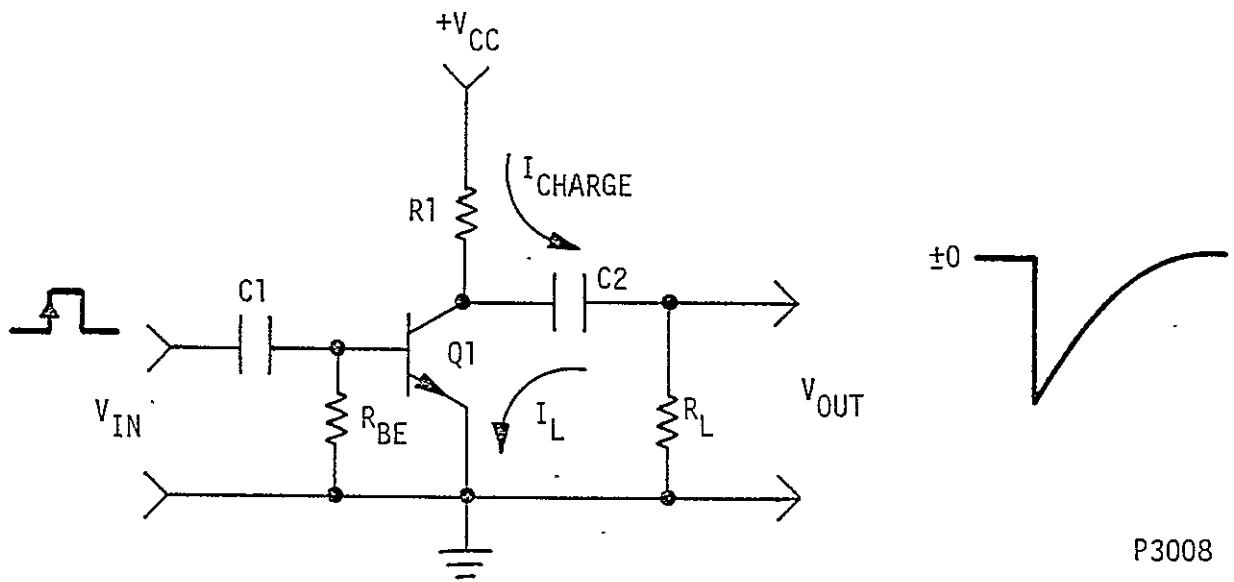
Assume that the circuit is biased in the quiescent-current mode. In the off or holding state, load capacitor C_2 is charged through resistor R_L . The voltage charge on capacitor C_2 is equal to BV_{CER} because the transistor diverts charging current for values of current less than I_{HOR} . It is assumed that the V_{CC} level is adjusted to produce a quiescent collector current through R_L which is less than I_{HOR} .

When a short positive pulse is applied to the base of the transistor Q_1 , the collector current and Q_1 exceeds I_{HOR} and the transistor avalanches to $V_{CE(sat)}$ to present a low impedance to the discharge loop. Capacitor C_2 is unable to discharge immediately because of the impedance of R_L ; therefore, most of the voltage charge of C_2 is impressed across R_L .

Because R_L is generally a very low value, the capacitor discharges rapidly. When the discharge loop current falls to a value below I_{HOR} , the avalanche transistor impedance again becomes high and the capacitor again charges to BV_{CER} through R_L . The cycle can now repeat.

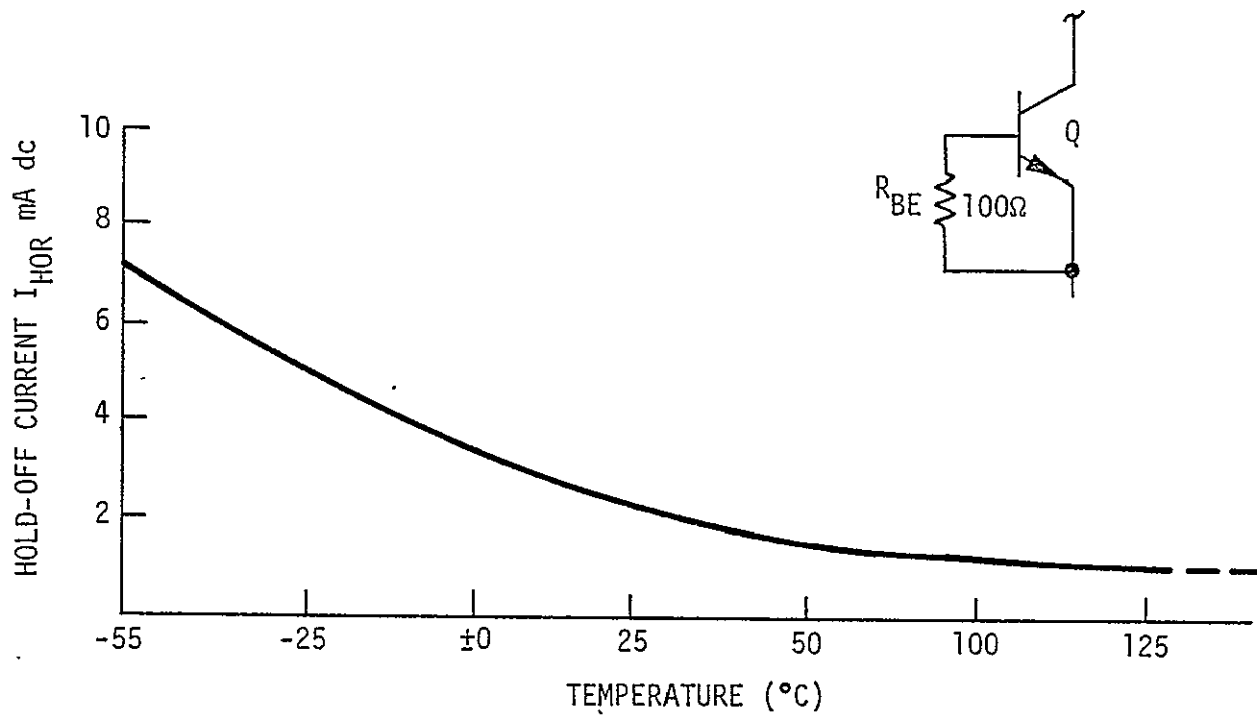
It is significant to note that once avalanche action is initiated, the base drive pulse provides no control and the cycle is irreversible.

Avalanche transistors can be successfully operated over a wide temperature range. When a wide temperature range is to be encountered, the prime parameter to consider is the I_{HOR} . Figure A-7 depicts the I_{HOR} change with temperature.



P3008

Figure A-6. Typical Avalanche Transistor Circuit



P3009

Figure A-7. I_{HOR} versus Temperature (typical)

A device with a 2.5- to 3.0-mA dc I_{HOR} at 25°C can be expected to exhibit about 1.0-mA dc I_{HOR} at 150°C and a 5- to 7-mA dc I_{HOR} at a temperature of -55°C. Surprisingly, the V_{CER} voltage value changes very little with changes in temperature. The change results in a ΔV slope which can be either positive or negative and generally exhibits a change $\leq \pm 200$ PPM/°C. Therefore, when the worst case drift is considered, a collector voltage stability of $\pm 1\%$ is achievable over a temperature excursion of $\pm 50^\circ\text{C}$. This stability factor is of significance because the output voltage is dependent primarily upon the BV_{CER} level.

d. Recovery Recharge Time

The remaining discussion of the preliminary characteristics of avalanche transistor circuits is the recover, or recharge, time. Again a current-bias technique will be assumed. Figure A-8 graphically illustrates the recovery.

Because R_L in Figure A-6 is many times R_L in the current-biased arrangement, Equation (A-1) represents the curve of capacitor recharge in Figure A-8.

$$V_{CE} = V_{CE}(\text{sat}) + [V_{CC} - V_{CE}(\text{sat})] [1 - e^{-t/RLC}] \quad (\text{A-1})$$

BV_{CER} is the final voltage, so Equation (A-1) simplifies to Equation (A-2)

$$e^{t/RLC} = \frac{V_{CC} - V_{CE}(\text{sat})}{V_{CC} - BV_{CER}} \quad (\text{A-2})$$

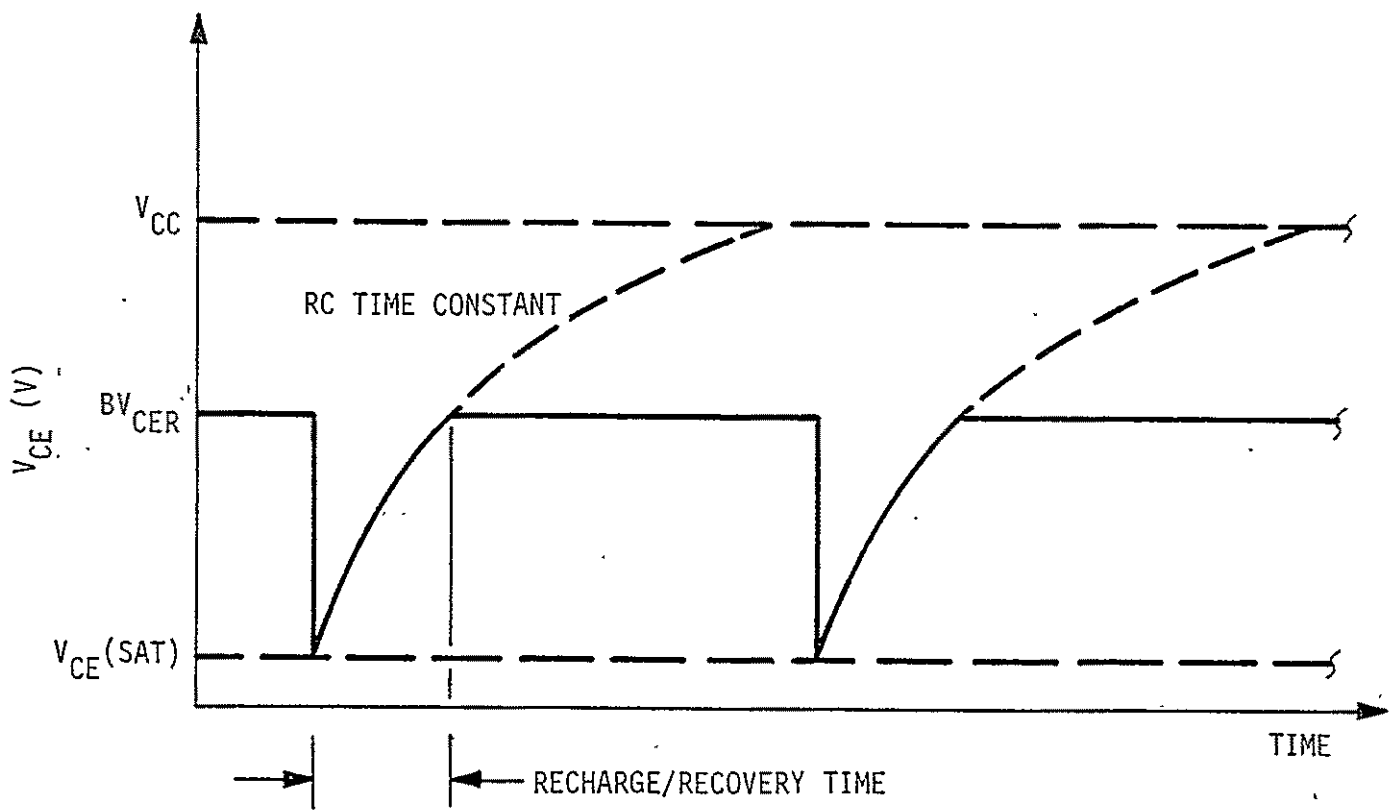
Thus, recharge time becomes:

$$t = RLC \ln \frac{V_{CC} - V_{CE}(\text{sat})}{V_{CC} - BV_{CER}}$$

When operating in the current biased mode, the maximum repetition rate is the reciprocal of recharge time, or $1/t$.

e. Specific Pockels Cell Driver Circuitry

The specific Pockels cell driver circuitry will now be discussed. As its name "Avalanche Transistor Pockels Cell Driver" implies, the driver circuitry relies upon the avalanche switch to generate the drive to the Pockels cell. The avalanche switch is



P3010

Figure A-8. Collector Waveforms for Current Biased Operation

selected because of the extremely short time interval required to collapse the impressed voltage across the transistor. Theoretically, the collector-emitter voltage collapses in less than 0.8 nsec.

Certain problem areas relating to transistor packaging technique -- lead inductance, inter-electrode stray capacitance, bonding lead resistance and miscellaneous other considerations -- increase the voltage collapse time significantly. International Laser Systems has innovated a novel Pockels cell driver construction technique to overcome most of the problem areas and to enhance the voltage collapse. A later discussion will illustrate the technique utilized.

The selected Pockels cell requires $\lambda/4$ voltage change to be effective. This voltage equates to approximately 3 kV. Obviously, the avalanche transistor driver must either switch a 3-kV voltage, or generate a 3-kV voltage.

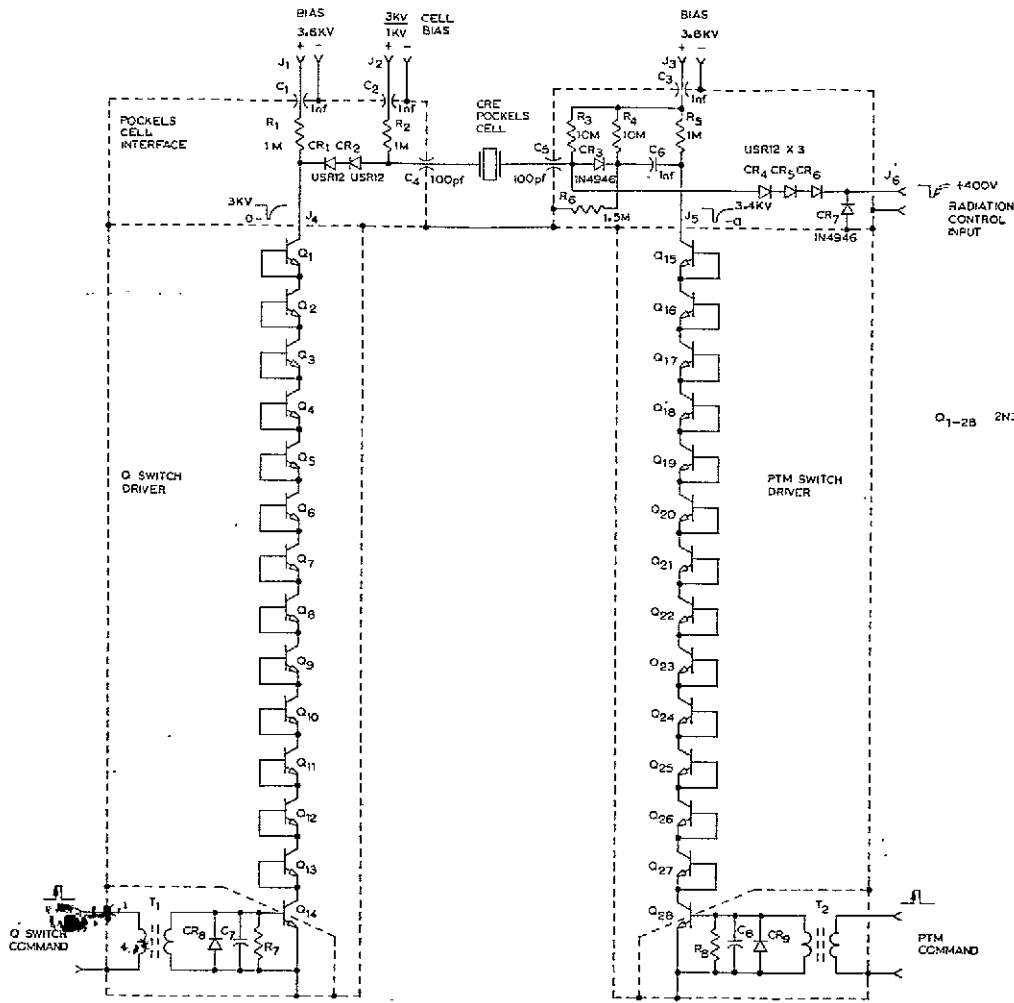
One technique, currently in use at ILS, consists of several avalanche transistors operated in a series configuration to generate voltage switching in the kilovolt region. Several stages of transistor groups are operated in a Marx generator connection to build additive voltages as required by the application. This technique is viable for most applications; however, where switching speed is paramount in the design criterion, the added inductance and stray capacitance associated with this technique renders the approach unsatisfactory.

The only viable approach to achieve the speed requirement necessitates the avalanche transistors be operated in the series configuration to discharge the $\lambda/4$ voltage of 3.25 kV. The selected collector-current bias mode is compatible with series connection of the transistors. A large value resistor establishes the bias-current level and removes the requirement that the high-voltage supply be closely regulated. Additionally, the low-bias current allows a small high-voltage supply to be chosen.

Schematic D1018734 illustrates the Pockels cell driver in schematic format.

The operation of the series configured switch is essentially the same as previously described for a single avalanche device. Transistors Q1 through Q14 comprise the avalanche switch. Resistor R1 establishes the bias current level and establishes the Pockels cell quiescent voltage at 3500-Vdc. The BV_{CER} composite

REVISIONS				
ZONE	LTR	DESCRIPTION	DATE	APPROVED



Q1-28 2N3019 (AVALANCHE GRADED)

FOLEBOT FRAME 2

FOLEBOT FRAME

QTY		RECD	ITEM	PART NUMBER	SYM	DESCRIPTION	CODE IDENT NO	MATERIAL AND SPECIFICATIONS
←		←		←		←		
LIST OF PARTS								
REFERENCE UNLESS SPECIFIED			SIGNATURE			DATE		
DRAWN			DRAFTSMAN			KEL		
CHECKED			CHECKER			DATE		
MATERIAL			MATERIAL			DATE		
DWG			DWG			DATE		
DWG			DWG			DATE		
DWG			DWG			DATE		
DWG			DWG			DATE		
DWG			DWG			DATE		
DWG			DWG			DATE		
DASH NO	QTY RECD	NEXT ASBY	USED ON	APPLICATION	SCALE		SHEET OF	
					A-41			

P4774

INTERNATIONAL LASER SYSTEMS INC. ORLANDO FLORIDA

TITLE
POCKELS CELL DRIVERS

SIZE CODE IDENT NO (DRAWING NO) REV
D 34860 1018734

D
C
B
A
REV 1018734

for the 14 transistors selected equates to 3.5-kVdc when biased at approximately 100 μ A. Only transistor Q14 is actively controlled by the event-initiate pulse.

Current flows in R7, and the base-emitter junction of transistor Q14 when the pulse is applied. Collector current flows in Q14 and Q14 enters avalanche conduction mode. The collector voltage of Q14 falls to near-ground potential or $V_{CE(sat)}$. Under this condition, transistor Q13 is voltage-stressed beyond BV_{CEr} and the I_{HOR} current is exceeded. Therefore, Q13 enters avalanche conduction. Similarly, each successive stage enters avalanche conduction until Q1 also is in the avalanche conduction mode. This action causes the collector voltage of Q1 to become a voltage level near zero $V_{CE(sat)} \times 14$; the Pockels cell voltage also is discharged through diodes CR₁ and CR₂.

At first inspection, the ripple action appears to occur rather slowly; however, this is not the case at all. Because the devices are biased in the current mode, each device is operating at a collector current of approximately 100 A in the direction approaching I_{HOR} . When the collector current of Q14 increases as the result of the drive pulse, all 13 other transistors also experience an increase in collector current because they are series connected. Thus, all transistors enter avalanche conduction essentially simultaneously.

The load resistance of the discharge circuitry consists of the series resistance component of the Pockels cell, the lead inductance/resistance and the "on resistance" of the avalanche switch. Because all of these are small, the Pockels cell capacity "sees" the minimum resistance and discharges rapidly. Typical indicated fall time from the 90% to 10% points is ≤ 4 nsec.

The input initiate command occurs through transformer T₁. Diode CR_g is reverse biased during the initiate command; however, when the avalanche string collapses the base of Q14 experiences a large negative spike pulse, which diode CR_g suppresses.

The PTM driver is identical to the Q-switch driver, with the exception that the transistors are selected to afford an output voltage excursion of 3,400 V.

APPENDIX B

GENERATION BREAKDOWN



International Laser Systems, Inc.

CODE IDENT NO.

34860

GENERATION
BREAKDOWN

GB *1016815*

REV

—

LINE	INDENTURE												QTY N/A	D S	PART/ITEM NUMBER	NOMENCLATURE	NEXT ASSY	EFFECTIVITY	
	1	2	3	4	5	6	7	8	9	0	1	2							
1	X													1		D1016815-9	LASER RANGEFINDER ASSY		
2	X													1		J1016270-9	OPTICAL BED, MACHINING		
3	X													1		J1016270-1	OPTICAL BED MACHINING		
4	X													1		C1016253-1	PAD, PRISM#1 MOUNTING		
5	X													1		C1016254-1	PAD, PRISM#2 MOUNTING		
6	X													1		C1016255-1	PAD, PRISM#3 MOUNTING		
7	X													1		C1016156-1	LOCATOR, PRISM#1		
8	X													2		B1016012-1	LOCATOR, PRISM SHOULDER		
9	X													1		B1016157-1	LOCATOR, PRISM#3		
10																			
11																			
12																			
13	X													1		C1015460-1	PRISM#1		
14	X													1		C1015461-1	PRISM#2		
15	X													1		C1015462-1	PRISM#3		
16	X													2		B1015853-9	RETAINER ASSY, PRISMS#1,#2		
17	X													1		C1015791-1	RETAINER, PRISMS#1,#2		
18	X													1		B1015794-1	PAD, SILICONE, PRISMS#1,#2		
19																			
20																			
21																			
22	X													1		B1015854-9	RETAINER ASSY, PRISM#3		
23	X													1		C1015792-1	RETAINER, PRISM#3		
24	X													2		B1015795-1	PAD, SILICONE, PRISM#3		
25																			

PREPARED BY
K. CHEEK

TITLE *LASER RANGEFINDER
ASSEMBLY*

JOB NO.
0739A

SHEET
1 OF *16*



International Laser Systems, Inc.

CODE IDENT NO.

34860

GENERATION
BREAKDOWNGB *D1016815*

REV

-

LINE	INDENTURE												QTY N/A	D S	PART/ITEM NUMBER	NOMENCLATURE	NEXT ASSY	EFFECTIVITY
	1	2	3	4	5	6	7	8	9	0	1	2						
1																		
2																		
3	X													6	B1015834-1	BRACKET, CORNER		
4	X													1	B1016887-1	INSULATING SHT, AMPLIFIER		
5	X													1	B1016889-1	INSULATING SHT, OSCILLATOR		
6	X													1	B1016886-1	INSULATING SHT, Q SWITCH		
7	X													1	C1015590-1	DOUBLE POLARIZER ASSY		
8	X													1	C1015391-1	PLATFORM, DOUBLE POLARIZER		
9	X													1	C1015387-9	MOUNT, DOUBLE POLARIZER		
10	X													1	C1015638-1	WEDGED POLARIZER		
11	X													1	C1015640-1	POLAZER, EXIT		
12																		
13																		
14	X													1	A1008451-9	ADJUSTER, POLARIZER		
15	X													1	C1015591-9	WEDGED RISLEY PRISM ASSY		
16	X													1	C1014649-1	BASE, RISLEY PRISM MOUNT		
17	X													1	C1014652-9	MOUNT RISLEY PRISM CELL#1,#2		
18	X													1	C1014652-1	MOUNT RISLEY PRISM CELL#1,#2		
19																		
20																		
21																		
22	X													1	C1014650-1	CELL, PRISM #1		
23	X													1	C1014651-1	CELL, PRISM #2		
24	X													1	C1015636-1	PRISM #1		
25	X													1	C1015637-1	PRISM #2		

PREPARED BY
*K. CHEEK*TITLE *LASER RANGEFINDER
ASSEMBLY*JOB NO.
*0739A*SHEET
2 OF



International Laser Systems, Inc.

CODE IDENT NO.

34860

GENERATION
BREAKDOWN

GB *D1016815*

REV

-

LINE	INDENTURE												QTY N/A	D S	PART/ITEM NUMBER	NOMENCLATURE	NEXT ASSY	EFFECTIVITY
	1	2	3	4	5	6	7	8	9	0	1	2						
1																		
2																		
3																		
4	X													2	A1012406-3	ADJUSTER, FOLDING MIRROR		
5	X													1	D1015794-9	AVALANCHE DRIVER ASSY		
6	X													2	B1015975-9	CONDUCTOR ASSY		
7	X													1	A1015976-1	CONDUCTOR		
8																		
9																		
10																		
11	X													2	A1015982-1	HOLDER, O-RING		
12	X													1	C1015984-1	HOUSING		
13	X													1	B1015983-1	COVER		
14	X													1	A1015986-1	GASKET		
15	X													2	A1015979-1	SPECIAL HEX NUT		
16	X													2	A1015977-9	CONTACT RING ASSY		
17	X													1	A1015978-1	HOLDER, CONTACT RING		
18	X													1	B1016268-3	RING, CONTACT		
19																		
20																		
21																		
22	X													2	A1015980-1	CONTACTOR		
23	X													2	B1015981-1	INSULATOR		
24	X													4	B1015241-1	STRAP		
25	X													2	B1012880-9	AVALANCHE DRIVER		

PREPARED BY
K. CHEEK

TITLE *LASER RANGEFINDER
ASSEMBLY*

JOB NO.
0739A

SHEET
3 OF



International Laser Systems, Inc.

CODE IDENT NO.

34860

GENERATION
BREAKDOWN

GB *D1016815*

REV

-

LINE	INDENTURE												QTY N/A	D S	PART/ITEM NUMBER	NOMENCLATURE	NEXT ASSY	EFFECTIVITY
	1	2	3	4	5	6	7	8	9	0	1	2						
1				X									1		A1012282-1	CAP, INSULATING		
2				X									1		B1012279-1	HOUSING		
3				X									1		B1012277-1	SLEEVE, INSULATING		
4				X									13		A1012891-9	AVALANCHE TRANSISTOR ASSY		
5				X									1		A1012281-1	RING, INSULATING		
6																		
7																		
8																		
9				X									1		B1012278-9	TRANSISTOR MOUNT ASSY		
10				X									1		B1012278-1	RING		
11				X									1		B1012278-3	MOUNT		
12																		
13																		
14																		
15				X									1		A1012283-1	CONTACTOR		
16				X									1		A1012280-1	CAP, HOUSING		
17				X									1		A1012896-9	FERRITE TRANSFORMER		
18																		
19																		
20																		
21				X									1		A1012897-9	PLUG ASSY		
22																		
23																		
24																		
25																		

PREPARED BY
K. CHEEK

TITLE *LASER RANGEFINDER
ASSEMBLY*

JOB NO. *0739A*

SHEET *4* OF *4*



International Laser Systems, Inc.

CODE IDENT NO.

34860

GENERATION
BREAKDOWNGB *D1016815*

REV

-

LINE	INDENTURE												QTY N/A	D S	PART/ITEM NUMBER	NOMENCLATURE	NEXT ASSY	EFFECTIVITY
	1	2	3	4	5	6	7	8	9	0	1	2						
1																		
2																		
3																		
4	X													1	B1016825-1	SUPPORT BLOCK, AVALANCHE DR		
5	X													1	C1014772-9	KD*P INDEX MATCHED CELL		
6	X	X												1	C1015880-1	CELL, KD*P		
7	X	X	X											2	B1014750-9	CONTACT ASSY		
8	X	X	X	X										1	C1014740-1	RETAINER, KD*P CELL		
9	X	X	X	X	X									1	C1014887-1	SPRING, CONTACT		
10	X	X	X	X	X	X								1	B1016268-1	RING, CONTACT		
11																		
12																		
13	X	X												1	C1015341-1	KD*P MODULATOR CRYSTAL		
14	X	X	X											1	C1015879-1	MOUNT, CELL BRACKET		
15	X	X	X	X										1	C1015878-1	BRACKET, CELL		
16	X	X	X	X	X									2	B1015608-1	SPACER, TEFLON		
17	X	X	X	X	X	X								1	C1014797-1	WINDOW, STEINMETZ CELL		
18	X	X	X	X	X	X	X							1	C1014797-3	WINDOW, STEINMETZ CELL		
19	X	X	X	X	X	X	X	X						2	C1014749-1	RETAINER, KD*P WINDOW		
20	X	X	X	X	X	X	X	X	X					3	B1003798-41	STUD, PORRO MOUNT		
21	X	X	X	X	X	X	X	X	X	X				3	B1003799-3	BALL, PORRO MOUNT		
22	X	X	X	X	X	X	X	X	X	X	X			2	C1015877-1	CONTACTOR, KD*P CELL RETAINER		
23	X	X	X	X	X	X	X	X	X	X	X	X		1	A1014798-1	SCREW, MODIFIED		
24																		
25																		

PREPARED BY
*K. CHEEK*TITLE *LASER RANGEFINDER
ASSEMBLY*JOB NO.
*0739A*SHEET
5 OF



International Laser Systems, Inc.

CODE IDENT NO.

34860

GENERATION
BREAKDOWN

GB *D1016815*

REV

1

LINE	INDENTURE												QTY N/A	D S	PART/ITEM NUMBER	NOMENCLATURE	NEXT ASSY	EFFECTIVITY
	1	2	3	4	5	6	7	8	9	0	1	2						
1																		
2																		
3	X													1	D1016343-9	MODELOCKER ASSY		
4	X													1	C1014772-19	KDXP INDEX MATCHED CELL		
5	X													1	C1015880-1	CELL, KDXP		
6	X													1	B1014750-19	CONTACT ASSY		
7	X													1	C1016266-1	RETAINER, MODELOCKER WINDOW#1		
8	X													1	C1014887-1	SPRING CONTACT		
9	X													1	B1016268-1	RING, CONTACT		
10																		
11																		
12																		
13	X													1	B1014750-29	CONTACT ASSY		
14	X													1	C1016267-1	RETAINER, MODELOCKER WINDOW#2		
15	X													1	C1014887-1	SPRING CONTACT		
16	X													1	B1016268-1	RING, CONTACT		
17																		
18																		
19																		
20	X													1	C1015341-1	KDXP MODULATOR CRYSTAL		
21	X													2	B1015608-1	SPACER, TEFLON		
22	X													1	C1014797-1	WINDOW, STEINMETZ CELL		
23	X													1	C1014797-3	WINDOW, STEINMETZ CELL		
24	X													2	C1014749-1	RETAINER, KDXP WINDOW		
25	X													1	A1014798-1	SCREW, MODIFIED		

PREPARED BY

K. CHEEK

TITLE

*LASER RANGEFINDER
ASSEMBLY*

JOB NO.
0739A

SHEET
6 OF



International Laser Systems, Inc.

CODE IDENT NO.

34860

GENERATION
BREAKDOWN

GB *D1016815*

REV

-

LINE	INDENTURE												QTY N/A	D S	PART/ITEM NUMBER	NOMENCLATURE	NEXT ASSY	EFFECTIVITY
	1	2	3	4	5	6	7	8	9	0	1	2						
1	X												1		C1016339-1	CAVITY, MODELOCKER		
2	X												1		C1016340-1	CONTACT, MODELOCKER CAP		
3	X												1			GROUND LUG		
4	X												1		C1016341-1	COIL, MODELOCKER		
5	X												1		B1016342-1	BRACKET, MODELOCKER CELL		
6	X												3		B1003798-41	STUD, PORRO MOUNT		
7	X												3		B1003799-3	BALL, PORRO MOUNT		
8	X												1		B1016346-1	STRIP, CONTACT		
9	X												1		B1016346-3	STRIP, CONTACT		
10																		
11																		
12																		
13	X												1		C1014760-9	LASER CAVITY ASSY (OSCILLATOR)		
14	X												1		D1014734-1	CAVITY BOX		
15	X												1		C1015342-1	LASER ROD		
16	X												3		B1015298-3	BAFFLE, FILTERED CAVITY		
17	X												2		A1000519-1	RETAINER, ROD O-RING		
18	X												2		A1000526-1	WASHER, ROD		
19																		
20																		
21																		
22	X												1		D1014734-3	CAVITY BOX		
23	X												1		C1015342-3	LASER ROD		
24	X												3		B1015298-1	BAFFLE, FILTERED CAVITY		
25	X												2		A1000519-3	RETAINER, ROD O-RING		

PREPARED BY
M. CHECK

TITLE *LASER RANGEFINDER
ASSEMBLY*

JOB NO.
0739A

SHEET
7 OF



International Laser Systems, Inc.

CODE IDENT NO.

34860

GENERATION
BREAKDOWN

GB *D1016815*

REV

1

LINE	INDENTURE												QTY N/A	D S	PART/ITEM NUMBER	NOMENCLATURE	NEXT ASSY	EFFECTIVITY	
	1	2	3	4	5	6	7	8	9	0	1	2							
1			X											2		A1000526-3	WASHER, ROD		
2																			
3																			
4																			
5			X											2		C1014733-1	REFLECTOR, LASER CAVITY		
6			X											2		C1014733-3	REFLECTOR, LASER CAVITY		
7			X											2		C1014733-5	REFLECTOR, LASER CAVITY		
8			X											2		C1014733-7	REFLECTOR, LASER CAVITY		
9			X											1		B1014731-1	FILTER		
10			X											1		B1014731-3	FILTER		
11			X											1		B1014731-5	FILTER		
12			X											1		B1014731-7	FILTER		
13			X											1		C1014732-9	CAVITY INSULATOR ASSY		
14			X											1		C1014732-1	INSULATOR, CAVITY		
15																			
16																			
17																			
18			X											1		B1015346-1	INSULATING SHEET		
19			X											1		C1016259-1	FLASHLAMP		
20			X											2		A1000518-1	RETAINER, FLASHLAMP O-RING		
21			X											2		B1003316-1	FITTING, COOLANT		
22			X											2		B1003316-3	FITTING, COOLANT		
23			X											1		B1008201-3	HOLDER, THERMOSTAT		
24																			
25																			

PREPARED BY
K. CHEEK

TITLE *LASER RANGEFINDER
ASSEMBLY*

JOB NO.
0739A

SHEET
8 OF

LINE	INDENTURE												QTY N/A	D S	PART/ITEM NUMBER	NOMENCLATURE	NEXT ASSY	EFFECTIVITY
	1	2	3	4	5	6	7	8	9	0	1	2						
1																		
2																		
3	X												1		C1014760-9	LASER CAVITY ASSY (AMPLIFIER)		
4	X												1		D1014734-1	CAVITY BOX		
5	X												1		C1015343-1	LASER ROD		
6	X												3		B1015298-3	BAFFLE, FILTERED CAVITY		
7	X												2		A1000519-1	RETAINER, ROD O-RING		
8	X												2		A1000526-1	WASHER, ROD		
9																		
10																		
11																		
12	X												2		C1014733-1	REFLECTOR, LASER CAVITY		
13	X												2		C1014733-3	REFLECTOR, LASER CAVITY		
14	X												2		C1014733-5	REFLECTOR, LASER CAVITY		
15	X												2		C1014733-7	REFLECTOR, LASER CAVITY		
16	X												1		B1014731-1	FILTER		
17	X												1		B1014731-3	FILTER		
18	X												1		B1014731-5	FILTER		
19	X												1		B1014731-7	FILTER		
20	X												1		C1014732-9	CAVITY INSULATOR ASSY		
21	X												1		C1014732-1	INSULATOR, CAVITY		
22																		
23																		
24																		
25	X												1		B1015346-1	INSULATING SHEET		

PREPARED BY
K. CHEEK

TITLE **LASER RANGEFINDER ASSEMBLY**

JOB NO.
0739A

SHEET **9** OF



LINE	INDENTURE												QTY N/A	D S	PART/ITEM NUMBER	NOMENCLATURE	NEXT ASSY	EFFECTIVITY	
	1	2	3	4	5	6	7	8	9	0	1	2							
1		X												1	C	1016259-1	FLASHLAMP		
2		X												2	A	1000518-1	RETAINER, LAMP O-RING		
3		X												2	B	1003316-1	FITTING, COOLANT		
4		X												2	B	1003316-3	FITTING, COOLANT		
5		X												1	B	1008201-3	HOLDER, THERMOSTAT		
6																			
7																			
8																			
9		X												1	C	1016085-9	APERTURE ASSY		
10		X												1	B	1016086-1	BASE, APERTURE MOUNT		
11		X												1	A	1016091-1	SIDE SUPPORT, APER MOUNT		
12		X												1	A	1016091-3	SIDE SUPPORT, APER MOUNT		
13		X												1	B	1016090-1	TOP, APERTURE MOUNT		
14		X												1	A	1016087-1	PLATE RETAINER, APER MT		
15		X												1	B	1016089-1	SLIDE, HORIZ, APER MOUNT		
16		X												1	B	1016088-1	APERTURE		
17		X												1	B	1016088-3	APERTURE		
18		X												1	B	1016088-5	APERTURE		
19																			
20																			
21																			
22		X												1	B	1014653-9	SCOPE, COMPENSATING		
23		X												1	B	1014656-1	BASE, ADJUST LENS MOUNT		
24		X												2	B	1014654-1	SLIDE, ADJUST LENS MOUNT		
25		X												2	B	1014655-1	MOUNT, LENS		

PREPARED BY

TITLE
LASER RANGE FINDER
ASSEMBLY

JOB NO.

0739A

SHEET

10 OF

LINE	INDENTURE												QTY N/A	D S	PART/ITEM NUMBER	NOMENCLATURE	NEXT ASSY	EFFECTIVITY
	1	2	3	4	5	6	7	8	9	0	1	2						
1		X											1	C	1017189-1	LENS		
2		X											1	C	1017189-3	LENS		
3																		
4																		
5																		
6	X												1	A	1016904-9	COMPENSATING WEDGE ASSY		
7		X											1	C	1006836-9	PLATFORM, MIRROR MOUNT		
8			X										1	C	1006836-1	PLATFORM		
9																		
10																		
11																		
12		X											1	B	1015351-9	MOUNT, WEDGE		
13		X											1	C	1015639-1	COMPENSATING WEDGE		
14		X											2	A	1008399-1	CLAMP, MIRROR MOUNT		
15																		
16																		
17																		
18	X												2	C	1015240-9	FOLDING POLARIZER ASSY		
19		X											1	C	1015239-1	PLATFORM, POLARIZER MOUNT		
20		X											1	B	1007323-49	MOUNT, POLARIZER		
21		X											1	C	1015640-1	POLARIZER, EXIT		
22		X											2	A	1008399-1	CLAMP, MIRROR MOUNT		
23																		
24																		
25																		

PREPARED BY

TITLE
LASER RANGEFINDER
ASSEMBLY

JOB NO.

0739A

SHEET

11 OF . . .



International Laser Systems, Inc.

CODE IDENT NO.

34860

GENERATION
BREAKDOWN

GB 1016815

REV

LINE	INDENTURE												QTY N/A	D S	PART/ITEM NUMBER	NOMENCLATURE	NEXT ASSY	EFFECTIVITY	
	1	2	3	4	5	6	7	8	9	0	1	2							
1	X													1	C	1015766-9	MIRROR MOUNT TO BKT ASSY		
2		X												1	C	1015248-1	BRACKET, MIRROR MOUNT		
3		X												1	B	1015764-9	MIRROR MOUNT ASSY		
4			X											1	C	1015249-1	MOUNT, MIRROR		
5			X											1	B	1015828-9	MIRROR AND CELL ASSY		
6				X										1	B	1015827-1	CELL, MIRROR		
7				X										1	C	1015765-1	MIRROR		
8																			
9																			
10																			
11			X											1	B	1015246-1	RETAINER, MIRROR		
12			X											3	B	1015247-1	STUD		
13																			
14																			
15																			
16		X												3	B	1003799-3	BALL, PORRO MOUNT		
17		X												3	B	1015852-1	NUT, HEX		
18																			
19																			
20																			
21		X												1	C	1016191-9	PORRO PRISM ASSY		
22			X											1	C	1016190-1	PLATE, ADJUSTING		
23			X											1	B	1016189-1	SLEEVE, PORRO PRISM		
24			X											1	C	1017188-1	PORRO PRISM		
25			X											3	B	1003799-3	BALL, PORRO MOUNT		

PREPARED BY

TITLE
LASER RANGEFINDER
ASSEMBLYJOB NO.
0739ASHEET
12 OF



International Laser Systems, Inc.

CODE IDENT NO.

34860

GENERATION
BREAKDOWN

GB 1016815

REV

LINE	INDENTURE												QTY N/A	D S	PART/ITEM NUMBER	NOMENCLATURE	NEXT ASSY	EFFECTIVITY
	1	2	3	4	5	6	7	8	9	0	1	2						
1		X											3	B	1003798-13	STUD, PORRO MOUNT		60
2																		
3																		
4																		
5	X												1	D	1016884-9	COVER ASSY		
6		X											1	D	1016884-1	FLANGE		
7		X											1	B	1016770-9	APERTURE		
8			X										1	B	1016771-1	HOUSING, APERTURE		
9			X										1	B	1016777-1	RING, RETAINER		
10			X										1	B	1016773-1	RETAINER DISC, THREADED		
11		X											1	C	1016776-1	WINDOW		
12																		
13																		
14																		
15	X												4	B	1016888-1	STANDOFF		
16	X												1	A	1016817-1	SLEEVE, FIB OP HOLDER		
17	X												1	A	1016818-1	NUT, FIBER OP HOLDER		
18	X												4	A	1016821-1	STUD, SUPPORT PLATE		
19	X												1	D	1016816-9	PLATE, SUPPORT		
20	X												1	D	1016816-1	SUPPORT PLATE		
21																		
22																		
23																		
24	X												2	B	1016820-1	ADAPTER, COOLING LINE		
25	X												2	B	1003316-7	FITTING, COOLANT		

PREPARED BY

TITLE
LASER RANGEFINDER
ASSEMBLY

JOB NO.
0739A

SHEET
13 OF



International Laser Systems, Inc.

CODE IDENT NO.

34860

GENERATION
BREAKDOWN

GB 1016815

REV

LINE	INDENTURE												QTY N/A	D S	PART/ITEM NUMBER	NOMENCLATURE	NEXT ASSY	EFFECTIVITY
	1	2	3	4	5	6	7	8	9	0	1	2						
1	X												2	C	1016885-9	BOX, ELECT COMP		
2	X												1	C	1016824-1	CONNECTOR PLATE		
3	X												1	C	1016823-1	BLOCK, SINGLE SUPPORT		
4	X												1	C	1016822-1	BLOCK, DUAL SUPPORT		
5	X												1	A	1016819-1	GASKET, CONNECTOR		
6	X												3	A	1015109-1	BALL, KINEMATIC MOUNT		
7	X												3	A	1015110-1	STUD, KINEMATIC MOUNT		
8	X												3	B	1015108-3	SOCKET, BALL		
9																		
10																		
11																		
12																		
13																		
14																		
15																		
16																		
17																		
18																		
19																		
20																		
21																		
22																		
23																		
24																		
25																		

PREPARED BY

TITLE
LASER RANGEFINDER
ASSEMBLY

JOB NO.
0739A

SHEET
14 OF



LINE	INDENTURE												QTY N/A	D S	PART/ITEM NUMBER	NOMENCLATURE	NEXT ASSY	EFFECTIVITY
	1	2	3	4	5	6	7	8	9	0	1	2						
1			X												D1018733-	S.B. PRF GENERATOR		
2			X												D1018737-	PTM SYNCHRONIZER		
3			X												D1013775-	SCH SIMMER SUPPLY		
4			X												1013775-	P.C. LAYOUT		
5			X												D1018734-	POCKEL CELL DRIVER		
6			X												C1008877-S	HIGH VOLT REGULATOR		
7			X												C1008877-CL	HIGH VOLT REG ASSY		
8			X												C1008879	SCH PWR CONV MOD		
9			X												C1008878	SCH HIGH VOLT ASSY		
10			X												A1008876-PL	LOW VOLT REG DRIVER		
11																		
12																		
13																		
14																		
15																		
16																		
17																		
18																		
19																		
20																		
21																		
22																		
23																		
24																		
25																		

PREPARED BY

TITLE
LASER RANGEFINDER
ASSEMBLY

JOB NO.
0739A

SHEET
15 OF



LINE	INDENTURE												QTY N/A	D S	PART/ITEM NUMBER	NOMENCLATURE	NEXT ASSY	EFFECTIVITY
	1	2	3	4	5	6	7	8	9	0	1	2						
1																		
2																		
3																		
4		X												1	C1000728-1	PLATE		
5		X												1	C1000727-1	HEATSINK		
6		X												1	C1014551-9	BOARD, COMPONENT MTG		
7		X												1	A1014562-1	4 POLE SWITCH, MODIFIED		
8		X												1	A1016809-1	FAN, VOLTAGE REG MTG PLATE		
9																		
10																		
11																		
12		X												1	D1018735-1	FREQUENCY SYNTHESIZER		
13		X												1	D1018738-1	RADIATION CONTROL		
14		X												1	D1018736-1	INTERFACE ELEC POKKEL CELL		
15		X												1	D1014553-1	SPACEBORNE POWER SUPPLY		
16		X												1	D1017712-1	SPACEBORNE HEAD WIRING		
17																		
18																		
19																		
20																		
21																		
22																		
23																		
24																		
25																		

PREPARED BY
K. CHEEK

TITLE *LASER RANGEFINDER ASSEMBLY*

JOB NO.
0739A

SHEET *16* OF *16*

APPENDIX C

OPTICAL BED THERMAL ANALYSIS

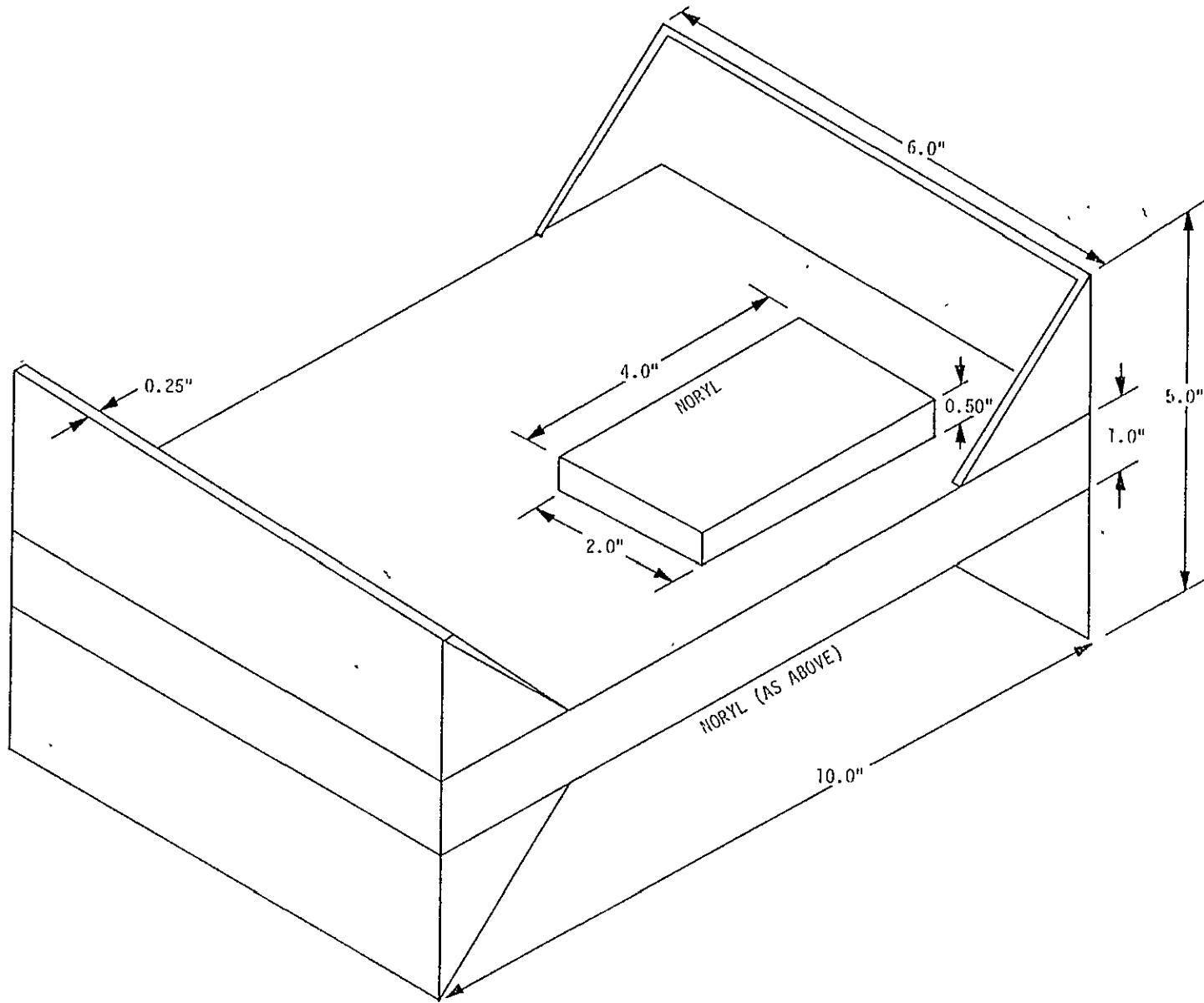
OPTICAL BED THERMAL ANALYSIS

1. BACKGROUND AND RESULTS

The thermal and g-load analysis presented in this appendix was performed on a preliminary design version of the Spaceborne optical bed. The bed configuration analyzed is shown in Figure C-1. The actual bed was shown previously in Figure 3-3. The latter bed has more Invar area for heat transfer to the surrounding environment. Thus, the temperature rise of the actual bed and the resulting distortions are 20% less than that of the bed analyzed. The actual optical bed is also more rigid structurally than that analyzed and distortions due to gravity are estimated to be approximately 10% less than those calculated for the preliminary bed design.

One basic result of the optical bed analysis was that the optical bed should be mounted vertically. This was implemented in the actual design via a kinematic mounting beneath the optical bed as shown previously in Figure 3-32. The actual mounting of the optical bed is more stable than the cases considered in the following analysis with respect to bed distortion by gravity. The kinematic mounting assumed in the analysis is fully equivalent to the actual kinematic mounting with respect to thermal distortion since, by definition, a kinematic mounting permits free thermal expansion in all three dimensions.

A second basic result of the analysis was the optical bed expansion in the direction parallel to the optical path. With reference to Figure C-2, this expansion corresponds to the net distance increase between nodes 34 and 44 or nodes 134 and 144. The analytical model assumes heat input into the bed from the noryl blocks on which the oscillator and amplifier pump cavities are mounted. As a worst case, the temperature of the noryl blocks were assumed to be 130°F due to heat from the pump cavities. Under this condition, with the bed initially at 70°F, the average of the expansion between nodes 34 and 44 and nodes 134 and 144 was 5.88×10^{-5} inches. The average rise in bed temperature was 5.5°F. Thus the optical bed expanded 1.07×10^{-5} inches per Fahrenheit degree increase in temperature. For the bed length of 10 inches along the laser optical paths, this expansion corresponds to an actual thermal coefficient of expansion of 1.07×10^{-6} in/in/°F. Thus, the analysis, shows that the optical bed expands with temperature very nearly the same as the INVAR material with a coefficient of 0.9×10^{-6} in/in/°F. This latter conclusion was the objective of the optical bed analysis. For vertical mounting,



C-2

Figure C-1. Optical Bed Configuration

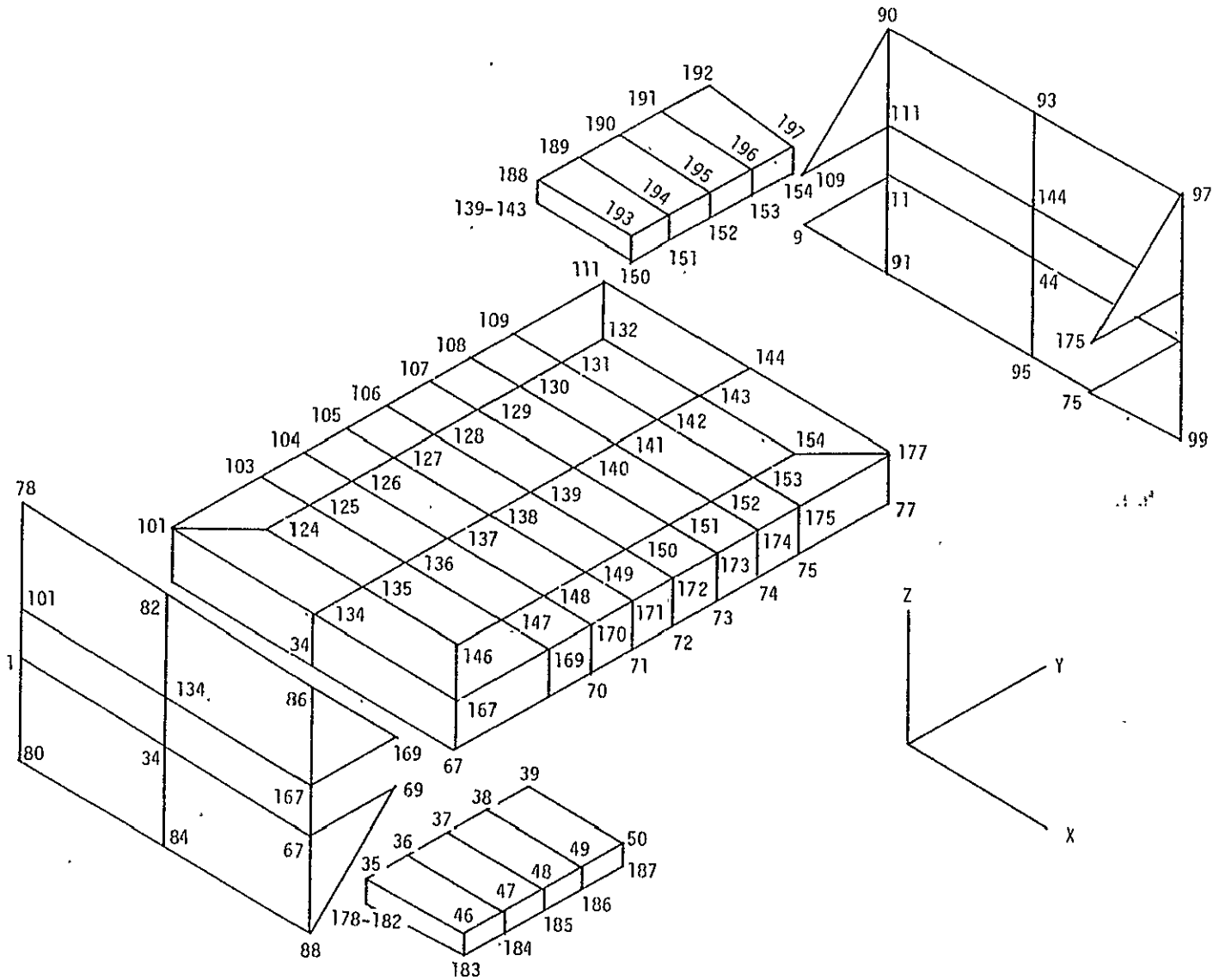


Figure C-2. Bed Model Node Description

gravity distortion of the bed was an order of magnitude less than those due to thermal distortion.

2. INTRODUCTION

A thermal structural math model of the Spaceborne Laser Rangefinder optical bed was constructed and four load cases were run with the ANSYS computer program (Engineering Analysis System). The cases considered were: 1) determine temperature distribution; 2) determine distortion due to temperature effects; 3) determine distortion due to weight-when horizontally mounted; 4) determine distortions due to weight when vertically mounted. The results obtained for each of these load cases are presented and discussed in this report.

3. MODEL DESCRIPTION

The math model is an assemblage of three dimensional isoparametric solid elements. Most of the elements are cubical but the elements representing the corner brackets have a triangular shape. Each element is identified by nodes at the corners of the geometric solid. It is at these corners (or nodes) that the temperatures and distortions are calculated. Figure C-1 shows a sketch of the physical configuration and Figure C-2 shows the model as defined by the node points. The nodes numbered from 1 to 77 are on the bottom of the 1.0 inch thick bed. Nodes 101 to 177 are on the top of the bed. These nodes are arranged such that node 1 is directly below node 101 etc. This system of numbering does not apply to the end plates nor to the Noryl plates. There are additional nodes in the printout which are not shown in Figure C-2. For example, directly behind node 78 is node 79. These additional nodes are of no interest to the reader but were necessary in formulating the problem. Note node 78 and 79 have essentially the same temperature and distortion. Table C-1 is a list of the physical properties for Invar and Noryl used in the analysis. Node 43 is constrained such that there is no displacement in the X, Y or Z directions. Node 24 is constrained in the X direction- and node 46 is constrained in the Z direction. There are no constraints on rotation in any direction.

4. TEMPERATURE DISTRIBUTION

The temperature on the surface of the Noryl pads facing away from the Invar slab was assumed to be 130°F. All exposed

TABLE C-1. MATERIAL PROPERTIES

	<u>INVAR</u>	<u>NORYL</u>
Modulus of Elasticity (psi)	20.5 (10) ⁺⁶	1.20 (10) ⁺⁶
Expansion Coefficient (IN/IN/°F)	.9 (10) ⁻⁶	1.2 (10) ⁻⁵
Poisson's Ratio	.27	.27
Density (#/IN ³)	.382	.0602
Thermal Conductivity (BTU/HR-IN-°F)	.50417	.00769

SYSTEM OF UNITS (BTU, POUND, INCH, HR, °F)

surfaces both on the Noryl and Invar are assumed to exchange heat with a 68°F sink. The effective coefficient for heat transfer was assumed to be 1.0 BTU/HR-FT-°F. This coefficient is representative of combined radiation and free convection for the temperature range considered. The resulting temperatures at each node are presented in Table C-2. Figure C-3 shows some of the temperature results in pictorial form. The maximum temperature is 78.89°F at the interface between the Noryl pad and the Invar (node 151) on the top face. The lowest temperature is 73.11 at node 80 which is located at the lower corner of the end bracket. The average temperature is about 75.5°F or 7.5°F above the 68°F sink.

The temperature distribution obtained from this run was used as input to determine the thermal distortions.

5. THERMAL DISTORTION

For the thermal distortion run the assumption is made that there is no distortion at 70°F. The distortion at each node is then calculated for the change in temperature from 70°F to the temperatures calculated previously. No stresses were calculated because they are very low and the computer cost for calculating them is not justified. Table C-3 is the computer printout of the distortions. Figures C-4 and C-5 are plots of the thermal distortion greatly exaggerated. The maximum distortion in the Invar slab is $0.5809 (10)^{-4}$ at node 67.

The Noryl has a maximum distortion of $0.1063 (10)^{-3}$ at node 185. The thermal distortions are much greater than those from gravity (at one g). It is worthwhile to remember that this is a linear problem and that the results may be extrapolated. If the temperature difference between the source and the sink is increased each temperature will increase proportionally as will each distortion. Maximum thermal distortions are of the order of 5×10^{-5} inches in the Invar and 10^{-3} inches in the Noryl. Since the average temperature is 5.5°F above the no distortion temperature of 70°F the thermal distortion is approximately $1. \times 10^{-5}$ in/°F.

6. GRAVITY EFFECTS (HORIZONTAL)

The horizontal configuration is defined as the Z direction being down or as shown in Figures C-1 and C-2. A one "g" acceleration was applied in the Z direction and the resulting distortions were calculated. The temperature is assumed to be 70°F for this run (no thermal distortions). Table C-3 is the computer printout of

Table C-2. TEMPERATURE DISTRIBUTION

NODE	TEMP	NODE	TEMP	NODE	TEMP	NODE	TEMP	NODE	TEMP
1	73.864	2	73.185	3	74.634	4	75.249	5	75.574
6	75.692	7	75.605	8	75.318	9	74.744	10	0.
11	74.022	12	73.983	13	0.	14	74.689	15	75.286
16	75.615	17	75.731	18	75.643	19	75.356	20	74.797
21	0.	22	74.138	23	0.	24	74.579	25	74.998
26	75.487	27	75.810	28	76.009	29	75.995	30	75.688
31	75.246	32	74.787	33	74.955	34	74.904	35	75.860
36	77.042	37	77.674	38	78.078	39	77.941	40	77.587
41	77.279	42	76.647	43	75.784	44	75.114	45	75.155
46	76.277	47	77.545	48	78.315	49	78.848	50	78.644
51	78.173	52	77.775	53	77.022	54	76.139	55	0.
56	75.211	57	0.	58	76.552	59	77.569	60	78.079
61	78.272	62	78.162	63	77.688	64	76.731	65	0.
66	75.484	67	75.122	68	0.	69	76.413	70	77.531
71	78.028	72	78.220	73	78.100	74	77.644	75	76.605
76	0.	77	75.409	78	73.113	79	73.162	80	73.113
81	73.163	82	73.587	83	73.532	84	73.588	85	73.531
86	73.827	87	73.845	88	73.906	89	73.925	90	73.232
91	73.185	92	73.233	93	73.625	94	73.575	95	73.629
96	73.579	97	73.934	98	73.955	99	73.949	100	73.966
101	73.866	102	0.	103	74.632	104	75.247	105	75.569
106	75.692	107	75.609	108	75.320	109	74.746	110	0.
111	74.021	112	73.985	113	0.	114	74.687	115	75.284
116	75.607	117	75.731	118	75.650	119	75.358	120	74.799
121	0.	122	74.137	123	0.	124	74.645	125	75.138
126	75.615	127	75.958	128	76.009	129	75.846	130	75.560
131	75.107	132	74.720	133	74.950	134	74.901	135	75.616
136	76.524	137	77.197	138	77.547	139	77.941	140	78.119
141	77.755	142	77.164	143	76.027	144	75.115	145	75.157
146	75.938	147	76.868	148	77.674	149	78.124	150	78.644
151	78.896	152	78.415	153	77.700	154	76.477	155	0.
156	75.228	157	0.	158	76.531	159	77.584	160	78.113
161	78.272	162	78.128	163	77.676	164	76.725	165	0.
166	75.460	167	75.137	168	0.	169	76.391	170	77.543
171	78.050	172	78.220	173	78.077	174	77.635	175	76.598
176	0.	177	75.387	178	130.00	179	130.00	180	130.00
181	130.00	182	130.00	183	130.00	184	130.00	185	130.00
186	130.00	187	130.00	188	130.00	189	130.00	190	130.00
191	130.00	192	130.00	193	130.00	194	130.00	195	130.00
196	130.00	197	130.00						

ORIGINAL PAGE IS
OF POOR QUALITY

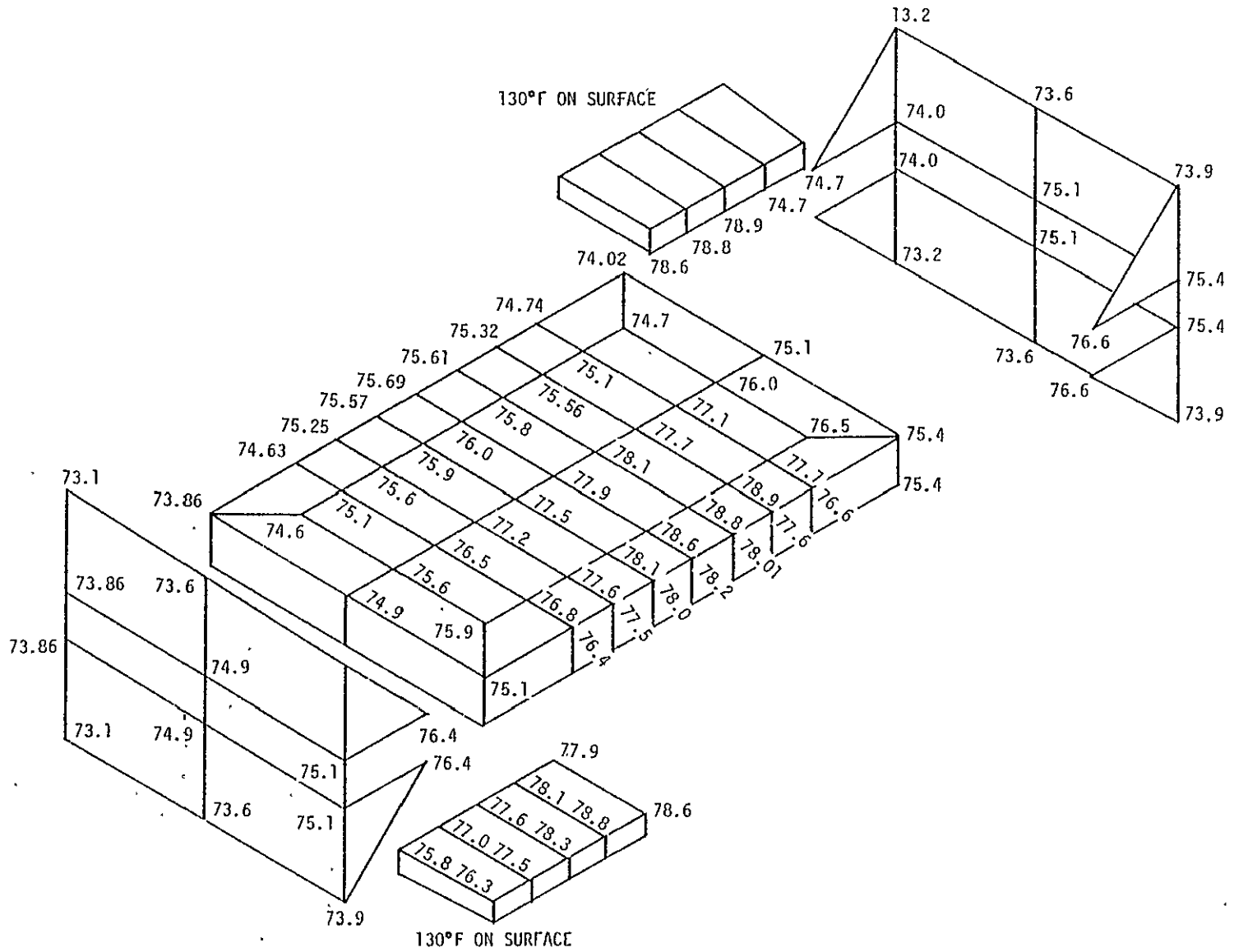


Figure C-3. Optical Bed Temperature Distribution

Table C-3. THERMAL DISTORTION

NOUE	UX	UY	UZ	NODE	UX	UY	UZ
1	.339H76F-05	.514942E-04	.370342E-05	99	.110051E-04	.645445E-05	-.990199E-05
2	-.170213F-04	.512710E-05	.369612E-05	100	.105510F-04	.433313E-05	-.862307E-05
3	-.47CO76F-05	.440030E-04	-.294871E-05	101	-.350070F-05	-.484755E-04	-.702844F-05
4	-.649488E-05	-.379285F-04	-.415390E-05	103	-.501026E-05	-.414296F-04	.147597E-05
5	-.782954E-05	-.316559E-04	-.389589E-05	104	-.659705F-05	-.376322E-04	.407197E-06
6	-.904538E-05	-.255800E-04	-.266758F-05	105	-.827477F-05	-.327852E-04	.929811E-06
7	-.100279F-04	-.200361E-04	-.135706E-05	106	-.992530E-05	-.272592E-04	.275427E-05
8	-.109865F-04	-.151396E-04	-.845797E-06	107	-.114419E-04	-.211689F-04	.350066E-05
9	-.120369E-04	-.112509E-04	-.152951E-05	108	-.126419E-04	-.149400E-04	.378175E-05
11	-.158748E-04	-.397714E-05	-.740086E-05	109	-.134821E-04	-.869015E-05	.261507E-05
12	-.255619E-05	-.506691E-04	.258252E-05	111	-.174317F-04	-.977875E-06	-.347730E-05
14	-.372073E-05	-.435369E-04	-.266049E-05	112	-.276497E-05	-.475793E-04	.627863E-05
15	-.542825E-05	-.375423E-04	-.416057E-05	114	-.392819E-05	-.411547E-04	.137687E-05
16	-.675032E-05	-.313224E-04	-.383985E-05	115	-.538778E-05	-.372094E-04	.435601F-05
17	-.781029E-05	-.252671E-04	-.246381E-05	116	-.702588E-05	-.324286E-04	.103527E-05
18	-.877113E-05	-.197355E-04	-.102722E-05	117	-.869010E-05	-.269149E-04	.249043F-05
19	-.976127E-05	-.149036E-04	-.433137E-06	118	-.102546E-04	-.208454E-04	.388430E-05
20	-.109316E-04	-.108707E-04	-.137436E-05	119	-.115590E-04	-.145783E-04	.422687E-05
22	-.143773E-04	-.424775E-05	-.628327E-05	120	-.124787E-04	-.850098E-05	.274721E-05
24	0.	-.478023E-04	0.	122	-.58958E-04	-.117272E-05	-.243629E-05
25	-.904367E-06	-.426002E-04	-.294303E-05	124	-.614740E-07	-.446296E-04	.418147E-05
26	-.209676E-05	-.366344E-04	-.454329E-05	125	-.491359E-06	-.405309E-04	.153475E-05
27	-.319600E-05	-.302750E-04	-.391591E-05	126	-.154802E-05	-.363244E-04	.405298E-06
28	-.399655E-05	-.241389E-04	-.202384E-05	127	-.307090E-05	-.316287E-04	.123090E-05
29	-.479188E-05	-.185762E-04	-.100533E-06	128	-.487658E-05	-.260038E-04	.337001E-05
30	-.587238E-05	-.138294E-04	-.913980E-06	129	-.667570E-05	-.199328E-04	.527960E-05
31	-.741963E-05	-.954018E-05	-.224184E-06	130	-.817788E-05	-.135260E-04	.592874E-05
32	-.959965E-05	-.532941E-05	-.287474E-05	131	-.958667E-05	-.748083E-05	.435329E-05
33	.898995E-05	-.530153E-04	.373655E-05	132	-.112829E-04	-.216961E-05	.143674E-05
34	.857814F-05	-.540410E-04	.476911E-05	133	.851709E-05	-.483269E-04	.785310E-05
35	.925641E-05	-.498100E-04	-.266050E-06	134	.835134E-05	-.493789E-04	.903042E-05
36	.930226E-05	-.435433E-04	-.543079E-05	135	.926574E-05	-.447995E-04	.480143E-05
37	.918802E-05	-.355127E-04	-.728278E-05	136	.993764E-05	-.400880E-04	.931047E-06
38	.896803E-05	-.271961E-04	-.598674E-05	137	.997077E-05	-.355022E-04	-.592653E-06
39	.845260E-05	-.197769E-04	-.107708E-05	138	.924067E-05	-.307665E-04	.142261E-05
40	.759401E-05	-.143118E-04	.342678E-05	139	.757166E-05	-.253188E-04	.594506E-05
41	.579092E-05	-.952233E-05	.542423E-05	140	.558023E-05	-.178819E-04	.108704E-04
42	.321836E-05	-.484441E-05	.388664E-05	141	.324865E-05	-.951344E-05	.121870E-04
43	0.	0.	0.	142	.824483E-06	-.139532E-05	.103565E-04
44	-.348477E-05	.477672E-05	-.423054E-05	143	-.176669E-05	-.500214E-05	.522348E-05
45	-.267329E-05	.367036E-05	-.304986E-05	144	-.501393E-05	.942830E-05	.207566E-06
46	.200576E-04	-.519772E-04	0.	145	-.405825E-05	.834965E-05	.122950E-05
47	.219158E-04	-.449720E-04	-.579622E-05	146	.196464E-04	-.464198E-04	.530043E-05
48	.235113E-04	-.356697E-04	-.768444E-05	147	.214183E-04	-.410616E-04	.962239E-06
49	.240862E-04	-.256175E-04	-.579927E-05	148	.228903E-04	-.359283E-04	-.701849E-06
50	.236041E-04	-.164942E-04	.566727E-06	149	.233053E-04	-.303053E-04	.207539E-05
51	.217621E-04	-.979992E-05	.629618E-05	150	.227223E-04	-.236322E-04	.782726E-05
52	.189845E-04	-.111023E-05	.904721E-05	151	.207610F-04	-.144857E-04	.142135E-04
53	.149502E-04	.113737E-05	.735695E-05	152	.177424E-04	-.436729E-05	.161202E-04
54	.106962E-04	.665489E-05	.300444E-05	153	.136879E-04	.504313E-05	.142572E-04
56	.222735E-04	-.565196E-04	.427084E-05	154	.934329E-05	.121989E-04	.849172E-05
58	.263384E-04	-.462994E-04	-.458175E-05	156	.219477E-04	-.514277E-04	.906844E-05
59	.284155E-04	-.365122E-04	-.690638E-05	158	.258289E-04	-.424058E-04	.853175E-06
60	.294271E-04	-.259199E-04	-.448422E-05	159	.280901E-04	-.368826E-04	-.552246E-06
61	.291527E-04	-.161415E-04	.130968E-05	160	.287732E-04	-.302753E-04	.234890E-05
62	.272448E-04	-.601085E-05	.734495E-05	161	.282708E-04	-.221650E-04	.840683E-05
63	.241564E-04	-.133332E-05	.102214E-04	162	.261343E-04	-.123658E-04	.142248E-04
64	.194886F-04	.432079E-05	.878440E-05	163	.227177E-04	-.169975E-05	.166673E-04
66	.112818E-04	.136822E-04	.549449E-06	164	.182264E-04	.822123E-05	.143692E-04
67	.229191E-04	-.588026E-04	.549650E-05	166	.983927E-05	.187410E-04	.558530E-05
69	.277471E-04	-.471740E-04	-.484016E-05	167	.226132E-04	-.529874E-04	.105793E-04
70	.298135E-04	-.368421E-04	-.679182E-05	169	.272957E-04	-.432184E-04	.133267E-05
71	.310345E-04	-.260382E-04	-.427728E-05	170	.298107E-04	-.372397E-04	-.541416E-06
72	.308734E-04	-.158623E-04	.165027E-05	171	.305840E-04	-.303310E-04	.244251E-05
73	.290670E-04	-.735174E-05	.749195E-05	172	.299915E-04	-.218446E-04	.850722E-05
74	.258999E-04	-.382161E-06	.106501E-04	173	.277528E-04	-.116444E-04	.144530E-04
75	.210026E-04	.574526E-05	.871493E-05	174	.241389E-04	-.774854E-06	.169957E-04
77	.113891E-04	.159167E-04	-.537838E-06	175	.196755E-04	.971091E-05	.151044E-04
78	-.267720E-05	-.425843E-04	.140633E-04	177	.992824E-05	.209878E-04	.483103E-05
79	-.230931E-05	-.414828E-04	.133294E-04	178	-.685490E-04	-.860121E-04	-.161483E-04
80	-.457030E-06	-.568764E-04	-.374266E-05	179	-.692232E-04	-.445062E-04	-.324726E-04
81	-.876425E-06	-.576817E-04	-.409300E-05	180	-.737457E-04	-.354917E-04	-.311047E-04
82	.755167E-05	.386226F-04	.157138E-04	181	-.681860E-04	-.260355E-04	-.332720E-04
83	.751223E-05	-.379163E-04	.144271E-04	182	-.673387E-04	.160141E-04	-.175697E-04
84	.910633F-05	-.583123E-04	-.24398E-05	183	.979106E-04	-.880617E-04	-.140718E-04
85	.967534F-05	-.576185E-04	-.27508E-05	184	.100361E-03	-.460280E-04	-.328195E-04
86	.180763E-04	.435608E-04	.195659E-04	185	.106322E-03	-.357160E-04	-.315091E-04
87	.179382E-04	-.420091E-04	.178846E-04	186	.101450F-03	-.244008E-04	-.330111E-04
88	.200274E-04	-.684270E-04	-.342450E-05	187	.996135E-04	.184892E-04	-.144577E-04
89	.200100E-04	-.664459E-04	-.436480F-05	188	-.690810E-04	-.611153E-04	.274403E-04
90	-.167090F-04	.489594E-05	.444478E-05	189	-.774317F-04	-.190481E-04	.381689E-04
91	-.112917E-04	-.988789E-05	-.147380F-04	190	-.804800E-04	-.954109E-05	.360326E-04
92	-.102633E-04	-.103598E-04	.135486F-04	191	-.784703E-04	-.440520F-06	.374283E-04
93	-.797335E-05	.134784E-04	.760035E-05	192	-.803208E-04	.411290E-04	.211671E-04
94	-.476571E-05	.127266E-04	.787701E-05	193	.978363E-04	-.588202E-04	.248541E-04
95	-.786527E-06	-.613524E-05	-.111038E-04	194	.971987E-04	-.156185F-04	.414378E-04
96	-.181598E-06	-.681994E-05	-.980009E-05	195	.995804E-04	-.432914E-05	.399739E-04
97	.317391F-05	.310714E-04	.140410E-04	196	.911302F-04	-.609072F-05	.413201E-04
98	.370087E-05	.205899E-04	.143938E-04	197	.861798E-04	.482033E-04	.246352E-04

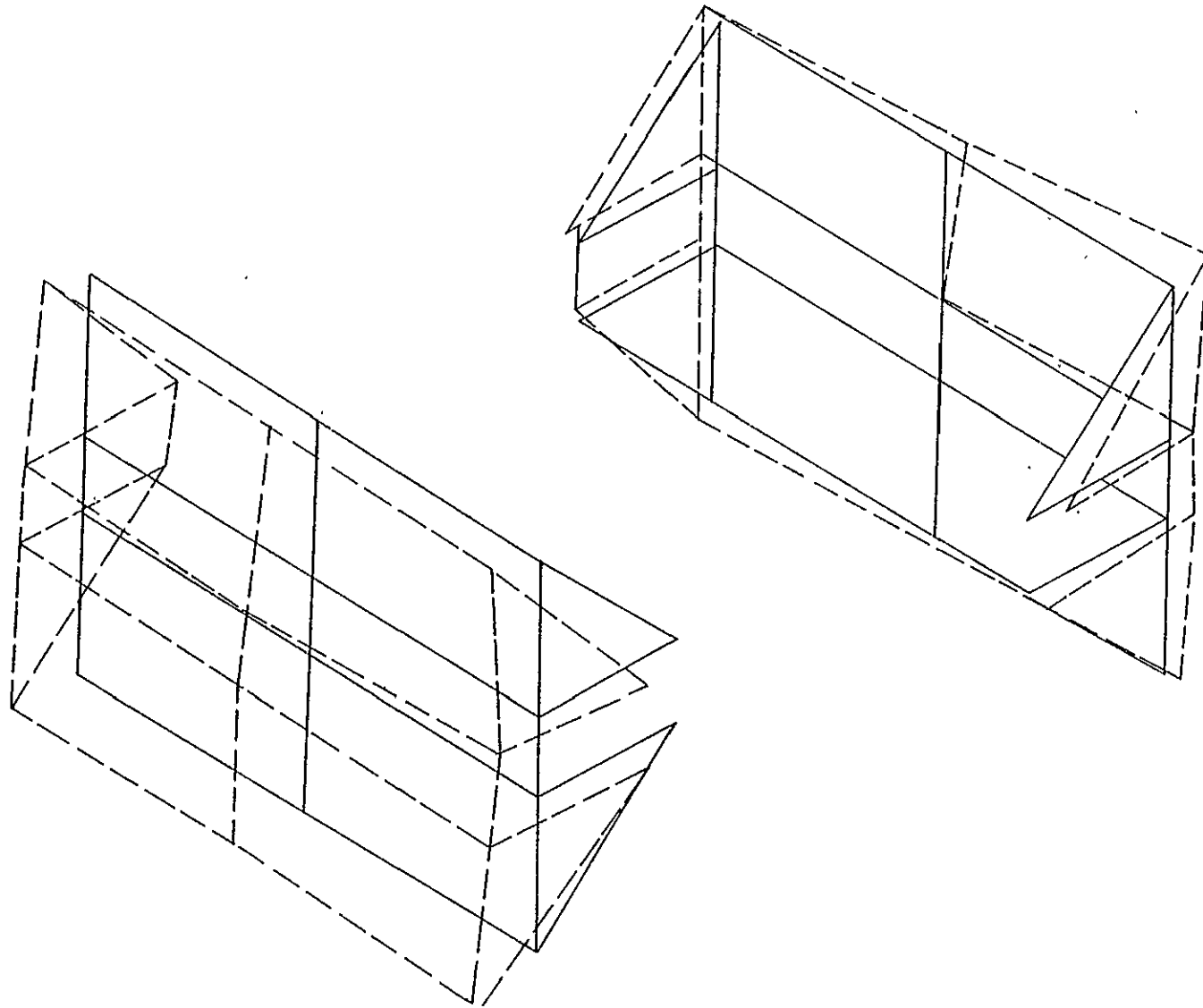


Figure C-4. End Plate Thermal Distortion

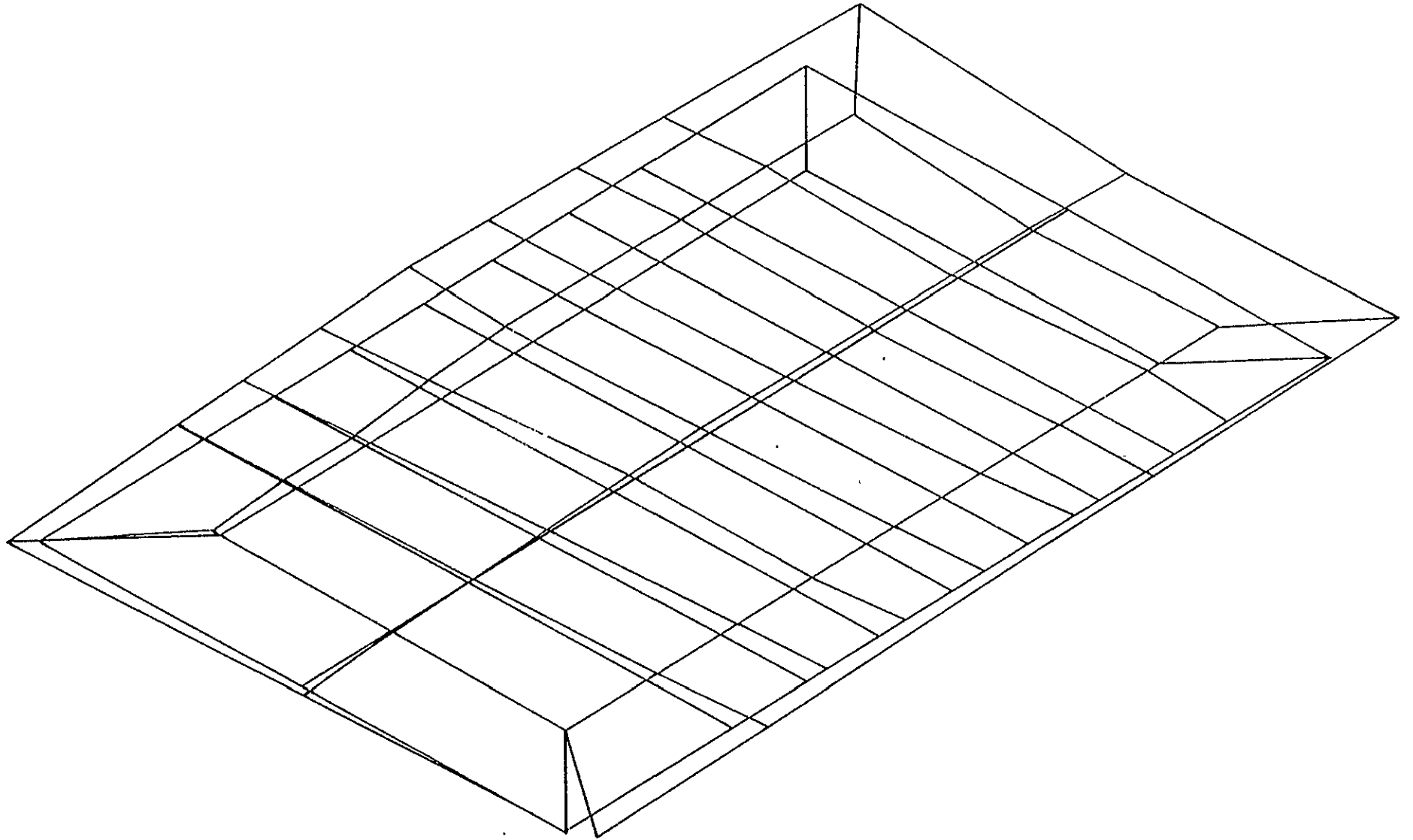
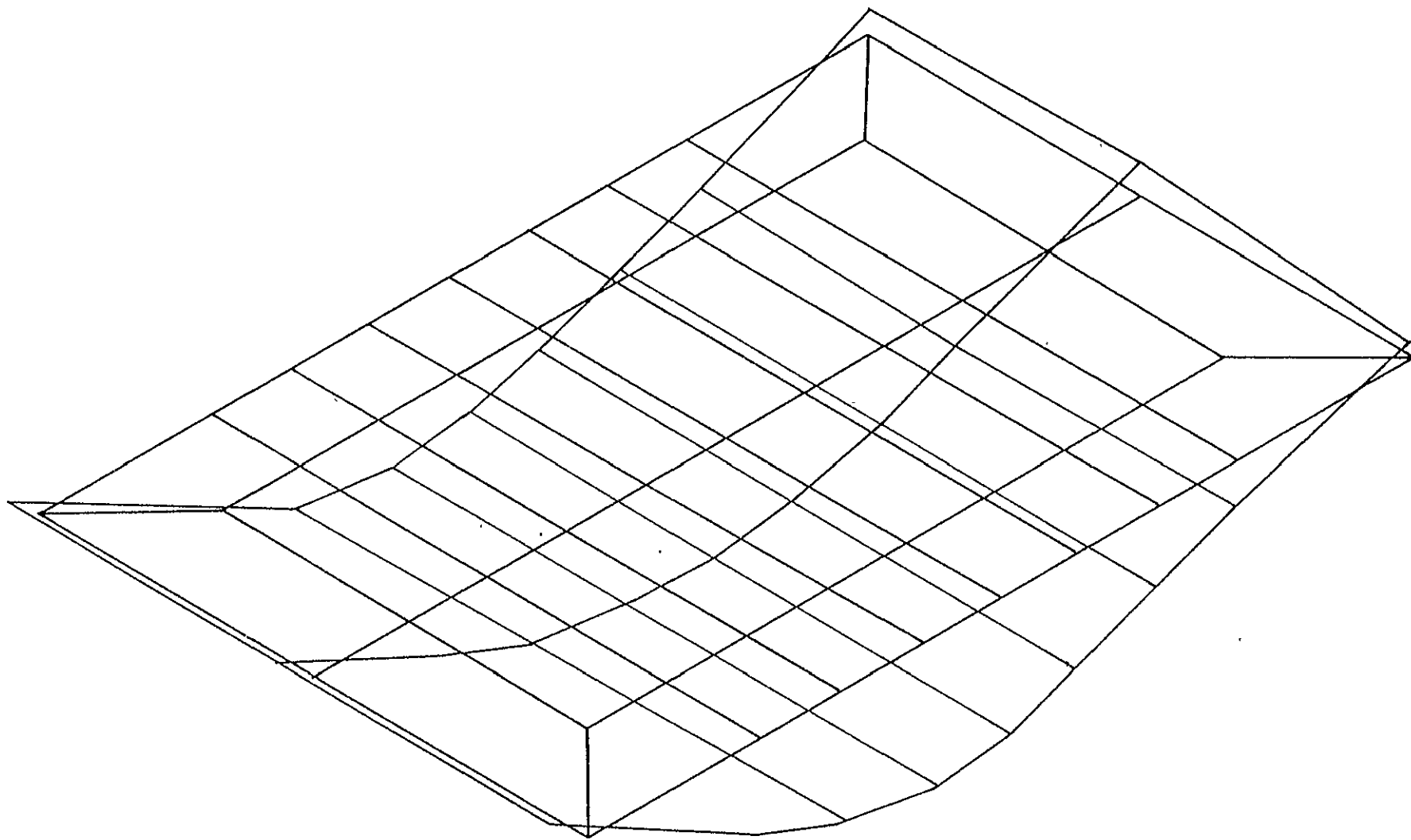


Figure C-5. Bed Plate Thermal Distortions

the resulting distortions. Figure C-6 is a highly exaggerated view of the distortion of the slab. The maximum Invar distortion is $0.1106(10)^{-4}$ inches at node 72. The maximum Noryl distortion is $0.104(10)^{-4}$ inches at node 187.

7. GRAVITY EFFECTS (VERTICAL)

The vertical configuration is defined as the -X direction down. A one "g" acceleration in the X direction was applied and the resulting distortions were calculated. Thermal distortions were not considered. Table C-4 is the computer printout of the distortions. Figure C-7 is the exaggerated distortion plot of the end plate. The maximum distortion of the Invar slab is $0.186(10)^{-5}$ inches at node 72. The Noryl is $0.539(10)^{-5}$ inches at node 192. The distortions in general are an order of magnitude smaller than those obtained in the horizontal orientation.



C-13

Figure C-6. Bed Plate Gravity Distortion-Horizontal

Table C-4. ACCELERATION IN Z

NODE	UX	UY	UZ	NODE	UX	UY	UZ
1	.728520E-08	-.334425E-05	.302294E-05	100	-.590578E-06	.713734E-05	.587207E-04
2	.222178E-06	-.104143E-04	.194329E-05	101	-.361228E-07	.100264E-04	.305395E-05
3	.923482E-07	-.335128E-05	-.410178E-05	103	-.970531E-07	.142917E-04	-.409887E-05
4	.255272E-06	-.209479E-05	-.755460E-05	104	-.249875E-06	-.192488E-04	-.755795E-05
5	.387343E-06	-.737963E-05	-.992618E-05	105	-.356484E-06	-.803824E-06	-.992448E-05
6	.462895E-06	-.166588E-05	-.108736E-04	106	-.411721E-06	-.412089E-05	-.108734E-04
7	.488611E-06	-.956475E-06	-.103028E-04	107	-.420027E-06	-.273419E-05	-.103025E-04
8	.480655E-06	-.371497E-06	-.836664E-05	108	-.405504E-06	-.282924E-05	-.934342E-05
9	.306851E-06	.370339E-07	-.577994E-05	109	-.233734E-06	-.323971E-05	-.527938E-05
11	.176372E-06	.148097E-06	.182042E-05	111	-.134847E-06	-.336198E-05	.180073E-05
12	.138923E-07	-.334879E-05	.214625E-05	112	-.449853E-07	.102131E-04	.220261E-05
14	.905880E-07	-.336577E-05	-.210703E-05	114	-.982292E-07	.161203E-06	-.406700E-05
15	.219653E-06	-.300985E-05	-.743402E-05	115	-.214162E-06	-.182512E-06	-.744131E-05
16	.342143E-06	-.239222E-05	-.975343E-05	116	-.311426E-06	-.797009E-06	-.975177E-05
17	.413898E-06	-.167156E-05	-.106672E-04	117	-.362392E-06	-.151945E-05	-.106667E-04
18	.444861E-06	-.958609E-04	-.102905E-04	118	-.376149E-06	-.223618E-05	-.102905E-04
19	.441173E-06	-.359538E-06	-.814313E-05	119	-.364845E-06	-.283991E-05	-.813988E-05
20	.319617E-06	.545946E-07	.519147E-05	120	-.249281E-06	-.325816E-05	-.519933E-05
22	.179148E-06	.137141E-04	.100694E-05	122	.127133E-06	-.334165E-05	.102743E-05
24	0.	-.339028E-05	0.	124	-.495009E-09	.161635E-06	-.328305E-06
25	.533578E-07	-.334103E-05	-.403567E-05	125	-.587773E-07	.167472E-06	-.396623E-05
26	.137723E-06	-.295911E-05	-.717995E-05	126	-.128596E-06	-.248689E-06	-.719323E-05
27	.223137E-06	-.236336E-05	-.936984E-05	127	-.194228E-06	-.840281E-06	-.935712E-05
28	.280511E-06	-.165831E-05	-.101902E-04	128	-.228473E-06	-.154263E-05	-.101915E-04
29	.318732E-06	-.956269E-06	-.957445E-05	129	-.247649E-06	-.224859E-05	-.957408E-05
30	.339162E-06	-.362760E-06	-.761214E-05	130	-.263028E-06	-.284259E-05	-.761586E-05
31	.359640E-06	-.572941E-08	-.446439E-05	131	-.287242E-06	-.318616E-05	-.447526E-05
32	.309480E-06	.984935E-07	-.147695E-05	132	-.286576E-06	-.326970E-05	-.132447E-05
33	.583887E-08	.334620E-05	.212914E-05	133	.627646E-08	.130563E-06	.213663E-05
34	.517329E-08	-.334625E-05	.301139E-05	134	.636319E-08	.131466E-06	.298567E-05
35	.579579E-08	-.333584E-05	-.690369E-06	135	.706451E-08	.118498E-06	-.539215E-06
36	.863899E-08	-.321162E-05	-.394206E-05	136	-.114899E-07	-.998489E-08	-.394849E-05
37	.101928E-07	-.288056E-05	-.492322E-05	137	.169941E-07	-.348302E-06	-.492481E-05
38	.827780E-08	-.234219E-05	-.896729E-05	138	.260747E-07	-.909570E-06	-.896558E-05
39	.103901E-07	.166041E-05	-.973666E-05	139	.430116E-07	-.160632E-05	-.973814E-05
40	.144529E-07	-.949351E-06	-.905317E-05	140	.554178E-07	-.229989E-05	-.905029E-05
41	.113153E-07	-.342427E-06	-.702647E-05	141	.625059E-07	-.287799E-05	-.704799E-05
42	.522562E-08	.536163E-07	-.399536E-05	142	.699347E-07	-.329703E-05	-.389987E-05
43	0.	0.	0.	143	.764527E-07	-.316257E-05	-.498643E-06
44	.156762E-08	-.614595E-07	.238308E-05	144	.768044E-07	-.304650E-05	.241211E-05
45	-.697404E-09	-.659161E-07	.159622E-05	145	.783570E-07	-.303605E-05	.167772E-05
46	.908185E-08	-.338198E-05	0.	146	.179067E-07	.157708E-06	-.375957E-06
47	-.375558E-07	-.334205E-05	-.405169E-05	147	.847387E-07	.165320E-06	-.397968E-05
48	-.118313E-06	-.297761E-05	-.721274E-05	148	.170918E-06	-.250478E-06	-.722142E-05
49	-.158919E-05	-.242140E-05	-.943028E-05	149	.259014E-06	-.836011E-06	-.942833E-05
50	-.258295E-06	-.172100E-05	-.103319E-04	150	.313276E-06	-.156121E-05	-.103336E-04
51	-.301606E-06	-.995084E-06	-.973604E-05	151	.349873E-06	-.226530E-05	-.973401E-05
52	-.324697E-06	-.403453E-06	-.781429E-05	152	.385181E-06	-.282352E-05	-.782147E-05
53	-.349955E-06	-.381957E-07	-.492214E-05	153	.422965E-06	-.315927E-05	-.493485E-05
54	-.303784E-06	.777163E-07	-.177336E-05	154	.434226E-06	-.327521E-05	-.162404E-05
56	-.754822E-08	-.335974E-05	.213819E-05	156	.572644E-07	.955592E-07	.219582E-05
58	-.733034E-07	-.338606E-05	-.409149E-05	158	.123375E-06	.155474E-06	-.406640E-05
59	-.195705E-06	-.365175E-05	-.748352E-05	159	.258980E-06	-.183889E-06	-.748686E-05
60	-.314734E-06	-.245168E-05	-.986169E-05	160	.380738E-06	-.796030E-06	-.985737E-05
61	-.389085E-06	-.173008E-05	-.108425E-04	161	.444177E-06	-.152052E-05	-.109424E-04
62	-.432637E-06	-.101190E-05	-.103196E-04	162	.475562E-06	-.223798E-05	-.103221E-04
63	-.430896E-06	-.408599E-06	-.843125E-05	163	.483842E-06	-.282983E-05	-.842985E-05
64	-.316648E-06	.186024E-07	-.554656E-05	164	.390968E-06	-.324527E-05	-.555543E-05
66	-.173711E-06	.110760E-06	.574129E-06	166	.281689E-06	-.333022E-05	.574668E-06
67	-.21554E-08	-.335639E-05	.301565E-05	167	.467639E-07	.926308E-07	.304724E-05
69	-.743711E-07	-.337239E-05	-.412406E-05	169	.121963E-06	.133106E-06	-.411980E-05
70	-.229699E-06	-.303985E-05	-.760968E-05	170	.294676E-06	-.199019E-06	-.761089E-05
71	-.359526E-06	-.243945E-05	-.100438E-04	171	.425495E-06	-.804955E-06	-.100415E-04
72	-.438560E-06	-.172404E-05	-.110627E-04	172	.493772E-06	-.152365E-05	-.110629E-04
73	-.476361E-06	-.100893E-05	-.105546E-04	173	.519107E-06	-.223755E-05	-.105555E-04
75	-.805488E-06	-.322807E-08	-.868298E-05	174	.523776E-06	-.282289E-05	-.868154E-05
77	-.170447E-06	.120315E-06	.133888E-05	175	.376497E-06	-.323163E-05	-.567243E-05
78	-.244014E-07	.722967E-05	.304857E-05	177	.290804E-06	-.335091E-05	.131947E-05
79	-.300276E-07	.724174E-05	.211095E-05	178	.185310E-06	-.497327E-05	-.677146E-06
80	.287672E-07	-.104500E-04	.300024E-05	179	.136397E-06	-.475698E-05	-.391103E-05
81	.392667E-07	-.104664E-04	.209585E-05	180	.149969E-06	-.410925E-05	-.684435E-05
82	.930216E-08	.730354E-05	.300770E-05	181	.362634E-08	-.302414E-08	-.877552E-05
83	.844518E-08	.730152E-05	.206418E-05	182	-.275716E-07	-.260223E-05	-.983403E-05
84	-.415934E-09	-.105603E-04	.299702E-05	183	-.547731E-08	-.527142E-05	-.896808E-07
85	.877401E-09	-.105590E-04	.207767E-05	184	-.163764E-06	-.497009E-05	-.397364E-05
86	.414136E-07	.723439E-05	.304743E-05	185	-.388911E-06	-.420563E-05	-.713473E-05
87	.487824E-07	.724671E-05	.210783E-05	186	-.421634E-06	-.310908E-05	-.923274E-05
88	-.270944E-07	-.104802E-04	.299168E-05	187	-.459477E-06	-.267607E-05	-.104028E-04
89	-.360985E-07	-.104911E-04	.208552E-05	188	.146043E-06	-.246242E-05	-.981008E-05
90	-.218658E-06	-.104157E-04	.100584E-05	189	.172574E-06	-.290266E-05	-.895908E-05
91	-.274784E-06	.723526E-05	.194117E-05	190	.203278E-06	-.407087E-05	-.694003E-05
92	.276485E-06	.724218E-05	.101563E-05	191	.420660E-06	-.472053E-05	-.388676E-05
93	.230467E-06	-.105213E-04	.276787E-05	192	.530339E-06	-.492388E-05	-.549615E-06
94	.237096E-06	.117970E-04	.117970E-05	193	.542156E-06	-.242125E-05	-.104255E-04
95	-.150237E-06	.739140E-05	.221072E-05	194	.517175E-06	-.285711E-05	-.941997E-05
96	-.157425E-06	.738766E-05	.116898E-05	195	.651091E-06	-.3498047E-05	-.774024E-05
97	.693316E-06	-.103211E-04	.146204E-05	196	.564754E-06	-.484004E-05	-.489948E-05
98	.690309E-06	-.103270E-04	.579538E-06	197	.513045E-06	-.489144E-05	-.165062E-05
99	-.586559E-06	.712418E-05	.146073E-05				

MAXIMUM VALUE 97 84 172
 MINIMUM VALUE 97 84 172
 DISPL .69336E-06 .105603E-04 .110629E-04

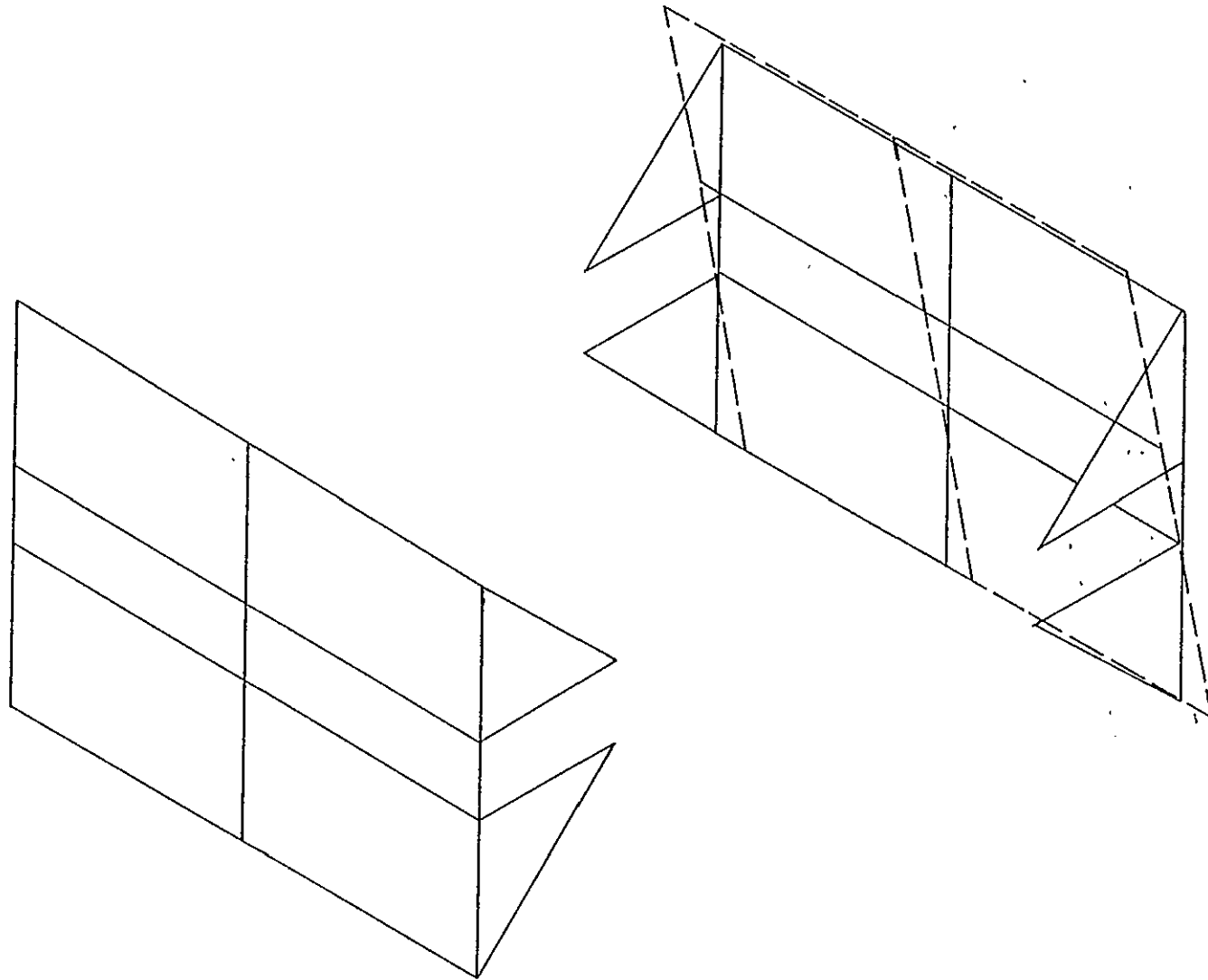


Figure C-7. End Plate Gravity Distortion-Vertical

APPENDIX D

ELECTRONIC DESIGN REVISIONS

1. Final System Modification

Various problems, arising from the radiation control loop concept adopted, necessitated re-evaluation of the overall system.

Specifically, the required event sequence necessary for proper system performance is as follows:

- The flashlamp imparts energy to the laser rod.
- Lase action occurs, controlled by the active modelocker modulator, and is allowed to circulate between the interferometer mirrors for a sufficient time interval to allow pulse narrowing. The lase action must be of extreme low level for this portion of the action.
- High "Q" is established within the interferometer by the "Q" switch, and the resonator energy builds rapidly.
- Pulse transmission switching occurs whenever the resonator energy is near the peak value, to provide a single pulse output.

Slight system modification is effected to allow deletion of the radiation control loop as originally conceived. Specifically, the "Q" switch bias voltage is adjusted to allow sufficient optical resonator gain to produce lase action at approximately 2% above lase threshold. The lase action is of the normal mode type and is controlled by the active modelocker modulator. Thus, this normal mode lase action is composed of a single short duration circulating photon packet of little energy, which is the "seed-pulse" when the high "Q" state is established.

The high "Q" switching action is initiated by the use of an energy detector, or threshold circuit. Whenever the low level "seed-pulse" is of a specific energy content, the threshold circuit generates an output command to activate the "Q" switch driver. This signal is synchronized to the photon-packet position within the resonator in order to prevent pulse slicing.

Various energy sequence illustrations are depicted in Figure 3-5. It is to be noted that the revised system concept energy sequence is identical to the original concept in all respects.

In view of the fact that the remainder of the system is configured as originally conceived, no additional description is considered necessary.

The temporal jitter, for a shot to shot basis, is slightly degraded in the revised concept, since the normal mode gain is somewhat dependant upon optical noise. High level noise results in a reduced time for the "seed-pulse" energy to reach threshold. Conversely, low level noise requires more time for the energy to achieve threshold level. This build time variation results in jitter, from "shot-to-shot", which is in the microsecond region.

2. Revised Q-Switch Interface

Modification of the radiation control loop circuitry allows simplification of the Q-switch Interface circuitry.

As originally conceived, the radiation control voltage was introduced to the Pockels cell at the PTM drive side. Connection was via connector J6, as depicted in Figure 4-6.

Introduction of this control function, required diode CR3 in series with the PTM driver voltage input. Additionally, resistors R3 & R4 were required to provide proper bias currents. The series diode and the stray-capacitance of the additional components degrade the fall time of the PTM driver.

The circuitry was revised to the simpler configuration as depicted in Figure D-1.

Indicated cell voltage transition was noted to be ≤ 6 nanoseconds.

C-4

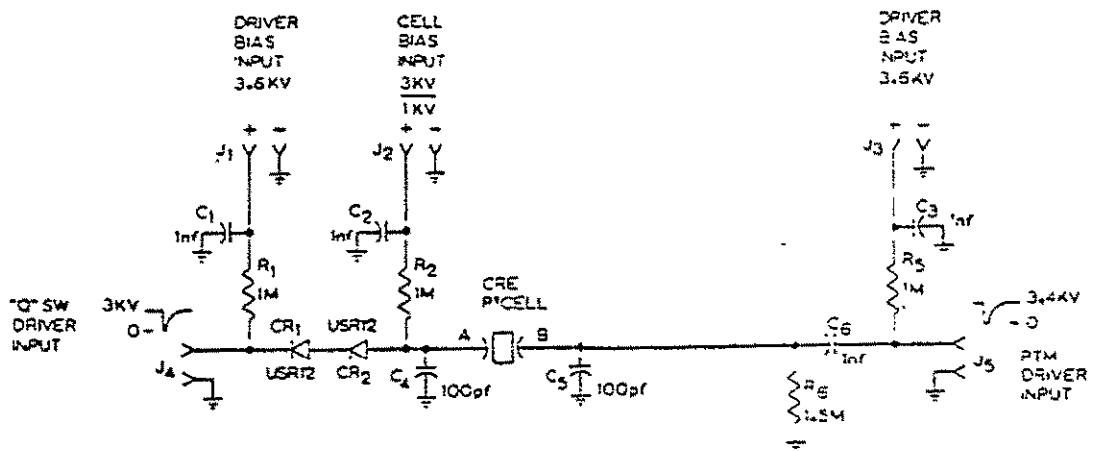


Figure D-1. Q-switch Interface Schematic (Revised)

3. R.F. Power Amplifier (Booster)

The power output of the ENI wide-band amplifier was found to be inadequate to achieve the required modulation depth of the picosecond laser resonator energy. If picosecond pulses were to be reliably generated, more drive voltage was required to the active modelocked modulator cell.

The most expedient move to obtain more drive voltage is the addition of a power amplifier to enhance the output power level. Careful consideration of the available amplifier configurations, i.e. wide-band versus narrow-band and the amplifier class, "A,B,C, or D", resulted in the selection of a narrow band class "C" circuit.

This choice resulted because:

- The resonator round trip frequency is fixed, and varies little with operating ambient temperature; thus, wide-banding is of little advantage. Additionally, by nature, the helical-resonator is a narrow-band mechanism.
- The very nature of the helical-resonator provides an excellent narrow band filtering action; thus, the amplifier distortion and harmonic content are of little consequence.
- Wide-band amplifiers are inherently hard to stabilize from self oscillations.
- Narrow band, class "C" amplifiers exhibit good operating power gain and power conversion efficiency.

The booster power amplifier is depicted schematically in Figure D-2. This circuit is designed to operate in the burst mode. It utilizes a single power source of 28 V ac nominal; it is self biased as a class "C" amplifier; it possesses input/output impedances of approximately 50 ohms; and it is "tuned" in a straight-forward fashion.

Transformer T1 is the input impedance matching transforming network. A ferrite bead transformer is utilized, since the power level is modest. Additionally, this network type requires no input tuning for obtaining match. The input impedance is ≈ 50 ohms, while the output to the transistor base is ≈ 3.5 ohms.

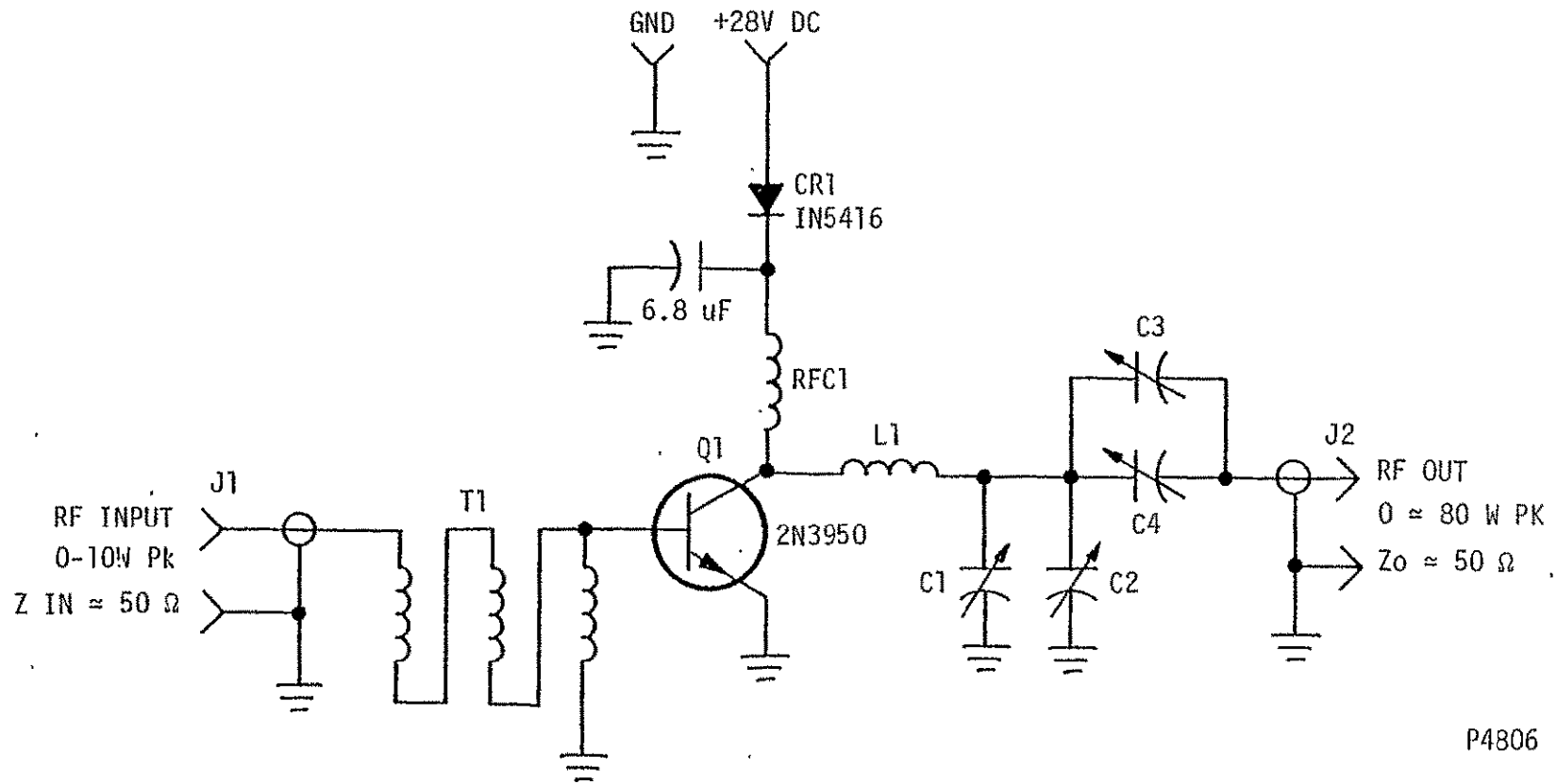


Figure D-2. R.F. (Booster) Power Amplifier

Transistor Q1 is the active gain device. A type 2N3950 is selected to afford the required power gain, and because the device is designed for operation at the 60 MHz frequency region. It is to be noted that selection of devices designed to operate at a much increased frequency generally results in severe parasitic products, since the device gain is optimized for the increased frequency region, additionally, the dc stability becomes annoying to achieve, since the low frequency gain for the extended frequency devices also is enhanced.

Diode, CR1 prevents damage in event of reverse voltage polarity application.

Inductor RFC1 provides a dc voltage path to the collector of Q1, and serves to decouple the R.F. energy from the power source. Capacitor, C5, aids in isolation of the RF energy from the power source.

Capacitors, C1-4, and Inductor L1 comprise the matching network for the collector of Q1. In actuality, this network is of the " π " section type, rather than the apparent "L" section illustrated. The collector output capacity forms the input capacitor for the network. Since this capacity is not a separate component, it is not illustrated.

Capacitors C1-4 are chosen to afford an output match to 50 ohms impedance i.e. the input impedance of the helical-resonator).

Tuning of the output network is accomplished in the following manner:

- a. Adjust C3 and C4 to minimum capacity.
- b. Apply 28 V dc power.
- c. Apply an input signal of the desired frequency (\approx 60 MHz), and increase level until a perceptible increase in collector current is observed (\approx 100 mA dc) in Q1.
- d. "Tune" C1 and C2 for a "dip" or minimum collector current.
- e. With the load connected, "tune" C3 and C4 for a broadening of the response in d. above, i.e. broad tuning null, and an increase in collector current.

f. Monitor the power to the load, and continue the loading, step e, for maximum output. As capacitors C3 and C4 are increased, the power output will rise to a point, then the power output will decrease as the capacitors are further increased. Proper tuning is the setting for maximum output. It is to be noted that interaction between step e. and step d. occurs. Each time step e. is accomplished, it is necessary to repeat step d. Also note that the collector current for the tuning operation is an approximate value.

g. Observe the power output, and increase the input drive level to a value which yields the desired output power. The input level will be ≤ 20 watts peak-pulsed while the output will be ≈ 80 watts peak-pulsed.

This amplifier is designed for burst mode usage only. Continuous wave (cw) operation may be utilized provided the peak output power is less than 30 watts, and provided that the load match is predominantly resistive.

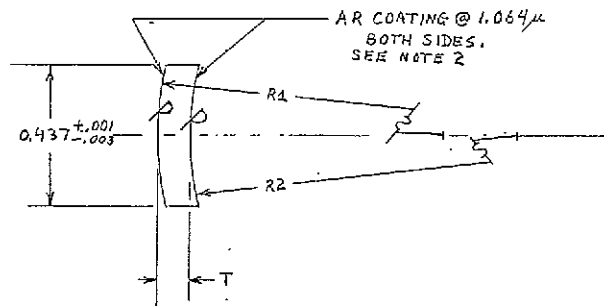
APPENDIX E
AMPLIFIER SUBSYSTEM
OPTICAL DRAWINGS

REVISIONS				
ZONE	LTR	DESCRIPTION	DATE	APPROVED
A		ADDED -7 AND REVISED NOTE 1, NOTE 2. b.		

NOTES: UNLESS OTHERWISE SPECIFIED MANUFACTURE PER ILS SPEC A1007726

- SURFACE QUALITY: (SCRATCH-DIG) 10-5 ON POLISHED SURFACES
- ANTI-REFLECTION COATINGS: MULTILAYER V-COAT
 - 0.2% NORMAL REFLECTION OR LESS AT 1.064 MICRONS
 - DAMAGE THRESHOLD OF AR COATING TO EXCEED 10 GW/CM² AT 1.064 MICRONS FOR 100 PICO SECOND PULSEWIDTH
- POLISH SURFACES MARKED "P", ALL OTHERS ROUGH GRIND.

DASH NO.	R1	R2	T
-1	3.909	0.866	0.100
-3	3.150	0.795	0.100
-5	1.600	39.370	0.125
-7	1.036	0.410	0.100



ORIGINAL PAGE IS OF POOR QUALITY

PODDOUT FRAME 2

PODDOUT FRAME

P4787

QTY	REQD	ITEM	PART NUMBER	SYM	DESCRIPTION	CODE IDENT NO	MATERIAL AND SPECIFICATIONS		
← ASSY									
LIST OF PARTS									
					TOLEANCE UNLESS SPECIFIED	SIGNATURES	DATES		
					XX ± RMS FINISH ✓	CRAPPEYMAN	2/15/77		
					XX ± ANGLE ±	C. B. ANDERSON	2/15/77		
					MATERIAL				
-5	1	B 1014653	0739A		MOSIL	APFD	2-15-77		
-3	1	B 1014653	0739A		QUARTZ	APFD	2-15-77		
-1	1	B 1014653	0739A			APFD			
DASH NO	QTY REQD	NEXT ASSY	USED ON	FINISH	APFD	APFD	APFD		
						SIZE	CODE IDENT NO	DRAWING NO	REV
						C	34860	1017189	A

INTERNATIONAL LASER SYSTEMS INC. ORLANDO, FLORIDA

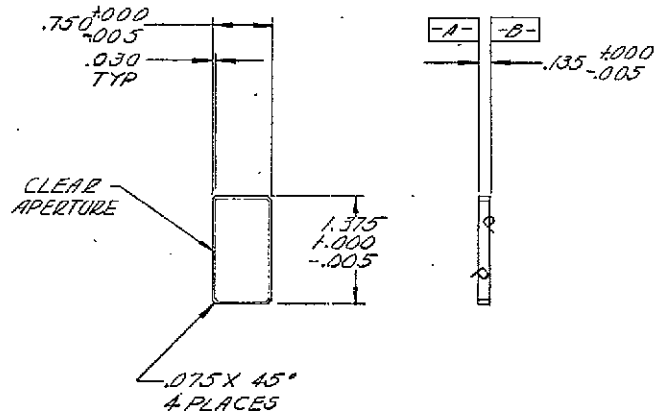
TITLE LENS, COMPENSATING SCOPE SPACEBORNE RANGEFINDER

4 3 2 1
 D D
 C C
 B B
 A A
 REV A
 SIZE DRAWING NO 1017189

NOTES:

UNLESS OTHERWISE SPECIFIED MANUFACTURE PER ILS SPEC A1010290

1. POLISHED SURFACES TO BE FLAT WITHIN $1/4$ WAVELENGTH OF SODIUM LIGHT, PARALLEL TO ONE ARC MINUTE.
2. POLARIZER MUST WITHSTAND FIELDS OF UP TO 10 GW/cm^2 PEAK AT PULSE RATES UP TO 10pps. NOMINAL PULSEWIDTH 100ps. COATING MUST MEET DURABILITY TEST PER MIL-C-675 AND MIL-M-135018.
3. SURFACE QUALITY: (SCRATCH-DIG) 10-5 ON POLISHED SURFACES.



FOLDOUT FRAME 1

FOLDOUT FRAME 2

QTY REQD		ITEM	PART NUMBER	SYM	DESCRIPTION	CODE IDENT NO	MATERIAL AND SPECIFICATIONS
← ASSY							
					LIST OF PARTS		
		TOLERANCE UNLESS SPECIFIED		SIGNATURES		DATES	
		RMS FINISH		OBATSMAN		10-2-76	
		ANGLES ±		CHECKER		10-2-76	
		MATERIAL		APPROV		10-2-76	
		POLARIZED EXIT		DATE		10-4-76	
2		C1015240-9		0-739A		SIZE CODE IDENT NO DRAWING NO	
DASH NO		NEXT ASSY		USED ON		REV	
				FINISH		C 34860 1015640 A	
		APPLICATION		AS SPECIFIED		SCALE FULL SHEET 1 OF 1	

P4790

INTERNATIONAL LASER SYSTEMS INC. ORLANDO, FLORIDA

POLARIZED EXIT

SIZE CODE IDENT NO DRAWING NO REV

C 34860 1015640 A

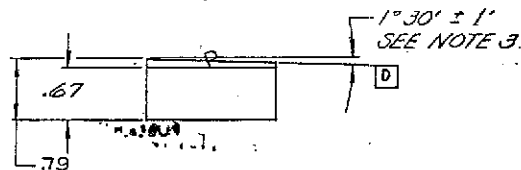
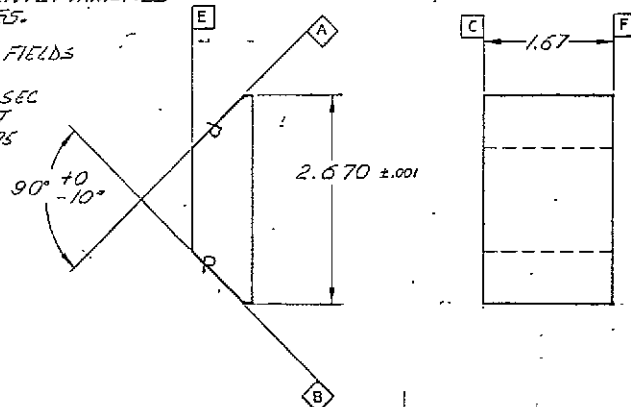
SCALE FULL SHEET 1 OF 1

NOTES:

UNLESS OTHERWISE SPECIFIED MANUFACTURE PER ILS SPEC A1007727

1. USE SURFACE C AS REFERENCE.
2. SURFACES A & B SHOULD BE NORMAL TO C ± 1 MIN.
3. SURFACE D $88^{\circ}30' \pm 1$ MIN TO SURFACE C.
4. SURFACE QUALITY: (SCRATCH-DIG) 10-5 ON SURFACES A, B, & C.
5. ROUGH GRIND ON C, E, & F.
6. ALL POLISHED SURFACES SHALL BE FLAT TO WITHIN $1/4$ WAVELENGTH OF SODIUM LIGHT.
7. TRANSMITTING FACE (SURFACE D) MUST BE ANTI-REFLECTION COATED WITH MULTI-LAYER V-COAT SO THAT NORMAL REFLECTIVITY @ 1.064μ IS $\leq 0.25\%$.
8. SURFACE C SHALL BE PERMANENTLY MARKED FOR IDENTIFICATION PURPOSES.

9. AR COATING MUST WITHSTAND FIELDS UP TO 10 GW/cm^2 AT 10 PPS FOR NOMINAL PULSE WIDTH OF 100 P SEC AT $1.064 \mu\text{m}$. COATING MUST MEET DURABILITY TEST PER MIL-E-475 AND MIL-M-13508.



FOLDOUT FRAME 1

FOLDOUT FRAME 2

REVISIONS				
ZONE	LTR	DESCRIPTION	DATE	APPROVED
B3	A	INC NOR. 1 ±.001 TOL. .050A	12-16-76	Paul J. ...
	B	ADDED NOTE 9		

QTY REQ	ITEM	PART NUMBER	SYM	DESCRIPTION	CODE IDENT NO	MATERIAL AND SPECIFICATIONS
LIST OF PARTS						
TOLERANCE UNLESS SPECIFIED				SIGNATURES	DATE	INTERNATIONAL LASER SYSTEMS INC. ORLANDO, FLORIDA
FINISH: RA15 ✓ XXXX.XX.XX ANGLES 2X				DRAPTSMAN: [Signature] CHECKER: [Signature]	9-23-76	
MATERIAL: FUSED QUARTZ				TITLE: PRISM #3		SIZE: CODE IDENT NO: DRAWING NO: REV. C 34860 1015462 B
DASH NO: 0-739A				APPD: [Signature] 9/24/76 APPD: [Signature] 9-24-76 APPD: [Signature] 1-24-76		
DASH NO	QTY REQ	NEXT ASSY	USED ON	FINISH: No Specified	SCALE: Full	SHEET 1 OF 1

P4789

DRAWING NO 1015462

4

3

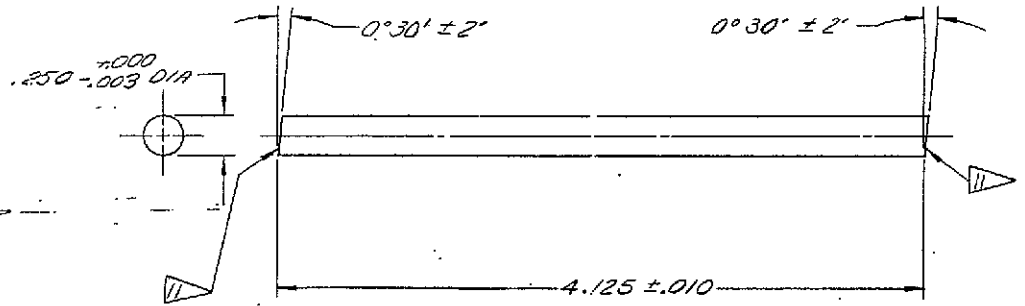
2

1

REVISIONS				
ZONE	LTR	DESCRIPTION	DATE	APPROVED
	A	REVISED NOTE 11	6-20-78	[Signature]

NOTES:

- MATL. MATERIAL TO BE Nd:YAG WITH A MEDIUM DOPING LEVEL OF 1.0% ± 0.1% UNIFORMLY DISTRIBUTED ALONG ROD LENGTH WITHIN ±0.05%. CRYSTAL ORIENTATION TO BE III WITH ROD AXIS PARALLEL TO III.
- CHAMFER: 45° ± 5° x .005 ± .002. (FINE GRIND, DO NOT POLISH CHAMFER)
- THERE SHALL BE NO VISIBLE VOIDS, INCLUSIONS, OR SCATTERING CENTERS; THE ROD SHALL EXHIBIT AN EXTINCTION RATIO ≥ 1000:1 (30dB) (BETWEEN CROSSED POLARIZERS @ λ = 0.6328 μm)
- WAVEFRONT DISTORTION TO BE LESS THAN 1/8 WAVE PER 1.0 INCH OF LENGTH FOR SINGLE PASS OF 0.6328 μm LIGHT (= VAWYMINN-GREEN FRINGE PER 25mm OF LENGTH)
- END FACES OF ROD TO BE FLAT WITHIN 1/10 WAVELENGTH AT 0.6328 μm.
- SCRATCHES AND DIGS ON END SURFACE NOT TO EXCEED SCRATCH 10, DIG 5 PER MIL-O-13530, WITH NO SCRATCHES, DIGS, OR PITS VISIBLE @ 20x IN THE CENTRAL 80% DIAMETER.
- EDGE CHIPS NOT TO EXCEED 0.127mm.
- SIDE OF ROD TO BE FINE GROUND.
- PACKAGE ROD IN REUSABLE CONTAINER PERMANENTLY MARKED WITH ROD SERIAL AND PURCHASE (I.L.S.) NUMBERS.
- END FACES OF ROD TO BE PARALLEL WITHIN 10" OF ARC.
- TWO GEOMETRIC PLANES - CONTAINING THE ROD AXIS AND A LINE BOTH PERPENDICULAR TO THIS AXIS AND PARALLEL TO A ROD FACE - EXIST CORRESPONDING TO EACH ROD FACE. THESE TWO PLANES ARE TO INTERSECT AT AN ANGLE OF 0° 0' ± 3'.



FOLDOUT FRAME 2

FOLDOUT FRAME 1

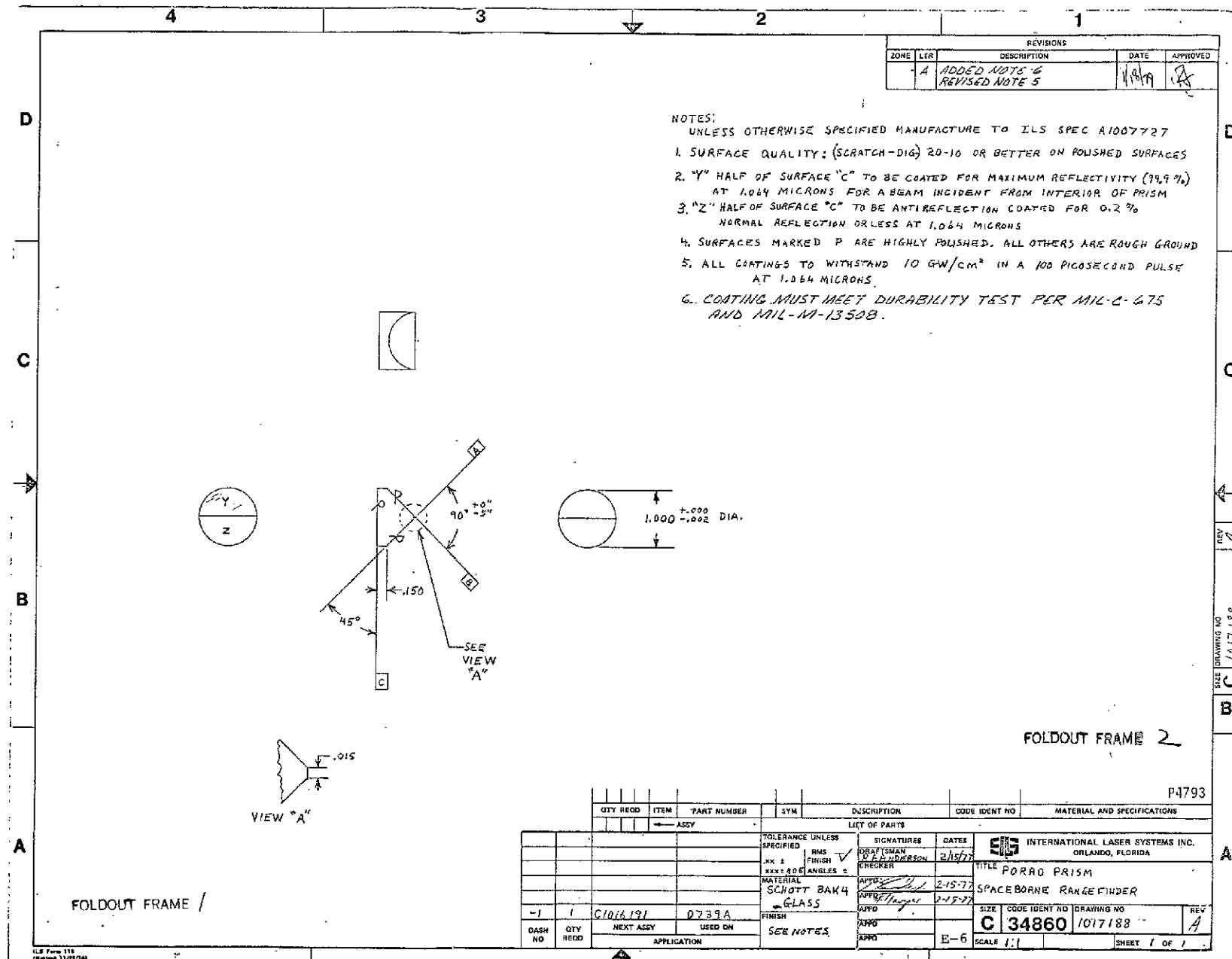
QTY REQD		ITEM	PART NUMBER	SYM	DESCRIPTION	CODE IDENT NO	MATERIAL AND SPECIFICATIONS
		← ASSY →					
		LIST OF PARTS					
		TOLERANCE UNLESS SPECIFIED		SIGNATURES		DATES	
		FINISH		DRAWN		7-16-78	
		ANGLES		CHECKER			
		MATERIAL		APPD		9-17-78	
		See Note 1		PER		11/7/78	
				FINISH			
- 1		0-739A					
DASH NO		NEXT ASSY		USED ON		APPLICATION	
						SEE NOTES:	
						E-5	
						SCALE 2x1	
						SHEET 1 OF 1	

P4783

INTERNATIONAL LASER SYSTEMS INC. ORLANDO, FLORIDA

TITLE LASER ROD AMPLIFIER

SIZE CODE IDENT NO DRAWING NO 34860 1015343



ZONE		REVISIONS		
LEA	DESCRIPTION	DATE	APPROVED	
A	ADDED NOTE 6 REVISED NOTE 5	1/19/77	[Signature]	

NOTES:
 UNLESS OTHERWISE SPECIFIED MANUFACTURE TO ILS SPEC A1007727

1. SURFACE QUALITY: (SCRATCH-DIG) 20-10 OR BETTER ON POLISHED SURFACES
2. "Y" HALF OF SURFACE "C" TO BE COATED FOR MAXIMUM REFLECTIVITY (99.9%) AT 1.064 MICRONS FOR A BEAM INCIDENT FROM INTERIOR OF PRISM
3. "Z" HALF OF SURFACE "C" TO BE ANTIREFLECTION COATED FOR 0.2% NORMAL REFLECTION OR LESS AT 1.064 MICRONS
4. SURFACES MARKED P ARE HIGHLY POLISHED. ALL OTHERS ARE ROUGH GROUND
5. ALL COATINGS TO WITHSTAND 10 GW/CM² IN A 100 PICOSECOND PULSE AT 1.064 MICRONS.
6. COATING MUST MEET DURABILITY TEST PER MIL-C-675 AND MIL-W-1350B.

FOLDOUT FRAME 2

P4793

FOLDOUT FRAME 1

QTY REQD	ITEM	PART NUMBER	SYM	DESCRIPTION	CODE IDENT NO	MATERIAL AND SPECIFICATIONS
				← ASSY		
				TOLERANCE UNLESS SPECIFIED RMS FINISH		
				xxx ± .006		SIGNATURES: D. E. ANDERSON 2/15/77 CHECKER: [Signature] APPRO: [Signature] 2-15-77 APPRO: [Signature] 2-15-77
						DATE: 2/15/77
						TITLE: PORRO PRISM
						INTERNATIONAL LASER SYSTEMS INC. ORLANDO, FLORIDA
						TITLE: SPACEBORNE RANGE FINDER
						SIZE: CODE IDENT NO: 34860 DRAWING NO: 1017188
						REV: A
						SCALE: 1:1 SHEET 1 OF 1

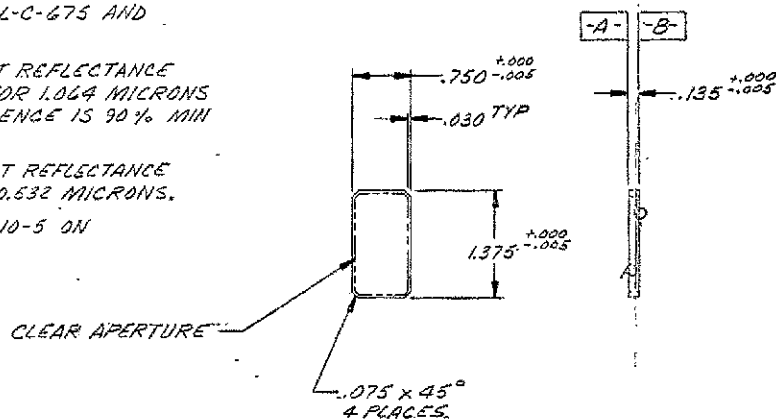
ILS Form 118 (revised 11/22/74)

SIZE: DRAWING NO: 1017188
 REV: A

REVISIONS				
ZONE	LTR	DESCRIPTION	DATE	APPROVED

NOTES:

- UNLESS OTHERWISE SPECIFIED MANUFACTURE PER ILS SPEC A1010290.
- POLISHED SURFACES TO BE FLAT WITHIN $\frac{1}{4}$ WAVELENGTH OF SODIUM LIGHT, PARALLEL TO ONE ARC MINUTE.
- (A) DICHOIC MUST WITHSTAND FIELDS OF UP TO 10 GW/cm² PEAK AT PULSE RATES UP TO 10 PPS WITH A NOMINAL PULSEWIDTH OF 100 PS. COATING MUST MEET DURABILITY TEST PER MIL-C-675 AND MIL-M-13508.
- (B) SIDE **A** TO BE COATED SO THAT REFLECTANCE AT 45° INCIDENCE IS 95% MIN FOR 1.064 MICRONS AND TRANSMISSION AT 45° INCIDENCE IS 90% MIN FOR 0.532 MICRONS.
- (C) SIDE **B** TO BE COATED SO THAT REFLECTANCE AT 45° INCIDENCE IS 0.2% FOR 0.532 MICRONS.
- SURFACE QUALITY:(SCRATCH-DIG)10-5 ON POLISHED SURFACES.



FOLDOUT FRAME 2

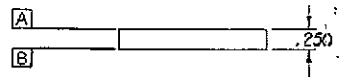
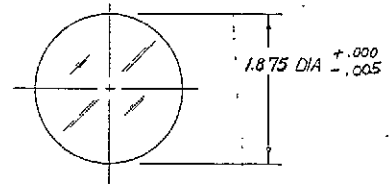
FOLDOUT FRAME 1

QTY RECD	ITEM NO.	CODE IDENT NO.	PART OR IDENTIFYING NO.	SPECIFICATION OR DOCUMENT NO.	NOMENCLATURE OR DESCRIPTION	MATERIAL DESCRIPTION						
← ASSEMBLY						LIST OF PARTS						
UNLESS OTHERWISE SPECIFIED DIMENSIONS ARE AFTER PLATING AND ARE IN INCHES						REV	REV STATUS OF SHEETS					
						4	3	2	1	MP	PL	SHEET
TOLERANCES						ADDITIONAL APPROVALS			CONTR. NO.			
X" ± .01						FCTM			SIGNATURE			DATE
X/16 ± .005						SIGNATURE			DATE			
MATERIAL						SIGNATURE			DATE			
HOMO SIL QUARTZ						SIGNATURE			DATE			
FINISH						SIGNATURE			DATE			
AS SPECIFIED						SIGNATURE			DATE			
PART DASH NO.						PART NO.			TITLE			
1						34860			DICHROIC MIRROR			
NEXT FINAL						CODE IDENT NO			DRAWING NO			
1						C			1023246			
QTY RECD PER ASSY						SCALE			SHEET / OF /			
						B-8			OUTSTANDING NORS			

REV 1023246

REVISIONS				
ZONE	LTR	DESCRIPTION	DATE	APPROVED
	A	INC NOR 1 - 3 ADDED	2-27-77	2-22-77
	B	NOTE 2 (C) WAS 1500 MW/CM ² 20-50 PICOSECOND NOTE 2 (C) WAS 5 GW/CM ² - 110 PICOSECOND	1/16/79	PJ

D
C
B
A



- NOTES -

1. EXCEPT AS NOTED, WINDOW SHALL BE FABRICATED IN ACCORDANCE WITH I.L.S. STANDARD WINDOW AND FILTER SPECIFICATION, DRAWING NO. A-1007729. [REPLACE PROVISION 9. OF A 1007729 WITH NOTE 2 BELOW]
2. SURFACES "A" AND "B" TO BE ANTI REFLECTION COATED FOR MINIMUM REFLECTIVITY WITH MULTILAYER V-COAT AS FOLLOWS:
 - 1 ONLY
 - a. 0.5 % NORMAL REFLECTANCE OR LESS AT 0.53 MICRON
 - b. 0.5 % NORMAL REFLECTANCE OR LESS AT 1.06 MICRON
 - c. ALL COATINGS TO WITHSTAND 10 GW/CM² IN A 100 PICOSECOND PULSE.
 - 3 ONLY
 - d. 0.25 % NORMAL REFLECTANCE OR LESS AT 1.064 MICRON.
 - e. ALL COATINGS TO WITHSTAND 10 GW/CM² AT 1.064 MICRONS - IN A 100 PICOSECOND PULSE.

ORIGINAL PAGE IS
OF POOR QUALITY

FOLDOUT FRAME 2

A FOLDOUT FRAME 1

QTY	REQD	ITEM	PART NUMBER	SYM	DESCRIPTION	CODE IDENT NO	MATERIAL AND SPECIFICATIONS	
← ASSY								
					LIST OF PARTS			
TOLERANCE UNLESS SPECIFIED					SIGNATURES	DATE	INTERNATIONAL LASER SYSTEMS INC. ORLANDO, FLORIDA	
RMS FINISH					12-15-76 12-20-76 12-20-76	TITLE		
MATERIAL						WINDOW, OUTPUT		
-3	1		0-739A	HOMOSIL		APFD	SIZE	
-1	1		0-759	QUARTZ	APFD	CODE IDENT NO	C 34860	
FINISH					APFD	DRAWING NO		
AS SPECIFIED					APFD	SCALE	1/1	
APPLICATION					E-9		SHEET	1 of 1

4 3 2 1
 REV B
 DRAWING NO 1016776
 SCALE 1/1
 SHEET 1 of 1

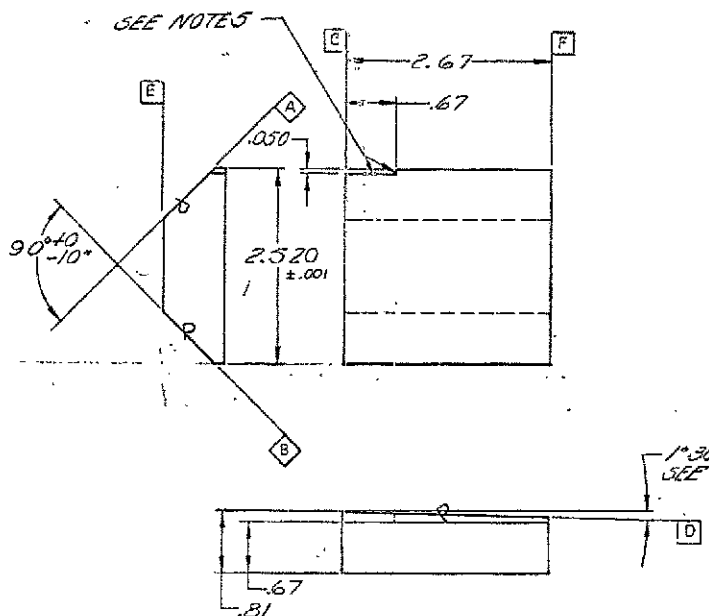
NOTES:

UNLESS OTHERWISE SPECIFIED MANUFACTURE PER IL0 SPEC #1007727

1. USE SURFACE C AS REFERENCE.
2. SURFACES A & B SHOULD BE NORMAL TO C ±1 MIN.
3. SURFACE D 0B°30'±1 MIN TO SURFACE C.
4. SURFACE QUALITY: (SCOTCH-DIG) 10-5 ON SURFACES A, B, & C.
5. ROUGH GRIND ON C, E, F, AND .050 RELIEF
6. ALL POLISHED SURFACES SHALL BE FLAT TO WITHIN 1/4 WAVELENGTH OF SODIUM LIGHT.
7. TRANSMITTING FACE (SURFACE D) MUST BE ANTI-REFLECTION COATED WITH MULTI-LAYER V-COATED SO THAT NORMAL REFLECTIVITY @ 1.064 μ IS ≤ 0.25%.
8. SURFACE C SHALL BE PERMANENTLY MARKED FOR IDENTIFICATION PURPOSES.
9. A/R COATING MUST WITHSTAND FIELDS UP TO 10 GW/CM² AT 10 PPS FOR NOMINAL PULSE WIDTH OF 100 PSEC AT 1.064 μM. COATING MUST MEET DURABILITY TEST PER MIL-C-675 AND MIL-M-13508.

REVISIONS					
ZONE	LTR	DESCRIPTION	DATE	APPROVED	
52	A	INC NOR 1 ±.001 TOL.	12-16-76		
1	B	ADDED NOTE 9			

FOURBIT FRAME 2



FOURBIT FRAME 1

QTY REQD	ITEM	PART NUMBER	SYM	DESCRIPTION	CODE IDENT NO	MATERIAL AND SPECIFICATIONS
← ASSY LIST OF PARTS						
				TOLERANCE UNLESS SPECIFIED	SIGNATURES	DATE
				RMS FINISH	DRAPSMAN	2-13-76
				ANGLES	CHECKER	12/16/76
				MATERIAL	APPR	7-24-76
				APPROVAL	APPR	7-24-76
-1	1	0-739A		FINISH	APPR	7-24-76
		NEXT ASSY USED ON		AS SPECIFIED	APPR	
DASH NO	QTY REQD	APPLICATION			SCALE	SHEET 1 OF

INTERNATIONAL LASER SYSTEMS, INC.
ORLANDO, FLORIDA

TITLE
PRISM #2

SIZE CODE IDENT NO DRAWING NO
C 34860 1015461

REV B

REV B
1015461